The Application of Non-Axisymmetric Endwall Contouring in a $1\frac{1}{2}$ Stage, Rotating Turbine

GLEN CAMPBELL SNEDDEN

The Application of Non-Axisymmetric Endwall Contouring in a 1½ Stage, Rotating Turbine

Glen Campbell Snedden

A thesis presented for the degree of
Doctor of Philosophy

School of Engineering
Durham University
England
2011

The Application of Non-Axisymmetric Endwall Contouring in a 1½ Stage, Rotating Turbine

Glen Campbell Snedden

Submitted for the degree of Doctor of Philosophy

2011

Abstract

Today gas turbines are a crucial part of the global power generation and aviation industries. Small improvements to the efficiencies of individual components within the gas flow path can, over time, lead to dramatic cost savings for the operator and at the same time improve on the amount of carbon dioxide gas emissions to the environment. One such technology is the reduction of secondary flow losses in individual blade rows within the compressor or turbine section of the gas turbine through the use of non-axisymmetric endwall contouring. By introducing subtle geometrical features onto the endwall it has been shown to be possible to improve the efficiency of individual blade rows by between 1 and 2%.

Few studies of these non-axisymmetric endwalls have been performed outside of the two dimensional cascade and computational domain, in addition these endwalls have been designed and tested to improve the performance of blade rows at a single design point with the off design performance having been ignored. The work presented here is aimed at investigating the use of such endwalls in a rotating blade row both at design and off-design conditions and in the presence of an upstream blade row. To this end a 1½ stage, low speed, turbine test rig has been refurbished and a new set of blades was designed to accommodate the profile of the Durham cascade at the hub. The Durham cascade is a *de facto* industry test case for non-axisymmetric endwall applications and therefore a generic, cascade proven, endwall design is available from the literature. The design of this new blade set is unique in that it is openly available.

The results include steady-state 5-hole pressure probe measurements between blade rows and computational fluid dynamics solutions to provide detailed analysis of the flow quality found within the turbine. These results are reproduced for a turbine with annular or reference endwalls and one with the generic P2 endwall design obtained from the Durham cascade.

Experimentally a 1.5% improvement in mixed out stage efficiency at the design condition has been found with a positive trend with increasing load. Additionally the rotor exit flows are show to be generally more uniform in the presence of profiled endwalls. The rotor torque is however reduced by as much as 3.5% and the improved flow uniformity does not always translate into a improved performance in the downstream row.

Insight into the overall performance and fluid mechanics of the generic non-axisymmetric endwall at a variety of load conditions has been gained and an analysis of the parameters commonly used in optimising these endwalls is discussed with C_{ske} being clearly shown to be the superior parameter in this case. CFD evidence suggests that while the cross passage pressure gradient is reduced by endwall profiling the extent of the effect of the change in hub endwalls reaches as far as the tip. The mechanism by which the overall loss is reduced appears to be a through a change in the relative strengths of the suction and pressure side horseshoe vortices and through the delayed migration of the passage cross flow, this change the relationship of these two vortex structures; dispersing the vortex structures as they leave the row and reducing the potential for mixing losses downstream.

"They hadn't dreamed, in the way that people usually used the word, but they'd imagined a different world, and bent metal round it."

Terry Pratchett

Declaration

The work in this thesis is based on research carried out at the Council for Scientific and Industrial Research (CSIR), South Africa by the author, while enrolled at the University of Durham. No part of this thesis has been submitted elsewhere for any other degree or qualification and it is all my own work unless referenced to the contrary in the text.

Acknowledgements

The author would like to thank the following people and institutions for their contributions to the completion of this work:

My supervisors Dr David Gregory-Smith and Dr Grant Ingram for their invaluable input and support in particular taking the time and trouble to travel out to South Africa during the course of this study.

Dwain Dunn for willingly taking the role of research assistant, programming the data reduction software and performing the CFD runs.

Thomas Roos for his expertise with NREC's design codes.

Professor Jeffery Bindon and the University of KwaZulu Natal for willingly giving the CSIR the 1½ stage test rig and their assistance with it.

Central University of Technology, and in particular Gerrie Booysen for providing the manufacturing technology that enabled this work, with skill and efficiency.

Abacus Automation for the installation of the test rig control systems. Siemens Automation and Control for supplying the equipment at cost.

The European Union and Project VITAL who by funding the parallel effort to look at unsteady measurements provided the author with the support and momentum required to make this thesis a reality.

Rhulani Mathebula and the staff at Maintenance Services for their constant willingness to help with the refurbishment and maintenance of the test rig.

Douggie van der Walt of ProMech Engineering also deserves thanks for his innovative solution to the traverse problem and providing us with a network of competent engineering services providers from his vast experience in the industry.

The CSIR and the Department of Science and Technology for funding the effort and sustaining the funding long enough to make it possible to complete a PhD degree. For this I also owe a special thanks to Beeuwen Gerryts.

Thomas Hildebrandt and the NUMECA Ingenieursburo for their software, friendship and assistance.

Jonathan Bergh for challenging me when I needed it most.

Finally I wish to thank Cynthia my wife and children Robert and Julia for their patience and love throughout the extended period of this study and the many hours that I could not spend with them.

Contents

List of Figures

Nomenclature

a	First axial location of interest
A	Area
ACARE	Advisory Council for Aeronautics Research in Europe
A/D	Analogue/Digital
AGS	Abu-Ghannam and Shaw transition model
ASME IGTE	American Society of Mechanical Engineers, International Gas Turbine Expo
b	Second axial location of interest
BPR	Booster Pressure Ratio
CAD	Computer Aided Design
CFD	Computational Fluid Dynamics
C_{ax}	Axial Chord
C_p	Pressure (Loss) Coefficient
CSIR	Council for Scientific and Industrial Research
$C_{\dot{m}}$	Mass flow rate coefficient
C_{ske}	Coefficient of Secondary Kinetic Energy
C_v	Specific heat at constant volume
C_V	Velocity coefficient
C_w	Work coefficient
C_x	Axial velocity
ETH	Swiss Federal Institute for Technology, Zurich
FPR	Fan Pressure Ratio
h	enthalpy
H	Helicity
ISABE	International Society for Air Breathing Engines
ITP	Industria de Turbo Propulsores, S. A.
k	Turbulent kinetic energy
LDV	Laser Doppler Velocimetry
LISA	Multistage Axial Turbine Research Facility at ETH
$\dot{m}$	Mass flow rate
MIT	Massachusetts Institute of Technology
N	Rotor wheel speed (RPM)
NGV	Nozzle Guide Vane or 1st Stator
NREC	Northern Research and Engineering Corporation
OPR	Overall Pressure Ratio
P2	Durham Cascade Endwall Profile 2
P_0	Total pressure
P	Pressure
PID	Proportional Integrative Derivative controller
PLC	Programmable Logic Controller
q	Dynamic head
r	Radius
r	Radius of curvature in the boundary layer
R	Radius of curvature in the freestream

Ř	Result function
RPM	Revolutions Per Minute
RTD	Resistance Temperature Device
SA	Spalart-Allmaras turbulence model
SKEH	Dot product of C_{ske} and Helicity
SST	Shear Stress Transport
T	Temperature
TET	Nominally Turbine Entrance Temperature (K) but defined as per Cumpsty (2009) as mixed NGV exit temperature after coolant addition
u	Specific internal energy
U	Rotor speed
UK	United Kingdom
US	United States (of America)
v	Velocity in the boundary layer
V	Absolute Velocity
w	Specific work
w_i	Uncertainty in measurement of x_i
w_r	Resultant uncertainty
W	Relative Velocity
x	Axial position
x_i	Independent variables
X0, X1, X2, X3, X4	Axial instrumentation Stations, see Figure 12
y^+	Near wall Reynolds number
Y	Any Dimensionless Coefficient
Y_R	Rotor Pressure Loss Coefficient

Greek

α	Absolute Flow Angle
ß	Relative Flow Angle
Δ	Difference
ΔP	Pressure drop
ε	Turbulent energy dissipation rate
η	Efficiency
ρ	Density
τ	Torque
ω	Specific turbulent energy dissipation rate

Subscripts

a	First position
0	Rig inlet or Total property
1	Turbine Inlet
1.5	1½ Stage property
2	Rotor Inlet
3	Rotor Exit
4	Exit to second stator

abs	Absolute (barometric)
ave	Average
b	Second position
bottom	5-hole probe bottom pitch port
centre	5-hole probe centre port
i, j	Matrix reference positions
in	Inlet
is	isentropic
left	5-hole probe left yaw port
max	Maximum
m,mid	Midspan
n	Maximum variable counter
N1	1st Nozzle
N2	2nd Nozzle
Pitch	Pitch property
ref	Reference (at inlet to rig)
r,relative	Relative reference frame
right	5-hole probe right yaw port
R	Rotor
sec	Secondary
Stage	Stage property
s, static	Static property
top	5-hole probe top pitch port
total	Total property
ts	Total-static
tt	Total-total
turbine	1½ stage turbine property
yaw	Yaw property

Superscripts

*	ideal

1 Introduction

The gas turbine has matured remarkably in its short existence, thanks both to its prevalence in military aviation and to the simple fact that it has enabled the civil aviation sector and with it the expansion of world trade. As a result of this success and the massive investment in research that has been a key feature of gas turbine development it is, however, unlikely that a dramatic breakthrough technology will emerge to allow the industry to meet and exceed the ACARE goals (Cumpsty, 2009). Instead a more painstaking approach of small incremental improvement is likely to bear fruit. It is important to note, however, that from 2008 data available for the US airline industry (Swelbar and Belobaba, 2010) it is immediately apparent that more than 2 million litres of fuel can be saved annually by the US civil aviation sector alone if a 0.1% improvement in fuel efficiency can be found at all operating points.

One approach towards the incremental improvement of gas turbines is the development of 3D optimisation of the gas flow path in these engines and one of the first technologies to emerge in this regard is non-axisymmetric endwall contouring of turbines.

The concept of profiling the endwalls between turbine blades and vanes is now a well-established technique (Brennan *et al.*, 2001, Rose *et al.*, 2001, Harvey *et al.*, 2002 and Gonzalez and Lantero, 2006) used to reduce unwanted secondary flows and tangential variation in exit pressure in gas turbines. The reduction of secondary flows is of particular interest as they can contribute as much as half of the loss in a low aspect ratio, high pressure turbine (Gregory-Smith, 2001).

The design of these endwalls has been extensively developed by Rolls-Royce plc and they have been tested in detail in linear cascades, in particular at Durham University, and the results validated in scale engine tests. There are, however, few detailed investigations in rotating turbine rigs.

This work attempts to address this gap by providing a new turbine designed to accept generic endwall designs, into the 1½ stage turbine test rig at the CSIR in South Africa. The following activities were undertaken as part of this study:

- The refurbishment of the 1½ stage turbine rig
- The design and manufacture of an appropriate turbine to accept a non-axisymmetric endwall of open design
- 5-hole probe measurements of the baseline annular and a contoured rotor turbines at 3 running conditions including a design point and a positive and a negative incidence case.
- CFD analysis of the same running conditions to provide detailed information on the fluid mechanics.

This thesis presents the synthesis of experimental and numerical (CFD) results for the first stage of a 1½ stage model test turbine designed such that the Durham cascade blade profile

is the hub profile for the rotor. This in turn allows for the application of a generic endwall modelled on the Durham P2 endwall (Ingram, 2003) to the rotor. The P2 endwall not only represents the most successful of the endwall designs tested in the cascade but is restricted to the blade passage geometrically, making it highly practical for application to the rotating test turbine.

The experimental results are those derived from 5-hole pressure probe measurements and measurements at the inlet of the test rig as well as of the rotor torque and speed. These are compared to CFD results at three load conditions for the rotor.

This thesis comprises the following chapters:

1. Introduction (this section)

2. Literature Review – this section will set the broader context of gas turbine development, the development of the understanding of secondary flows and some of the methods applied to control them before examining some of the literature directly relevant to the study of secondary flows and rotating turbine rig tests.

3. Experimental Method – the layout and instrumentation of the 1½ stage turbine test rig, the design of the blading, and use of the 5-hole probe is explained in this chapter. In addition the uncertainty and repeatability of the test setup is examined in some detail.

4. Computational Method – the use of the commercial CFD code, Numeca Fine^{TM}/TURBO, is expanded on in this section giving details of the mesh and turbulence modelling.

5. Results - this section includes the full set of results both experimental and CFD, drawing direct comparisons between them wherever possible..

6. The effect of endwall profiling on the structure of three dimensional flows – here CFD data such as pressure data and flow visualisations using streamlines are investigated to reveal the nature of the effects on endwall geometry and incidence on the structure of the flow in the turbine passage.

7. Discussion – this chapter discusses the data presented in the previous two chapters to draw together the results and summarise the effect of endwall profiling across the loading conditions of the turbine. Comparisons are also drawn to the cascade data of Ingram (2003). In addition the available parameters are analysed with respect to their suitability as objective functions in the optimisation of endwalls.

8. Conclusions and recommendations

Appendices – The full detail of the turbine blading design is included here in order that the work may be reproduced.

The author was employed by the CSIR in Pretoria, South Africa as Research Group Leader for the Propulsion and Power activities at the Aeronautical Systems Competency while

completing this work part time. Two members of this group of 4 permanent staff were primarily involved with testing on the 1½ stage turbine rig with technical support provided by the wind tunnel contingent of the competency.

Much of this work was carried out in parallel with unsteady measurements of the same turbine as part of the European Union funded Framework Programme 6 project VITAL. As a result, much of the CFD was structured to yield the unsteady results required downstream of this work. In addition the role of this project and the consequent assistance of Dwain Dunn must be acknowledged for their part in accelerating the project and providing much needed research assistance and technical support. Unless otherwise stated in the text all the work reported and discussed within this thesis is that of the author.

2 Literature Review

2.1 The development of gas turbines

Although turbines, and steam turbines in particular, have been in existence since the late 1890's it was Sir Frank Whittle's efforts in a small factory in Rugby in 1936 that ushered in the gas turbine. Today they are to be found in the fields of marine propulsion, power generation and dominate the aviation propulsion market. Part of the attraction of gas turbines, and the reason why Frank Whittle could even think of attempting such a ground breaking development on a budget of just £2000 (Whittle Commemorative Trust), or roughly £95000 today (Shah, 2006), is their simplicity. In their earliest and simplest form they comprised only three components and a single moving part: A single centrifugal compressor wheel, a combustor to heat the compressor outlet flow, and a turbine linked to the compressor by a shaft and generating just enough power to drive the compressor. The excess energy in the turbine out flow was then used to generate thrust.

The development of the gas turbine engine since the late 1940's was driven first by the needs of war, and then the cold war and later by the needs of civil aviation. Figure 1 shows the development of gas turbines in the context of the South African military since it entered the jet age in 1950 in terms of thrust to weight ratio.

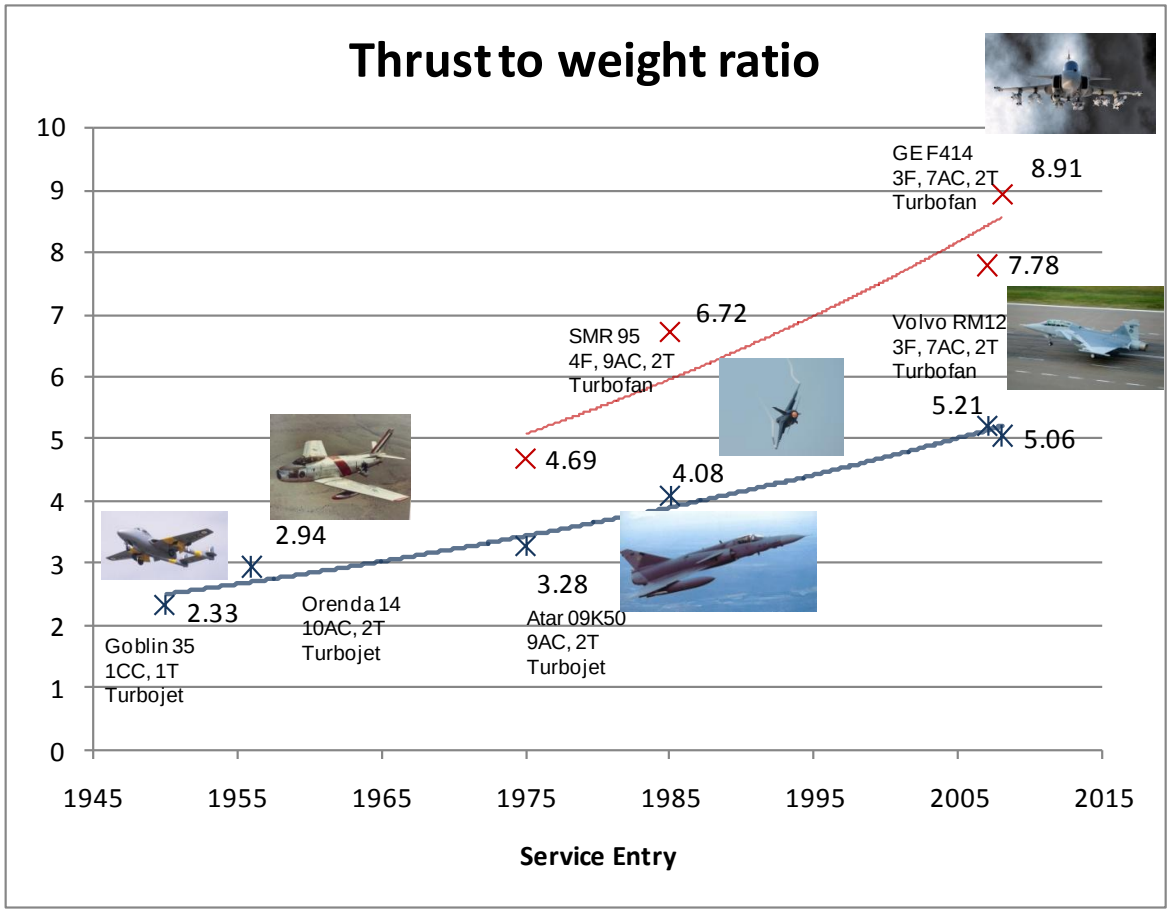

Figure 1: Historical thrust to weight ratios of South African Air Force fighter jet gas turbine engines (red indicates reheat)

In the area of civil aviation (Figure 2) the Rolls-Royce Trent XWB will produce approximately 93000 lb of thrust, more than 100 times the thrust of the first of Power Jet's flying engines in 1941, 69 years previously. A thrust to weight ratio increase from 1.2:1 to greater than 6.2:1.

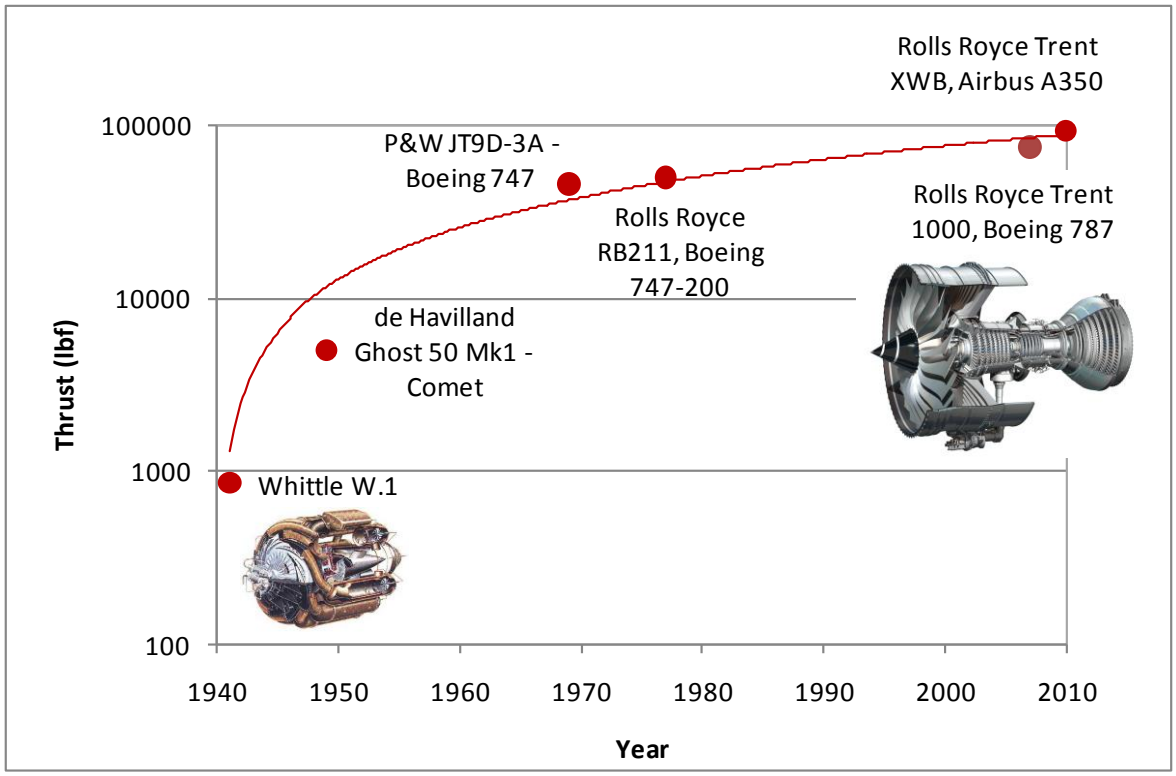

Figure 2: Thrust history of high thrust airliner gas turbine engines on a logarithmic scale (Whittle W.1 and Rolls-Royce Trent XWB inset)

This rapid advance has been achieved by adding complexity only in terms of the details, fundamentally the engine still consists of only three components, although the turbine and compressor are now divided into low, intermediate and high pressure spools resulting in just three moving parts to the propulsive unit. It is at the detailed engineering level that the advances have been made: improvements in materials, cooling, combustion and aerodynamics have resulted in steady increases in component and cycle efficiency over the last 69 years. Cumpsty (2009) believes that apart from the possibility that constant volume combustion and open rotors have for advances in propulsive efficiency, it is down to the detailed design of components to eke out the last small advantage in terms of fuel burn, noise and the reduction of pollutants.

The results of an analysis of the contribution of a 1% efficiency improvement to individual subsystems to the overall efficiency of the ideal engine after Cumpsty (2009) are shown in Table 1. A 1% efficiency improvement in the turbine is shown to result in a 0.4% improvement in the engine efficiency. This makes improvements to the turbine the most attractive in terms of investment in research and development for future engines and agrees with the assessments of both Olsson (2004) on a somewhat bold engine design with an overall pressure ratio of 80, as well as Cumpsty's (2009) own assessment.

Table 1: Effect of module efficiency improvements on the overall system efficiency of a gas turbine engine (method reproduced from Olsson, 2004)

	Efficiency
Datum engine (TET=1475/OPR=40/FPR=1.8/BPR=12.75)	36.4%
+ Fan efficiency +1%	+0.3%
+ Booster Efficiency +1%	+0.1%
+ Compressor Efficiency +1%	+0.1%
+ Combustor Pressure Loss -1%	+0.1%
+ Turbine Efficiency +1%	+0.4%
+ Metal Temperature +1%	+0.1%

Even small advances in efficiency, however, quickly compound given the ever increasing popularity of air travel and freight. A 0.1% improvement in engine efficiency across the operating range equates to nearly 53 million litres saving in fuel for the American aviation business alone (extracted from data from MIT Airline Data project for 2008, (Swelbar and Belobaba, 2010)) if it is applied across the full operating range of the engine. As only 87.4% of airline bulk hours in this study were spent in flight, and many of these would have been at conditions other than cruise, the off-design performance of the engines too becomes important. Therefore even a small advance of 0.1% in turbine efficiency at all engine operating points could result in a saving of 2.1 million litres of fuel annually in North America. In the field of military gas turbines, where the cost of fuel may not be at issue, improvements in turbine efficiency mean more thrust and range.

To study efficiency improvements is to study loss mechanisms and this in turn reveals the increasing importance of the study of turbine endwalls to the future of turbine efficiency improvements.

Losses in a turbine can be attributed to three sources historically identified as: profile loss, leakage loss and endwall loss (Denton, 1993). The first refers to loss generated as a result of boundary layers on the blade where the flow can be described as two dimensional. The second category refers to losses resulting from the flow over the tip of the blade, whether free tip or shrouded and the integration of that flow with the mainstream flow. The last is a combination of factors when studied in depth but is often referred to as loss resulting from secondary flows or three dimensional flows within the blade passage. The fraction that this last category represents of overall loss is influenced by tip clearance and highly dependent on the aspect ratio of the stage.

As engine pressure ratio rises, so the aspect ratio of the high pressure stages is reduced and the secondary losses increase as a fraction of overall loss. In addition the pressing need to reduce engine weight results in highly loaded stages and blades in an effort to reduce the number of stages and blades respectively. Increasing load is a well-known driver in the production of secondary flows as it translates to higher turning angles (Saravanamuttoo *et al.*, 2001 and Denton, 1993).

In addition to the civilian engine market the current trend is for military engines to be made up of the high pressure cores of civilian engines and hence to contain the smallest aspect ratio components. Furthermore the increasing use of drone aircraft by the military means a trend towards smaller engines with an emphasis on range or time on station.

In summary it has been shown that:

- turbine efficiency represents one of the best opportunities to improve the performance of the overall gas turbine cycle
- secondary flow loss mechanisms are of particular interest given the trends towards low aspect ratio components and higher stage and blade loading
- both design and off design performance is important given the compounding effects of millions of bulk hours in the aviation industry world-wide.

What follows in this chapter is a discussion of:

- the current understanding of secondary loss mechanisms in turbines
- some of the methods previously employed to mitigate against these losses with a focus on non-axisymmetric endwalls, which are of particular interest to this study
- and the influence of tip clearance flows which have already been mentioned as a factor in influencing the relative importance of secondary flows, but will also be shown to be influenced by the introduction of endwall contouring.

2.2 Turbine endwall secondary flows

Secondary flows arise when any non-uniform flow is turned (Gregory-Smith, 1984). In a turbine blade passage this as a result of the endwall boundary layer. For a curved flow the radial pressure gradient is given by:

$$\frac{1}{\rho}\frac{\partial P}{\partial R} = \frac{V^2}{R} = \frac{v^2}{r} \qquad \textbf{2-1}$$

Where R is the radius of curvature of the streamline and assuming that the static pressure across the boundary layer is constant, then the pressure gradient at the wall is the same as that set up by the mainstream. In the boundary layer $v \ll V$ and therefore $r \ll R$ leading to overturning of the flow near the wall and to compensate there is underturning further from the wall.

In addition the velocity differential between suction and pressure sides of the blade passage results in the skewing of the vorticity vector. This vorticity vector results from the inlet boundary layer and starts normal to inlet plane but as flow progresses through the passage there is a resultant component of vorticity perpendicular to the mainstream flow.

These factors combine to produce a number of undesirable flow structures and loss generating mechanisms within the blade passage.

Denton (1993) states that approximately two thirds of the endwall loss can be attributed to entropy generation in the annulus boundary layers within, upstream and downstream of the blade row, but this is an inverse function of aspect ratio. A second component is a result of

the mixing loss of the inlet boundary layer amplified by the secondary flow which is an unknown function of:

- Turning
- Blade load
- The ratio of boundary layer thickness to span. (Although this is disputed by Sauer *et al.* (2010), who found no relationship between secondary losses and inlet boundary layer displacement thickness but instead found there to be a dependency on the wall shear stress or coefficient of skin friction)

The third component is that of secondary kinetic energy which is of the order of ¼ of the total loss. The exact proportions of these losses will depend on inlet boundary layer thickness, skew, blade loading and turning. Other contributions may arise from local flow separations, early transition and thickening of boundary layers as a result of the secondary flows.

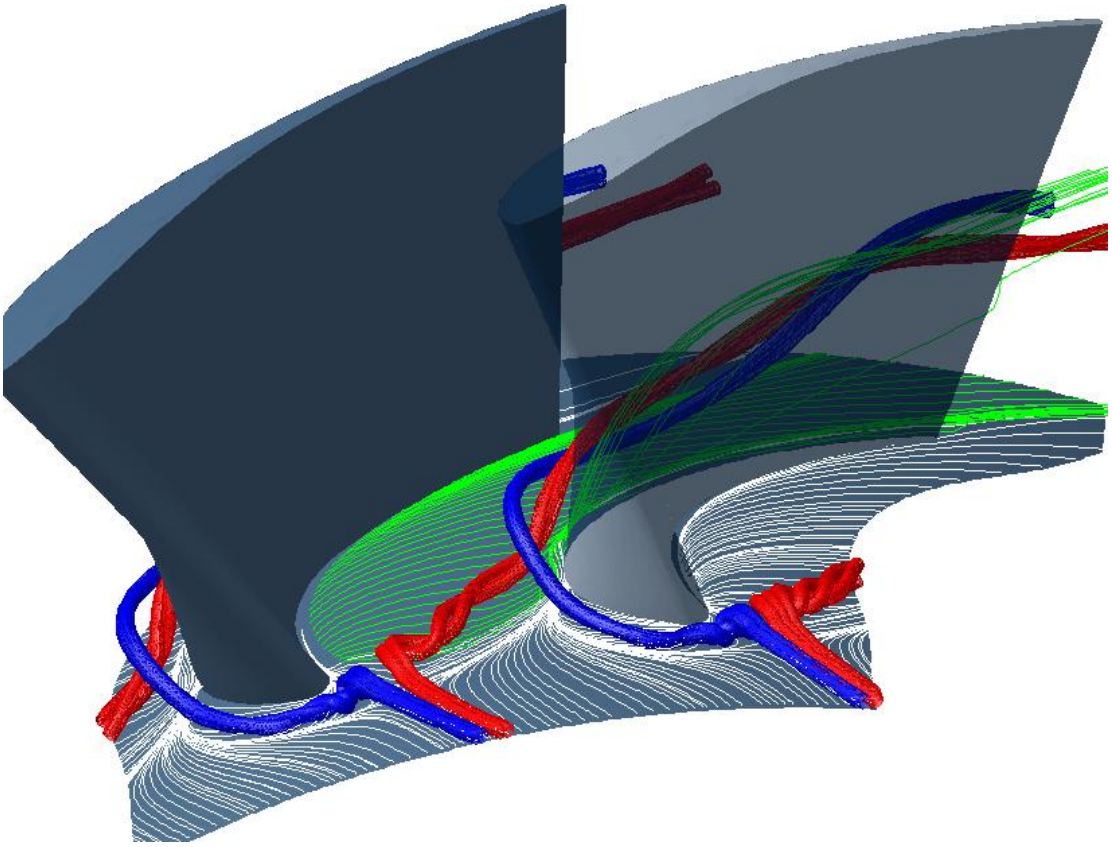

Figure 3: Turbine secondary flows

2.2.1 Main features of turbine endwall secondary flows

To illustrate the complexity of the flows concerned, Figure 3 shows the secondary flows observed as part of this study (Snedden *et al.* 2009b, 2010b) and is similar to those found elsewhere with the exception that vortex structures are accurately indicated in both position and structure, in particular the number of rotations of the vortices are more accurately indicated. Coloured streamtubes are used to indicate the suction side leg of the horseshoe vortex (blue) which remains close to the suction surface, held there by the pressure gradient, and the pressure side leg of the horseshoe vortex (red). The pressure side leg of horseshoe vortex is driven across the passage by the pressure gradient in the same direction

as the endwall cross flow (green streamlines). The pressure side leg of the horseshoe vortex is then observed to collide and combine with or wrap around the suction side leg of the horseshoe vortex and together climb the suction surface and grow in physical size with the further combination of the passage cross flow. The passage vortex results from low momentum flow on the blade and endwall boundary layer being driven across the passage by the pressure difference between pressure and suction surfaces of adjacent blades. An increase in blade turning or loading increases the angle at which the pressure side horseshoe vortex and passage vortex crosses the passage, causing the vortex structure to reach the suction surface sooner (Denton, 1993 quoting Hodson and Dominy, 1983).

Sieverding (1985), Langston *et al.* (1977) and Langston (2001) offer excellent papers on the understanding of secondary flows and propose diagrammatic explanations similar to that of Moon (2001) which is included as Figure 4. In Figure 4 H_s denotes the suction side leg of horseshoe vortex and H_p the pressure side leg of horseshoe vortex and these vortices are often observed to collide, and because they rotate in the opposite sense, wrap around each other, and climb the suction surface, growing in physical size with the further combination of the passage cross flow.

Further pairs of vortices have been observed, in latter day detailed studies and also denoted in Figure 4, to occur at the blade root corners, emanating from behind the saddle point. These are known as corner vortices (Sauer *et al.,* 2001 and Wang *et al.,* 1997) and are often observed to be responsible for a reduction in the overturning close to the hub endwall (Gregory-Smith *et al.,* 1988).

One of the common failings of these illustrations from the literature (for example Langston's model as reproduced by Sieverding, 1985, and other illustrations including Goldstein and Spores, 1998, Sauer *et al.,* 2001, and Moon, 2001) is the large number of turns indicated for each vortex. This serves to illustrate the rotational sense of each vortex but in practise the horseshoe vortices may only rotate fully once or twice through the length of the blade passage as is indicated by the CFD results illustrated in Figure 3 and by Vogt and Zippel, (1996) as reproduced by Eymann *et al.* (2002).

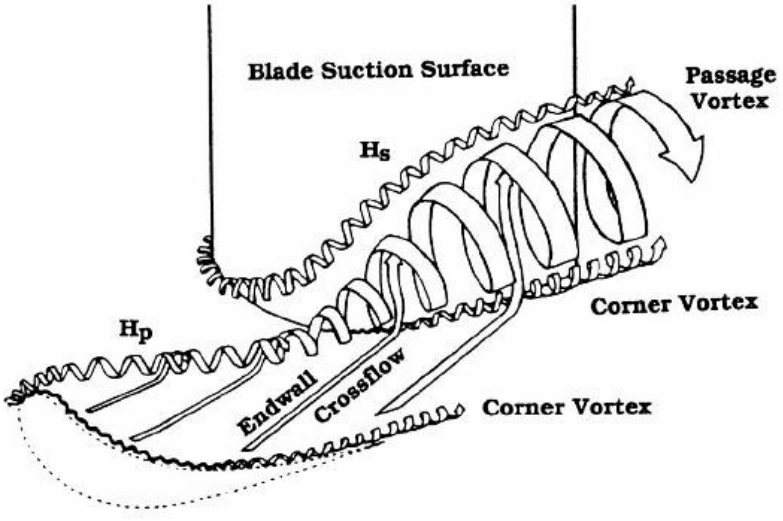

Figure 4: Vortex structure in a turbine cascade (reproduced from Moon, 2001)

2.2.2 Other features of interest

2.2.2.1 The effect of secondary flows on the endwall boundary layer

Harrison (1990) measured endwall shear stresses and found that the boundary layer was laminar over much of the endwall, highlighting the renewal and redevelopment of the boundary layer after the vortex structures of the endwall secondary flow have rolled up the original boundary layer flows. These findings were confirmed by Moore and Gregory-Smith (1996) who extended the work to examine the effect on the production of loss within the cascade.

A similar study by Snedden *et al.* (2009a) reveals similar results regarding the re-laminarisation of the boundary layer for the rotating turbine that is the subject of this study (see Figure 5). Sparse measurement points on the endwall, and either upstream wake unsteadiness or electronic noise through the slip ring make interpreting the results from the thin film sensors difficult, however, sensors 3 and 8 indicate a significant reduction in the turbulent nature of the boundary layer when compared to sensor 2. The greatest implication of this discovery is that the boundary layer on the endwall can be expected to be in transition over quite wide regions and hence fully turbulent computational fluid dynamics simulations cannot accurately capture the wall shear stresses on the endwall.

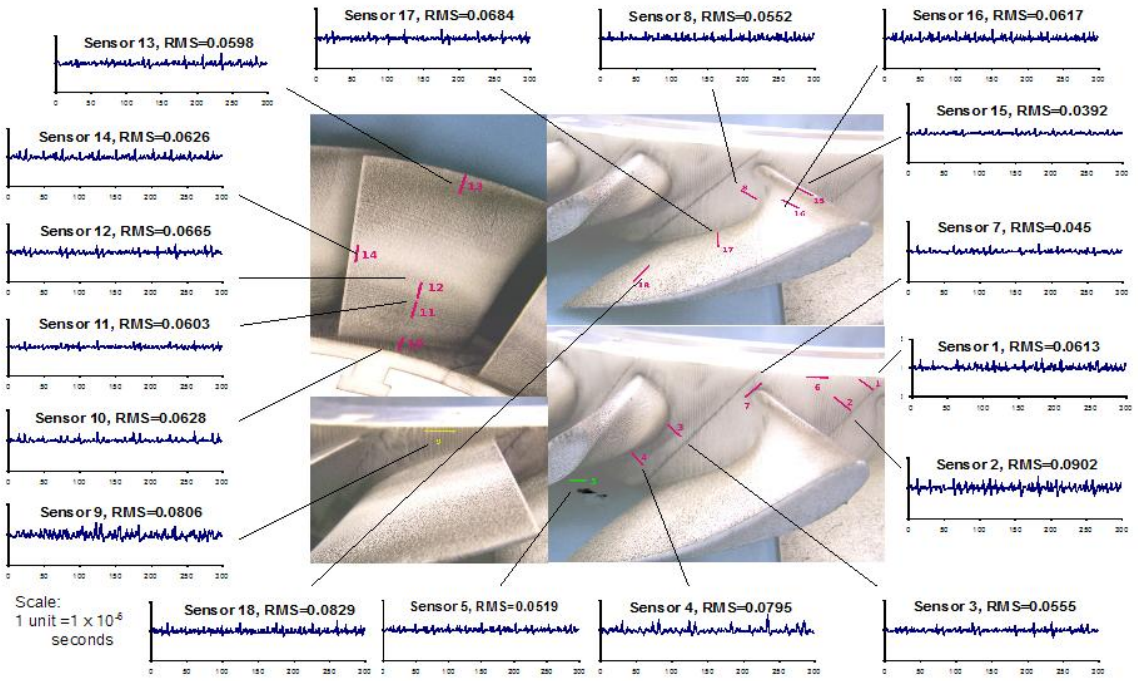

Figure 5: Endwall Shear Stress Meansurements (Snedden *et al.* 2009a)

2.2.2.2 Effects resulting from rotation

Walsh and Gregory-Smith (1987 & 1990) studied the effects of inlet skew on the secondary flows within the Durham cascade using a driven belt upstream of the blades. Negative inlet skew such as that found in the real turbine case had a significant effect on increasing secondary loss, more significant than that of inlet boundary layer thickness. In addition it was noted that the passage vortex became integrated with pressure leg of horseshoe vortex. The opposite was true for positive skew.

Richards and Johnson (1988) noted only that the effect on secondary flows as a result of rotational effects on the stator outlet flow of their 1 stage turbine test rig was increased radial migration resulting from the radial pressure gradient when compared to results from cascades.

Sieverding (1985) identifies inlet incidence as an important driver of flow conditions at the leading edge which is in turn a major driver of secondary flows and one which has not been studied in depth.

2.2.2.3 Effect of off-design operation

Hodson and Dominy (1987a & b) first established that endwall secondary flows for a cascade of low pressure turbine blade profiles were no different to those for a high pressure turbine cascade, exhibiting all the same features. They then proceeded to test a wide array of off-design modes including: incidence, inlet boundary layer thickness, pitch to chord ratio and Reynolds number.

- Increased pitch to chord ratio increases blade loading and therefore increases the cross passage driver for secondary flows resulting in increased loss
- Reynolds number results were somewhat complicated by the presence of a suction surface separation at design which worsens as the Reynold's number drops. Exit angle variation increases with increasing Reynold's number but the position of this peak in underturning does not change. The peak loss on the other hand moves toward the hub at off-design and the peak increases. Interestingly the secondary losses and midspan profile losses were not found to vary with the same function of Reynold's number with profile loss showing the greater sensitivity. Low Reynold's numbers resulted in the greater production of new secondary losses
- Doubling of the boundary layer thickness spread the loss at exit over a greater span but reduced the peak. Overall the increased loss was found to be associated with the increase in inlet loss rather than new secondary loss generation
- Incidence tested was both positive (8.6°) and negative (20.3°) to represent the extremes of operation for this particular blade. Incidence dramatically impacts on the distribution of load on the blade from fore to aft. Yamamoto and Nouse (1988) performed similar tests, confirming the findings and the importance of incidence as a key influencer of secondary flow development.
    - Positive incidence eliminated a pressure side, leading edge separation bubble, however, the increase in forward loading resulted in an increase in the cross passage flow washing onto the suction surface. The separation line on the endwall associated with the pressure side leg of the horseshoe vortex shifted towards the circumferential direction. There was also an increase in the span-wise movement of secondary flow up the suction surface in the latter half of the cascade. Downstream the increased incidence results in notably stronger vortex structures and flow angle deviation; peak vorticity increased by 65% over the design with distinct movement of the vortex centres and deviation towards midspan

- Negative incidence caused a “negative stalling” of the blade increasing the severity of the pressure side separation bubble, otherwise the trends are all opposite to that of the positive incidence case

The results for positive incidence are confirmed by Benner *et al.* (1997) who also found the saddle point to move toward mid-pitch with increased incidence and increased forward loading of the blade. Overall pressure loss in the row did not increase significantly at 10° incidence but doubled at 20°. Tsujita *et al.* (2006) also noted a sharp increase (150% with 5° incidence) in C_{ske} at a plane 50% of axial chord downstream of the blade row. This was less marked at full axial chord downstream (30%). Negative incidence had as little as 10% influence at the latter location with up 20° of negative incidence.

Zoric *et al.* (2007b) presented results for the relatively lightly loaded PAK-B cascade as well as the highly loaded aft and forward loaded PAK-D designs at three incidences. The conclusions from this work noted the increasing strength of the passage vortex with increased loading and the good performance of the forward loaded PAK-D cascade across the incidence range while the aft loaded design stalled at positive incidence. This work, however, did not include the effect of profiled endwalls that have been developed for this cascade at off design incidence.

2.2.2.4 Effects resulting from practical turbine installation features

Moustapha *et al.* (1985) examined the difference between a planar and an annular cascade. They found that the move from planar to annular resulted in a coalescence and doubling in magnitude of exit pitchwise averaged loss and underturning peaks which moved to the increased span of the highest span peak originally measured in the planar cascade.

De la Rosa Blanco *et al.* (2005 & 2006) investigated the effects on endwall secondary flows of upstream platform geometries and leakage flows. Steps between the adjacent platforms caused an increase in the endwall loss and a forward facing step resulted in stronger endwall flows. The introduction of leakage flows had a strong effect on endwall loss and secondary flows that was dependant on flow rate and could in part be likened to increased inlet skew.

Schuepenbach *et al.* (2008b) investigated the effects of suction and injection purge flows in the endwall secondary flows. Injection was found to increase losses by 0.7% in comparison to the purge flow case. Secondary flow structures increased in radial extent but peak magnitude reduced with injection. They also concluded that the fillets between the endwall and blade must be modelled for accurate CFD prediction of loss.

Denton (2010) reports inter-platform strip-seal or slash face leakage as resulting in up to 1.5% additional loss in a turbine stage, while Piggush and Simon (2005) identified these assembly features being the most significant, of the practical features included in their study, to the overall performance of a turbine cascade row.

2.3 Tip clearance flows

Most of the studies of endwall secondary flows have been conducted in planar cascades without tip clearance flows and this is particularly true of studies involving endwall

contouring. Even fewer have been done in rotating rigs that have necessitated the presence of tip clearance with Germain *et al.* and Scheupenbach *et al.* (2008)'s work on the LISA turbine being the most notable exception to date. The presence of tip clearance on all three rows in this study, resulting from the rotation of the casing to provide a tangential traverse component necessitates some understanding of these flows. In addition the effect of the profiling of the hub endwalls extends over the entire blade span, something that few researchers comment on but is visible in the results, such as those of Vazquez and Fidalgo (2010).

Sjolander and Amrud (1987) quote much earlier authors in saying that tip clearance flows are dominated by pressure effects and inertia rather than viscous forces, except at very small clearances. From their own work in a cascade they established that flow over the tip follows the maximum pressure gradient, namely that it is strong over the leading edge where there is forward loading, and weak over the aft sections of the blade where the pressure gradient is lower, and roughly perpendicular to the chamber line in the aft section.

More than one tip leakage vortex was seen by Sjolander and Amrud (1987), one at 15% chord the other at 35% but only at large clearances of, in their case, 2.86%. Classic endwall secondary flow structures like horseshoe vortices only appeared at small tip clearance but the passage vortex remained. The pressure side horseshoe vortex was swallowed into the tip gap along with the inlet boundary layer, but the passage vortex was still present and rotating in opposite sense to the tip clearance vortex with a clearly distinguishable separation line on the casing. Increased tip loading as a result of the leakage flow vortex interactions was also observed and the tip leakage flow structure diameter was seen to be roughly 7.2 times the tip gap for the large tip gap case.

Bindon (1989) broke down tip clearance losses into components and suggested that 39% of the loss came from mixing losses within the gap, 48% from suction side corner losses and the remaining 13% from endwall and secondary flows. He then attempted to propose a model for the flow structure within the tip gap that might explain the observations of tip leakage flows (Bindon, 2010). His measurements within the tip gap of a cascade suggested that flow within the separation bubble on the pressure side of the blade tip converged towards the mid chord region bursting the bubble and destabilising the flow ultimately causing the location of the tip clearance vortex structure at this mid chord location. Much of this explanation is confirmed in the more recent flow visualisations performed by Rao and Camci (2005). Loss structures in the leading edge region were not thought to cause much loss apart from that resulting from the lack of turning.

Yamamoto (1988 & 1989) investigated the effect of tip clearance ratios and incidence on the flows and loss mechanisms within and behind a turbine cascade and suggested the following:

- Loss increases with increasing tip clearance and incidence.
- The passage vortex is more sensitive to incidence than the tip clearance vortex
- Tip clearance flows contributed a higher percentage of overall loss at design than at off-design.

- And that the front part of the tip gap is dominated by the ingestion of the inlet boundary layer.

Zhou and Hodson (2009) summarise the work of the previous authors in this field by distinguishing between ‘thick’ and ‘thin’ blades as a function of tip gap size.

- Thick blades: In the tip gap a separation bubble is formed resulting in a *vena contracta* after which diffusion and mixing occurs followed by reattachment, leakage and vortex formation in the mainstream.
- Thin blades: For thin blades there is no opportunity after the separation bubble and *vena contracta* for diffusion and mixing to occur before the flow leaks into the mainstream and vortex formation occurs.

In general a blade acts as a thick blade over most of its chord and then as a thin blade near the trailing edge.

Yamamoto (1989) gives a highly informative illustration of the secondary flows within a passage including the leakage flows and casing secondary flows, see Figure 6. This illustration is also quite consistent with the results observed as part of this study.

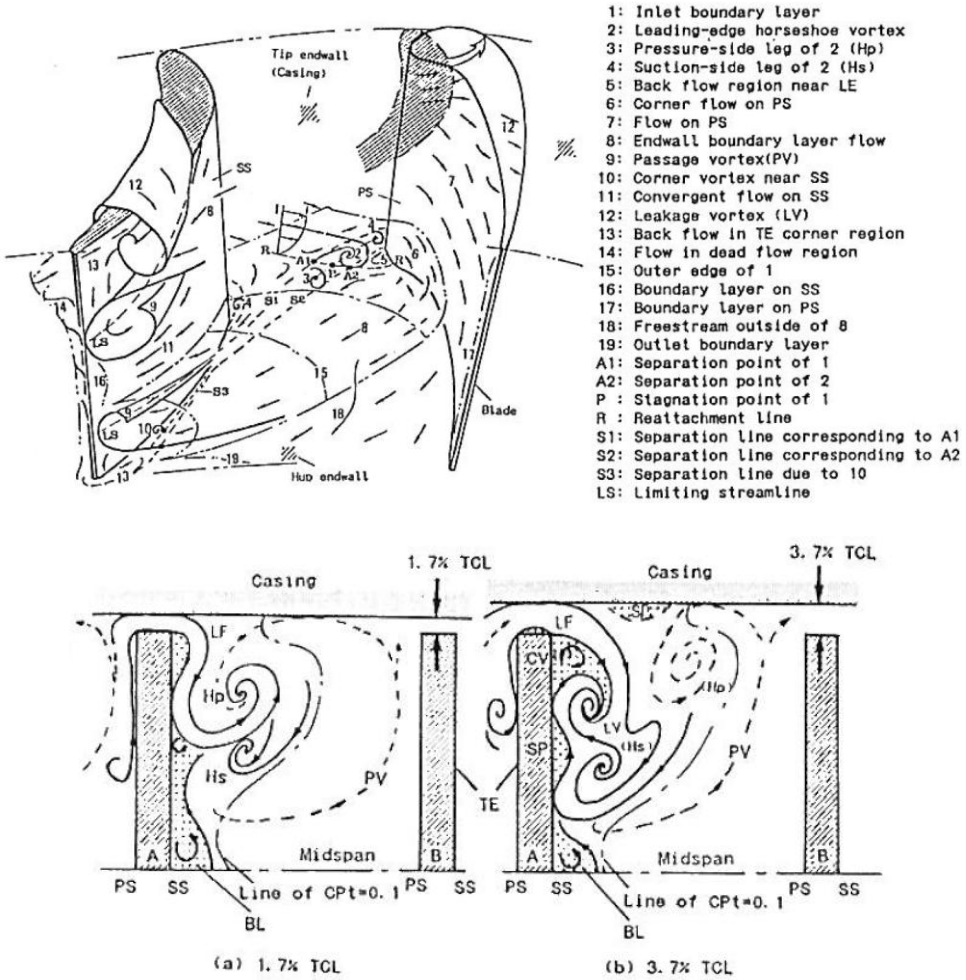

Figure 6: Schematic representation of secondary flows including tip leakage (Yamamoto, 1988)

2.3.1 Effect of rotation on tip clearance flows

Morphis and Bindon (1988) then utilised an annular cascade with rotating endwalls to investigate the effect of relative motion. The effect was found not to alter previous stationary cascade findings. Tip clearance variation affected the size of the separation bubble within the tip gap. Ristic *et al.* (1999) examined the exit flowfield of a low speed, rotating, 1 stage model turbine using LDV and found that unlike cascade tests the secondary flows and relative motion reduced tip leakage confining it to the top 5% of span and largely in the suction surface corner region.

Discussion from Williamson regarding casing relative movement was included in the journal article of Sjolander and Amrud (1987). Vortex size was seen to increase in diameter as a result of the relative movement approaching 8 times the tip gap. No evidence of the vortex structures on the casing was apparent but on the blade suction surface evidence was found to support the presence of multiple vortices; one major and two minor.

2.4 Methods of limiting the generation of endwall loss

This section discusses the methods attempted to date to mitigate endwall loss. For the purposes of this discussion they have been grouped into four main methods: Air injection or suction, three dimensional airfoil design, endwall modifications and combinations of these.

2.4.1 Air injection or suction

Bloxham and Bons (2010) in their recent study present a comprehensive case for blowing or suction that resulted in reduced loss of up to 28% at the higher Reynolds number tested and the power needed to implement this flow control scheme was assessed at 23% of that gained. Their investigations included the removal of low momentum fluid from the region of the pressure side leg of the horseshoe vortex through suction in locations calculated using computational fluid dynamics. Alternatively redirection of the flow by blowing downstream of the pressure side leg of the horseshoe vortex was studied. At a Reynolds number of 25000 both methods yielded similar improvements but at the higher Reynolds numbers of 50000 suction at the higher rates proved more effective than redirection. Their experimental results where only taken at a plane 35% of axial chord downstream and hence one cannot assess the mixing losses fully. In an earlier study Funazaki *et al.* (1996) also utilised suction, this time to reduce the upstream boundary layer thickness in an effort to reduce secondary flows particularly the pressure side horseshoe/passage vortex, however although suction may appear attractive it is difficult to achieve in practise as the holes are normally in use to inject coolant flows to mitigate the extreme temperatures found in turbines.

Biesinger and Gregory-Smith (1993) investigated the use of upstream tangential blowing rate and injection angle as a means to counteract secondary vortex structures. Inlet blowing is a practical means of reducing secondary losses given the presence of platform film cooling. Their intention was, similar to that of Bindon (1979) who attempted to eliminate inlet skew and so improve aerodynamic performance, to simulate the effect of positive inlet skew. They found that low flow rates actually increased the secondary loss by

increasing the quantity of low energy fluid, while low injection angle and high flow rates served to counteract the vortices as hypothesised, too much blowing resulted in countersense vortices which persisted through the cascade. The results showed that at low blowing rates the thickness of the inlet boundary layer was increased, but at high blowing rates the inlet boundary layer was re-energised and with increased counter streamwise vorticity weakened the passage vortex with a resultant reduction in loss. There was however no net effect given the energy required for inlet blowing with jet mixing losses accounting for this failure.

2.4.2 Three-dimensional airfoil design

Denton and Xu (1999) provide an excellent review of nearly all aspects of three dimensional turbomachinery design strategies including several aspects of airfoil design, along with fluid mechanics explanations for the cause and effect of each feature. The design features relevant to this section are:

- blade sweep
- blade lean and curve
- work distribution management
- and localised blade twist.

2.4.2.1 Blade sweep

Forward sweep at the hub endwall occurs naturally in turbine stages in ducts of increasing radius, as is commonly found in intermediate pressure turbines. The effect of sweep can be understood by considering a streamline just outboard of the span-wise location of interest (Denton and Xu, 1999). If the blade is forward swept at the hub then at the leading edge the location of interest will exhibit reduced loading at the leading edge as the loading falls rapidly as one moves towards the streamline outboard of the location of interest as there is no blade and by the opposite reasoning the loading is increased at the trailing edge. Similar logic can be utilised to understand the effect of sweep at the tip.

According to Denton and Xu (1999) sweep is not commonly used in subsonic blading but has the potential to reduce leading edge loading with localised forward sweep or to reduce load at the trailing edge by sweeping the trailing edge downstream. In practise this would resemble a localised lengthening of the blade chord either at the leading edge or trailing edge. Bagshaw *et al.* (2008a & b) have however utilised forward sweep of the leading edge in combination with other techniques to influence endwall flows in a subsonic cascade case and their work is discussed later.

Sharma *et al.* (2003) utilise sweep in a different way, reducing the chord at hub and tip and moving both leading and trailing edges towards the blade centre of gravity. This is done to reduce the blade wetted area in this region and so reduce form drag. Their research is discussed in more detail as part of the discussion on blade lean.

Two further studies represent cases of leading edge sweep, so extensive in geometrical influence that they might be considered to incorporate aspects of non-axisymmetric endwall contouring, are reported in the literature. Leading edge bulbs (Sauer *et al.*, 2001, Becz *et al.*, 2003) and fillets (such as the work by Lethander *et al.*, 2003 and Zess and

Thole, 2002) appear very similar in design and resultant geometric features, however these two distinct concepts are designed with different reported purposes. Sauer *et al.* (2001) claim that the bulb has the potential to strengthen the suction side horseshoe vortex, thereby weakening the passage vortex, as they rotate in opposite senses. This in turn weakens the interaction of the passage vortex with the blade boundary layer. Sauer *et al.* (2001) report an unprecedented 47% reduction in secondary flow or endwall loss, although this was not entirely successfully reproduced by Becz *et al.* (2003). Fillets, such as the work by Lethander *et al.* (2003) and Zess and Thole (2002), are designed to accelerate the endwall boundary layer and flatten the inlet total pressure gradient in an attempt to prevent the development of the horseshoe vortex. The study of fillets has largely centred on the reduction of the high heat transfer levels associated with secondary flows and there is little discussion of loss but bold assertions are made regarding the potential of the method to eliminate the horseshoe vortices. Given the nature of these respective geometries it is reasonable to expect that off-design incidence would dramatically affect the efficacy of these designs, but there is no literature in this regard.

2.4.2.2 Blade lean and curve

By exploiting the fact that the constant pressure lines within the passage of the turbine remain nearly radial and frozen relative to the blade section one can alter the load distribution from hub to tip by leaning, either linearly or on an arc (compound lean). This is possible as the streamline curvature is at least an order of magnitude greater in the axial rather than tangential plane (Denton and Xu, 1999). Therefore one can move the hub and tip sections of a blade into regions of higher pressure and thereby reduce the load at the hub and tip and increase it at midspan, this is known as positive compound lean, where the pressure side of the blade forms an acute angle with the endwall. The opposite is known as negative (or reverse) compound lean, where the suction side of the blade forms an acute angle with the endwall.

Denton and Xu (1999) list several possible explanations as to why lean reduces endwall loss, and while the correct answer may not be known, it is clear that positive compound lean reduces loss near the endwall, but the increased load at midspan resulting in little or no net gain. Harrison (1992) showed that the loss cores behind compound leant blades were generally not as intense as a result of the diminished free stream velocities near the hub but the wakes were reported to be thicker as a result of the increased load at midspan. Outlet flows were more uniform however and resulted in reduced mixing losses downstream of the cascade as well as higher and more consistent turning angles and it was therefore believed that the true benefit of compound blade lean was to be found in the downstream blade rows.

Han *et al.* (1994) investigated the effects of simple lean, as well as compound lean, both positive and negative, and like Harrison (1992) discovered that positive compound lean reduces the radial influence of the endwall loss structures while the opposite is true for reverse compound lean. These changes were the result of significant influence of the compound lean over the radial pressure gradients in the passage.

After initial 1½ stage rig tests of positive lean airfoils yielded almost no discernable

improvement; Sharma *et al.* (2003) investigated the effects of compound lean, both negative as well as positive lean in combination with sweep in some detail. Cascade tests of reverse or negative lean airfoils showed the lowest loss at midspan while the midspan loss of the positive lean airfoil was higher than the baseline. This was explained by the migration of low momentum flow from the endwall region to midspan as a result of the positive lean. Positive lean therefore reduced loss close to the endwall but increased loss at midspan, while the exit flow angle was higher at the endwall and reduced at midspan. Negative lean had the opposite effect on loss, decreasing turning from the endwall to 40% span and matching that of the baseline at midspan. By designing the airfoil to exhibit uniform radial static pressure distributions on the blade suction surface using a series of Euler solutions and utilising sweep to reduce the effective wetted area of the blade root and tip the best overall results were obtained. In addition, later rotating rig results across a range of speeds showed the 0.5% benefit of positive lean blades with sweep to be consistent across a wide off-design envelope, something confirmed by the results of Wang *et al.* (1991). Purely leant (positive) blades showed no benefit over the baseline over an even wider operating range.

2.4.2.3 Work distribution management

Aft loading of the blade profile is one method designed to delay the point at which the driving force for secondary flows comes into effect, this is achieved by moving the profile maximum thickness and work distribution aft. Weiss and Fottner (1995) investigated the secondary flow losses generated in two cascades, one aft loaded, and the other front loaded, while the other design features remained the same. Aft loading reduced all measures of loss far downstream and exhibited weaker passage vortex flows. Close to the blade exit however, secondary losses were almost equivalent. The aft loaded blade featured a peak pressure gradient only in the throat where the boundary layer is thin, while that for the front loaded blade occurs in a region where a relatively thick boundary layer exists and where velocity gradients are high, this results in the generation of stronger vortex structures in the front loaded case.

Pullan *et al.* (2005) investigated the use of mid-chord and aft loaded nozzle guide vanes and achieved a 0.5% loss reduction with the use of the aft loaded nozzle guide vanes in the test facility. Entropy production on the endwall and blade surfaces was reduced by 24% over the baseline mid-chord loaded blading.

2.4.2.4 Localised blade twist

Early evidence of this approach is given by Schlegel *et al.* (1976) who present a dramatically altered research turbine described as being redesigned by radial work redistribution. The design objectives were to increase midspan work over that of the baseline and thereby enable lower loading at hub and tip to reduce endwall losses in the low aspect turbine in question. In part this was achieved by specifying a parabolic stator exit angle distribution. The results indicated a roughly 1% improvement in efficiency over a broad range of load. Above design load the turbine improvements decline however, matching those of the baseline.

Lampart *et al.* (1999) describe both compound lean and twist as increasing the pressure at the endwalls and hence reducing the velocity there, which in turn reduces the secondary flow strength. With compound twist designs the decreased velocities at the endwalls result in increased stagger angles, which have the potential to increase profile losses. Mass flow is not redistributed to the endwall in the rotor however. Lampart *et al.* (1999) indicates 0.4% efficiency increases as possible, but refers to other authors as having obtained 1.2%.

The blade stacking approach of Watanabe and Harada (1999) is also aimed at reducing the cross passage flow, not by altering the work distribution but rather by increasing the product of radius and outlet absolute tangential velocity at midspan by altering the stacking only. Increases of 2 to 2.5% in stage efficiency are claimed. Like Lampart *et al.* (1999), Watanabe and Harada (1999) refer to their method of controlled stacking or twist as superior to blade lean and curve as a result of the latter's resultant increased loading of the midspan which would naturally tend to increase loss in this region. This was not observed after the implementation of their method.

Watanabe and Harada (1999) proposed maintaining a constant value of blade exit circulation (the product of radius and tangential velocity components) by varying the blade or stacking angle through an inverse 3D design method utilising CFD. They claim a 2 to 2.5% increase in efficiency across a range of operating conditions although this claim is less impressive when one discovers that this value represents the same order of magnitude as their maximum uncertainty. Furthermore they claim reduced cross passage migration of the flow at the endwall and reduced disturbance of the streamlines at the leading edge resulting from the pressure side leg of the horseshoe vortex.

Overall this method seems simple to implement compared to sweep and twist and was referred to by Denton at the presentation of his paper Denton (2010) and is described in Denton and Xu (1999) as such.

2.4.3 Endwall modifications

These include endwall fences and axisymmetric and non-axisymmetric endwall profiling.

2.4.3.1 Endwall fences

As with wing fences this is a direct method to obstruct and correct secondary flows, Chung *et al.* (1991), effectively reducing individual blade loading in a localised manner by increasing solidity at the hub. Kawai (1994) claims the additional advantages of diminishing the thickness of the endwall vorticity and loss regions and attenuating over-turning at the endwall while reducing under-turning at midspan. While Kawai (1994) clearly showed that endwall fences could overcome the losses introduced into the flow as a result of their presence and be used to reduce overall loss and improve the flow quality entering downstream stages, the major question regarding their practical application is their survivability in the extremely harsh temperatures of a real gas turbine (Beisinger and Gregory-Smith, 1993).

There is little evidence of their use in practise although Sharma *et al.* (2003) did mention them in passing although they were not ultimately used.

2.4.3.2 Axisymmetric contouring

This method has been investigated by many authors and is commonly known as the Russian kink. One such study is that of Boyle *et al.* (1981) whose experiments showed a 22% reduction in loss or a 0.8% increase in efficiency, see Figure 7. These radial contractions are generally used to accelerate the flow in the latter half of the stator row after the majority of the turning has taken place at favourably low velocities. The acceleration then reduces the boundary layer thickness in the latter half of the passage, thereby reducing the propensity for cross channel flows as well as reducing the radial driving forces for secondary flows.

Haas (1982) investigated two such contoured stators in comparison to an annular baseline and discovered that the contouring failed to have a significant effect on secondary flow losses. Instead the decrease in losses and kinetic energy loss was attributed to a reduction in boundary layer growth as a result of the acceleration provided by the contouring. Atkins (1987) investigated seven different endwall profiles and asserts that a significant reduction in the loss generated with a blade row was possible, but his results indicate that these loss reductions lose significance the further downstream of the blade row one measures total pressure loss.

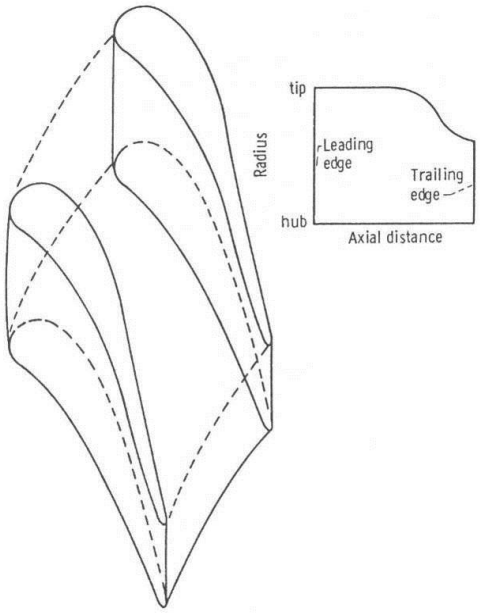

Figure 7: Axisymmetric endwall contouring or the so called 'Russian kink', reproduced from Boyle *et al.* 1981

Sharma *et al.* (2003) also included an endwall contour in their extensive matrix of tests. The endwall reported was divergent and resulted in distinctly higher loss overall and across the span except in the 0-25% span region. Like the endwall tested by Michelassi *et al.* (1998) the endwall tested by Sharma *et al.* (2005) may have originally been intended for use in a transonic stage in which case the design intent was to increase the flow velocities in the latter part of the passage through endwall contouring and yet at subsonic speeds the opposite would occur with resultant pressure recovery.

2.4.3.3 Non-axisymmetric contouring

In this department Gregory-Smith together with Rolls-Royce and Alstom were first in presenting their findings, largely of CFD results and highly detailed measurements of the linear rotor cascade dubbed the 'Durham Cascade' which has in fact become an industry test case (Gregory-Smith, 1995). Ingram *et al.* (2002) show a 24% reduction in secondary loss as a result of implementing non-axisymmetric endwalls in a cascade, while Brennan and Harvey *et al.* (2001 & 2002) claim a one-third reduction in endwall loss or a 0.59% increase in stage efficiency for the high pressure turbine, and even 0.9% efficiency improvement in the intermediate pressure turbine of the Rolls-Royce Trent 500 engine, using non-axisymmetric contouring, see Figure 8. ITP (Gonzalez and Lantero, 2006 and Torre *et al.*, 2006) have also shown contoured endwalls to have a distinct advantage over annular endwalls, even at high aspect ratios.

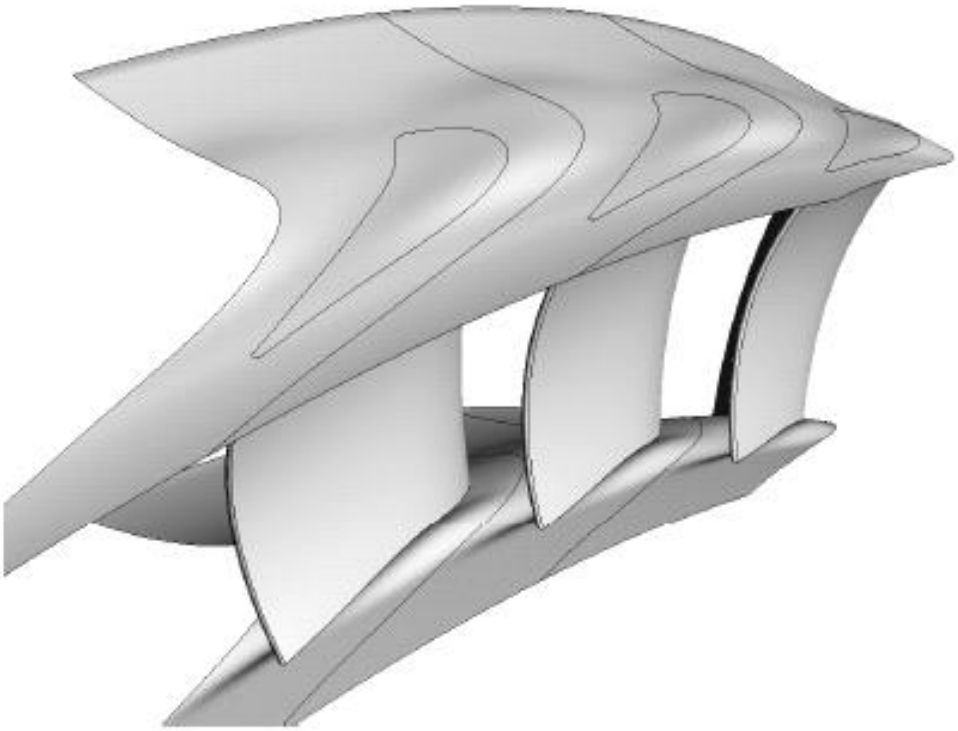

Figure 8: High pressure NGV with non-axisymmetric endwall contouring (reproduced from Brennan *et al.*, 2001)

This technique can yield very different results to the endwalls seen in the Durham cascade as a result of the methods ability to affect shock positioning in transonic turbine stages. In the absence of transonic flow the basic endwall design is aimed at reducing the endwall cross flow by affecting the pressure gradient (see Figure 9). Essentially a "hill" reduces the local passage area in an attempt to increase the flow speed and hence decrease the pressure against the pressure surface of the blade. A "valley" strategically placed close to the suction surface reduces the velocity, increasing the local pressure. Another way to look at this is that the blades become effectively aft loaded in the vicinity of the contoured endwalls, changing the work distribution.

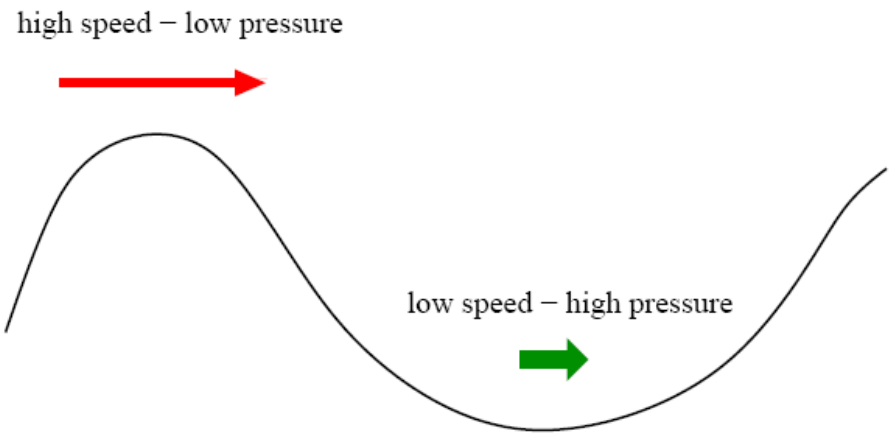

Figure 9: Stream line curvature - the basic idea (reproduced from Ingram, 2003)

For the Durham Cascade, which forms the two dimensional foundation to this work the following results (Table 2) are of interest in this work with respect to the comparison of the planar and P2 contoured endwall.

Table 2: Durham cascade results (reproduced from Ingram, 2003)

	Planar	P2
Total Loss @ 128% C_{ax}	0.1574	0.1322
% Planar Case	100%	84%
Mixed Loss	0.2086	0.1724
% Planar Case	100%	82.6%
C_{ske}	0.0203	0.0092
% Planar Case	100%	45.3%
Maximum Overturning*	0°	2.4°
Maximum Underturning*	0°	-2.7°
Estimated Efficiency Improvement	0%	1.55%

* Versus a spanwise pitch-averaged design flow angle profile

As this technique is the focus of this study, the literature will be discussed in greater depth in later sections.

2.4.3.3.1 Design methods

Initially non-axisymmentric endwalls were designed by examining the predicted pressure field and adjusting the endwall accordingly (Rose, 1994, Hartland *et al.*, 1998 and Yan *et al.*1999). The more modern approach is to parameterise the endwall and perform optimisation against some objective function.

There are two main approaches to the parameterisation of non-axisymmetric endwalls, the first is that common to Rolls-Royce plc (Harvey *et al.*, 2000, Hartland and Gregory-Smith, 2002, Ingram *et al.*, 2003, Corral and Gisbert, 2006 and MacPherson and Ingram, 2010) and their partners and is governed by a patent (Rose, 1995 and Harvey and Rose, 2001). The fundamental approach used in this method is to define the endwall as a series of sinusoidal functions on tangential lines stepping through the passage. By adjusting the phase and amplitude the endwall is efficiently defined. The second is more generic and flexible and generally is the result of creating Bezier splines through a number of control height point (Nagel *et al.*, 2001 and Avio SpA, 2009). This second method may be more flexible but is prone to adjust the mass flow rate through the row in question, which the first does not and is more expensive computationally as more simulations are necessary to perform the optimisation.

The choice of objective function is naturally the next requirement for an optimisation calculation. The leading quantity in use is dot product of C_{ske} and Helicity often referred to as SKEH. The choice of these two quantities arises as few other quantities such as loss and efficiencies are consistently well predicted by CFD and whereas C_{ske} is computed from primary variables (velocity) and Helicity is merely used to identify those components of C_{ske} of most interest. The objective being to minimise C_{ske} or the unwanted secondary kinetic energy in the flow and Helicity therefore is a bystander to the main event. There are exceptions however and Avio SpA, (2009) appear to use efficiency directly and Carleton University appear to favour total pressure loss coefficient (Mahallati *et al.*, 2007, Knezevici *et al.*, 2008 & 2009, Zoric *et al.* 2007a & 2007b, and Praisner *et al.*, 2007).

Two papers highlight some of the pitfalls of the automated optimisation approach using SKEH:

- Ingram *et al.* (2005) presents an aggressive (increased amplitude) endwall design which resulted in a separation in the endwall which was not predicted by the CFD used during optimisation or even in subsequent analysis following the discovery. This work highlights the possibility that loss may be increased even if C_{ske} or other factors commonally used as objective functions for the optimisation of endwalls are reduced. This begs the question, is there a direct link between secondary kinetic energy coefficient and loss? Chapter 7 will attempt to answer this question.
- Vazquez and Fidalgo (2010) question the use of $C_{ske} \cdot H$ as an objective function in their paper which looked at the sensitivity of endwall contoured blade to Mach and Reynolds number in an annular cascade of stator vanes with an aspect ratio of 4. They not only found that, in terms of kinetic energy losses, Reynolds number had little effect and that the results were sensitive to Mach number, but also discovered that the endwall had induced a separation not unlike that discovered by Ingram *et al.* (2005). Their questioning of the validity of the use of $C_{ske} \cdot H$ as an objective function stems from what appears to be their optimisation routine having found a local minima dominated by helicity rather than C_{ske}. This together with the separation phenomenon only serves to reinforce Ingram *et al.* (2005)'s cautionary note on ensuring the use of experiment to verify results before implementing designs based purely on CFD. Another piece of interesting information to be gained

from the work of Vazquez and Fidalgo (2010) is the clear differences in outlet flow features that extend all the way to the tip of their very high aspect ratio blading as a result of contouring at the hub.

Perhaps it may be more expedient to introduce a compound function (such as that of Reising and Schiffer, 2009) of loss, C_{ske} and exit flow angle and even off-design parameters as suggested by Snedden *et al.* (2010a).

2.4.3.3.2 Cascade research

Much of the body of knowledge surrounding the use of non-axisymmetric endwalls emanates from the use of 2D cascades to study the flows in detail. Apart from the highly detailed studies of the Durham cascade that have already been mentioned, various authors from Carleton University and Pratt and Whitney (Mahallati *et al.*, 2007, Knezevici *et al.*, 2008 & 2009, Zoric *et al.* 2007a & 2007b, and Praisner *et al.*, 2007) have published extensively on the use of non-axisymmetric endwall contouring to counter the increased endwall secondary losses of a series of more highly loaded blades in a cascade. This has been in an effort to exploit the inherently low midspan loss of forward loaded blades profiles in low pressure turbines while exploiting non-axisymmetric end wall technology on the hubs to mitigate the associated increased secondary flows resulting from forward loading.

2.4.3.3.3 Rotating rig tests

Relatively few detailed measurements have been made of rotating turbines with and without non-axisymmetric endwalls. An exception is Germain *et al.* (2008) and Schuepbach *et al.* (2008a), they show a 1% improvement in stage efficiency for a turbine with contoured endwalls on both stator and rotor. This latter detailed study indicated that endwall contouring could affect secondary losses but also had a strong effect on midspan loss, significantly most of the improvement was found to result from the first vane passage and not in the rotor despite both being contoured. They also found significant effects on the modelling of the flows as a result of the introduction of root fillets and transition modelling into the models.

This leaves the only two studies available to the author that examine the use of profiled endwalls at off-design incidence to be the model Trent engine rig tests presented by Rose *et al.* (2001) and Harvey *et al.* (2002). These authors found conflicting trends for their high pressure and intermediate pressure turbine designs however. Despite using the same end wall optimisation approach and achieving the expected stage efficiency improvements at design, the HP turbine stage efficiency results showed the profiling to have the greatest effect at the highest loading and virtually no effect at the lightly loaded case, while the complete opposite was true of the IP turbine. In both cases the end wall profiling was observed to restrict the secondary losses to closer to the end wall and therefore to deteriorate the total pressure profile at exit to the turbine but without significantly impacting on the efficiency of the downstream row. Furthermore they noted in the latter paper (Harvey *et al.*, 2002) that it might be interesting to use an off-design component during optimization, something that seems more broadly accepted in the compressor

community where profiled endwalls are being investigated of late and have been shown to delay the effects of corner stall (Reising and Schiffer, 2009).

Although Abdelfattah and Schobeiri (2010) did not look at the use of profiled endwalls in the 3 stage turbine rig at Texas A&M University it was interesting to note their comparisons between CFD and experimental results. There CFD results were as much as 4.2% below those measured in terms of efficiency with the CFD calculating mass flow rates in excess of that obtained by experiment. In addition they state that the use of the SST k-ω turbulence model does not give accurate results in the near wall region despite its reputation to the contrary and gives increasingly poor results as one move away from the design point.

2.4.3.3.4 Effect of rim seal flows

A frequent assertion by detractors of non-axisymmetric endwall contouring at conferences is that the improvements offered by the profiles and the painstaking research undertaken in cascades and rotating rigs is meaningless in the face of the practical application where the secondary cooling circuit and disc cavity flows purge into mainstream at the rim seal between stationary and rotating components. It must be remembered however that endwall profiling first stemmed from research aimed at optimising the pressure field at exit to the stator in order to make these purge flows more uniform (Rose, 1994).

At the 2009 ASME Turbo Expo two papers emerged that dealt directly with this issue. Lot *et al.* (2009) looked at the influence of these flows on the design of the endwall. They concluded the following:

- Isentropic efficiency was not sufficient to fully describe the improved performance of turbomachinery rows given the effect of secondary flow features and exit angles on downstream rows.
- Steady CFD simulations were not sufficient to optimise endwalls in the presence of highly time dependant features resulting from rim seal purge flows
- Improvements were possible.

Schuepenbach et al. (2009) investigated the use of profiled endwalls in the prescence of purge flows in the representative environment of the LISA turbine and likewise concluded that the endwalls were still effective. The purge flows resulted in a strengthening of the rotor hub passage vortex structure in both magnitude and extent. In this latter case the endwall had been designed by steady CFD calculations, and although the efficiency improvements resulting from the implementation of profiled endwalls was in some cases diminished it was still present and in the order of 0.5%, with most of the improvement stemming from the vane rather than the rotor as was the case before the introduction of purge flow.

2.4.4 Combined approaches

Two studies stand out in the literature surveyed. The first concerns the combination of axisymmetric endwalls with an airfoil designed to redistribute work in an attempt to decrease the overall loss in the blade row. The second study is focused on the same result but with lean, sweep and non-axisymmetric endwall contouring in combination.

Duden *et al.* (1999) investigated the use of work redistribution through thickening of the blade profiles at hub and tip in combination with axisymmetric endwall contouring of a tapered cascade typical of a low pressure turbine in the high speed cascade rig at the Bundeswehr University in Munich. A 26% reduction in secondary losses was achieved but this gain was largely eliminated by an increase in inlet boundary layer losses as a result of the thicker endwall profiles. The reduction in secondary losses resulted from a reduced span-wise pressure gradient at midspan, which restricted secondary losses to regions closer to the endwalls while the reduced load at hub and tip increasing the midspan load where a thin and efficient blade profile was employed. The effect of the contoured endwall was most felt in the reduction of over- and under-turning in the exit flow angle which was already improved with just the airfoil redesign. Duden and Fottner (1999) took this study one step further adding off design incidence (both negative and positive) to the test matrix. This latter study showed that the secondary flow structures increased in radial extent for all blades with increasing incidence or load and that the lightly loaded off-design case saw little or no benefit, and were even slightly worse with the addition of first the airfoil improvements and then the contoured endwall. The three-dimensional designs did however act more favourably at high loads with most of the benefit resulting from the airfoil design rather than the endwall.

In probably one of the more comprehensive of such studies Bagshaw *et al*. (2005, 2008a & b) investigated the use of first reverse compound lean and then combined this with forward sweep at the endwall leading edge of the blade before non-axisymmetric endwalls were added. The design intention was to reduce midspan losses through reverse compound lean, then reduce the suction side endwall loading with the application of sweep in preparation for profiled endwalls intended to further reduce secondary losses strengthened by the application of reverse compound lean initially. Two different profiled endwalls were implemented at the hub and tip respectively despite evidence that the design of the one impacted on the other. The outcome was to show that as much as 3% more loss reduction could be achieved through the application of all three of these techniques rather than pure endwall design and that the combination was 8% more effective than simply applying compound lean. Interestingly these gains were achieved despite the presence of a small separation on the endwall which was not predicted during the CFD design process.

A number of other studies such as that of Sharma *et al.* (2003) and the extensive cascade testing at Carleton University (Mahallati *et al.*, 2007, Knezevici *et al.*, 2008 & 2009, Zoric *et al.* 2007a & 2007b, and Praisner *et al.*, 2007) also represent combination studies to some extent but are discussed in other sections of this survey for expediency.

2.5 Overview

The scale and structure of secondary flows in turbines have been discussed in some detail along with the state-of-the-art in terms of the means employed to reduce the effects of secondary flows.

From the literature it is clear that the majority of methods, particularly blade lean and sweep as well as axisymmetric endwall design are unsuccessful in reducing overall loss but instead redistribute the loss towards the midspan. Improvements may be realised from the

more uniform flows entering the downstream rows however. It is also clear that few of these methods have been extensively studied at off-design conditions or in the rotating frame.

Localised twist adjustments and non-axisymmetric endwall design appear to offer a solution which directly influences endwall secondary flows by attempting to reduce the endwall cross passage pressure gradient. Bagshaw *et al.* (2008b) have also shown that non-axisymmetric endwall contouring can be used in combination with other approaches to exploit the benefits of methods which reduce midspan loss but are known to increase endwall secondary flows and losses without suffering the full penalty of this technique.

This study addresses two gaps in the current knowledge base on the effect of non-axisymmetric endwalls, firstly the effect of rotation and the correct annular, three dimensional geometry and secondly the effect of off design flow conditions on the effectiveness of non-axisymmetric endwalls. A number of smaller geometric features are naturally present in these tests and are consistent with industrial turbines, these include tip gaps and split lines in the endwalls.

Furthermore this thesis uses generic endwall contours rather than customised profiles and is therefore a severe test of the robustness of the non-axisymmetric endwall approach.

Finally, this work represents a unique new test case for the validation of turbine endwall secondary flow models. The complete geometry is open for use and is given in the Appendices. Inherent in the analysis of the results therefore is an evaluation of the quantities used as objective functions in the design of endwall loss reduction geometries. Pressure fields and flow streamlines are used to provide a physical understanding of the extent and nature of the effect of the introduction of the profiled endwalls on the flowfield with the rotor row.

3 Experimental Method

One of the key elements of this work is the generation of and access to a unique and rich experimental database previously not available to researchers in this field. The test facility, its instrumentation, the design of the test articles and the data reduction methods as well as the reliability of this data are described here.

3.1 The 1½ stage test rig

3.1.1 Origins and refurbishment

A 1½ stage, low speed, turbine test rig, originally located at the University of KwaZulu Natal was installed and refurbished at the CSIR in Pretoria, South Africa. This test rig was previously used for tip loss measurements (Morphis and Bindon, 1994). The rebuilding and refurbishment (see Figure 10) of the test rig took place as part of ongoing efforts to rebuild and maintain gas turbine technology and skills within South Africa. The work described has all taken place under the author's direction but has seen the involvement of a large number of technicians, contractors, vacation work students and internship technicians in the execution of the following steps:

- Breaking down the test rig, cleaning and removing corrosion, replacing bearings and identifying problem instrumentation and equipment
- Specification and purchasing of new instrumentation necessitated by a combination of age, inaccuracy by modern standards and damage to existing instrumentation. New instrumentation included:
    - Pressure Transducers, both for monitoring atmospheric conditions and differential pressure transducers for inlet velocity and 5-hole probe measurements.
    - Temperature measurement equipment (RTD PT1000) to facilitate inlet density measurements.
    - A new torque and speed transducer of the same make and better accuracy specification to both fit in the same space and without modification to the installation and improve the accuracy of some of the key outputs of this work, in particular efficiency.
- Replacement of the main drive for the compressor:
    - At the university a powerful, centrally located hydraulic pump had been used to drive the compressor and the turbine power was then fed back into the system.
    - No such hydraulic power pack was available at the CSIR and based on cost the decision was made to make use of a variable speed drive and electrical motor. This in turn meant that the compressor was completely overhauled, and new, longer supports with the electric motor directly coupled to the compressor rotor.
- Dynamometer specification and acquisition:
    - A dedicated feed pump and tank, complete with cooling, gear motor and solenoid valve system was purchased to provide the brake system.

- Specification, design, acquisition and testing of a control and data acquisition system:
    - A PLC system was selected for its robustness and was integrated with the main drive, hydraulic brake and primary instrumentation of the test rig.
- Improvements:
    - A new inlet measurement ring was added
        - The advantage of this ring was to locate the inlet measurement plane away from the blockage effects of the inlet supports.
        - In addition the ring can be removed and set aside as a single piece ensuring that the equipment is not damaged.
    - A new main traverse casing was machined to replace the original which had been modified to include increased tip gap heights and hence was no longer suitable for this study.
    - The tangential traverse gear was replaced
        - The original geared system had a limited travel of 10° and was replaced with a stepper motor driven cable drive capable of more than 100°.
        - At the same time the vertical location of the casing elements was improved with the addition of new pinned vertical straps offering superior control over the traversing casing's gap height and hence allowing greater freedom of movement.
    - The severely corroded radial and yaw traverse gear was replaced with a Rotadata RTM100 available in the CSIR laboratory, and later when this system became unserviceable, by an alternative locally designed and constructed traverse.

Before: September 2004 After: April 2007

Figure 10: The refurbishment of the test stand at the CSIR

- The exit diffuser casing was replaced with a sturdier stainless steel design
- A blank hub was machined for the 2nd stator location giving the rig a 1 stage capability as well as its original 1½ stage design
    - This in turn required the replacement of the exit support vanes, which was done with pins to make the rig capable of any test article exit flow angle without moving or replacing the exit vanes.

3.2 General assembly

Figure 11 shows an exploded, cutaway view of the test rig in order to give an overall impression of its construction, a diagrammatic view of the assembly can be found as Figure 12. The test rig has a hub and tip radius of 0.142m and 0.203m respectively and is designed for a maximum wheel speed of 3000RPM.

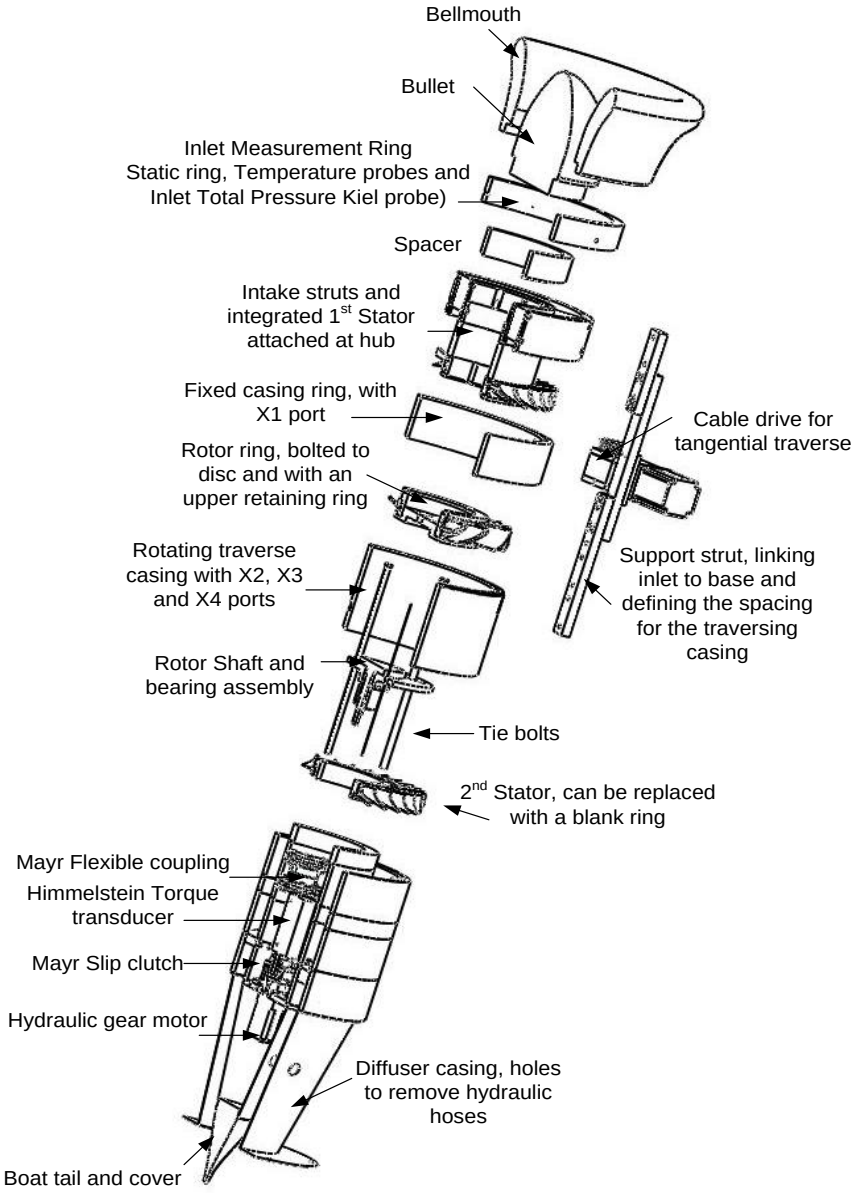

Figure 11: General assembly of the 1½ stage test rig

3.3 Instrumentation and control

Figure 12 indicates the general layout and instrumentation of the test rig. A radial fan draws atmospheric air through the rig, inducing a pressure drop of 4.8kPa for a mass-flow of 2kg/s, corresponding to an inlet velocity of about 30m/s at the atmospheric densities experienced in Pretoria, some ±1360m above sea level. The radial blower (bottom) is driven by an electric motor with variable speed control. The turbine power is absorbed by a hydraulic motor, giving independent rotor speed control by means of a variable flow rate valve for coarse setting and a solenoid electronic control valve for fine adjustment. Control and data acquisition is achieved through a Siemens S7-200 PLC with 12 bit A/D and compatible WinCC Flexible Scada software.

Table 3 indicates the instrumentation and their associated uncertainties.

Table 3: Instrumentation

Primary Instrumentation		
Parameter	**Instrument**	**Uncertainty**
Torque	Himmelstein MCRT 28002T(5-2)CNA-G + Model 721 Mechanical Power Instrument	±0.03N.m
Speed		2RPM
Barometric Pressure	Siemens Sitrans P 7MF4233-1FA10-1AB6-Z A02+B11	0.075% of full scale
Differential Pressure	5 x Siemens Sitrans P 7MF4433-1CA02-1AB6-Z A02+B11	0.075% of full scale
Temperature	PT1000 RTD's	±0.05°C
Secondary Instrumentation		
Steady Flow mapping	Aeroprobe CPC5-C159-305-015.3-16 5 hole cobra probe (1.59mm Ø head)	0.2m/s and 0.4° in flow velocity and angles
Turbulence	TSI 1211-20 single component film	±0.77% mean velocity*
Tangential Traverse	Custom cable system rotating the outer casing	Better than 0.01°
Radial and Yaw traverse	Custom two component backlash free traverse driven by Cool Muscle® drives	0.01mm 0.1° respectively

*Stamatios (2002)

3.3.1 Transducer Calibrations

Secondary standards were used throughout to calibrate the test instrumentation. The absolute pressure transducer was calibrated against a Delft 605 and set to the minimum range possible that covers the barometric range for Pretoria, the data for which was provided by the South African Weather Bureau. The differential pressure transducers were calibrated against Betz Manometers and the RTD's were emmersed in an oil bath and a glass and mercury thermometer marked in 0.01°C graduations was used as the secondary standard. Torque was calibrated statically used dead weights and an inclinometer. All calibrations were of the entire measurement chain, including the A/D converter.

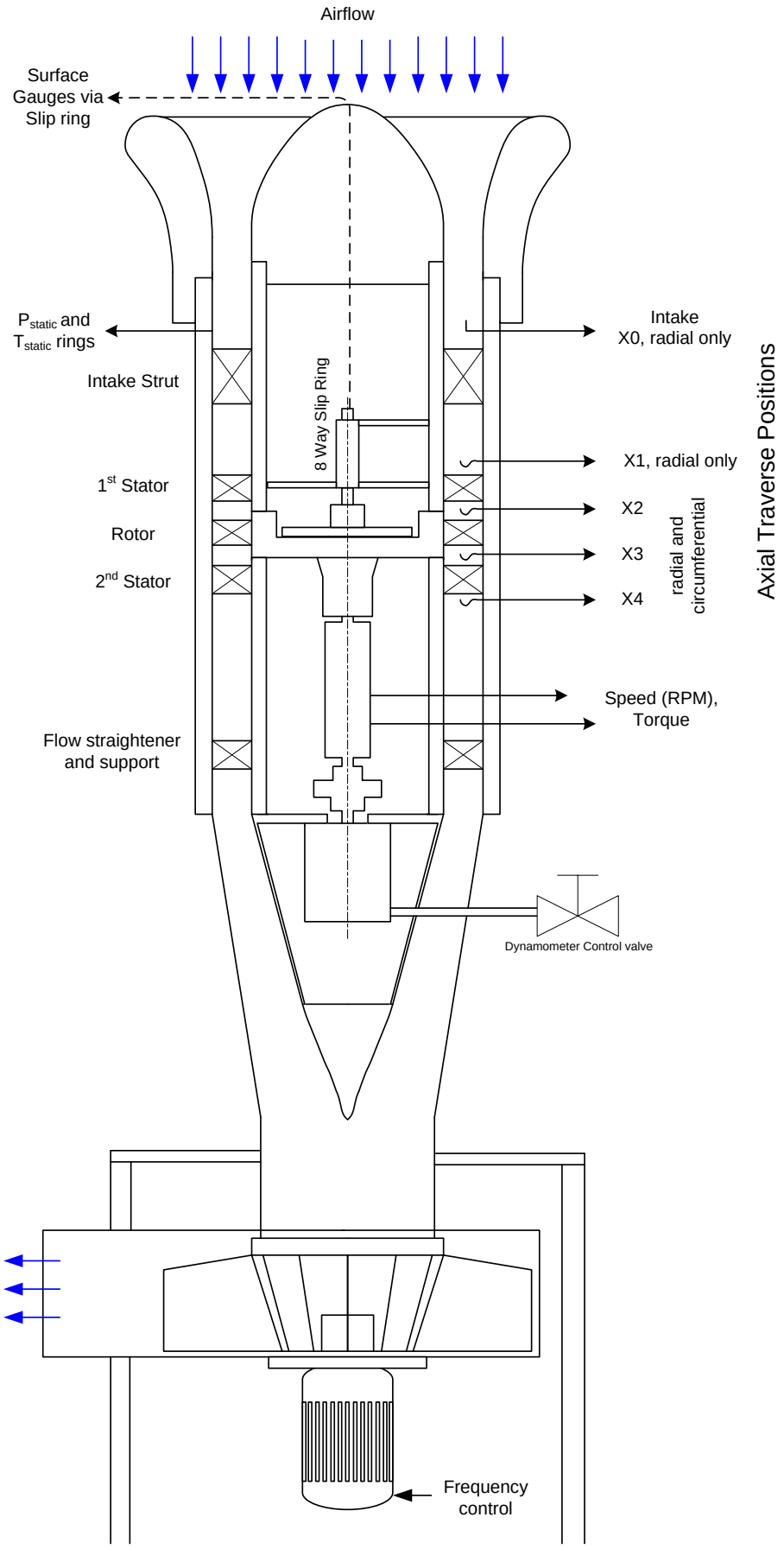

Figure 12: Schematic of 1½ stage turbine and control and measurement instrumentation

3.3.2 Inlet measurement ring

The inlet measurement ring is used to determine air velocity at inlet. Figure 13 shows the United Sensor Kiel probe (middle) and RTD (bottom) with their brass holders (top). Three static pressure taps (0.5mm in diameter) are spaced 120° apart and the same number of RTD's are placed in between the static ports. The Kiel probe is placed between an RTD and a static port to give inlet total pressure. A further probe mount is provided to facilitate the introduction of a hot-wire probe into the inlet. The layout is illustrated in Figure 14.

Both intrusive probes are 3mm in diameter.

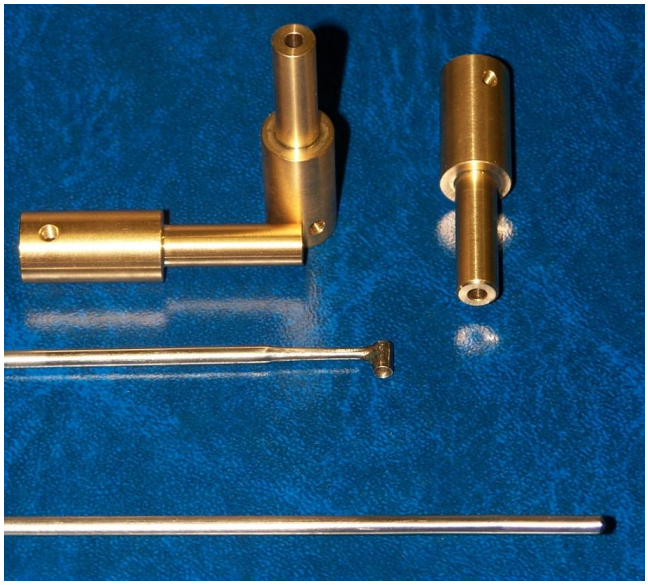

Figure 13: Inlet probes

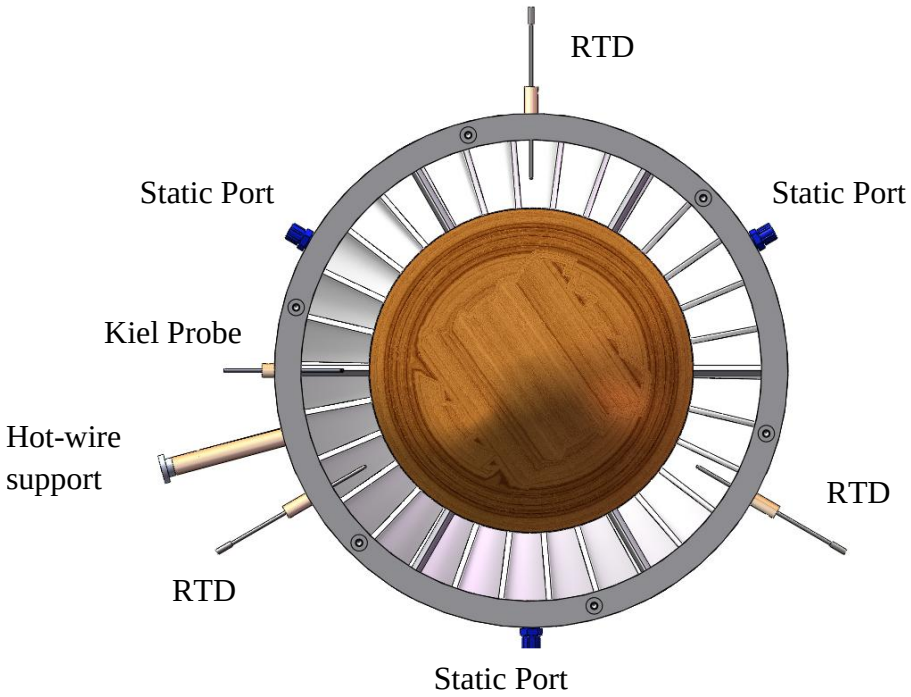

Figure 14: Inlet probe locations

3.3.3 Hot-film probe

The TSI 1211-20 Hot-film illustrated in Figure 15 was used exclusively for inlet turbulence measurements in conjunction with the TSI IFA300 system and a TSI automatic calibrator.

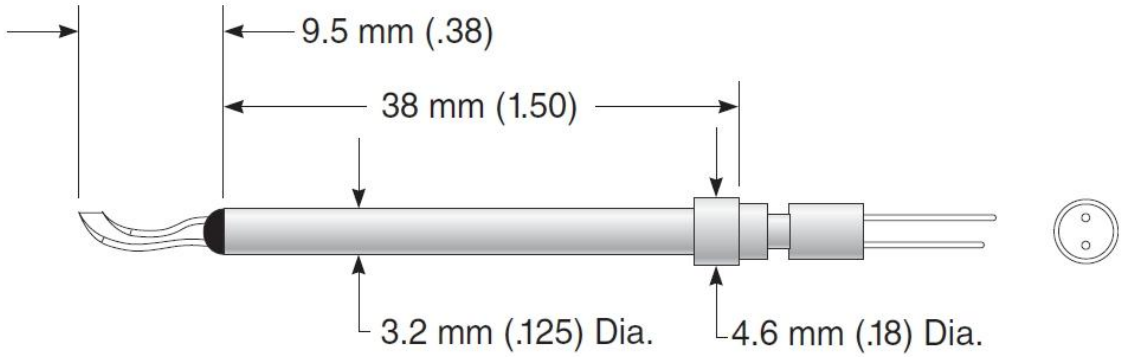

Figure 15: TSI 1211-20 Hot-film probe (reproduced from TSI, 2006)

3.3.4 Inlet turbulence intensity measurements

Inlet turbulence intensity was measured utilising the single hot-film probe and TSI's Thermal Pro software and found to be less than 1%. Table 4 gives the results for two different inlet access points.

Table 4: Inlet turbulence

Intake, X0	
Maximum	0.71%
Mean	0.64%
Minimum	0.58%
X1 Traverse Position	
Maximum	0.94%
Mean	0.74%
Minimum	0.63%

3.3.5 Control philosophy

The PLC controller was programmed to always control the inlet speed and rotor rotational speed, thereby setting the C_x/U ratio. In addition to this it can then automatically perform a traverse according to a text file giving it the traverse locations. A number of modes are available:

- Null yawing
- Fixed probe angle traverses
- Calibration mode, whereby the 5-hole probe calibration stand can be fitted to the blower outlet and each pitch angle is then automated through the yaw control.

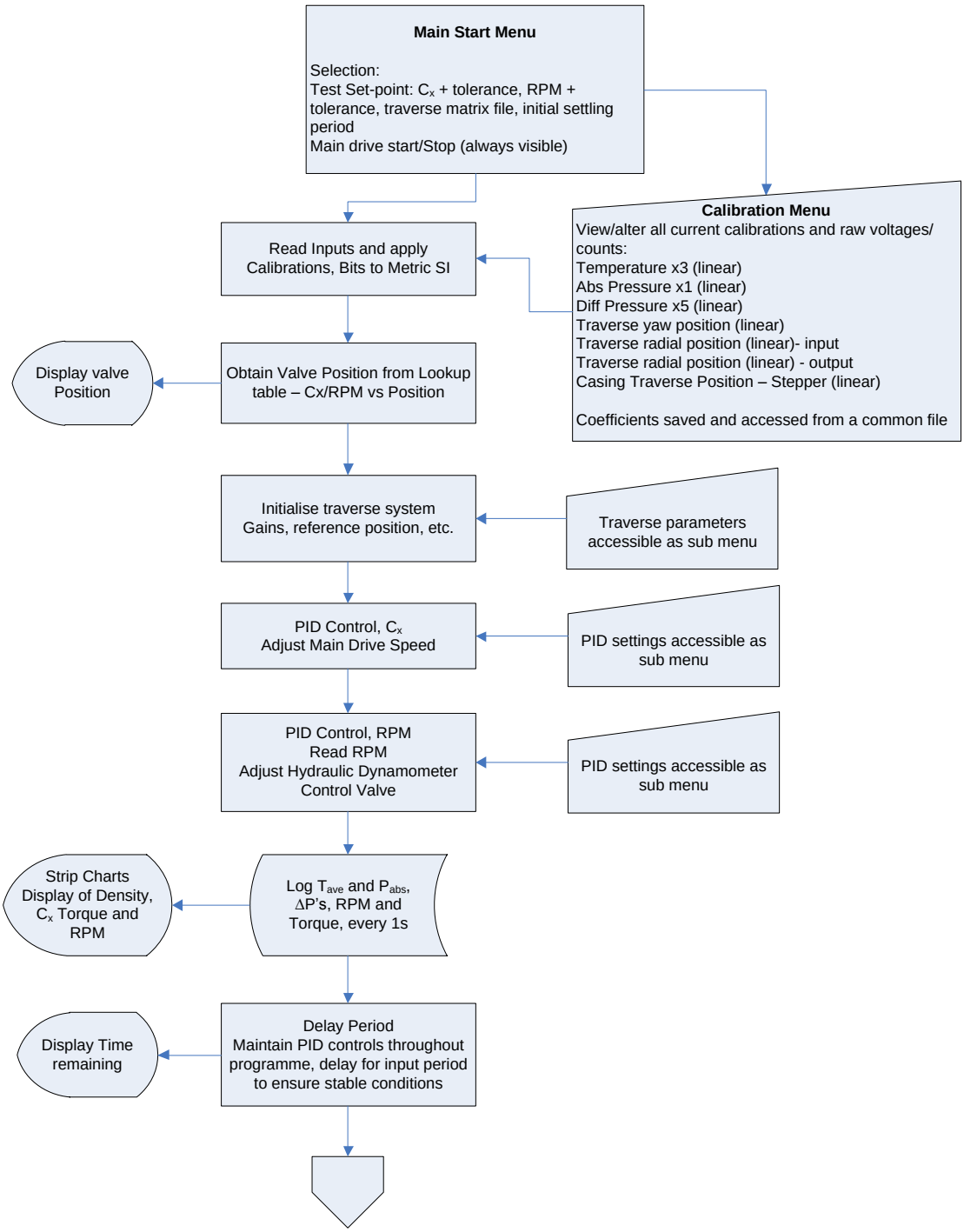

Figure 16: Test rig control flowchart

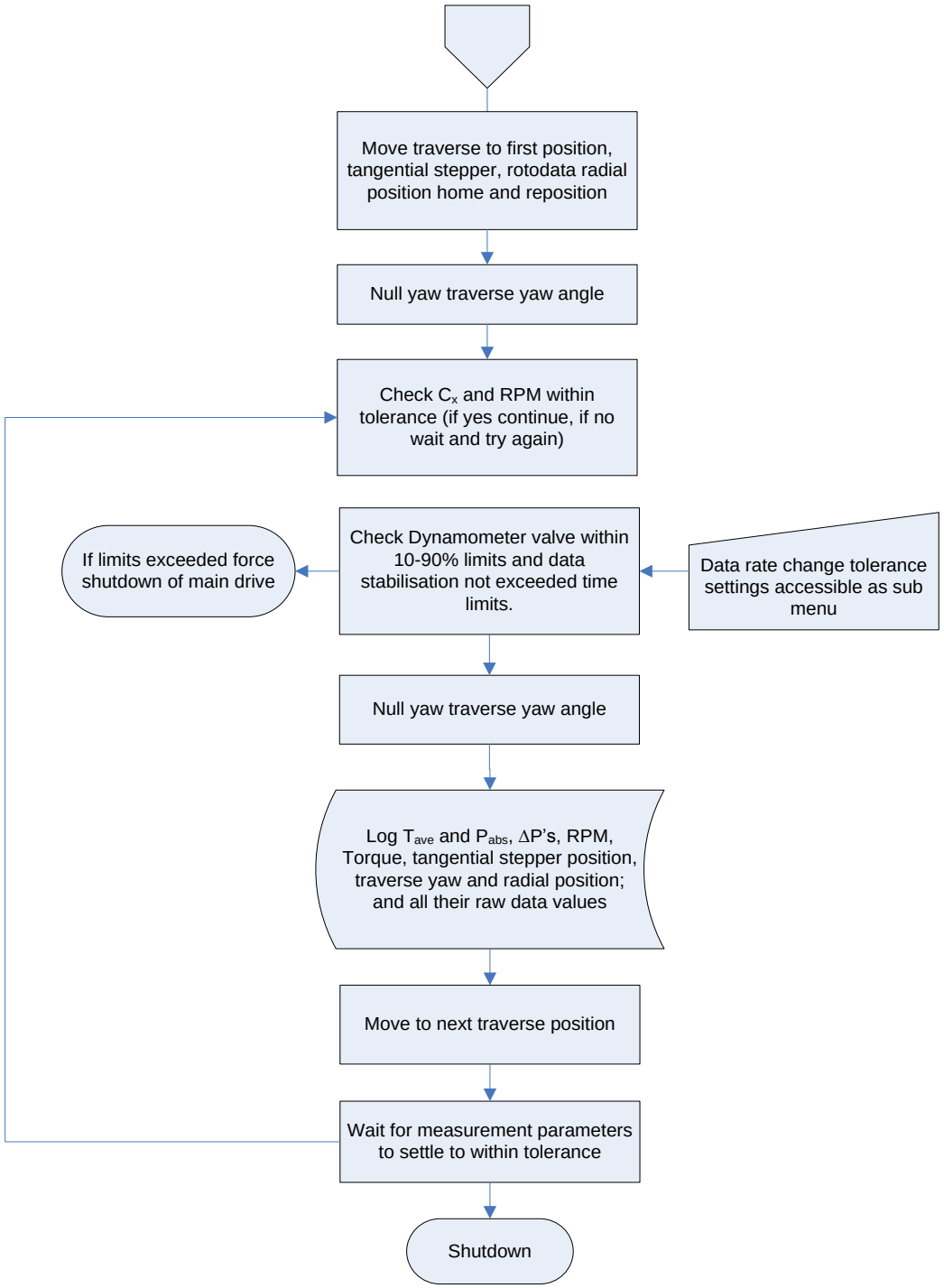

Figure 17: Test rig control flowchart (continued)

In addition the controls would not take data when the control limits are exceeded or if the rate of change of both the measured and controlled parameters is in excess of limits set by the user. Furthermore the test stand will automatically shut down should these limits not be met within the required period and should the dynamometer valve run out of control authority, the traverse will be suspended pending a restart of the test rig. This control philosophy is captured in the flowchart contained in Figures 16 and 17.

3.4 Blade and Profiled Endwall Design

3.4.1 Design Constraints

The major constraint placed upon the design of blading for this thesis, apart from the obvious geometrical constraints to the existing structure of the test facility, was that it was to share the same profile on the rotor hub as that used in the Durham cascade and hence the most successful of the Durham endwall profiles could be adapted to this blading.

The initial idea was to have a repeating stator design, but the constraints imposed by the test rig capabilities and the rotor hub design resulted in a highly twisted rotor blade this concept was abandoned in favour of a design with non-axial rotor outlet, reducing blade twist. The final result was a 1½ stage design in which the Durham cascade profile could be repeated on the hub of both the rotor and 2nd stator.

In this case the aerofoil design was not designed in great detail as it is meant only to facilitate the application of the endwalls. Hence the final constraint was that the design inlet and outlet angles varied linearly with span in order to reduce the blade design effort to just 4 profiles:

- Hub and tip of the 1st Stator
- Tip of the Rotor (the hub having been provided by Durham University)
- Tip of the 2nd Stator (the hub having been provided by Durham University)

3.4.2 Aerofoil design

Having shown that the concept of repeating the rotor hub design on the 2nd stator was feasible by means of velocity triangle calculations, the design was performed using the commercially available turbine design software from NREC (Now Concepts ETI) by a colleague (Roos, 2006).

The blading was designed utilising the three step process laid out by the NREC software, firstly a mean-line design, followed by a 3D design and then taking these inputs into an inverse design method for the blades (NREC, 1972) whereby a Mach number profile is imposed to produce blade coordinates and with a degree of user experience this is corrected, both by returning to the 3D design and by adjustments to the Mach number profile, until a satisfactory results is obtained. This design was then run through an Euler solver and boundary layer code to ensure that there were no large flow separations.

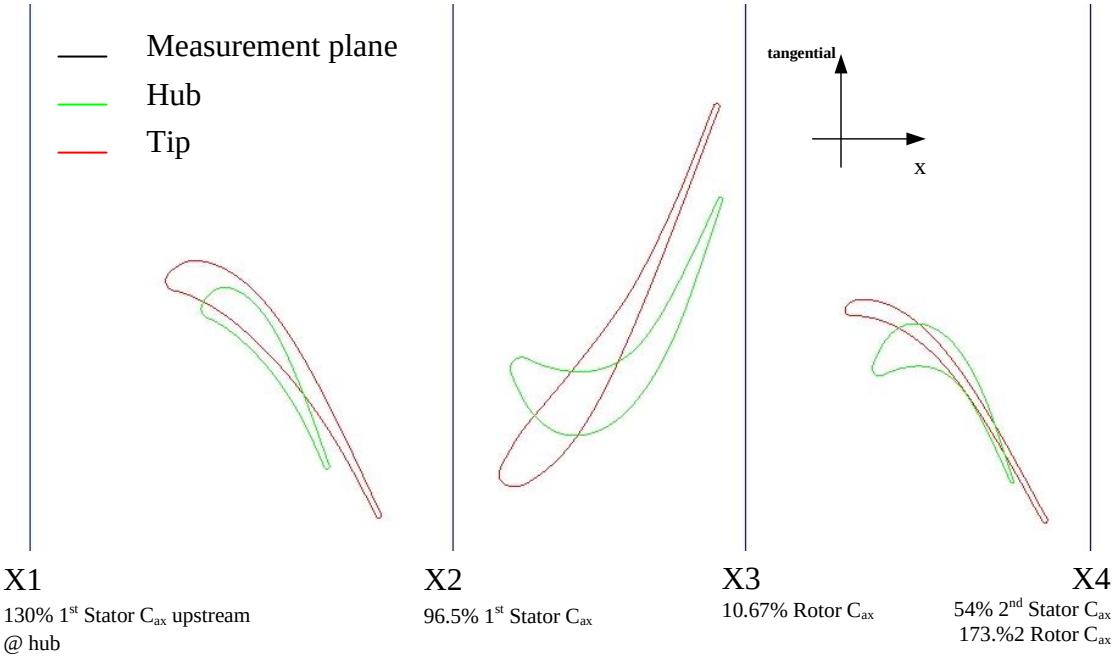

Figure 18: 1½ Stage turbine design

Initial testing, however, indicated under-turning from the stator in particular. This was found to result from of the low Mach number and NREC's inability to account for this under-turning. In addition this blade was particularly thin and untwist at the tip was suspected and confirmed after prolonged testing resulted in permanent deformation. New, longer chord, thicker 1st stator blading was then designed and manufactured with modified outlet angles calculated utilising low Mach number corrections to the cosine rule available in Saravanamuttoo *et al.* (2001). Testing showed these new stators to be performing as expected. The rotor remains unchanged as the effect is not as strong as the absolute outlet flow angles are low. The final design is detailed in Appendix A and summarised in Figure 18. The resulting design axial velocity was 21.38m/s at 2300RPM, producing approximately 3.42kW once the reduced flow angles were properly accounted for. The hub Reynold's number, based on axial chord at the rotor relative velocity at rotor exit, is approximately 127 500. This is lower than that of the Durham cascade of 400 000.

Blade numbers are suggested by the NREC code, but are generally considered very high for such a small turbine with extremely low blade loading. Instead the blade numbers were initially selected to be prime and to give Zweiffel coefficients at the hub of close to optimum. However the final blade numbers owed more to the desire to match experiment with all possible permutations of CFD, including the use of the domain scaling method for later unsteady CFD analysis, and to restrict axial chord length to that available in the test rig while maintaining a sufficient gap to accommodate the 5-hole probe. The resulting blade numbers were 20 stators and 30 rotor blades.

Appendix B contains further details of the measurement positions, rotor/stator gaps and probe wells.

Table 5: Design summary

Inlet		
Axial Velocity		21.38 m/s
Rotational Speed		2300 RPM
1st Stator		
No. of Blades		30
Inlet Angle	Hub	0°
	Casing	0°
Outlet Angle	Hub	68.26°
	Casing	61.20°
Midspan Outlet Absolute Velocity		46.4 m/s
Rotor		
No. of Blades		20
Inlet Angle	Hub	42.75°
	Casing	-23.98°
Outlet Angle	Hub	-68.00°
	Casing	-71.15°
Midspan Outlet Relative Velocity		57.4m/s
Modified Stage Power Rotor outlet angle adjusted according to Saravanamuttoo *et al.*, 2001		3.42kW
Stage Pressure Ratio		1.0393
Zweiffel Coefficient @ hub Zweiffel (1945)		0.94
Stage Reaction	Hub	0.38
	Midspan	0.60
	Casing	0.70
Flow Coefficient	Hub	0.625
	Midspan	0.52
	Casing	0.439
Blade Loading Coefficient	Hub	1.08
	Midspan	0.70
	Casing	-0.10
Exit Reynold's Number		127 500
2nd Stator		
No. of Blades		30
Inlet Angle	Hub	42.75°
	Casing	35.45°
Outlet Angle	Hub	68.00°
	Casing	61.77°

3.4.3 Test conditions

Test conditions for experimentation are indicated in Table 6 and illustrated in Figure 19.

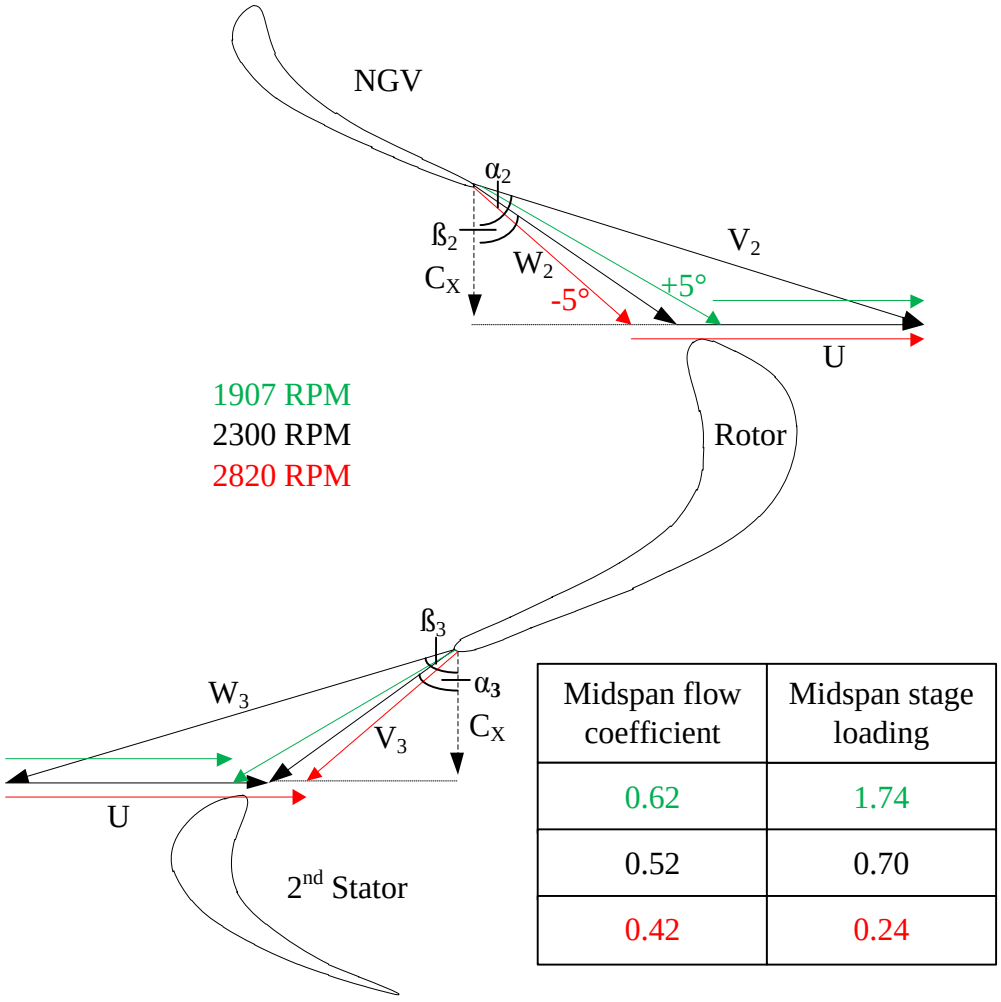

Midspan flow coefficient	Midspan stage loading
0.62	1.74
0.52	0.70
0.42	0.24

Figure 19: Test condition velocity triangles

Table 6: Nominal Test conditions

Axial Velocity (m/s)	Rotor Speed (RPM)	Reason
21.38	1907	+5° incidence at rotor hub
21.38	2300	On-design flow into rotor
21.38	2820	-5° incidence at rotor hub

The off-design conditions are designed to result in a ±5° incidence at the rotor inlet at the hub. No changes in the inlet velocity were tested as the capability of the test rig would result in only small variations in Reynold's Number whereas the incidence variation results in significant changes in the rotor blade loading.

3.4.4 Blade attachment design

The test rig's blading can be rapidly changed, redesigned and manufactured. This is in part due to the low speed operation of the rig, which allows for the chosen, direct laser sintering, manufacturing technique for the blades and the simple attachment method utilising a helical t-slot. The t-slot is machined in two passes with a woodruff cutter, reducing the machining cost. The blade "firtree" is then designed for a tight fit and finished by hand.

Figure 20 shows the rotor attachment ring with its helical t-slots. The blades are restrained axially between the rotor disc and a retaining ring.

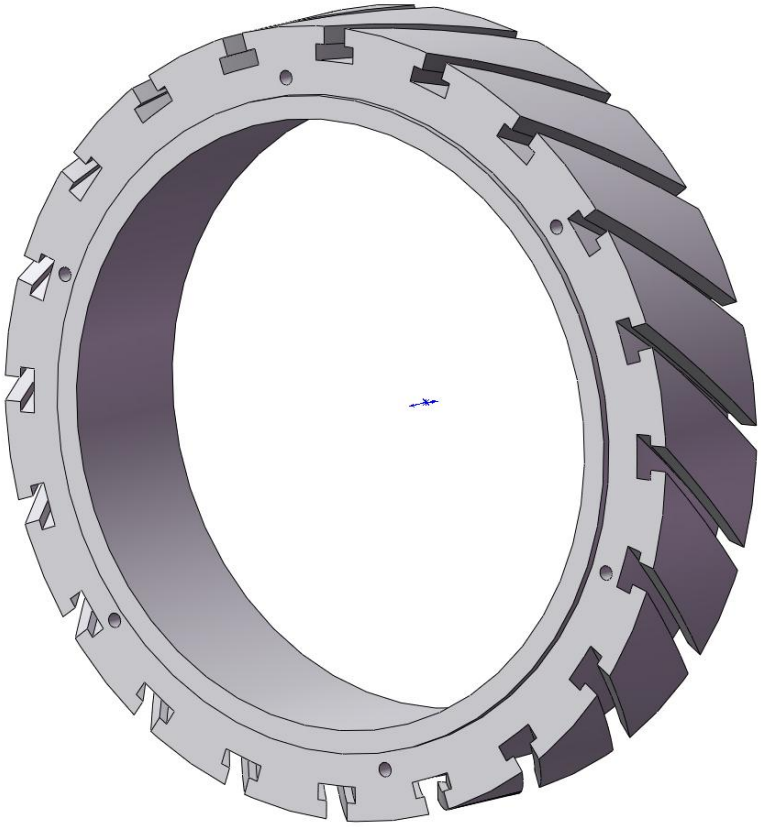

Figure 20: Rotor attachment ring

3.4.5 Endwall design

No automated optimisation routine was available in South Africa or Durham University at the time and hence a generic profile was considered. The Durham P2 endwall design (Figure 21) was chosen as it was both the most successful of the Durham endwall designs and the most practical. The most practical as it limits the profiling to the blade passage without upstream or downstream extensions to interfere with the respective stators across the rotational interface. The endwall design was reverse-engineered. These coordinates were then scaled in axial position and perturbation height to fit the final axial chord of the new rotor blade hub by the ratio of original and new axial chord. Pitchwise the profile was scaled by the ratio of original to the new design's pitch.

Finally the points were converted from planar to polar coordinates and the perturbation height of the contours added to the radius. This resulted in the surface to be seen in Figure 21.

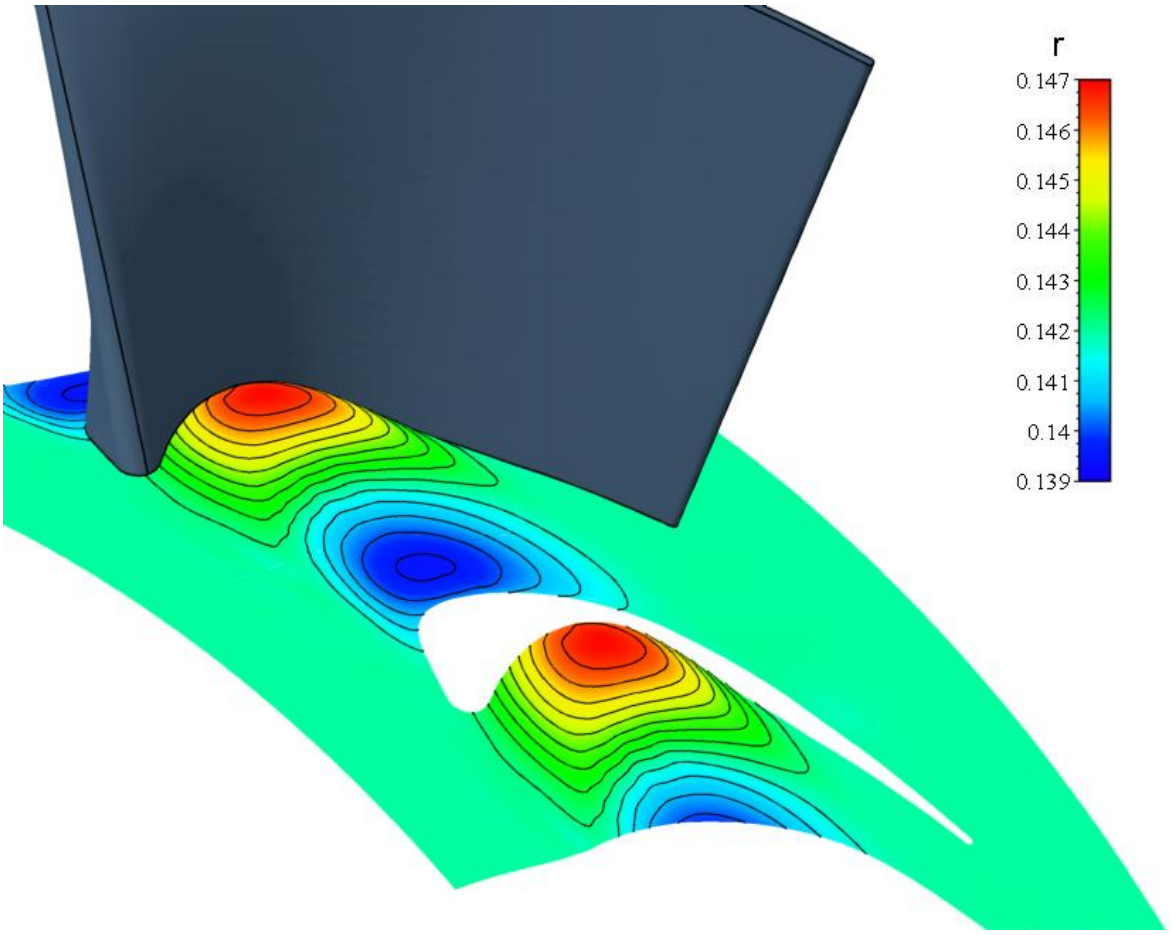

Figure 21: The Durham P2 contoured endwall as reverse engineered and transformed onto the annular surface of the CSIR turbine

3.4.6 Blade Manufacturing technique

Rapid prototyping was chosen as the manufacturing technique. A laser sintering capability available at the Central University of Technology in Bloemfontein, South Africa, was used. The material is Fine Polyamide PA2200 as used on the EOSINT P system. This material was a late selection resulting from the failure of the rapid prototyping machine using a Renshape SL7580 epoxy and offered equivalent strength to weight ratio, but a reduced flexural modulus. Stress calculations following Saravanamuttoo *et al.* (2001) showed the material's nominal strength to give safety factors of over 10. In fact the material has remarkable resilience and can easily be repaired using cyanoacrylate gel.

The rapid prototyping material has proven highly capable of producing the complex shape of the endwall features quickly and cheaply. However the low flexural modulus of the material means that thin blade sections should be avoided, as was discovered by Snedden *et al.* (2007) and led in part to the redesign of the nozzle guide vane with a thicker section.

One of the great successes of this method is the simplicity for the transfer of the blade design to the manufacturer. Once the aerofoil profiles have been converted to annular

coordinates they are integrated together with the platform and t-slot in CAD and a tip gap added. The rotor tip gap is relatively large at 1.7% of span, while that for the stators is 0.8% of span. Fillet radii of 1mm are used at the junction between blade and endwall. The final design is then saved in a standard stereolithography format and emailed to the manufacturer who scales the design to account for shrinkage and prints the blades as a batch.

Figure 22 shows the completed blading, showing two blades for the rotor, the annular hub on the left and non-axisymmetric contoured hub on the right.

Measurements of the blading has revealed little variation from the design. Measurements of both the tip gap and throat sizes vary about the design values by less than 0.2mm which is consistent with the manufacturing tolerance of 0.2mm sintered layers.

3.5 5-hole Probe Measurements

3.5.1 Traverse Gear

Area traverses were performed using a two component (Radial and yaw) traverse for radial movement and null yawing (used behind the rotor). Tangential movements were made by rotating a section of the casing via a stepper drive; this necessitates a tip clearance for both the stator and rotor rows.

The radial and yaw component of the traverse gear incorporates an off the shelf Parker linear slide and backlash free sprung gearing to eliminate any hysteresis The Cool Muscle® drives together with the gearing give positioning accuracy to well within 0.01mm and 0.1° in radial and yaw motion respectively.

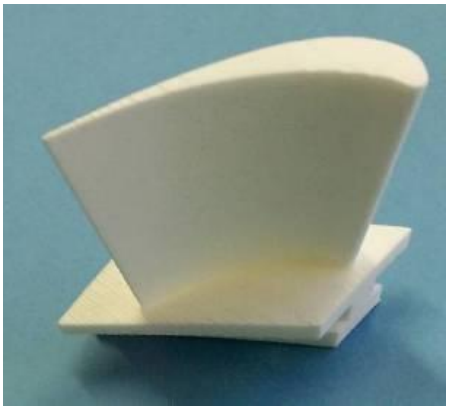

(a)

(b)

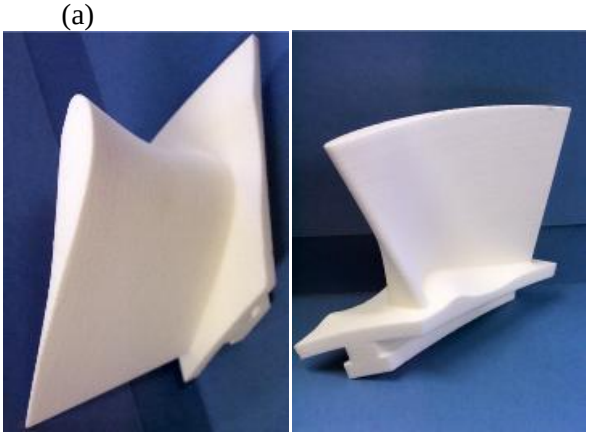

(c)

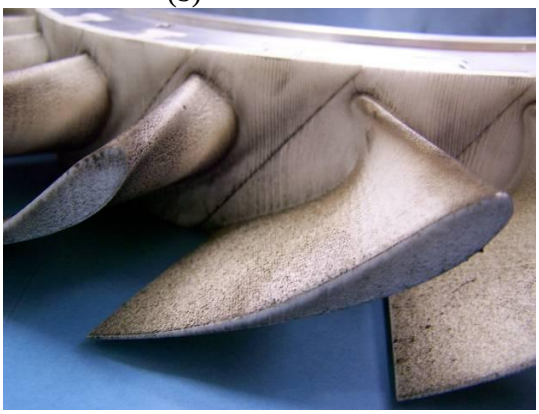

(d)

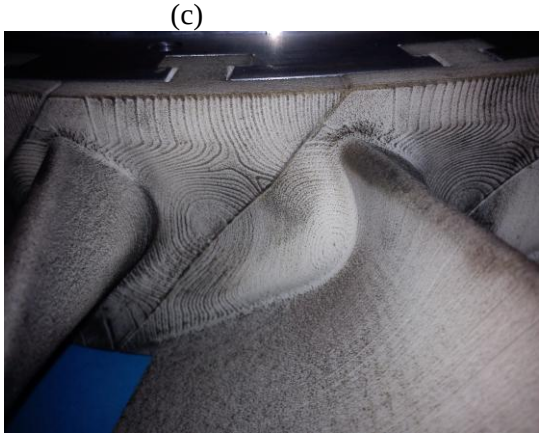

(e)

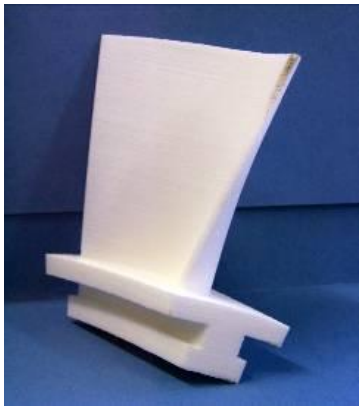

(f)

Figure 22: Final blading as sintered

(a) 1st Stator, (b) Annular rotor, (c) Contoured rotor, (d) Annular and (e) Contoured rotors attached to the ring clearly showing the split lines (f) 2nd Stator

3.5.2 Traverse Points

Three different traverses are performed at the different axial locations. At X1, in front of the first vane, the inlet flow is assumed uniform and no tangential traversing capability is available. Hence a single radial traverse is performed, placing 21 points between 3.3% and 98.4% span.

Behind the vanes a full area traverse is performed, placing 33 measurements 0.5˚ apart in a pitchwise line with 30 points radially positioned between 2.5% span and 97.5% span, 990 points in total. A single pitch is 12˚ and hence 1.375 pitches are captured. The area traverse is illustrated in Figure 23.

Three pitchwise measurements 9˚ apart are taken behind the rotor where the steady probe captures averaged data in the absolute frame, in the radial direction the spacing is the same as that for the vane area traverses, 90 points in total.

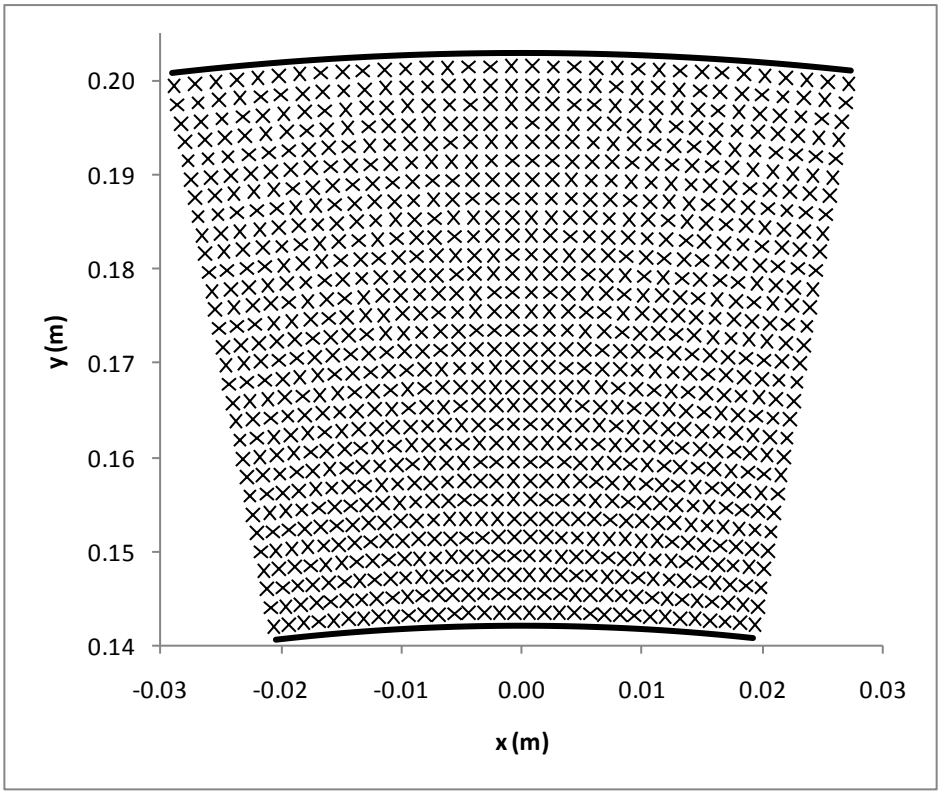

Figure 23: Area traverse points at vane exit

3.5.3 5-hole Pressure probes

The Aeroprobe CPC5-C159-305-015.3-16 5 hole cobra probe pictured in Figure 24 was used throughout this work to map the flow. This probe was selected for its accurately machined conical tip and small tip diameter of just 1.59mm which offers accuracy and a minimum of blockage. Maximum probe blockage of 0.32% of the total flow area is obtained when the probe is deployed behind a blade row and fully extended radially to the hub.

Figure 24: Aeroprobe 5-hole probe

3.5.4 5-hole probe setup

Steady experimental measurements utilising a 5-hole probe were performed by two techniques, both with the same setup and data reduction or post-processing procedures:

- Null yawing the probe at midspan at X1, X2 and X4, fixing the yaw angle and relying on the probe calibration to cover the flow angle range
- Null yawing at each point during an X3 run and using the calibration to adjust the result within the dead band on the null yawing algorithm.

To achieve these measurements, the probe was connected to differential pressure transducers using the method for minimum measurement uncertainty of Kaiser (1996) shown in Figure 25. This method of connections successfully attempts to measure the smallest possible differential pressure per transducer, allowing the researcher to set small transducer spans and obtain high accuracy readings.

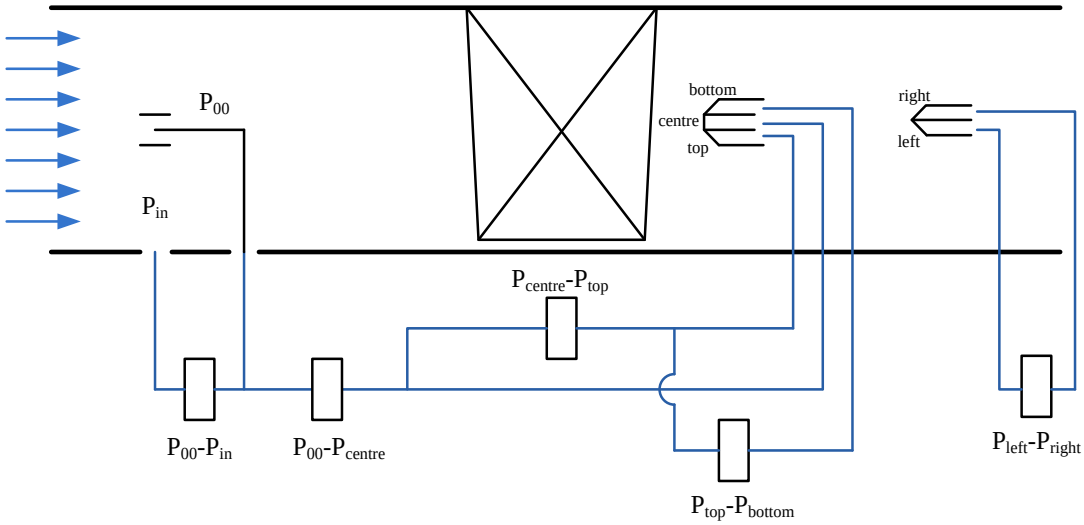

Figure 25: 5-Hole pressure probe connections after Kaiser (1996)

These connections allow one to extract all the pressures with the exception of the yaw port pressures and hence the coefficients for the probe are defined as follows:

$$C_{Pyaw} = \frac{P_{left} - P_{right}}{P_{centre} - P_{ave}} \quad \textbf{3-1}$$

$$C_{Ppitch} = \frac{P_{bottom} - P_{top}}{P_{centre} - P_{ave}} \quad \textbf{3-2}$$

$$C_{Ptotal} = \frac{P_{centre} - P_{abs}}{P_{centre} - P_{ave}} \quad \textbf{3-3}$$

$$C_{Pstatic} = \frac{P_{ave} - P_{static}}{P_{centre} - P_{ave}} \quad \textbf{3-4}$$

where:

$$P_{ave} = \left(P_{bottom} + P_{top}\right)/2 \quad \textbf{3-5}$$

and P_{abs} is obtained from the Barometric pressure transducer while:

$$P_{static} = P_{abs} - (P_{00} - P_{in}) \quad \textbf{3-6}$$

3.5.5 Calibrations

Probe calibrations were performed on a dedicated test stand located at the exit to the test rig, see Figure 26. The test stand is setup by reconfiguring the exit piping and installing a specially designed nozzle which incorporates flow straightening. A laser pointer and pin hole device is then used to ensure proper alignment of the tube to the stand. The radial and yaw component traverse can then be bolted to the stand which can be set up to place the probe at ±30° pitch with notches every 5° for ease of location.

Figure 26: Calibration test stand (Pictures by Charles Moate)

3.5.5.1 Calibration Schedule

A full calibration was performed before testing each rotor and checked rigorously between extended runs (X2 and X4) and between movements of the probe between axial stations. The full calibration consist of 375 points between ±30° pitch and ±30° yaw, with pitch angles set by hand and the yaw angle and data capture automated through the test rig control and the traverse system. Check calibrations were typically 3 or 5 pitch settings of the full calibration.

The post-processing of this data was performed using a purpose written C^{++} programme utilising the method of Ingram (2003) and Ingram and Gregory-Smith (2005) with the only modification being to the quasi-static pressure measurement which in this system relies

only on the pitch ports rather than an average of all four side ports. Typical calibrations are shown in Figure 27, which also gives an indication of the repeatability of the probe by plotting pitch and yaw calibration factors against one another. Each column of points represents a fixed pitch setting from -30° to 30° (left to right) in 5° increments and 2.5° close to 0°, of yaw angles (automated by yawing the traverse) through -30° to 30°.

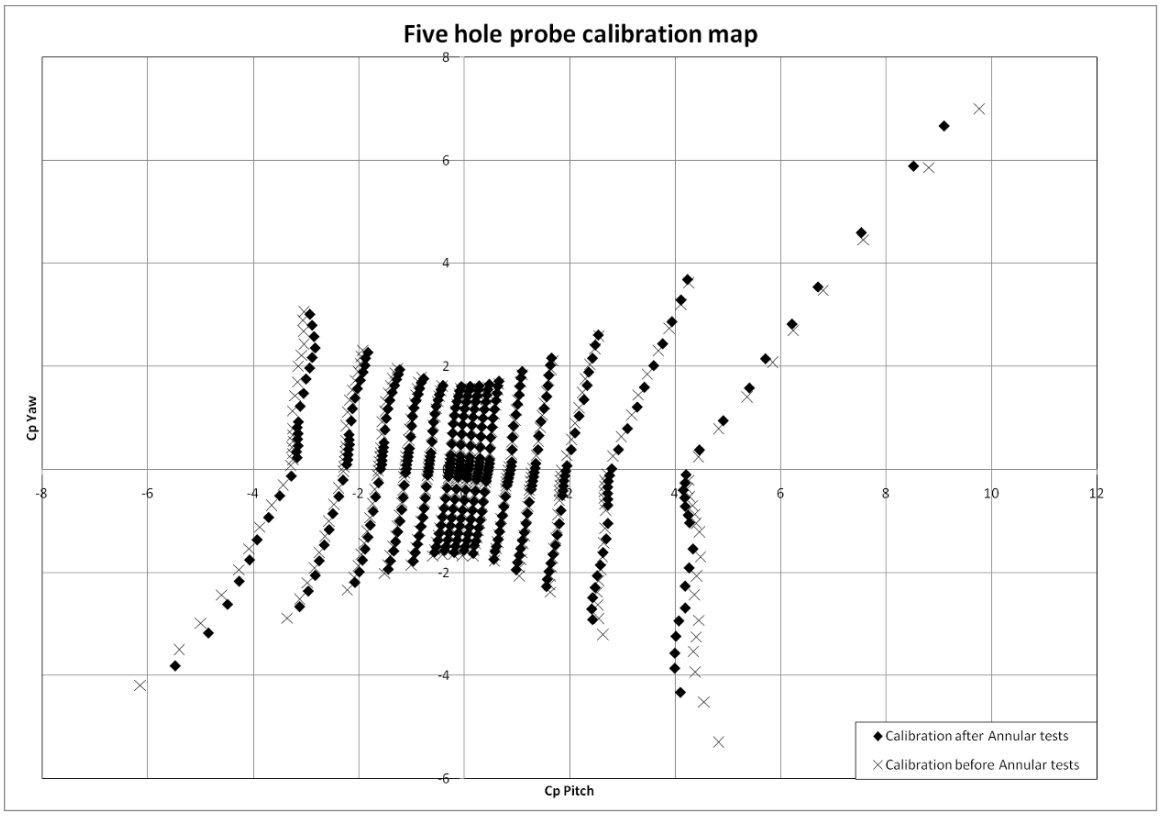

Figure 27: Typical calibration map indicating the level of repeatability achieved

3.5.6 Flow angle and pressure data recovery

The 5-hole pressure probe measurements are processed against the calibration by calculating the pitch and yaw coefficients and performing a box search to find the position of the given measurement point on the calibration map. The yaw and pitch angles as well as the total and static pressure coefficients are then interpolated from within the four corners of the box. Once the total and static pressure coefficients are known the velocity can be computed and together with the pitch and yaw angles the velocity components can be computed. This is consistent with the method of Ingram and Gregory-Smith (2005) and the software to do this owes much to the same reference but was reworked as part of the work of Dunn *et al.* (2009) to make the process of calibration and data reduction seamless with the data acquisition system.

This data can then be passed to further post-processing in order to calculate the performance parameters of the turbine.

3.5.7 Performance calculations

The method of obtaining the turbine performance, used extensively throughout this work, was the same as that of Kaiser (1996) and Morphis (1993) who used the same experimental test rig for tip clearance and tip profile tests over a decade previous.

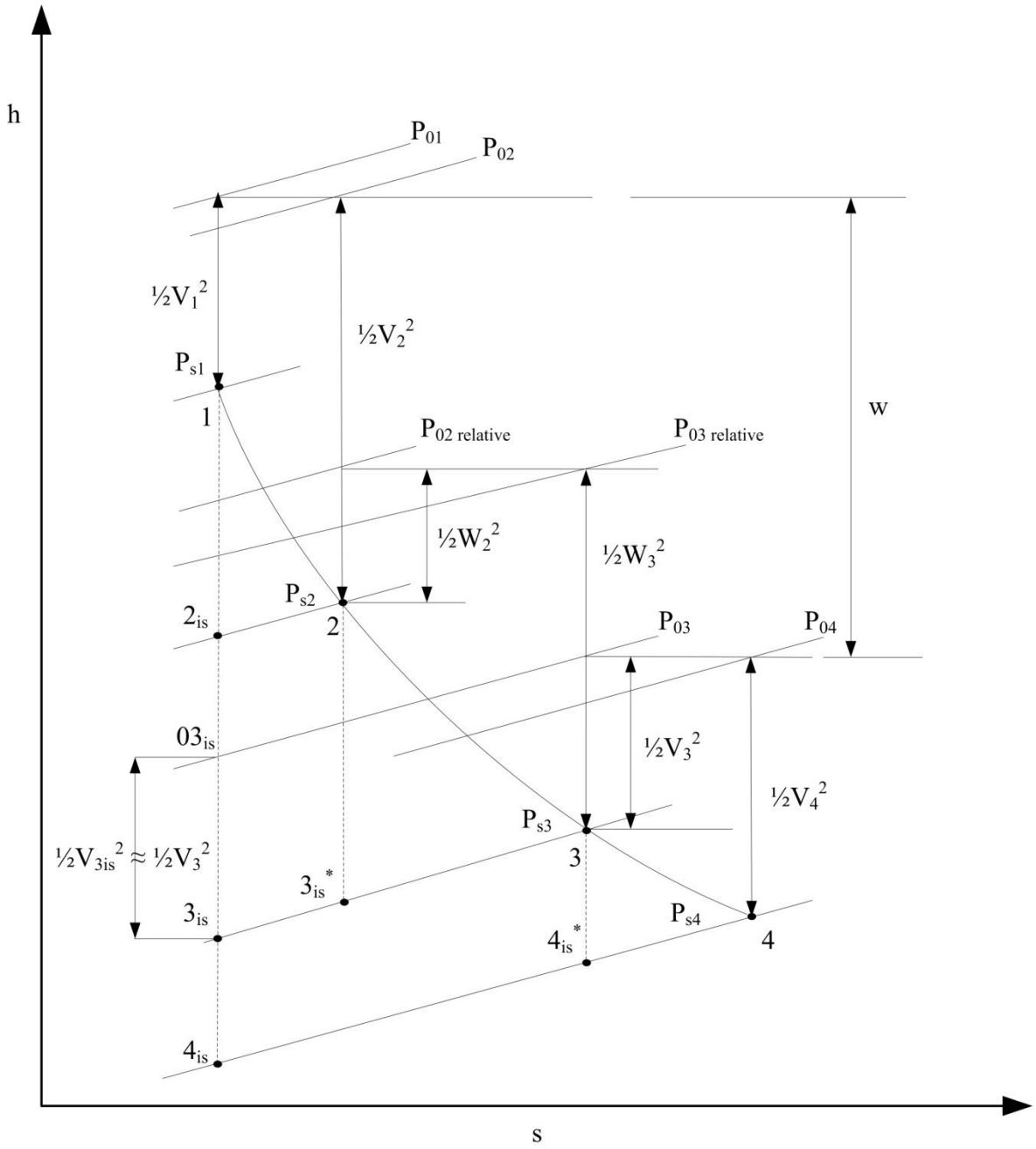

Figure 28: The specific enthalpy-entropy diagram for the expansion of a gas through an axial 1½ stage turbine (redrawn from Kaiser, 1996)

Starting with the overall efficiency of the 1½ stage machine and with reference to Figure 28:

$$\eta_{1.5} = \frac{w + \frac{1}{2}V_4^2}{h_{01} - h_{4is}} \qquad \textbf{3-7}$$

Expressing enthalpy in terms of specific quantities:

$$h_{01} = u_1 + \frac{P_{01}}{\rho_1}$$

$$h_{4is} = u_{4is} + \frac{P_{4is}}{\rho_{4is}}$$

where:

$$u_1 = C_v T_1 \quad and \quad u_{4is} = C_v T_{4is}$$

Assuming that the flow is incompressible, then:

$$\rho_1 = \rho_{4is} = \rho \quad and \quad T_1 = T_{4is}$$

And therefore

$$u_1 = u_{4is}$$

Therefore by substitution equation 1 becomes:

$$\eta_{1.5} = \frac{\rho w + \frac{1}{2}\rho V_4^2}{P_{01} - P_{s4}} \qquad \textbf{3-8}$$

(note: $P_{s4} = P_{4is}$)

This can also be expressed as:

$$\eta_{1.5} = \frac{\frac{\rho w}{q_{ref}} + \frac{\frac{1}{2}\rho V_4^2}{q_{ref}}}{\frac{P_{01} - P_{s4}}{q_{ref}}} = \frac{\overline{C_w} + \overline{C_{V4}}}{\overline{C_{(P_{0\,1} - P_{s4})}}} \qquad \textbf{3-9}$$

Where the dimensionless coefficients are defined as follows:

Work coefficient:

$$C_{w\,ij} = \frac{\frac{2\pi N \tau_{ref\,ij}}{60\dot{m}_{ref\,ij}}}{q_{ref\,ij}} \qquad \textbf{3-10}$$

Velocity coefficient:

$$C_{V\,ij} = \frac{\frac{1}{2}\rho_{ij} V_{ij}^2}{q_{ref\,ij}} = \frac{(P_o - P_s)_{ij}}{(P_0 - P_s)_{ref\,ij}} \qquad \textbf{3-11}$$

Static pressure coefficient:

$$C_{(P_{0\,ref} - P_s)ij} = \frac{\left(P_{0\,ref} - P_s\right)_{ij}}{(P_0 - P_s)_{ref\,ij}} \qquad \textbf{3-12}$$

Total pressure coefficient

$$C_{(P_{0\,ref}-P_0)ij} = \frac{\left(P_{0\,ref} - P_0\right)_{ij}}{(P_0 - P_s)_{ref\,ij}}$$

3-13

Now these quantities must be converted into mass averaged quantities obtained from measurements taken at discrete points. In addition the quantities must be normalised by the mass flow rate at the time of taking the discreet measurement with a reference value, in order that the differences between atmospheric conditions can be removed. Hence a mass flow coefficient is defined:

$$C_{\dot{m}\,ij} = \frac{\dot{m}_{ij}}{\dot{m}_{ref\,ij}}$$

3-14

where:

$$\dot{m}_{ref\,ij} = \rho_{ref\,ij} \cdot A_{ij} \cdot V_{ref\,ij}$$

Note: 1) $\dot{m}_{ref\,ij}$ corresponds to the time that the (i,j)th grid point was measured

2) The area A_{ij} is measured halfway between the previous point to halfway to the next point in both radial and tangential directions. At the boundaries this extends to the solid walls.

3) The velocity at the solid wall is assumed to be zero.

4) The reference velocity is taken as the inlet velocity while the axial velocity at the point of measurement is used to calculate the (i,j)th grid point velocity.

Mass averaged quantities are the obtained from the following function, where $\overline{Y}$ represents any dimensionless coefficient.

$$\overline{Y} = \frac{\sum_i \sum_j Y_{ij} C_{\dot{m}\,ij}}{\sum_i \sum_j C_{\dot{m}\,ij}}$$

3-15

Or to observe radial trends the coefficients may be mass averaged in the tangential direction only:

$$\overline{Y_j} = \frac{\sum_i Y_{ij} C_{\dot{m}\,ij}}{\sum_i C_{\dot{m}\,ij}}$$

3-16

Finally the static pressure loss coefficient and total pressure loss coefficients may be determined respectively as follows where a and b represent two locations of interest:

$$\overline{C_{(P_{0a}-P_{sb})}} = \overline{C_{(P_{0\,ref}-P_{sb})}} - \overline{C_{(P_{0\,ref}-P_{0a})}}$$

3-17

$$\overline{C_{(P_{0a}-P_{0b})}} = \overline{C_{(P_{0\,ref}-P_{0b})}} - \overline{C_{(P_{0\,ref}-P_{0a})}}$$

3-18

By similar means the following expressions for efficiency can be derived:

Single stage total and total static efficiency:

$$\eta_{tt} = \frac{w}{h_{01} - h_{03}} = \frac{w}{(h_{01} - h_{3is}) - \frac{1}{2}V_{3is}^2} = \frac{\overline{C_w}}{\overline{C_{(P_{01}-P_{s3})}} - \overline{C_{V_3}}}$$

3-19

$$\eta_{ts} = \frac{w}{h_{01} - h_{3is}} = \frac{\overline{C_w}}{\overline{C_{(P_{01}-P_{s3})}}}$$

3-20

Rotor total and total static efficiency:

$$\eta_{R_{tt}} = \frac{w}{h_{02} - h_{03}} = \frac{w}{(h_{02} - h_{3is}) - \frac{1}{2}V_{3is}^2} = \frac{\overline{C_w}}{\overline{C_{(P_{02}-P_{s3})}} - \overline{C_{V_3}}}$$

3-21

$$\eta_{R_{ts}} = \frac{w}{h_{02} - h_{3is}} = \frac{\overline{C_w}}{\overline{C_{(P_{02}-P_{s3})}}}$$

3-22

Nozzle efficiency:

$$\eta_{N1} = \frac{\frac{1}{2}V_2^2}{h_{01} - h_{2is}} = \frac{\overline{C_{V_2}}}{\overline{C_{(P_{01}-P_{s2})}}}$$

3-23

$$\eta_{N2} = \frac{\frac{1}{2}V_4^2}{h_{03} - h_{4is}^*} = \frac{\overline{C_{V_4}}}{\overline{C_{(P_{03}-P_{s4})}}}$$

3-24

3.5.8 Measures of loss in rotating turbine test facilities

A large number of parameters exist that can be used to define the loss in turbines and in particular turbine cascades. This study is however limited by what can be measured in the available test rig. The following is a discussion of previous work in the field of the experimental determination of loss in turbines.

3.5.8.1 Pressure loss coefficients

This quantity has largely been defined for cascade measurements and is not readily available for rotating turbine test rigs.

Moustapha *et al.* (1986) define two pressure loss coefficients for a nozzle and a rotor row respectively:

$$C_{P0} = \frac{P_{01m} - P_{02}}{P_{01m} - P_{s2m}} \quad \textbf{3-25}$$

$$Y_R = \frac{P_{0r2} - P_{0r3}}{P_{0r3m} - P_{s3m}} \quad \textbf{3-26}$$

Hunter (1982) studied a low pressure rotating test rig with two different spacing's between vane and blade, performing traverses behind the stator and rotor in each case. In his results he presents rotor loss as a span-wise function showing negative areas, but does not present his calculation method. However by using averaged values for the upstream quantities it can be expected that at some spans the loss calculated by the above method will emerge as negative.

3.5.8.2 Coefficient of Secondary Kinetic Energy

Another popular measure is that for secondary kinetic energy. The formulation below is that of Ingram (2003).

$$C_{ske} = \frac{V_{sec}^2 + V_r^2}{V_{in}^2} \quad \textbf{3-27}$$

where:

$$V_{sec} = V \sin(\alpha - \alpha_{mid})$$

Like most such measures it is developed for the 2D cascade environment and for the purposes of this work α_{mid} is replaced by the scalar average of the outlet flow angle, α.

3.5.9 Calculation method

Once the data from the 5-hole probe was been processed to calculate the velocity, pressures and flow angles it is combined with data such as the measured speeds and torques and output to a file ready for importing to a spreadsheet. This spreadsheet then applies all of the above equations and is used to graph and compare the data.

3.5.10 Reliability of the experimental data

The uncertainty of data generated experimentally is often a contentious issue, particularly when it comes to aggregated results such as turbine efficiency. Using the same rig as this study albeit with older and less accurate instrumentation Morphis and Bindon (1994) presented their results as having repeated to within 0.05% of rotor efficiency over 5 separate runs. However Kaiser (1996) re-examined this and concluded that the measurement uncertainties lay between ±0.17 and ±0.34%.

Three approaches are outlined in this section.

3.5.10.1 Uncertainty

Utilising Kline McKlintock analysis, as described by Holman (1985), the uncertainty of a result, Ř, where Ř is a function of a number of independent variables x_i each with an uncertainty of w_r can be calculated as follows:

$$w_r = \left[\left(\frac{\partial \check{R}}{\partial x_1}.w_1\right)^2 + \left(\frac{\partial \check{R}}{\partial x_2}.w_2\right)^2 + \cdots + \left(\frac{\partial \check{R}}{\partial x_n}.w_n\right)^2\right]^{\frac{1}{2}}$$

3-28

Applying this method to equations 3-9, and 3-19 to 3-24 and using the uncertainties found in Table 3 the uncertainty on the efficiency at a discrete point is approximately ±0.2 to 0.25%.

In a further analysis, again at a single discrete point, one can simply determine the effect should all the uncertainties work together in a worst case scenario. This result indicates the maximum possible uncertainty to approach ±0.6%. This is however only possible if the uncertainties are not random in nature.

Neither of these approaches are satisfactory however, as the overall efficiency computed for the machine is a function of a number of different data points, taken over a substantial time span, requiring mass averaging and combination with results measured at different stations. To cope with these statistical variances stochastic analysis is required.

3.5.10.2 Stochastic Analysis

Using the technique outlined by Wild and Hockman (2007) and an experimental dataset as the basis, the input data to the efficiency calculation was varied by a random function of the transducers uncertainties described in Table 3. Using a macro function the spreadsheet is recalculated over 1000 times until the average efficiency is no longer varying significantly. The result of this statistical approach, which assumes a normal distribution to the uncertainties experienced on each transducer, shows the uncertainty on the efficiency to be less than ±0.2%, and it is this that will be indicated on future graphs.

3.5.10.3 Repeatability

The repeatability of the experimental results was ascertained by taking multiple measurements downstream of the rotor. The probe was calibrated or at very least checked between measurements and reinstalled, in some cases the rig was broken down and rebuilt

between experiments and the traverse sequence altered, these are described as Builds 1 to 3 in Table 7. The experiments were in other respects identical with data taken at identical locations.

From Table 7 it can be seen that these repetitions reveal the results for efficiency to repeat to better than ±0.13%. The repeatability in the efficiency results for these three runs is therefore clearly better than the uncertainty calculated stochastically and hence the latter result will be utilised as a more conservative case. Likewise the rotor pressure loss coefficient and coefficient of secondary kinetic energy repeat extremely well, to within ±0.14% and ±0.075% respectively.

Table 7: Repeatability on efficiency and loss measures

	Stage Total Efficiency (/%)	**Rotor Pressure Loss Coefficient (/%)**	**C_{ske} (/%)**
Build 1	76.55	28.43	21.66
Build 2	76.38	28.67	21.79
Build 3	76.34	28.57	21.71
Average	76.42	28.56	21.72
Average Deviation	0.084	0.084	0.047
Standard Deviation	0.111	0.121	0.066
Uncertainty (95% confidence level) Coleman and Steele (1989)	±0.126	±0.136	±0.074

Span-wise distributions of this data (see Figures 29 to 33) show excellent agreement particularly between all three builds. The greatest variation in the efficiency and pressure loss results takes place around midspan and the C_{ske} results show almost no variation.

In the chapter which follows the numerical method for the analysis of the test turbine will be described and further experimental results will be used to show the validity of the computational modelling approach, after which the main output of this work will be described in figures similar to those shown in Figures 29 to 33 which resulted from tests performed on two builds of the turbine, one with annular endwalls and the other with the generic contoured rotor endwall. These results will furthermore be presented for three rotor inlet flow angle conditions, and at four axial stations through the turbine. These results and the validation they provide for the computational results will then be utilised to provide insights into the ability of the generic endwalls to effect secondary flows in the turbine over the entire span of the blade as well as investigate the effectiveness of the endwalls at off design conditions. In addition it is possible to examine the effectiveness of a number of commonly used measures of endwall effectiveness in the rotating environment.

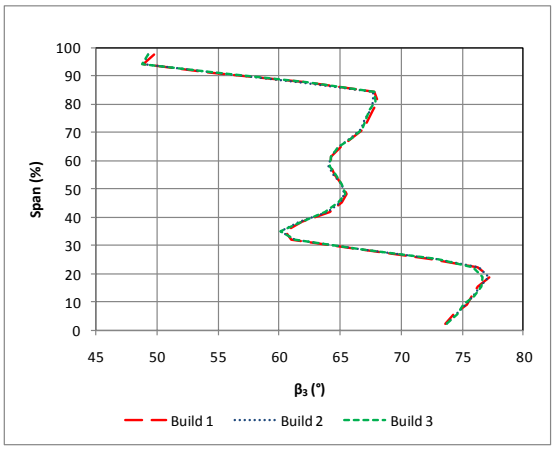

Figure 29: Comparison of span-wise distributions of pitch averaged rotor relative outlet angle for three builds

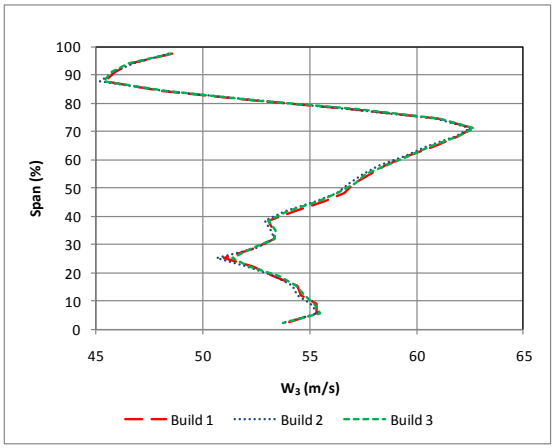

Figure 30: Comparison of span-wise distributions of rotor relative outlet velocity for three builds

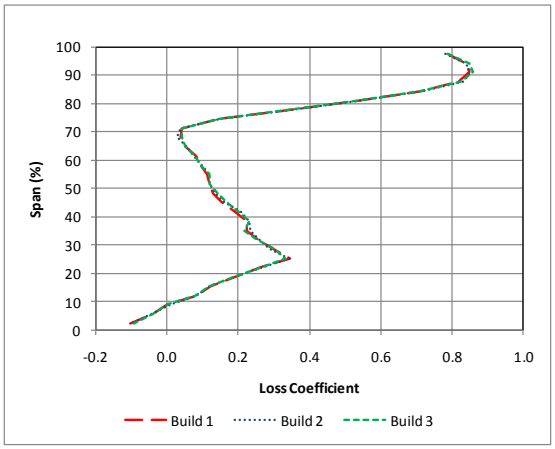

Figure 31: Comparison of span-wise distributions of rotor exit pressure loss coefficient for three builds

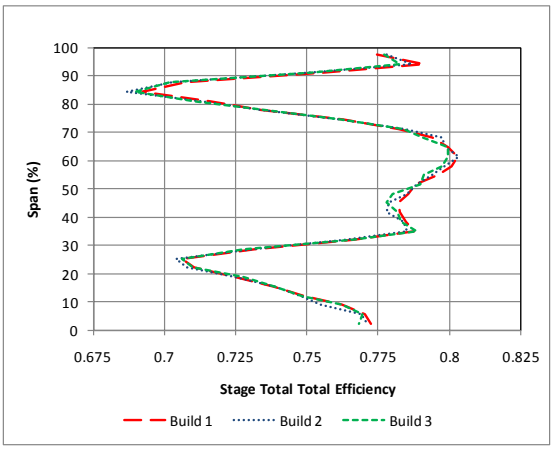

Figure 32: Comparison of span-wise distributions of stage efficiency for three builds

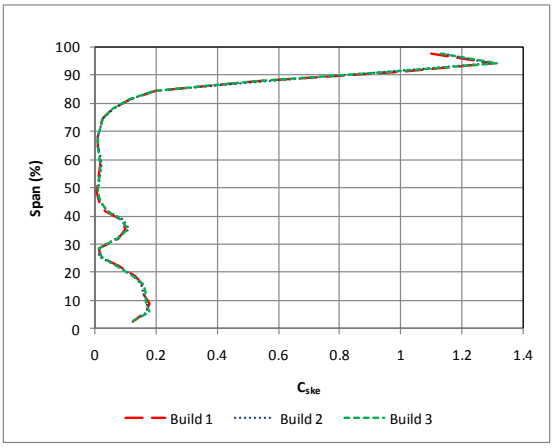

Figure 33: Comparison of span-wise distributions of rotor exit secondary kinetic energy coefficient for three builds

4 Computational Method

Computational Fluid Dynamics (CFD) has been in use since the 1960's (Versteeg and Malalasekera, 1995) first as a research tool and later as a design aid to the aeronautical community. By solving the Reynolds Averaged Navier Stokes (RANS) equations numerically one can obtain a wealth of information regarding the detailed structure of a given flowfield and predict trends and effects as a result of geometrical and flow parameter changes.

Denton (2010) however points out the "CFD is not an exact science" and indicates that the following may be sources of error in CFD simulations of turbomachines:

- Numerical error resulting from the finite difference approximations
- Modelling errors where the true physics is too complex to model, in particular turbulence modelling
- Unknown boundary conditions
- Imprecise geometry
- and the assumption of steady flow

The prediction of highly sheared and vortical flows which are dominated by turbulence as well as separated flows and transitional boundary layers are all particular challenges identified by Denton (2010),

With these shortcomings in mind, two pieces of literature stand out as providing guidelines in the pursuit of improved computational results and best practises. These are the test case studies of Gregory-Smith (1995) who examined the results of a wide variety of code against the Durham cascade results, and that of Dunham and Meauze (1998) who looked at a further two test cases.

Gregory-Smith (1995) found that there was "wide variation" in the results obtained from some 27 authors using 25 different codes and turbulence model combinations over three years in the early 1990's. These variations were obtained in nearly all parameters studied: strength and position of the passage vortex, strength and position of the loss core at exit, while the average loss prediction was 2.5 times that of the experimental determination. The following were recommended:

- Highly orthogonal meshes were preferred
- Convergence to at least 4 or 5 orders of magnitude in the residuals
- Codes that allow for specification of transition point.

No conclusions with respect to turbulence model could be conclusively made. One of the results did share good agreement with the experimental data however, that of Ho and Lakshminarayana (1996) but as is typical of this confusing set of results they did not used the recommended H-O-H mesh to achieve the best orthogonality possible, neither did they model transition and only converged their solution 2 orders of magnitude. Ho and Lakshminarayana (1996) did however use probably the most advanced turbulence model available, a low Reynolds number k-ε model and one of the larger meshes (approximately 400 000 grid points). In their journal article they pointed out that possibly more grid points would have been better and that they could not distinguish the pressure side horseshoe vortex from the passage vortex in their solution, believing it to have merged very rapidly with the latter. A similar study by Luo and Lakshminarayana (1996) investigated mesh

independence further by roughly doubling the mesh and settled on one of 790 000 grid points and suggested that a further doubling of the mesh, investigated in two dimensions only, showed no benefit.

Dunham and Meauze (1998) performed a study to determine best practice for turbomachinery CFD. Using the Rotor 37 compressor and the DLR turbine cascade as test cases they determined the following:

- 300 000 cells per blade passage are required for loss capture,
- 500 000 cells per blade passage are needed for accurate capture of the three dimensional flow features
- no one turbulence model is good in all situations, algebraic or mixing length models such as Baldwin-Lomax gave consistent results across all codes and turbulent convection models such as k-ε and one-equation models performed better for separated or highly three dimensional flows but wide differences were found resulting not from modelling practise but implementation of the models in the codes.

Despite Denton (2010)'s warnings regarding the assumption of steady state in what is clearly a highly unsteady case in practise, there is evidence to suggest that there is little to be gained from the additional computational effort of performing unsteady calculations, at least in terms of determining parameters such as loss or efficiency. This evidence stems from the 1½ stage Aachen turbine test case performed as part of the APPACET programme (Gregory-Smith and Crossland, 2001). Hence this study was performed using conservative mixing planes in a quasi-steady calculation. This results in a smearing of the secondary flows entering and exiting the rotor.

4.1 Choice of CFD codes

The CFD code chosen for this work was Numeca FINE/Turbo® v8, which is dedicated for use with turbomachinery and includes the capability to distort the mesh onto non-axisymmetric endwall geometries.

The solver is EURANUS which features Runga-Kutta central (viscous) and upwind (inviscid) differencing and the code uses full multigrid for accelerating the solution time, Numeca (2005).

4.2 Boundary conditions and Convergence criteria

Boundary conditions were chosen to best mimic those experienced in the experimental case. Inlet velocity was set to 21.38m/s and the outlet pressure set to a value approximating that found in the test rig. A mixing plane with conservative coupling was located at the stator/rotor and rotor/stator interfaces and the rotor speed varied to produce the off design results.

The solutions were converged to within 6 orders of magnitude in overall residual and better than 0.001% error in mass flow throughout.

4.3 Mesh Generation

The mesh used for the CFD computations was a fully structured hexagonal mesh in a HOH topology optimised to reduce cell skewness using the wizard and tools available within

FINE/Turbo®. There are 49 cell rows in the radial direction for the NGV and the 2nd stator and 81 cell rows for the rotor. The cells are given a parabolic distribution to increase mesh density in the boundary layer region at the endwalls. The cell width at the hub and at the shroud (casing) is set at 0.5 mm. The tip gaps each contain 17 cells, also distributed in a parabolic manner like those in the blade passage. Images of the final mesh are to be found in Figure 34. The final mesh statistics are as follows:

- Total: 2 030 954 points
    - NGV: 405 256 points
    - Rotor: 999 085 points
    - 2nd Stator: 626 613 points.

This yields a mesh with y^+ values on average less than 1 and a maximum of 2.2 on the blade surface. This mesh was used for all the subsequent CFD solutions.

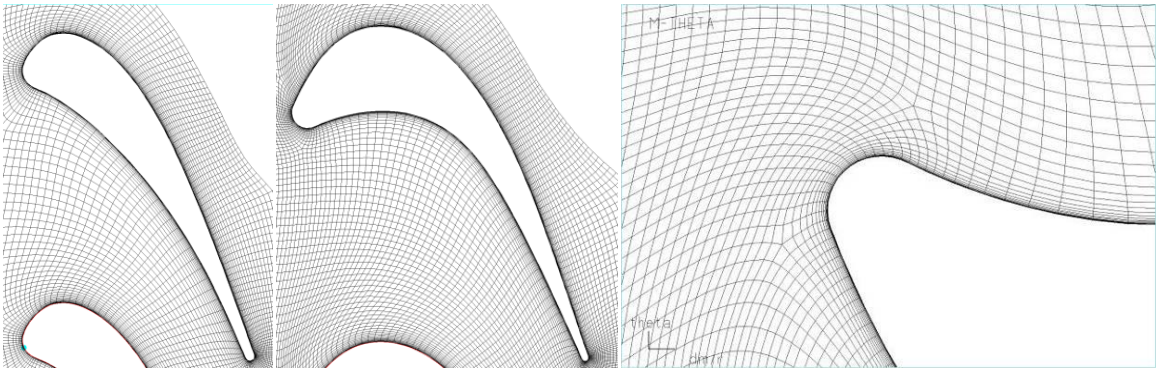

(a) (b) (c)

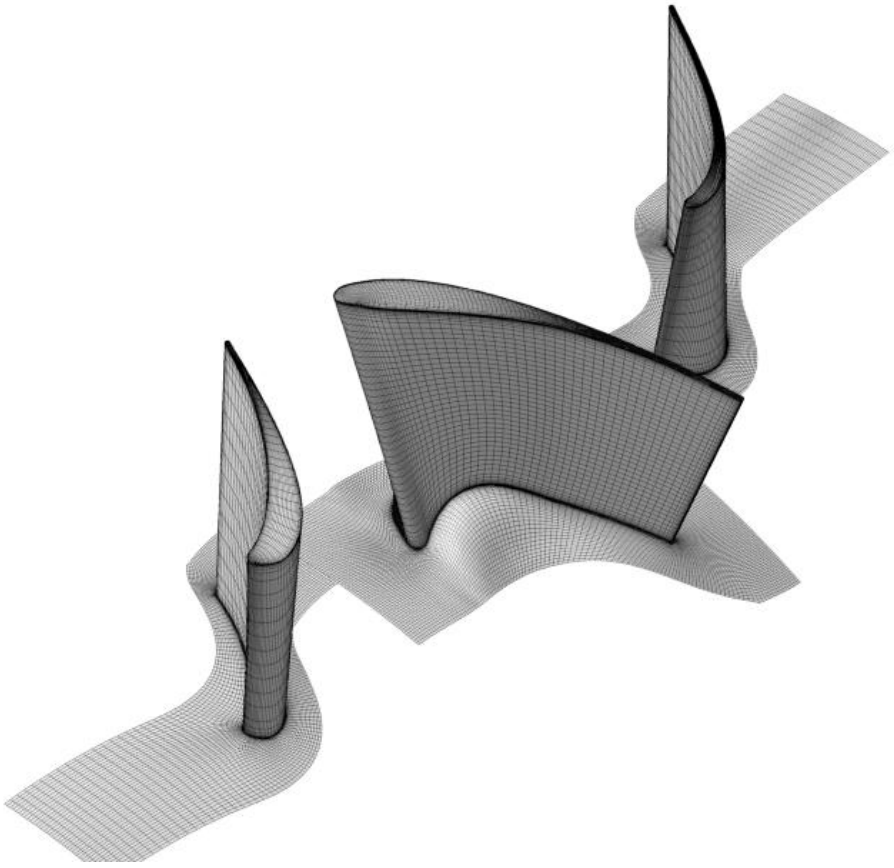

(d)

Figure 34: Final CFD mesh, (a) 1st Stator, (b) Rotor, (c) Close up of rotor leading edge, (d) Isometric view of the surface meshed (contoured rotor)

In all cases three full multigrid levels are available resulting in 3 meshes of increasing number of points:

- 222 48 936 points
- 111 276 394 points
- 000 2 030 954 points

This results in decreased solution times and facilitates a mesh independency study which was conducted with one additional mesh featuring the same number of span-wise points in the stators as for the original rotor mesh as well as other minor changes. This more dense mesh featured 2 635 018 points in total.

The fillets between the blade and endwall are not modelled despite the advice of Schuepenbach *et al.* (2008b) at the software vendor's suggestion (Hildebrandt, 2010) that this meshing feature did not function satisfactorily due to the increased cell skewness and often had the opposite effect to that which is expected.

4.3.1 Grid independence

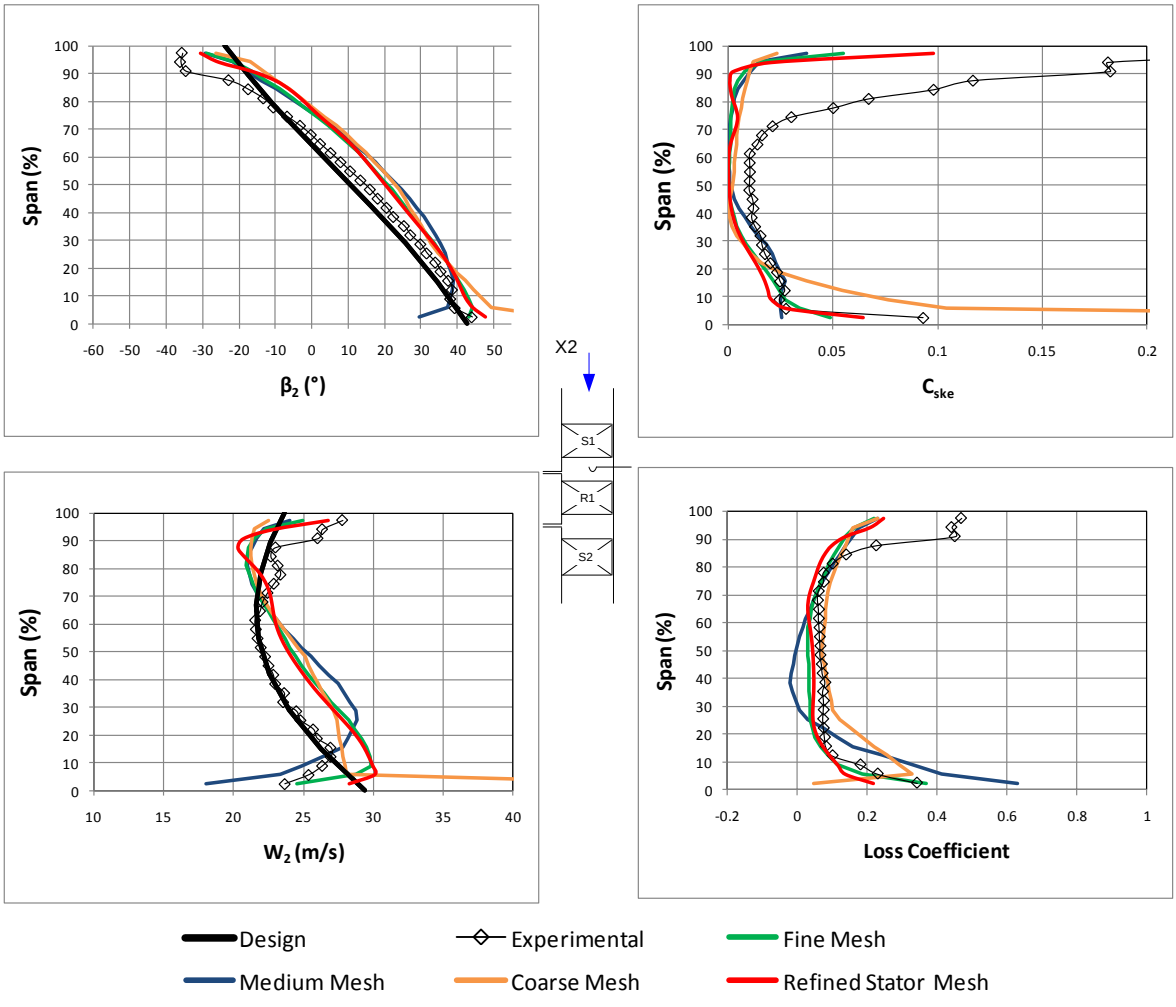

Figure 35: Comparison of selected mass averaged quantities at 1st Stator exit for various numerical meshes

All the mesh guidelines for best practise outlined by Gregory-Smith (1995) and Dunham and Meauze (1998) have been met or exceeded with the exception of the number of cells in the stator rows which is marginal. An interrogation of the multigrid results, presented in

relation to the annular rotor results at design speed and utilising the k-ω SST turbulence model (Figures 35 to 37), show the results to be largely grid independent in the 'fine mesh', particularly at stator exit. Differences do still exist between the 'fine' and 'refined stator' mesh in the rotor, but the features remain at the same span-wise locations and are limited to small variations in scale for example between 1 and 2° in exit angle and both of these meshes are consistent in terms of their variation from the experimental results.

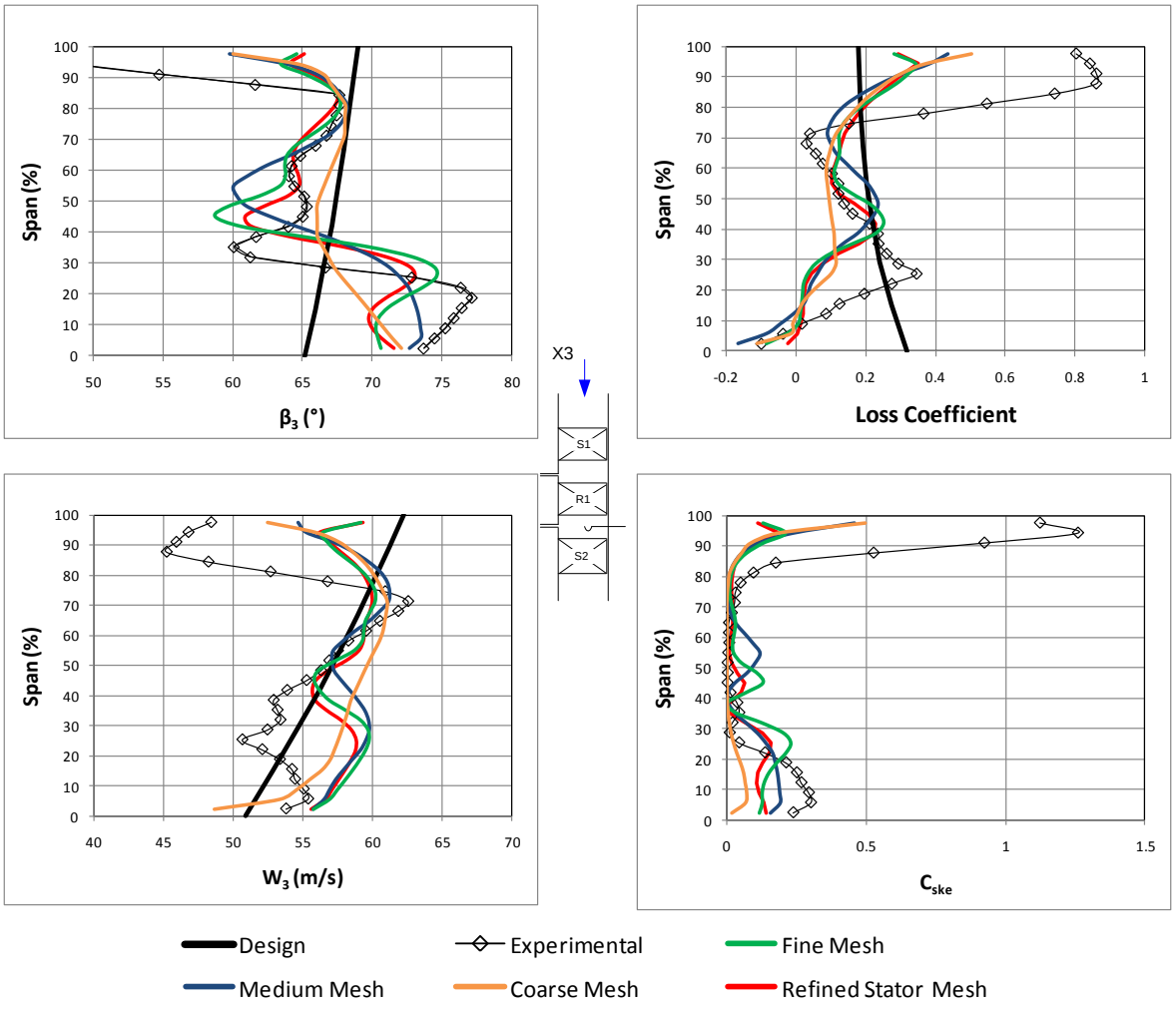

Figure 36: Comparison of selected mass averaged quantities at Rotor exit for various numerical meshes

The largest discrepancy in the mesh independency study occurs at the 2nd stator exit plane (Figure 37) where the additional span-wise points in the 'refined stator' mesh clearly allows improved capture of flow features as is evident from the exit flow angle plot. This does not affect the accuracy of the 'fine' mesh in terms of its ability to capture the general level of the parameters especially that of the pressure loss coefficient.

In addition the mesh size of just over 2 million points is already large in the context of a mesh suited to design iterations and while larger meshes can easily be solved, given time, the turnaround time for solutions is large and hence the 'fine' mesh was thought to be reasonable given the resources available.

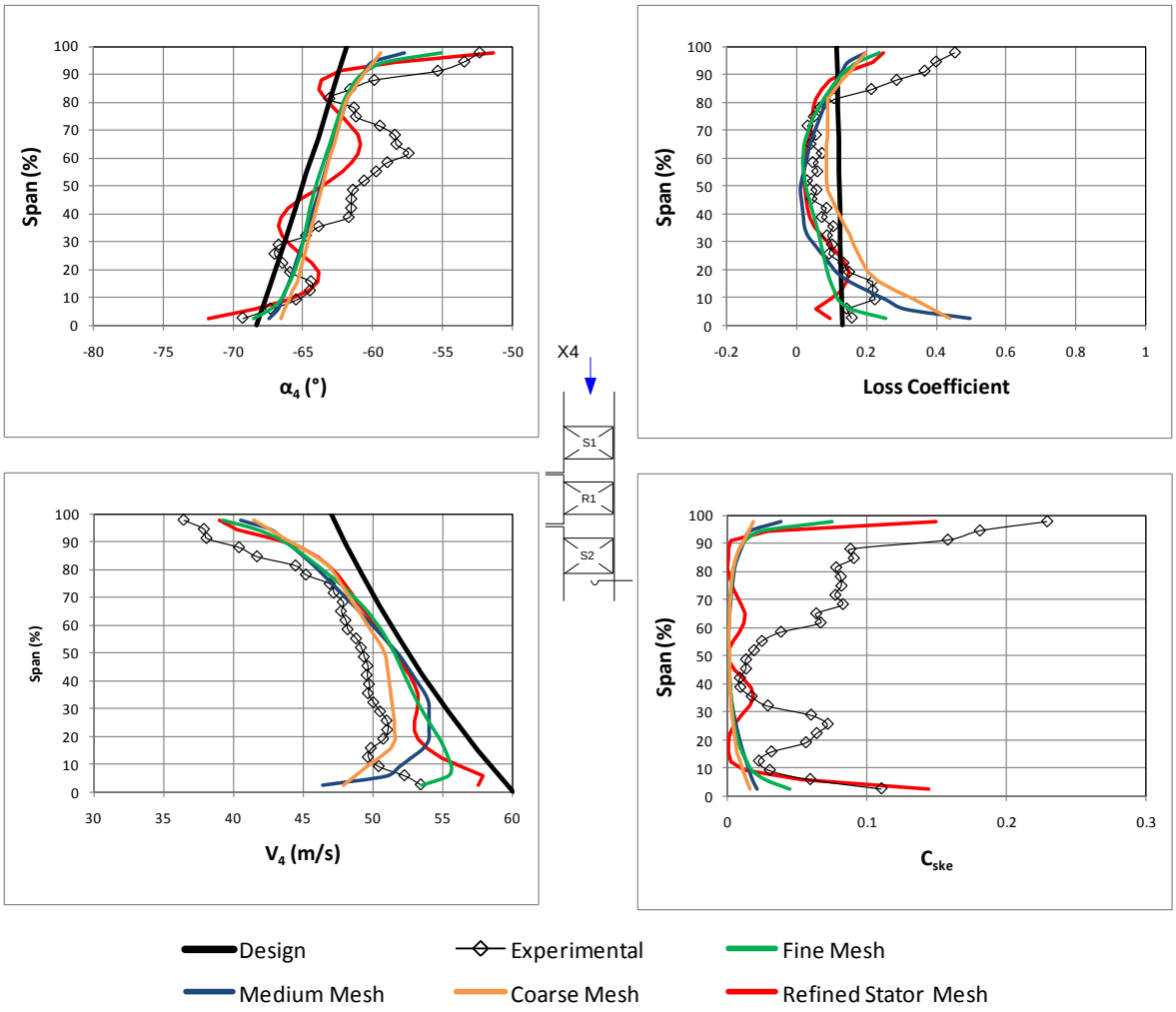

Figure 37: Comparison of selected mass averaged quantities at 2nd Stator exit for various numerical meshes

4.4 Modelling of the tip gap

One of the features of this rig is that all of the blade rows have a tip gap. This is done to facilitate the operation of the tangential component of the traverse mechanism. In the experimental setup the tip gap at rest is 0.5mm for the stators and 1mm for the rotor. This was originally faithfully modelled in the CFD mesh. The question of the correct method for modelling the tip gap arose as a result of the apparent mismatch between CFD and the experiment in this region as well as the large discrepancy between measured and predicted torque values.

Changes to the tip gap geometry can be justified in a number of different ways:

- The plastic blading has a low flexural modulus and long thin sections can be bent easily
- The tip gap was not a strictly controlled dimension given the emphasis on the endwall geometry
- The presence of a well in the casing which accommodates the cobra probe head when fully retracted to take measurements near the casing

Measurements of the blading at rest in the test rig confirmed the design tip gaps to within 0.2mm – which is the minimum sinter layer thickness. Some evidence of rubbing was

found but this is clearly a temporary phenomenon as the blading quickly erodes on contact with the casing. A crude finite element analysis of the rotor blade indicates that the tip gap should actually close slightly towards the trailing edge as a result of the gas forces and centrifugal loading.

This led to the examination of three tip gap geometries: A fully shrouded turbine, the nominal experimental setup and finally one with a tapered tip gap over the rotor, expanding from 1mm at the leading edge to 2mm at the trailing edge as a linear function of axial chord.

Further expansion of the work to investigate increased gaps on the rotor and the introduction of a taper to the tip gaps of the stators resulted in unstable flow solutions. Attention then turned to the investigation of the effect of the inlet boundary layer profile, and two simulations are provided in Figure 38, one being a turbulent Blasius flat plate profile (White, 2006) for the parallel inlet length and the second the average inlet profile measured at X1 both have constant tip gaps in the rotor geometry.

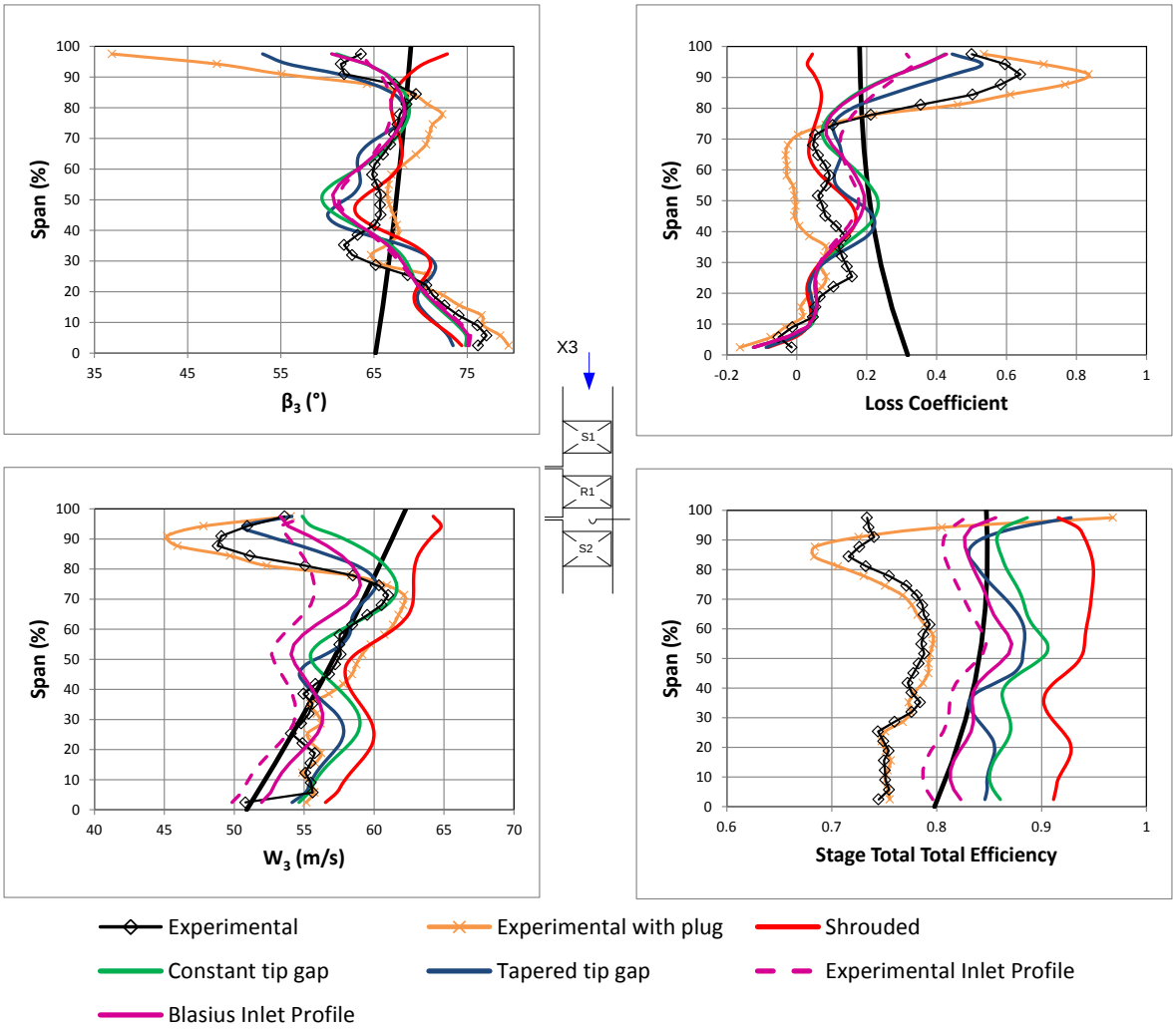

Figure 38: Comparison of tip gap models at rotor exit

The pitch averaged results of selected parameters are presented against the experimental data in Figure 38 for these models, in this case against the contoured rotor at design speed. Again the CFD results utilise the k-ω SST turbulence model. In addition a further

measurement was made with the probe well plugged with a ¾ insert, this insert was not used in any of the further experiments presented in this work.

Firstly it is apparent that the plug results in large difference in the experimental data at the tip with smaller differences extending over the span from 30-100%. Below 80% span these differences are limited to less than 2° in relative outlet flow angle and 4m/s in speed. The difference in loss coefficient should not be evaluated at its face value however due to its reliance on average values which are effected by the large changes at the tip, while the efficiency shows no discrepancy below 80% span and this quantity is an indication of the consistency in the pressure profile. Similar differences are visible between annular and contoured experimental results (see Figure 49). In addition Van Den Berg and Bertelrud (1988) suggest that 5-hole probes yield questionable results in highly sheared flows, such as is found in the tip gap region, when compared to non-intrusive laser based techniques, something that is likely to be exacerbated by the need to use the probe in a null yawing mode given the lag in the pressure measurement system. Due to the variation in results near the tip gap, either as a result of the highly sheared flows, exacerbated by the use of the pitch ports only in determining the static pressure; or the presence of the probe well means that all area averaged results presented for the X3 location, immediately behind the rotor will exclude the outer third of span in order to remove this uncertainty from the results. The presence of the probe well is further acknowledged as having a significant effect on the results presented at all measurement locations, throughout this thesis.

As the tip gap at the rotor trailing edge is increased in the CFD results so the CFD results trend towards the experimental data in the tip gap region, with only small changes evident below 80% span. There remains a large discrepancy in the efficiency predicted versus that measured for the stage, in the order of 10%, some of which (~1%) might be explained by disc windage and bearing losses in the experimental case and the lack of transition modelling in the CFD. Increased stator tip gaps and the pursuit of greater changes to the rotor tip gap was thought to be both impractical (as the solutions proved difficult to converge) and not physical. Hence the use of the tapered rotor tip gap was continued as best practice to cope with the effects of the measurement well. The inlet boundary layer investigations were introduced into the work at a late stage and were not utilised throughout the work. There is clear evidence that the reduced massflow rate in the experimentally derived inlet boundary layer profile reduces the torque and hence the efficiency significantly. There is an average mass flow reduction of 4.2% for all six cases comparing measurements at location X1 to the single point total pressure measurement at location X0, chiefly as a result of the deficit at the casing (Figure 44) where the probe is in the influence of the probe well and measurement points are sparse. However the effect on the pitch averaged profiles (chiefly a reduction in the inflection values at 90% and 50% span) of the all the quantities shown in Figure 38 is not enough to convince one that this modelling simplification is responsible for the discrepancies between experimental and numerical data profiles.

Few authors in the field have, as yet, shown direct comparisons between CFD and experimentally generated efficiency values, preferring instead to use the relative change between cases and compare these. Abdelfattah and Schobeiri (2010) show a comparison between an unsteady CFD computation across a broad speed range and a experiment on a 3

stage machine where the efficiency differs by between 1 and 4.2%. Gregory-Smith and Crossland (2001) compare computational results from three different sources, both steady and unsteady, where the efficiency varies by as much as 6.4% and there is little consistency in terms of the effects of changing to unsteady solutions. With this backdrop the discrepancy in the absolute value of the efficiency predicted and measured in this study cannot be seen as abnormal and is most likely due to a combination of unknown geometry and boundary conditions, turbulence modelling and unsteady effects, to use Denton (2010)'s classification as well as uncertainty in the bearing losses in the experimental results as well as the effect of the inlet boundary layer which has not been simulated correctly.

4.5 Choice of turbulence model

Dunn *et al.* (2009) presents a comparison of results for this same turbine and grid intended to make a selection of the best turbulence model for application to further CFD analyses. The conclusions were based on comparisons with measurements of fundamental parameters such as velocity profiles at exit to the rotor. On the basis of this preliminary analysis the k-ω SST turbulence model was selected as best for capturing the flow features, however, for the purposes of this work CFD results have been generated using three models for comparison:

- Baldwin-Lomax
- Spalart-Allmaras
- k-ω SST

4.5.1 Baldwin-Lomax turbulence model

This two layer algebraic (zero equation) model is ideal for design cycle analysis where a robust and fast model is required. Dunham and Meauze (1998) noted the consistency of the results it produced across a wide range of codes. One of its notable advantages is its good prediction of sheared flow (Versteeg and Malalasekera, 1995). However this is not propagated upstream as it is a zero equation model without turbulent transport, limiting the span-wise expansion of the vortices.

4.5.2 Spalart-Allmaras turbulence model

This is a one equation model. The transport equation for eddy viscosity is solved making it always continuous. It is now very popular due to its robustness and simplicity and has found favour in a wide variety of aeronautical applications not least of which is in the design of profiled endwalls where authors such as Shahpar and Lapworth (1998) and Ingram (2003) describe its use.

Numeca FINE/Turbo® does offer the coupling of the Spalart Allmaras turbulence model with the transition model of Abu-Ghannam and Shaw (1980) obtained using experimental data of transition on a flat plate with pressure gradients. This system was only available for application to the aerofoil surface however, and no advantage was found to its use in this application. This may be partly due to the high levels of unsteadiness in the rotating rig which reduce the effect and extent of laminar flow regions in the boundary layer, and is certainly a result of not being able to model the laminar regions on the endwall. This failure to implement transition modelling coupled to the rough surface of the blades tested

might, in part, account for the discrepancy between experimental and numerical results for efficiency as the numerical results overestimate the torque generated by the blading.

4.5.3 The SST k-ω turbulence model

The final turbulence model used was developed to blend the robustness and accurate formulation of the k-ω and the free stream independence of the k-ε. The k-ω and the k-ε are both multiplied by a blending function and added together (Mentor, 1994). The blending function is created such that in the near wall regions the k-ω is used, and in the free stream regions, far from the walls, the k-ε is used (Numeca, 2005). The Wilcox k-ω model (Wilcox, 1998) is said to predict free shear flow spreading rates that show good agreement with experiments for far wakes, mixing layers and planar, round and radial jets (Numeca, 2005). Mentor (1993) does however make statements to the effect that the SST k-ω model has a tendency to over-predict turbulence levels in regions of stagnation, which could result in an over-prediction of the horse-shoe vortex strength, exaggerating its effect.

All turbulence models are implemented as standard in Fine/TURBO® v8, without calibration.

4.6 Post-processing of the CFD results

All results were processed through CFVIEW®. In particular, however the pitch averaged results are the product of the turbomachinery module within CFVIEW® which was used to extract the same data available from the experiments at the identical locations in both axial and radial directions. This data was then processed identically to that of the experiment using the method laid out in the previous chapter. This eliminates any discrepancy derived from software or programming, as well as pressure variations at inlet. This applies to all pitch averaged plots of data and to any area averaged result given throughout this work.

4.7 Conclusions

In the following chapter the CFD results for the three turbulence models will be combined with the data from the experimental test rig to both validate the CFD and also examine the flow mechanisms in greater detail. Simulations and experimental results are presented both for the change in endwall design and at three different load conditions varied by changing the rotor speed.

5 Results

The results presented in this chapter are those generated experimentally along with the equivalent CFD data which is compared for validation purposes. Similarly the area averaged data is presented comparatively in order to ascertain the quantitative predictive capabilities of CFD and its suitability for use as inputs to the objective functions used in the optimisation of endwall shapes.

Section 5.1 highlights the differences in the purely experimental data as incidence changes and juxtaposes equivalent data for the annular cases and contoured cases. Section 5.2 introduces the CFD data for validation against a broader set (than Section 5.1) of pitch averaged information before Section 5.3 draws all the data up to the area averaged results for each of the builds and incidence conditions tested and computed. These builds and conditions are summarised in Table 8.

Table 8: Experimental results build key

Build	Stages	Rotor Endwall	Measurement locations	Key	Rotor RPM		
					Incidence angle		
A	1½	Annular	X1	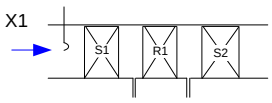	2820	2300	1907
					-ve	design	+ve
			X2	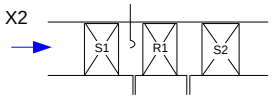	2820	2300	1907
					-ve	design	+ve
			X3	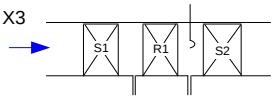	2820	2300	1907
					-ve	design	+ve
			X4	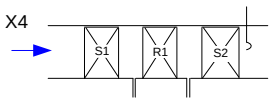	2820	2300	1907
					-ve	design	+ve
B		Profiled	X1	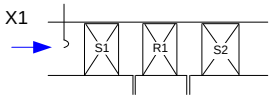	2820	2300	1907
					-ve	design	+ve
			X2	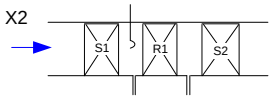	2820	2300	1907
					-ve	design	+ve
			X3	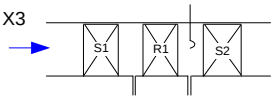	2820	2300	1907
					-ve	design	+ve
			X4	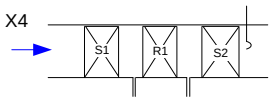	2820	2300	1907
					-ve	design	+ve
C	1	Annular	X4	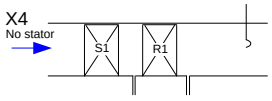	2820	2300	1907
					-ve	design	+ve
D		Profiled	X4	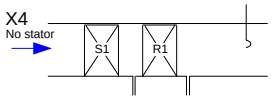	2820	2300	1907
					-ve	design	+ve

Some of the figures which follow may not be referenced in detail but have been included to complete the dataset.

5.1 Pitchwise averaged experimental results

The first group of pitchwise averaged figures (Figures 39 to 42) represent only experimental results, and as such the meaning of the line colours are different to all other graphs in that they represent the incidence angle or rotor speeds tested.

5.1.1 Rotor Exit

Comparing Figure 39 (a) and (b) which show the relative outlet flow angle for the annular and contoured rotors respectively, two features of the impact of endwall contouring stand out:

- Above 30% span the results for the contoured endwall show the exit flow angle to be more tightly centred about an outlet flow angle of 65° than for those of the annular endwall. This is most clearly evident at the tip.
- The overturned flow in the lower 30% of span is clearly suppressed towards the hub although the peak magnitude is unaltered

The same conclusions can be drawn from (c) and (d) of the same figure. There is no clear trend with changing load in these figures, but the effect of the endwall is clear.

Figure 39 (e) and (f) compare the rotor exit relative velocity for annular and contoured endwalls respectively. For this parameter the effect of changing load is clearly evident in the spread of the graphs below 40% span, however in the same span-wise region there is little clear evidence of the effect of changing the endwall. The inflections in the same graphs at 70% and 90% span do not change with load but are reduced in deviation from the average by the introduction of the endwalls by as much as 5m/s with the exception of the lowest load case which is almost entirely unaffected by load or endwall variation.

The large variations between annular and contoured rotors seen in the tip gap region, 90-100% span, for all parameters shown in Figure 39 as well as in Figure 40 are unexpected as the effect of the endwall shaping is intended only to have a localised effect in the span-wise direction.

For the derived quantities shown in Figure 40, the loss coefficient, graphs (a) and (b), show a strong influence from endwall variation but not load. The inflection points at 25% span and 90% span reducing in magnitude by approximately 0.2 in both cases. Stage efficiency (graphs (c) and (d)) is affected by both load and endwalls with the largest effect coming from load variation with the effect being located at the casing. The effect of the endwalls on stage efficiency is seen in the elimination of a 5% trough in the efficiency at 25% span, the same location as seen in the loss coefficient. Only the coefficient of secondary energy graphed in (e) and (f) of the same figure shows a strong influence from both load and endwall variation in the hub region. Below 30% span the secondary kinetic energy varies in both magnitude with load and in form or radial extent with a marked suppression of the coefficient towards the hub as a result of the profiling of the endwall. The secondary energy in the span-wise region influenced by the tip gap leakage (>80% span) is more than halved by the profiling of the endwalls and therefore dwarfs the changes seen at the hub

masking the effect of the flow directly influenced by the endwall. This is confirmed by the results shown in Figure 86.

5.1.2 2nd Stator Exit

Figure 41 examines the pitchwise averaged results at the stator exit. Graphs (a) and (b) indicate a broad range of changes in the flow structure. Firstly the inflection found at 65% span in the annular case is eradicated in the contoured equivalent and instead replaced with a broad span-wise section of constant flow angle between 45 and 65% span. This is especially noticeable at the highest load. This would appear, from Figure 69, to be the span at which the rotor secondary flow emerges from the stator. At 10-15% span a further inflection indicates the presence of endwall secondary flows initiated in the stator row and in both the annular and contoured case there is a significant increase in the severity of this peak for the highest load case, however the contoured case exhibits a higher magnitude peak in all cases and even a greater span-wise extent for the highest load case which may suggest that some separated flow may be present. This would also account for the distinct offset in stage efficiency and loss coefficient found in Figure 42 for this case as well as the thicker wakes seen in Figure 74.

Graphs (c) and (d) of Figure 41 are included largely for completeness but do indicate minor changes at the hub as a result of changes in load, while none of the clear changes evident in the exit flow angle (Graphs (a) and (b)) are read through to the flow velocity profiles.

Neither the loss coefficient nor the 1.5 stage efficiency show much of particular interest, in Figure 42 however C_{ske} graphs (e) and (f) clearly indicate the position of the rotor secondary vortices emerging from the stator at 65% span and the secondary kinetic energy present in the contoured endwall, high load case is spread over a slightly greater span range but the peak value is roughly 25% reduced. No clear evidence of the stator secondary flows is visible in the plots of C_{ske}.

5.2 Pitchwise averaged comparative and area contour results

The figures discussed in this section (Figures 43 to 78) cover a broad range of parameters and represent measurements, design data and three CFD solutions for all the build and flow conditions described in Table 8. To study this large array of data the following information regarding the format and content of the figures may be of use to the reader:

- Each set of six graphs of pitchwise averaged data represents a full set of both rotor endwall shapes at all three rotor speeds as per Table 8
    - Annular endwall results are plotted in the left hand column, and contoured results appear to the right
    - Each row represents a rotor speed set
- The lines colours used in graphing the data are used consistently throughout these and later area averaged plots, the colour key for which is contained in the table below
- In all X2, X3 and X4 measurement locations an area contour plot of the data is provided both inset and on a subsequent figure at a larger scale.
    - Experimentally derived contour plots are used wherever possible namely at the X2 and X4 measurement locations. In some of these contour plots blank

spaces appear. These represent points at which the flow angle was outside the cone of acceptance for the 5-hole probe

- At X3 the contour plots are CFD based as no rotor relative contours can be extracted behind the rotor utilising a steady state probe.

Table 9: Results key

Line colour	Description
	Design
	Experimental result
	Baldwin-Lomax CFD result
	Spalart-Allmaras CFD result
	k-ω SST CFD result

5.2.1 Inlet

The inlet velocity profile indicated in Figure 44 is essentially flat (within 0.2m/s) over 80% of the span with a clear drop in velocity in the boundary layer below 10% span and above 90% span. It is also important to note that the uncertainty of the probe quoted from the manufacturer in Table 3 would equate to 0.17m/s.

The yaw angle results shown in Figure 43 also indicate non-zero results ranging from -4° yaw at the hub to 2.5° yaw at the casing which is not matched by the flat CFD inlet profile defined. This disparity can potentially impact on downstream results but is limited to one data point and the effect small enough that it was not considered further.

5.2.2 Stator Exit

The rotor inlet flows shown in Figures 45 to 48 serve to show that the flow entering the rotor is in all experimental cases highly consistent across all rotor speed and endwall variations.

The rotor inlet data (Figures 45 to 48) show a clear set of wakes for the upstream stators and in the case of the loss coefficient plots (Figure 48) a very weak secondary flow vortex in the bottom corner, below the diagonal wakes. The rotor inlet flow is, however, not preconditioned with large-scale endwall secondary vortices.

5.2.3 Rotor Exit

Figures 49 to 58 show pitchwise averaged experimental data as a function of span and the equivalent values for the CFD predictions for each of the three turbulence models. Inset are the Spalart-Almaras contours to indicate the tangential variations and these same contour plots are reproduced in the next figure as is the case for all the rotor exit results.

With the exception of the tip region (see Section 4.4) the CFD results match the experimental results well. The general form, the span-wise location of the inflection points and overall effect of the profiling of the endwalls are reproduced faithfully. There is some discrepancy in the magnitudes of the inflections with the Baldwin-Lomax model performing best in this regard while the higher order models tend to slightly overestimate

the span-wise migration of the inflections and underestimate the magnitudes, with the Spalart-Almaras assuming the middle ground.

Results of particular interest include:

- Profiling of the endwall results in the suppression of the overturning in relative outlet flow angle towards the hub (Figure 49) by 10-13% of span
- The SST k-ω model predictions add an additional inflection point in relative outlet flow angle profile at 20% span for the contoured cases for which there is no strong supportive experimental evidence, but is likely to indicate the increased separation of vortex structures in the bottom third of the span which is also shown by the Spalart-Allmaras area plots (Figure 49)
- As the design profile of rotor relative outlet flow angle is derived from a streamline throughflow method the effects of secondary flows are omitted and hence the viscous effects and secondary flows result in a deviation from the expected profiles (Moustapha *et al.*, 2003). The deviations from design (Figure 51) closely reflect the results for the exit flow angle in Figure 49 but can be more readily area averaged to create a number by which to evaluate the performance of the design than can the raw rotor relative outlet angle
- Rotor exit loss profiles from the CFD, as shown in Figure 51, indicate a weakening of the loss cores (±2%) as well as an increase in their radial location (upto 15% span for the SST k-ω case) with profiling of the endwalls, similar observations are true for total efficiency (Figure 55) although the magnitude is in the opposite sense and the peaks are clearer (1-5% variation 25 and 35% span)
- The span-wise profiles of total efficiency (Figure 55) show good agreement in form, but are offset in magnitude by upto 9% as a result of a mismatch in the torque values measured versus predicted.
- C_{ske} results show good agreement between CFD and experiment with the main area of disagreement being the radial location and intensity of the small peak predicted at midspan but experimentally located at 35% span for the design annular case (Figure 57). The general trends in the area plots show increased intensity and extent in the peaks with increased loading and clear reductions (5% at 5% span for the design case) in the same peaks in the profiled turbine (Figure 58).

5.2.4 Rotor exit measured downstream

These plots are aimed at complementing those discussed in the previous section as the measurement location is approximately one axial chord length downstream and is therefore representative of cascade tests in which results are often available at a variety of axial locations including those far downstream. As is clearly visible from the CFD area plots in Figures 59 to 68 the tangential variations in the rotor flow are largely mixing out by the time they reach this downstream location; remembering that the stator wakes are averaged out by the stator-rotor interface upstream of the rotor. This means that the discussion can be limited to the two dimensional pitchwise averaged plots. No attempt was made to compute fully mixed out values, only downstream measurements and the results from similar CFD simulations are presented.

When compared to Figures 49 to 58 they exhibit smoothed inflections and fewer small inflections and the magnitudes of the peaks and throughs are grouped closer to the average.

In Figure 59 the exit flow angle no longer indicates a suppression of the overturning towards the hub with the introduction of contouring as it did in Figure 49, but instead the peak values at roughly 15% span are significantly diminished by 2 to 3°. The CFD tends to over predict the variation of these peaks and throughs from the average by 2 or 3°, in one instance 5°; and for the design case in particular overestimates the radial positions of the inflections by as much as 10%.

None of the measures of loss produce any distinctive features in the pitchwise averaged profile which suggest a strong shift in the performance of the turbine. Once again there is a clear offset in the efficiency results (Figure 65) between CFD and experiment as a results of the discrepancy between the measured and predicted torque values. Both experimental and CFD results do, however, indicate subtlety improved performance through a general shift in level.

The true value in these particular results is to be found in the area averaged form (see Section 5.3).

5.2.5 2nd Stator Exit Plane

As was discussed in the CFD methodology section the CFD results presented in this section do not have sufficient radial resolution to capture secondary flows well in this row, and the upstream rotor stator interface will smear the flows from the rotor as they enter the row. Thus it is noted that the CFD generally attains good agreement to the overall magnitude (with the exception of efficiency values where the rotor torque prediction is required) and simplified span-wise trends in the data only.

The experimental data presented in Figures 69 to 78 can be summarised as follows:

- The wakes from the rotor stage emerge from the downstream stator row at between 40 and 80% span with the effects listed below (Figure 72):
    - A thickening of the loss wakes and 5 to 7° less turning at 60-65% span (Figure 72)
    - This effect increases in severity with load (Figure 72)
    - The effect of the profiled endwalls in the rotor is to extend the area of underturning, although the peak value is reduced by roughly 2° compared to the annular case (Figure 49). The extension of the area of underturning leads to a stronger coupling of the loss cores resulting from the endwall secondary flows of the rotor and the 2nd stator (Figure 72).
    - The coefficient of secondary kinetic energy graphs (Figure 77) also indicate an increase at these span-wise locations of 60-70% span, but the real interest lies in the emergence of a parallel ridge structure, at 45° to the radial direction, in the area plots of this parameter (Figure 78). One exhibits radial upward flow and the second downward flow with the features growing in intensity with increased load.
- The endwall secondary flows close to the hub, which are attributed to the 2nd stator itself appear at 15% span
    - These appear far stronger in the profiled case than in the annular one, resulting in 3° less turning increase in the local loss peak of 0.05 and clearly intensified cores on the area plots of loss (Figure 71), nozzle (Figure 73)

and 1.5 stage efficiency (Figure 75) although barely evident on the secondary kinetic energy plots (Figure 77) there are small changes there too.

- There is a strong shift in loss and efficiency (Figures 71, 73 and 75) results associated with the highly loaded non-axisymmetric case of roughly 10% this appears to be associated with the dominance of the wake structures over the passage flows. The exact origins of this shift are difficult to diagnose as the CFD does not provide sufficient resolution of the stator flows and there is no evidence in the existing CFD results of vortex shedding for instance.
- There is no strong trend on the experimentally derived tip clearance flows associated with the introduction of non-axisymmetric endwalls (Figures 69 to 77).

5.2.6 Overview of pitch averaged results

Reasonable agreement between CFD and experiment both in terms of load variation and the effect of endwall profiling has been demonstrated for both sets of rotor exit results, particularly in terms of the radial location of flow features and radial distribution. The general levels are also well captured with the exception of the efficiency results. Thus the rotor exit CFD results can be considered validated, and further conclusions are drawn from the Spalart-Allmaras results in particular using pressure plots at stations that cannot be measured using the 5-hole probe and techniques such as the drawing of streamtubes.

Experimental results for the 2nd stator exit also demonstrate clear differences resulting from changes in rotor speed and endwall geometry.

5.3 Area averaged results

These figures (Figures 79 to 90) are divided into two columns with the left column looking at each rotor speed case with increasing load as one moves from the top to the bottom of the page, with area averages of each third of span (top third of span at the top of each graph, the middle third of span (middle) and the lower third of span (bottom of each graph) compared for annular and contoured rotor cases. The right hand column contains the full or lower 2/3^{rds} area averaged results and feature a trendline of a parabolic nature inserted through the points in *Excel* as these generally fit the data well but the lines should be used tentatively to indicate a trend only. The line colouring is used in accordance with Table 9 with the addition of solid lines to indicate the annular baseline and dashed lines for the contoured endwalls.

Stage efficiency improvement is one of the key aims of contouring the endwalls of a turbine. The efficiency trends indicated in Figure 79 show that the experimental, contoured turbine has no net gain or loss in efficiency at the design speed. At increased turning, as the secondary flows increase in strength there is a drop of 0.2% and at part load the effect of the endwalls is an even larger reduction of 0.7%. None of the CFD results indicate the same reductions at off design, with the Spalart-Allmaras indicating a 0.5% improvement resulting from the implementation of endwall contouring and an improving trend with increasing load; the absolute values are quite different, but this is thought to be as a result of the torque prediction which does not account for the effect of transition or the experimental bearing loss. As for the one third span averages in the left hand column, the tip region demonstrates a fluctuating trend in the difference between annular and contoured cases with load variation while in the lower third of span the results consistently favour the

contoured case but this advantage is eroded in the midspan region which demonstrates consistently better performance for the annular cases.

Figure 80 gives the same results as Figure 79 except that the measurement station is further downstream and the radial and tangential variations have been mixed out to a greater extent. Once again the CFD results are offset from those of the experiment but the trend with increasing load is reasonable. The endwalls show a significant improvement across the entire speed range, and the profiled turbine is 1.5% more efficient at design with the gains reducing with the reducing strength of the secondary flows and decreasing load. Likewise the third span results show an across the board improvement with the top third of span showing as much improvement as the lower sectors. The absolute value of efficiencies at measured at X3 and X4 cannot be directly compared as the averaged area varies.

The second gain expected from a contoured turbine is the improvement in efficiency in downstream rows resulting from improved flow qualities emanating from the profiled row. Figure 81 and 82, which show results downstream of the second stator, are indicators of the efficiency of the downstream row and the effect is dramatically opposed the conventional logic. Only the design case approaches parity and the negative effects of the introduction of the endwall are felt across the span with similar magnitude decreases at the tip as at other stations. The CFD results are inconclusive.

The next most common measure of the effectiveness of endwalls is total pressure loss and these results are given in Figures 83, 84 and 85. Total pressure loss is generally used throughout the literature which deals with cascade testing where no torque is generated and therefore the pressure drop across the blade row is substituted for power in the output term in the efficiency equation. Rotor loss is improved in all cases by the introduction of profiling in the experiment. Improvements are dramatic immediately downstream of the rotor (6.4% at design point) but more modest further downstream (2% at the equivalent speed). The improvements are seen at all spans immediately downstream of the rotor but further downstream the loss in the outer third of span is increased at off design speeds while the largest gains are found close to the hub at increased load. The CFD results bear little resemblance to the experiment apart from being on the same axes in terms of overall magnitude unlike those for efficiency. CFD predictions generally indicate improved loss (0.5% at design) but the gains are more modest than indicated by the experiment. As with the equivalent efficiency results the loss in the second stator is increased and the overall effect of the introduction of the endwall is negative in terms of its effect on the downstream row particularly at off design conditions. CFD results for the stator are inconclusive at best.

The next set of graphs (Figures 86, 87 and 88) examines the effect of the endwalls on the secondary kinetic energy present in the flow. Figure 86 indicates a clear improvement in the experimentally derived results close to the rotor exit, the coefficient of secondary kinetic energy is reduced by 1.5% at design and 3.7% at high load but only 0.3% at part load. The CFD results produce similar improvement and trend predictions. The span-wise trends also indicate a clearly improving trend at the top and bottom sectors of the span and little or no change in the midspan regions where there is little activity. Further downstream

(Figure 87) the vortices are mixing out and the experimental trend is not as clear with the only significant change being an increase in secondary kinetic energy at the lowest rotor speed which is where the largest efficiency improvement is predicted. This increase stems from both the casing and hub sectors with a 0.6% improvement in the midspan region. At increased speed the values of C_{ske} diminish both in the CFD and experimentally as do the differences between the two endwall configurations. Again the higher order turbulence schemes perform better than the zero-order Baldwin-Lomax model which performed better in trending efficiency. This is a result of the more complex schemes ability to model the mixing processes and vorticity generation which is absent in the Baldwin-Lomax scheme. The Baldwin-Lomax model does, however, produce good overall results despite its simplicity, at least as good as those for the more sophisticated models in this case; and should not be overlooked in further investigations.

Only the experimental results are shown in Figure 88, as the radial resolution is not sufficient in the CFD mesh to capture these results well. There is a slight decrease in secondary kinetic energy for the contoured rotor endwall configuration at the design speed which emanates mostly from endwall (bottom third of span) secondary flow reduction while the secondary energy for the lightly loaded case is increased, particularly in the casing region. The highly loaded case yields no real net effect with gains in the tip region being balanced by increased secondary energy at the hub with the introduction of the contoured endwall.

The final parameter presented in this way is the deviation in rotor exit angle from the designed value. Close to the rotor hub (Figure 89) the contoured endwall configuration introduces a marked improvement, but this gain is eroded with distance (Figure 90) and there is essentially no difference between the endwalls at the downstream station as measured experimentally. The CFD on the other hand continues to predict improvements in the same order although the overall value of the deviation has decreased. The total deviation generally increases with load, but the profiling shows an increasing improvement over the annular case with load. The CFD results are either bracketed by the experiment or within 2°. The significance of the good correlation of the CFD and experimental results for this particular measure lies in the potential of deviation from design angle to be used as an objective function in a multistage environment where one can only afford the computational resources to optimise one row at a time. By matching the actual rotor exit flow angle to the design one sets up the flow into the downstream row correctly.

5.4 Overview

By comparing the experimental results for different endwall configurations and at different load conditions it was possible to isolate rotor relative outlet flow angle, loss coefficient and C_{ske} as the most effective parameters for indicating the effects of the endwall configuration change while others indicated the load variation. Efficiency was influenced by both.

Despite good correlation between span-wise profiles of most measured and calculated parameters providing confidence in the accuracy of the CFD method few of these parameters translated well into usable parameters with potential for use as optimisation objective functions. Notable exceptions include C_{ske} and exit flow angle deviation, while

total pressure loss coefficient close behind the rotor has potential of use despite the poor correlation between the trends indicated between area average experimental and CFD results. Spalart-Allmaras is indicated as the preferred turbulence model as it provides a consistently well behaved dataset.

The next chapter deals with CFD derived results to examine the flow structures in greater detail before a discussion of the full dataset and the use of selected parameters as optimisation objective functions is examined in Chapter 7.

5.5 Figures

5.5.1 Pitch averaged experimental results

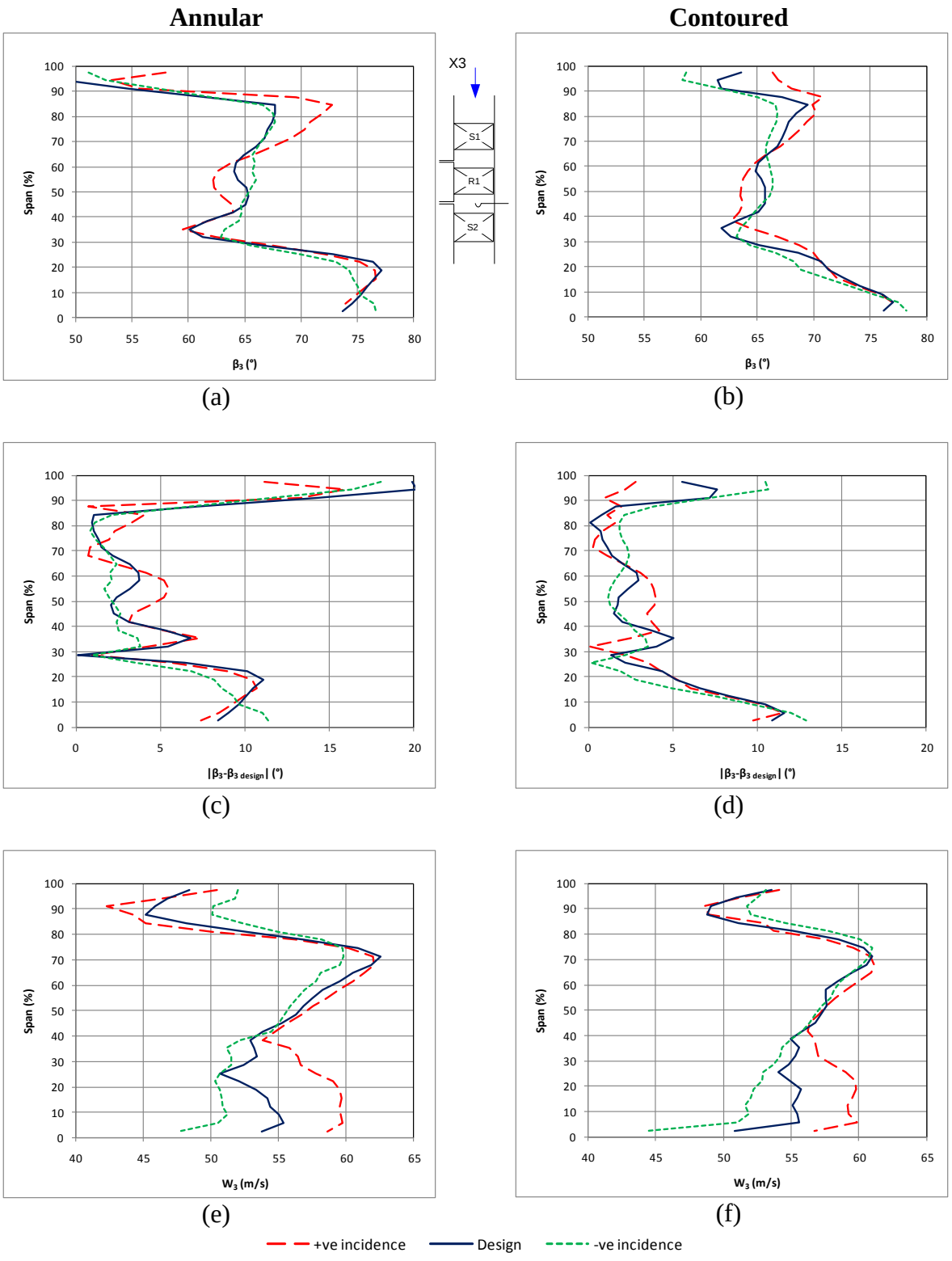

Figure 39: Comparison of rotor exit span-wise distributions of primary experimental data at different loads

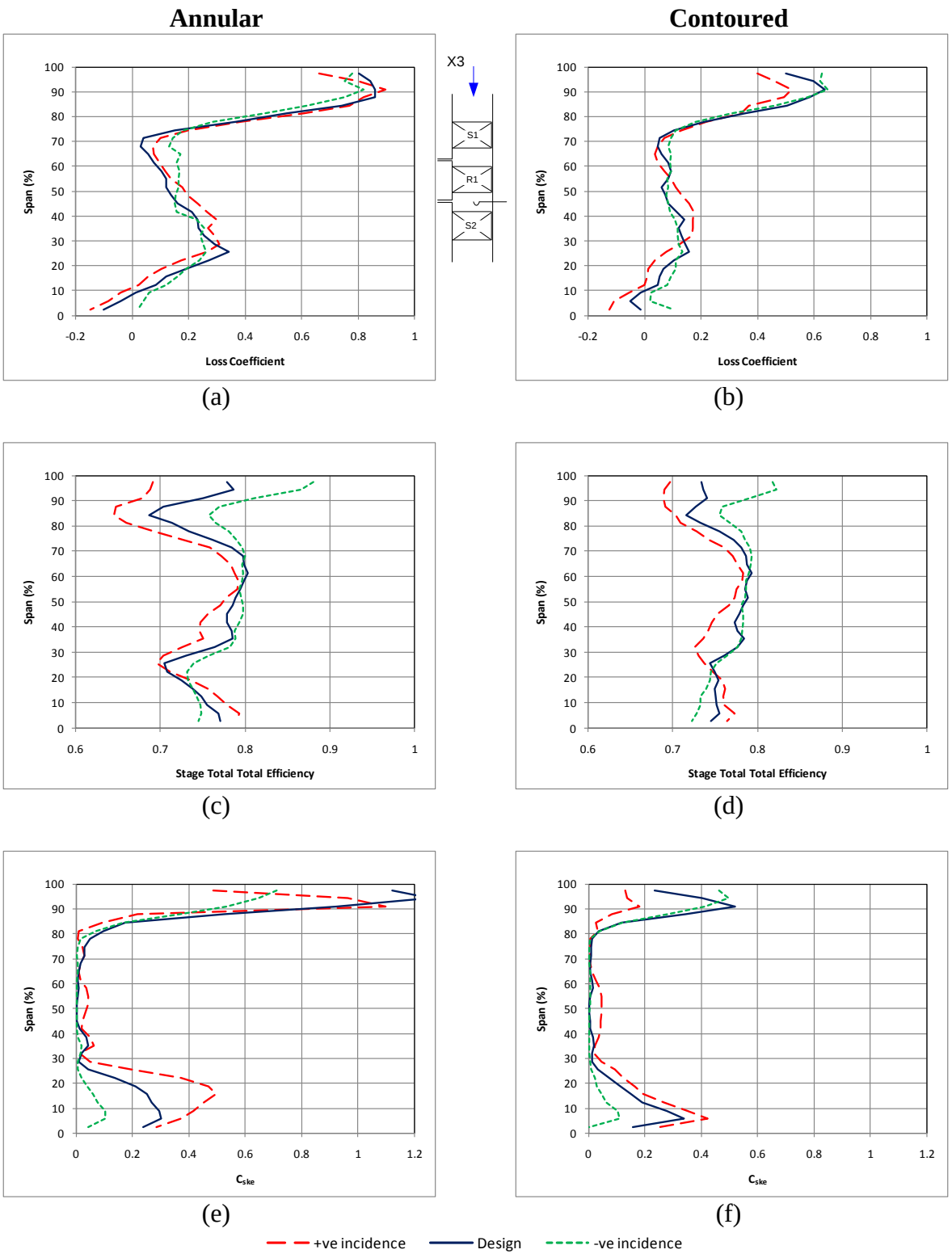

Figure 40: Comparison of rotor exit span-wise distributions of loss measures derived from experimental data at different loads

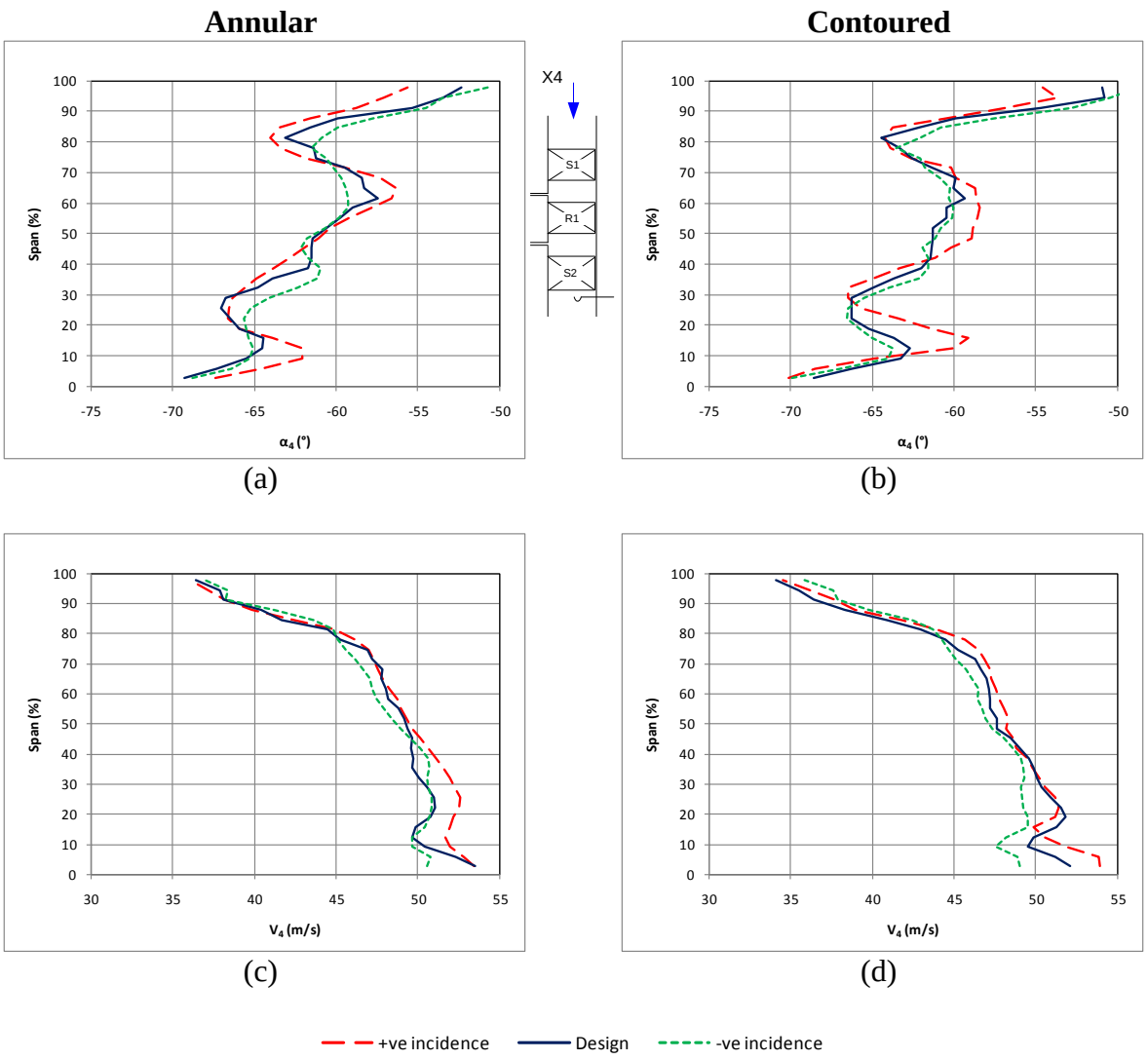

Figure 41: Comparison of 2nd stator exit span-wise distributions of primary experimental data at different loads

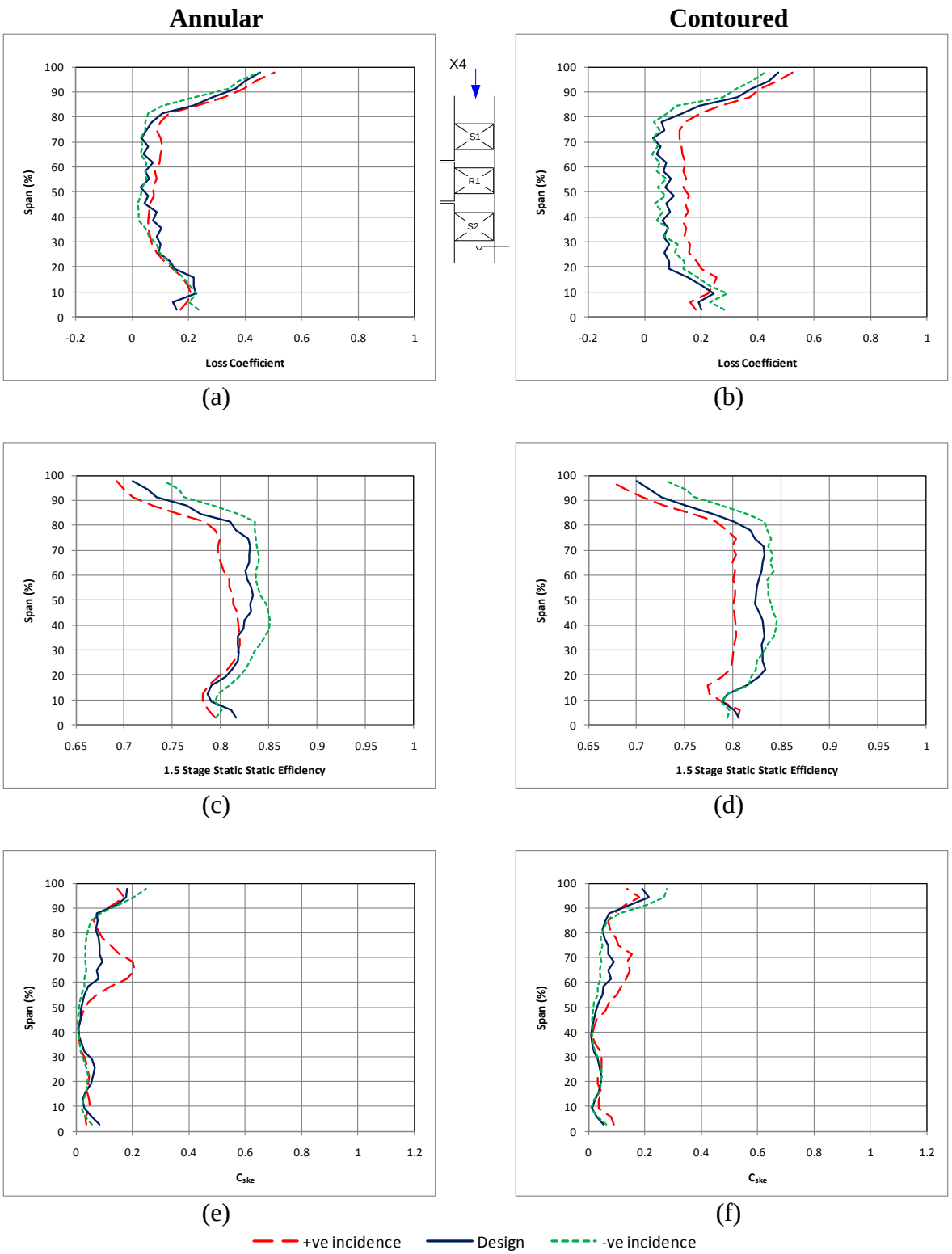

Figure 42: Comparison of 2nd stator exit span-wise distributions of loss measures derived from experimental data at different loads

5.5.2 Pitch averaged experimental and CFD results, area contour plots inset

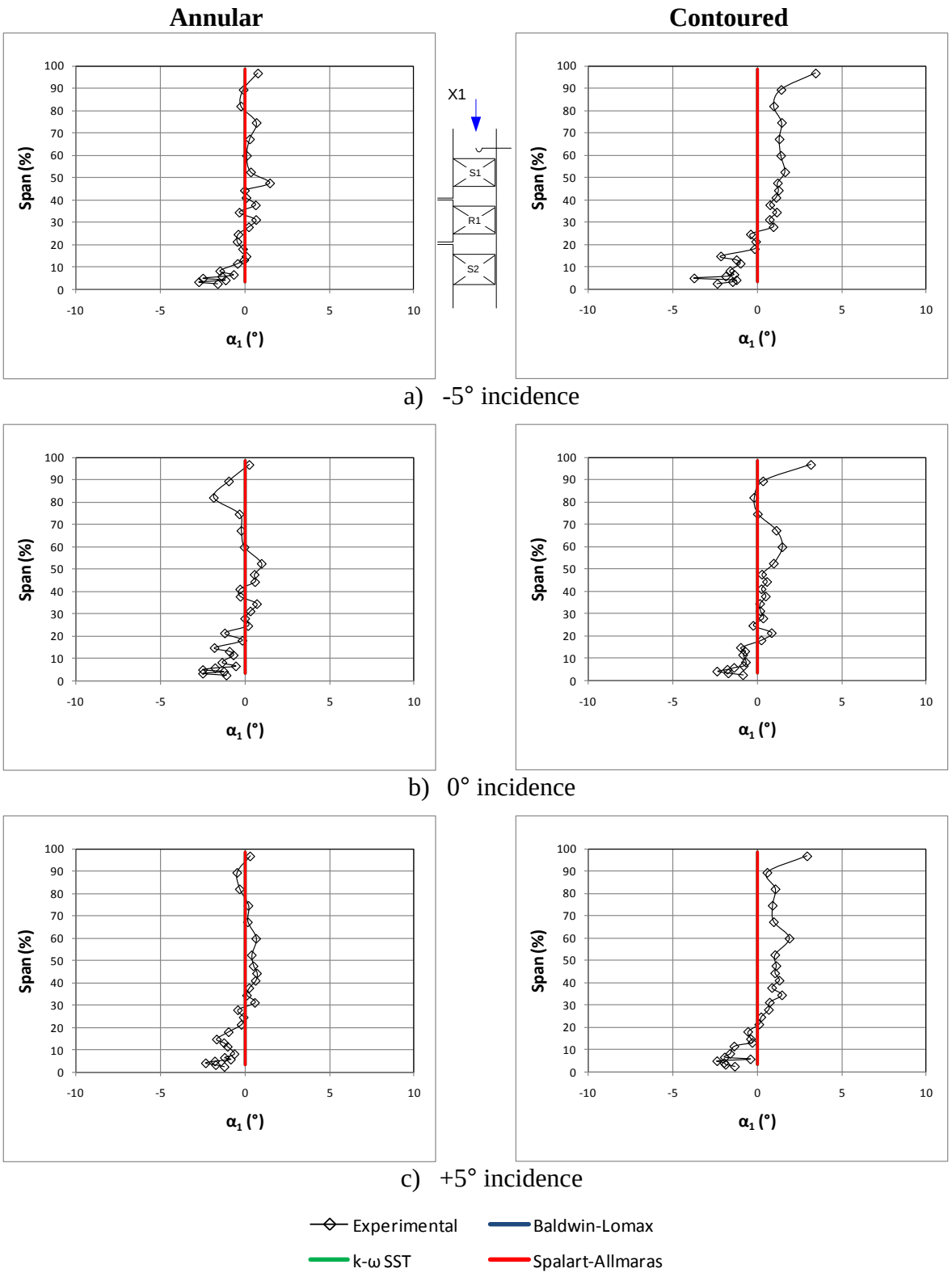

Figure 43: Comparison of inlet flow angle predictions and experimental data

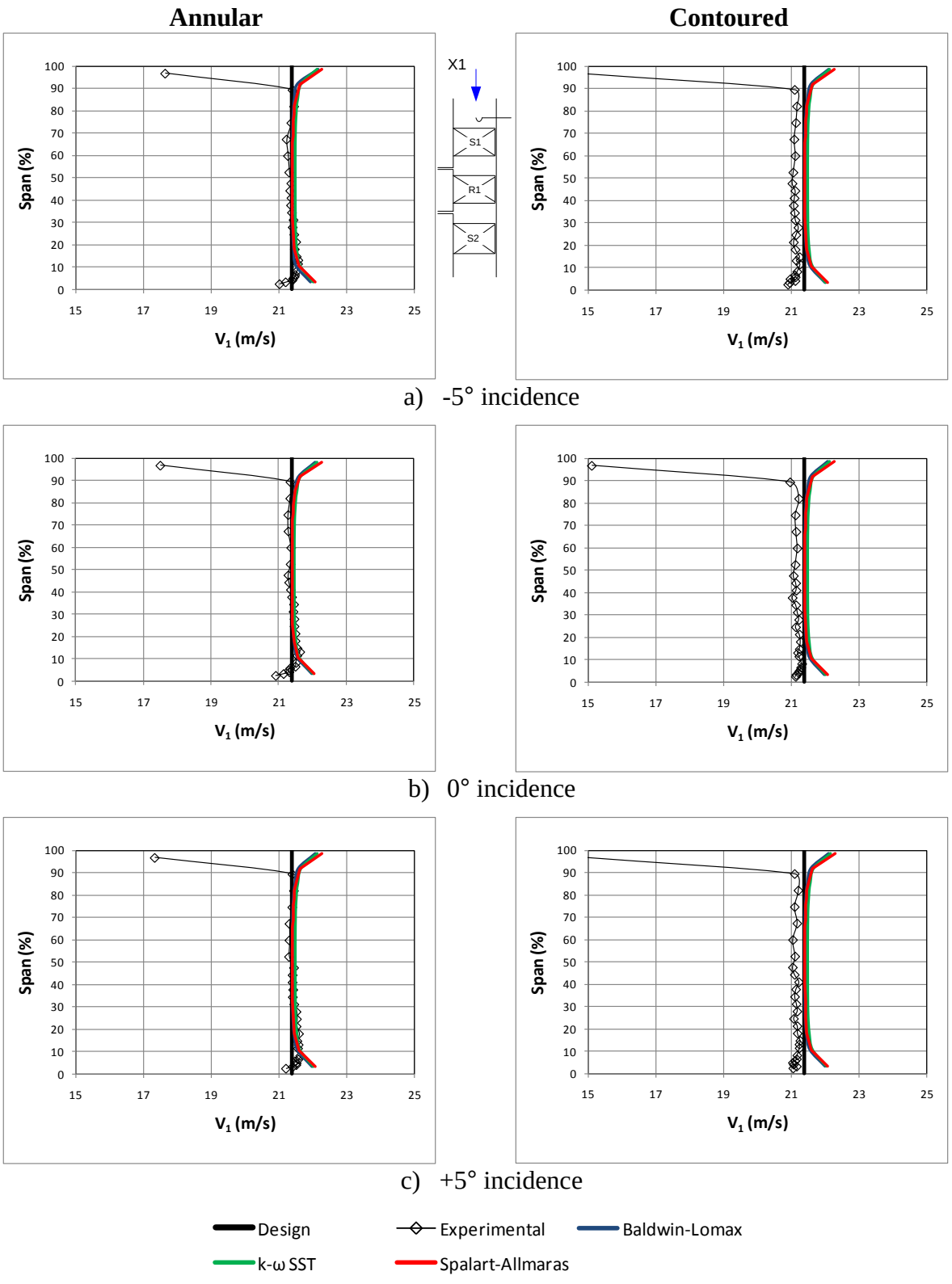

Figure 44: Comparison of inlet flow velocity predictions and experimental data

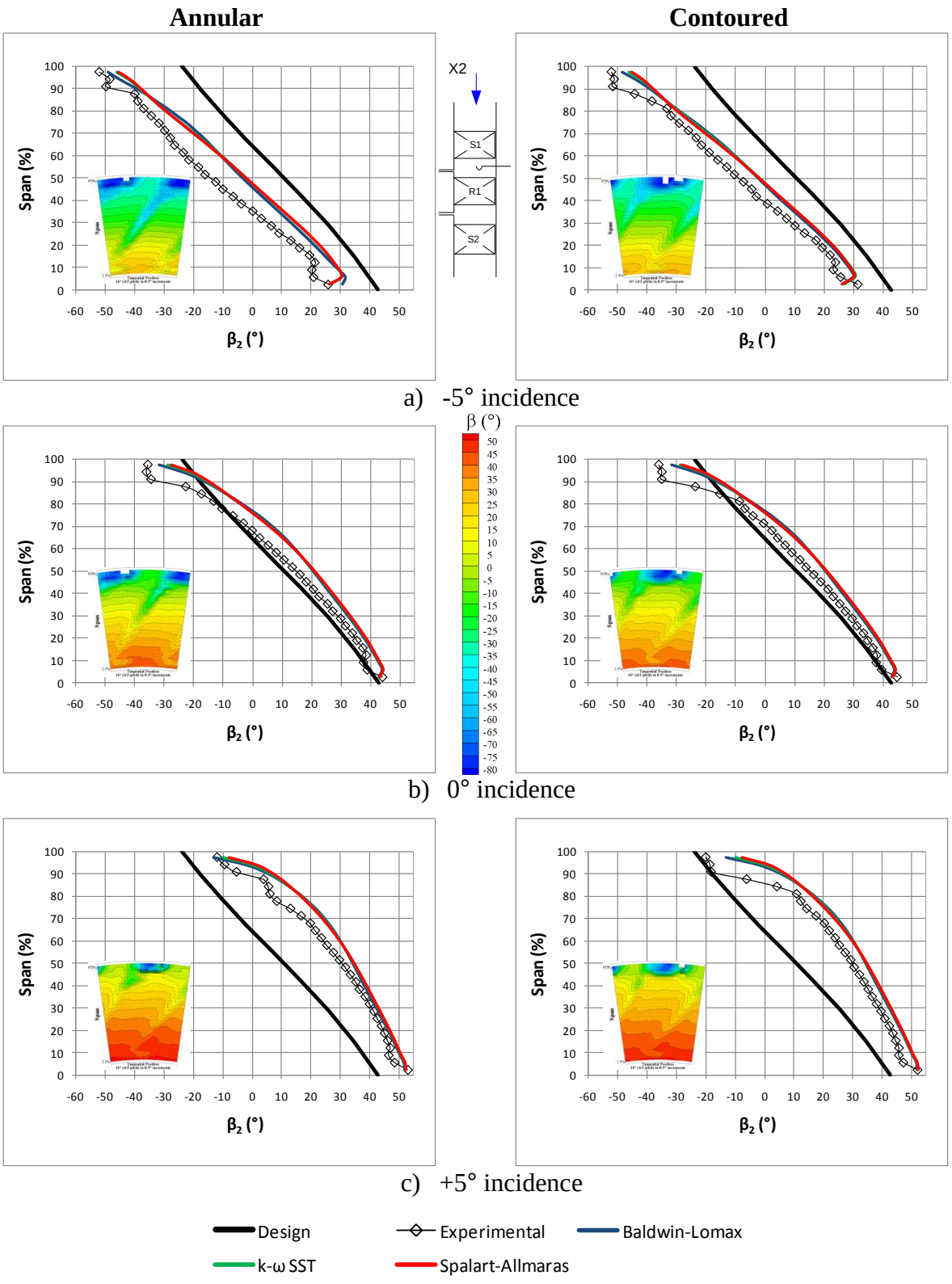

Figure 45: Comparison of stator exit relative flow angle predictions and experimental data (experimental contour plots inset for reference)

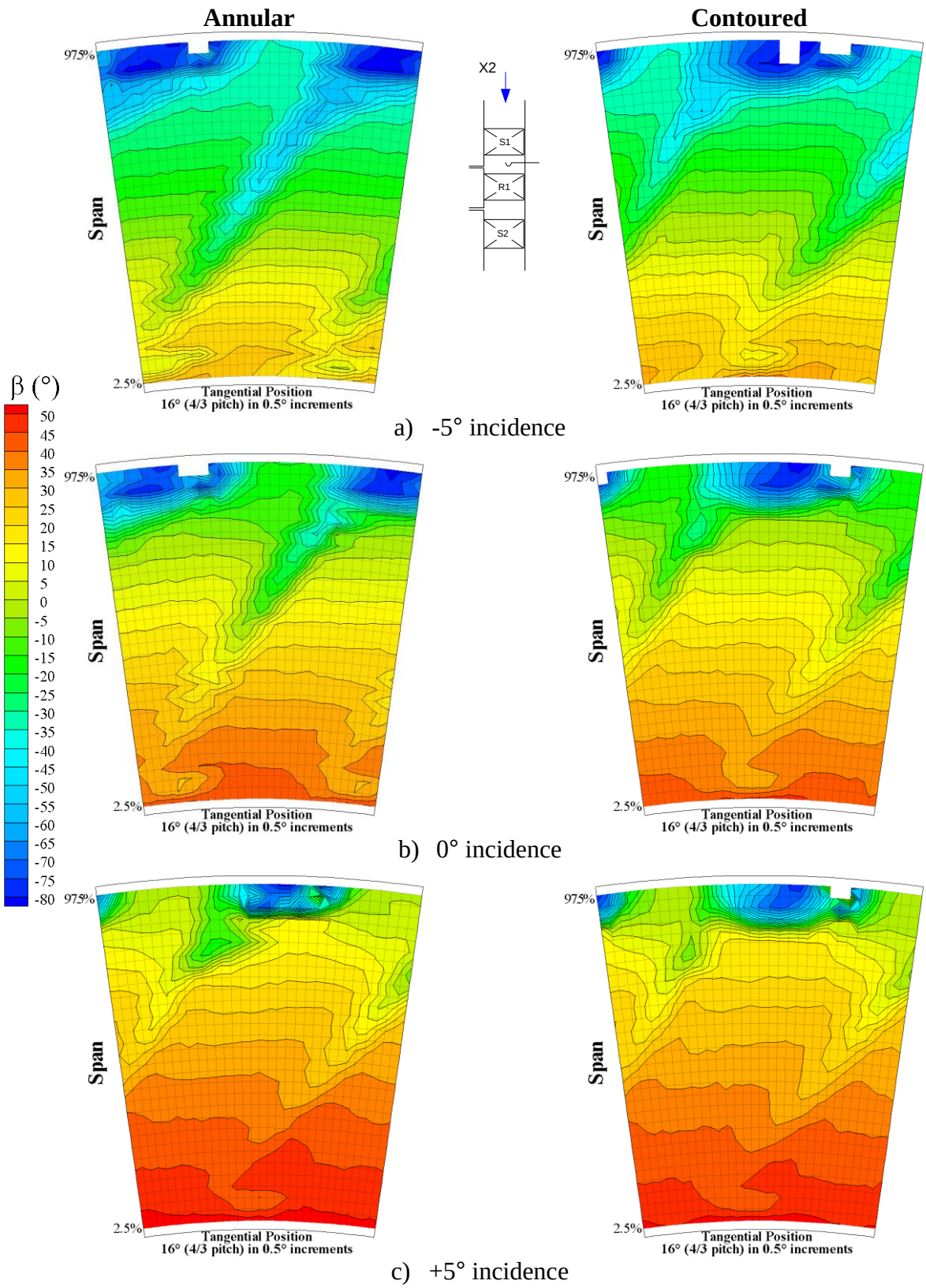

Figure 46: Comparison of stator exit relative flow angle contours for the experimental results

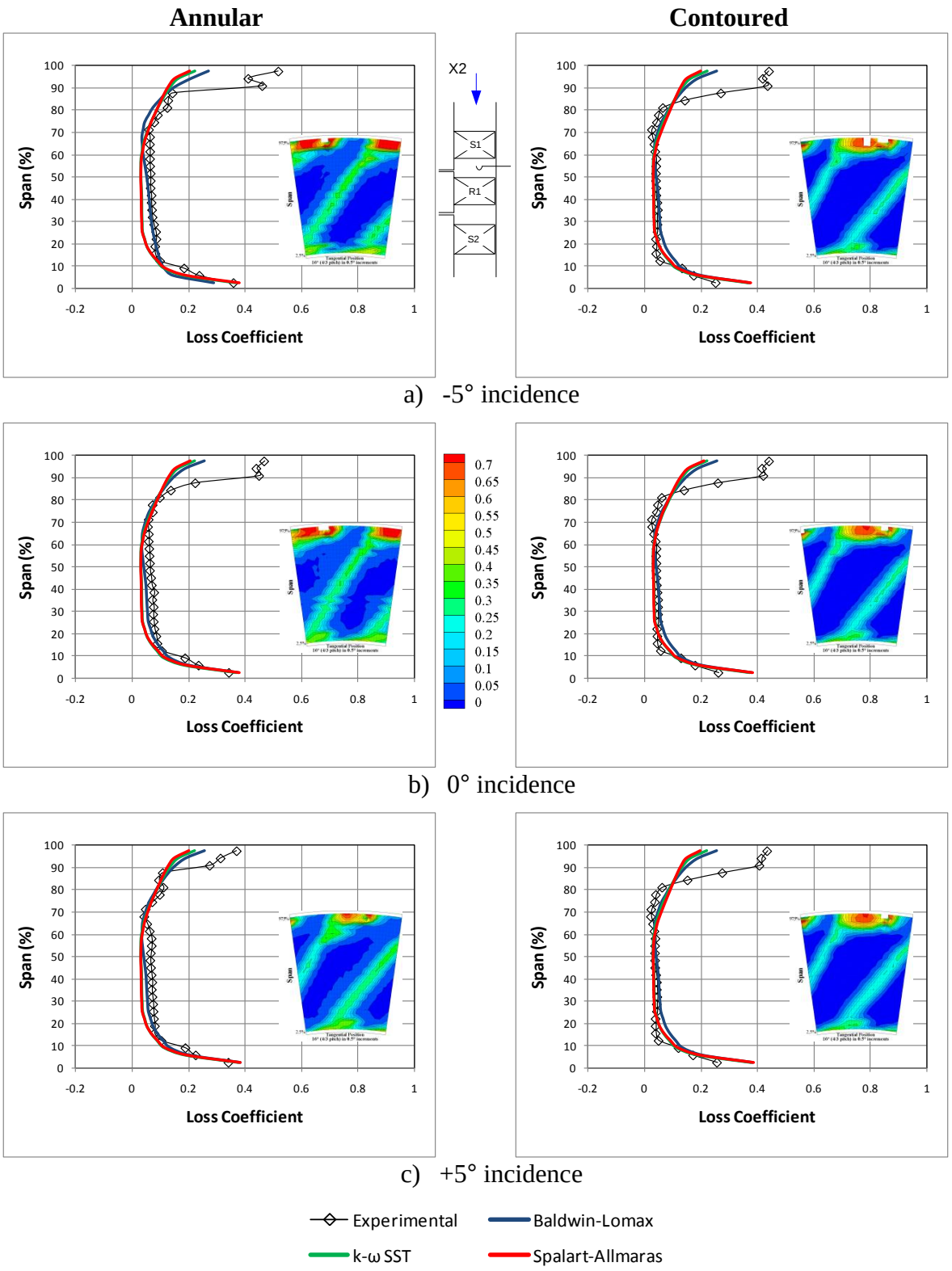

Figure 47: Comparison of 1st nozzle pressure loss coefficient predictions and experimental data (experimental contour plots inset for reference)

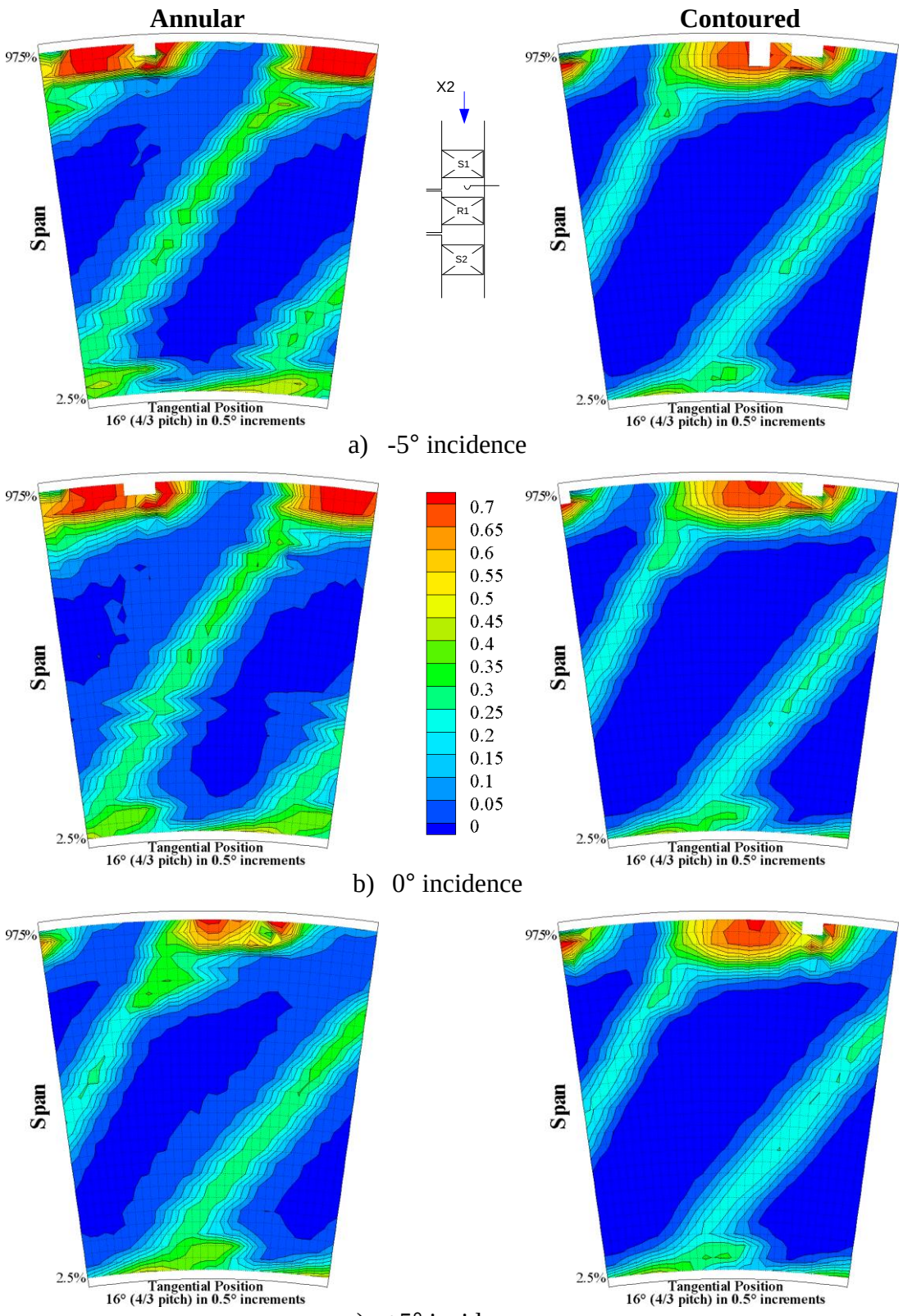

a) -5° incidence

b) 0° incidence

c) +5° incidence

Figure 48: Comparison of 1st nozzle pressure loss coefficient contours for the experimental results

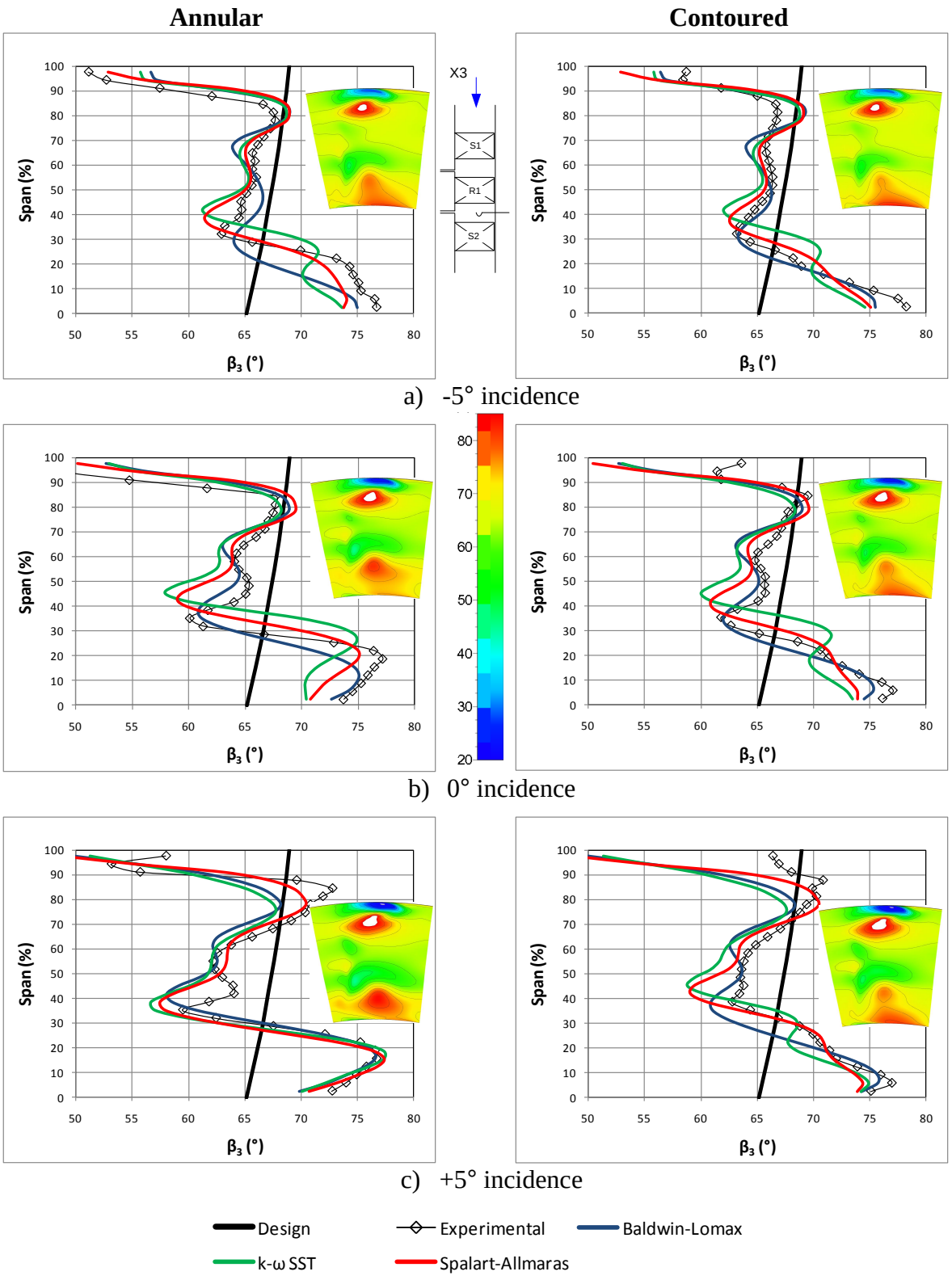

Figure 49: Comparison of rotor exit relative flow angle predictions and experimental data, CFD contours inset.

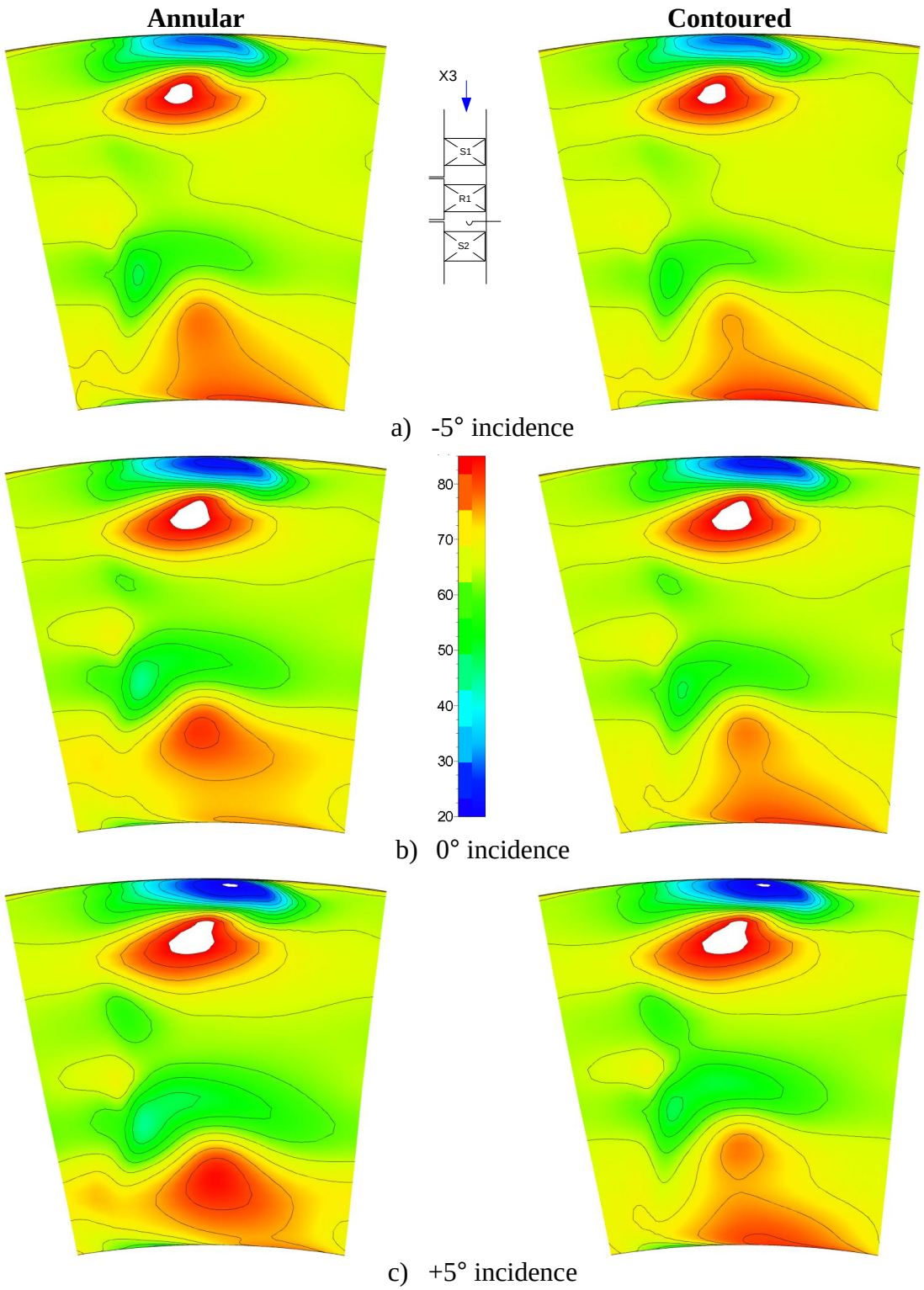

a) -5° incidence

b) 0° incidence

c) +5° incidence

Figure 50: CFD predictions of rotor exit relative flow angle

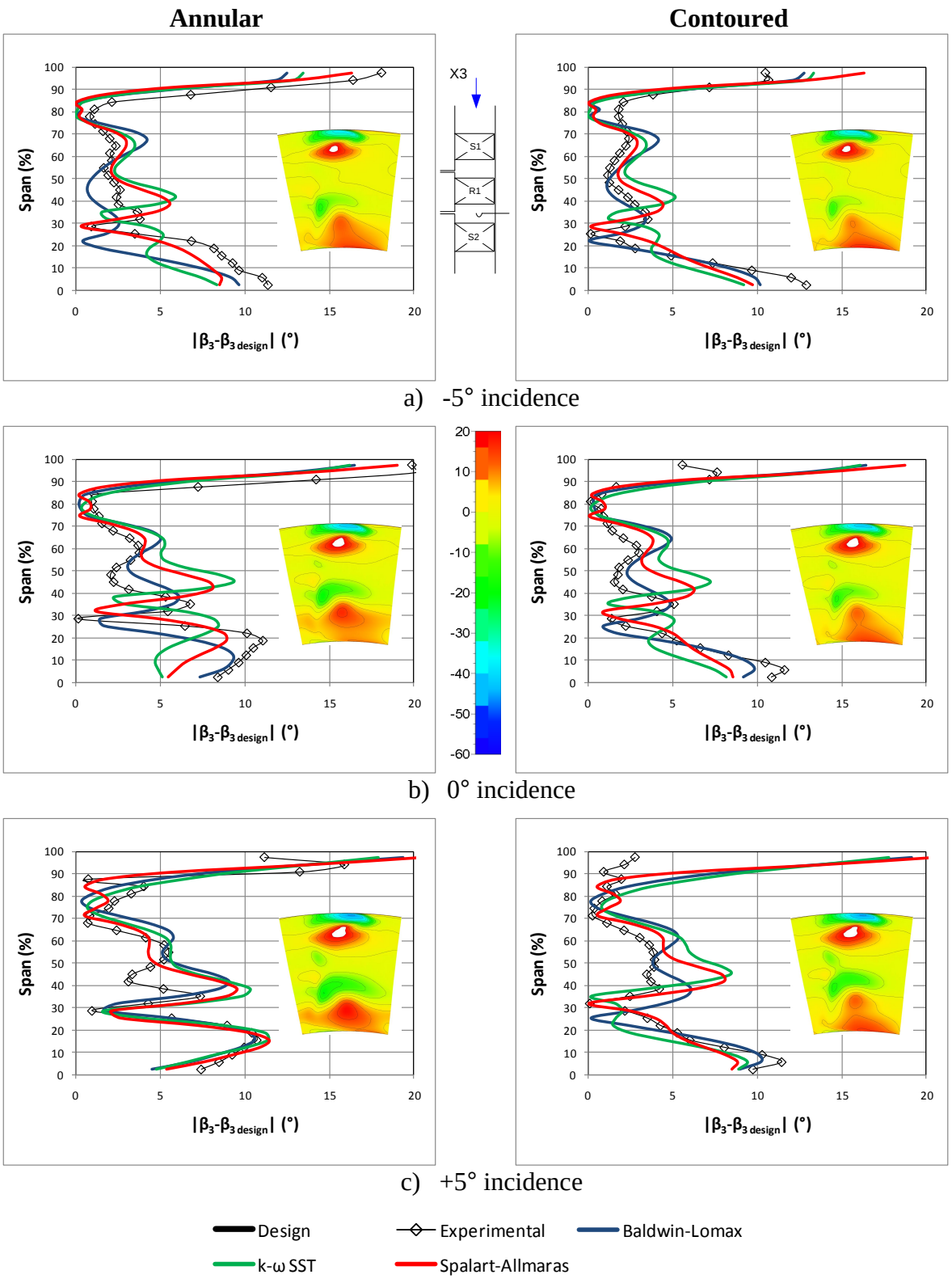

Figure 51: Comparison of the deviation of rotor exit relative flow angle from the design value, predictions and experimental data, CFD contours inset

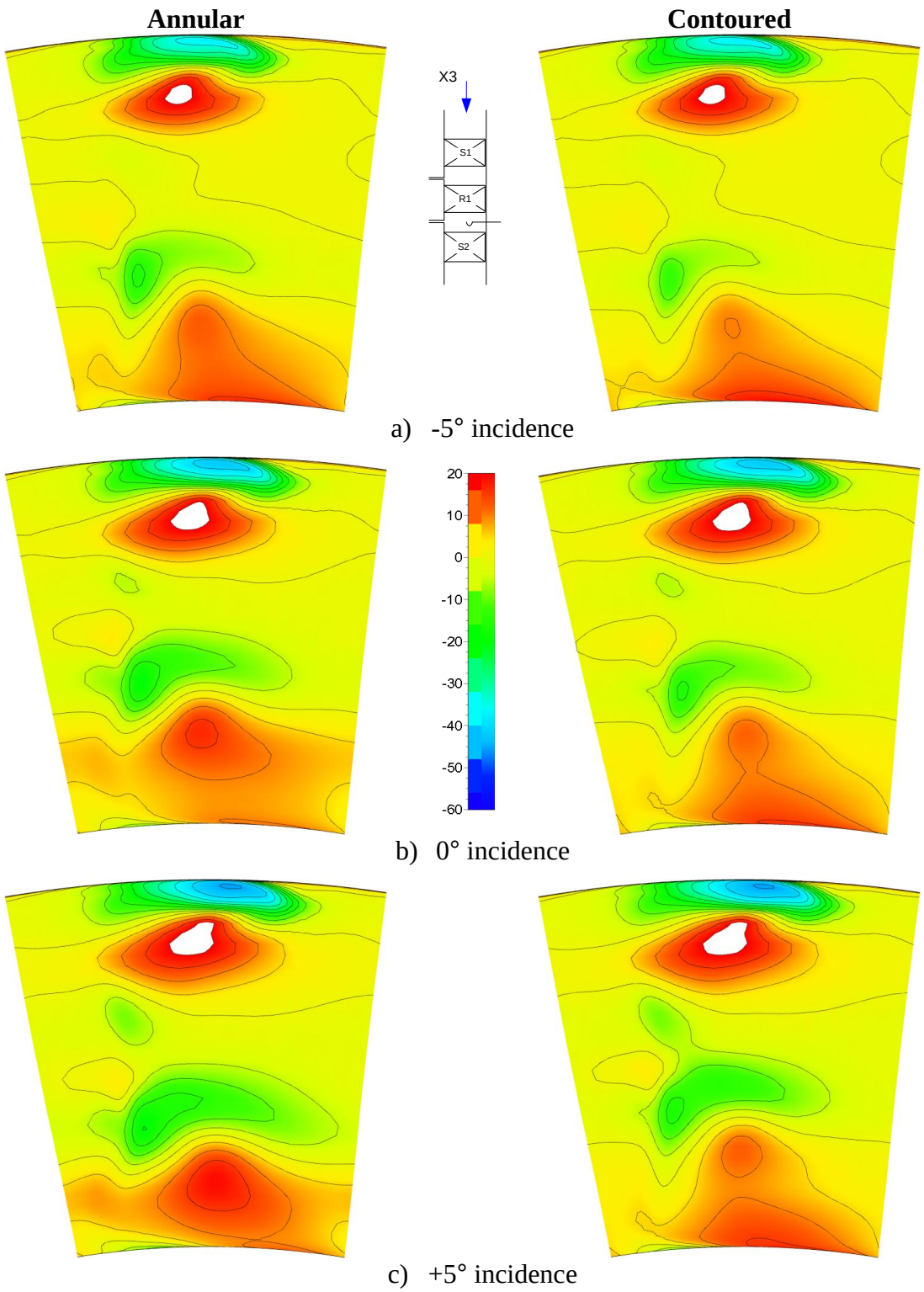

a) -5° incidence

b) 0° incidence

c) +5° incidence

Figure 52: CFD predictions of the deviation of rotor exit relative flow angle from the design value

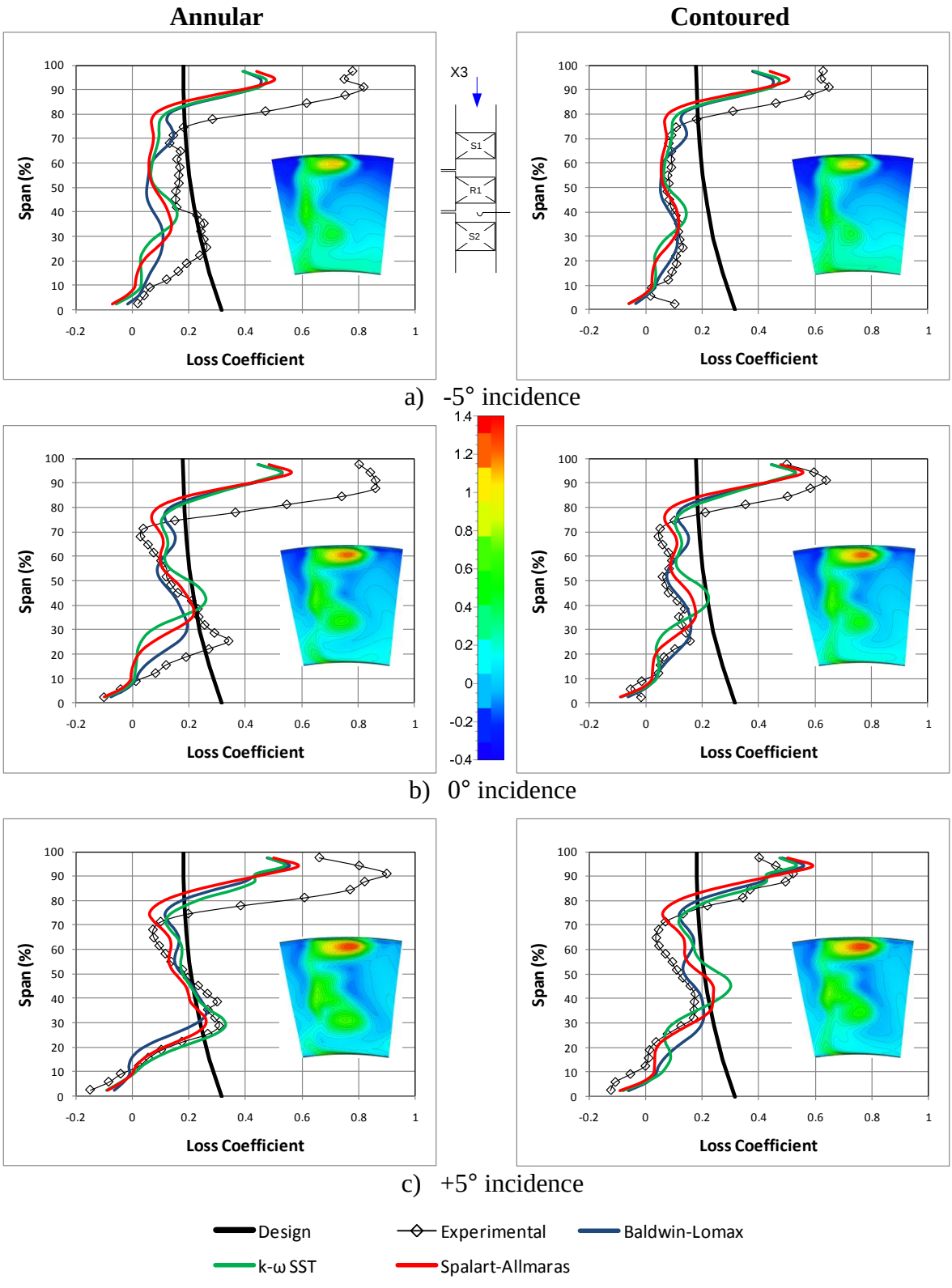

Figure 53: Comparison of rotor loss coefficient predictions and experimental data, CFD contours inset

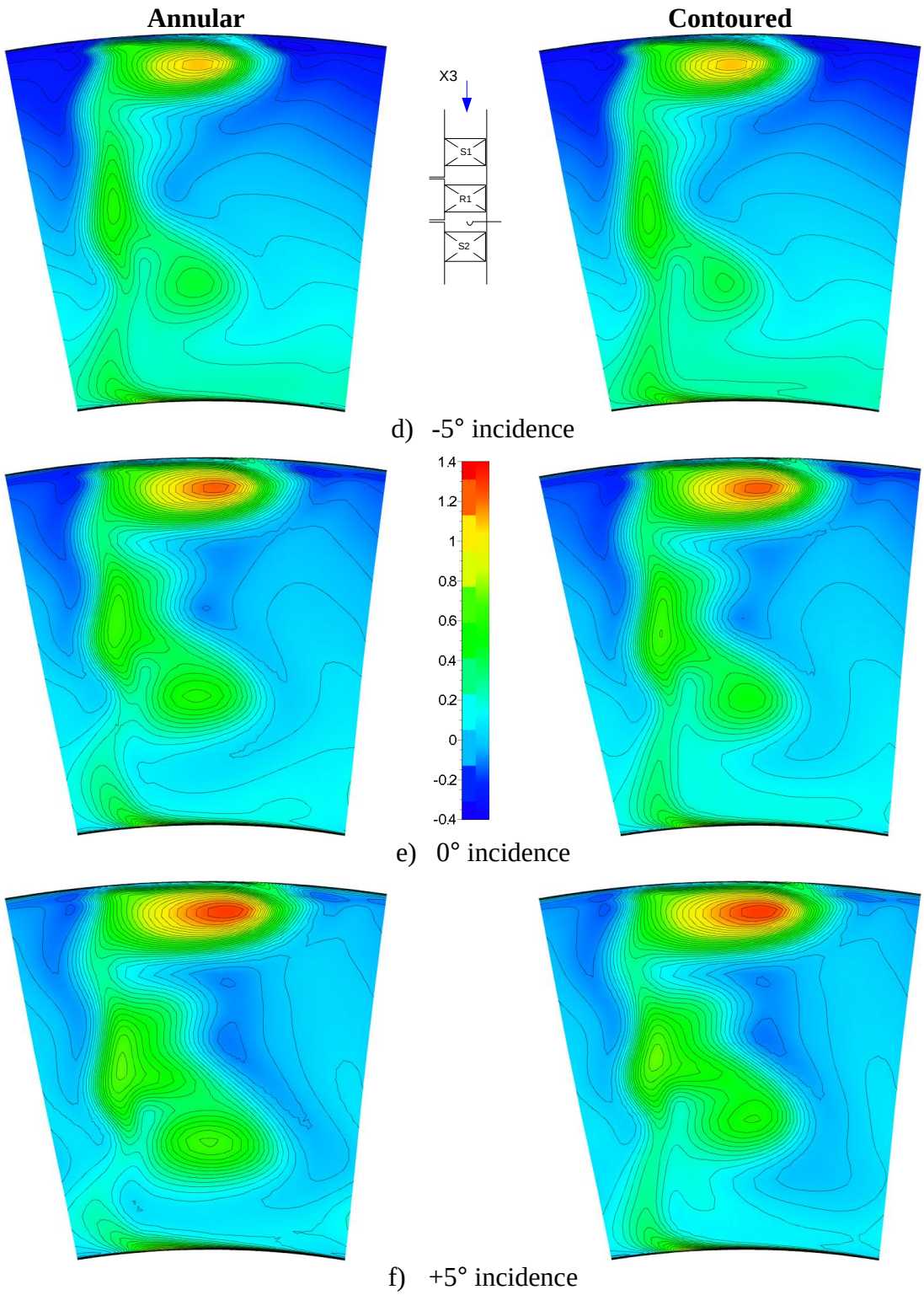

d) -5° incidence

e) 0° incidence

f) +5° incidence

Figure 54: CFD predictions of rotor loss coefficient

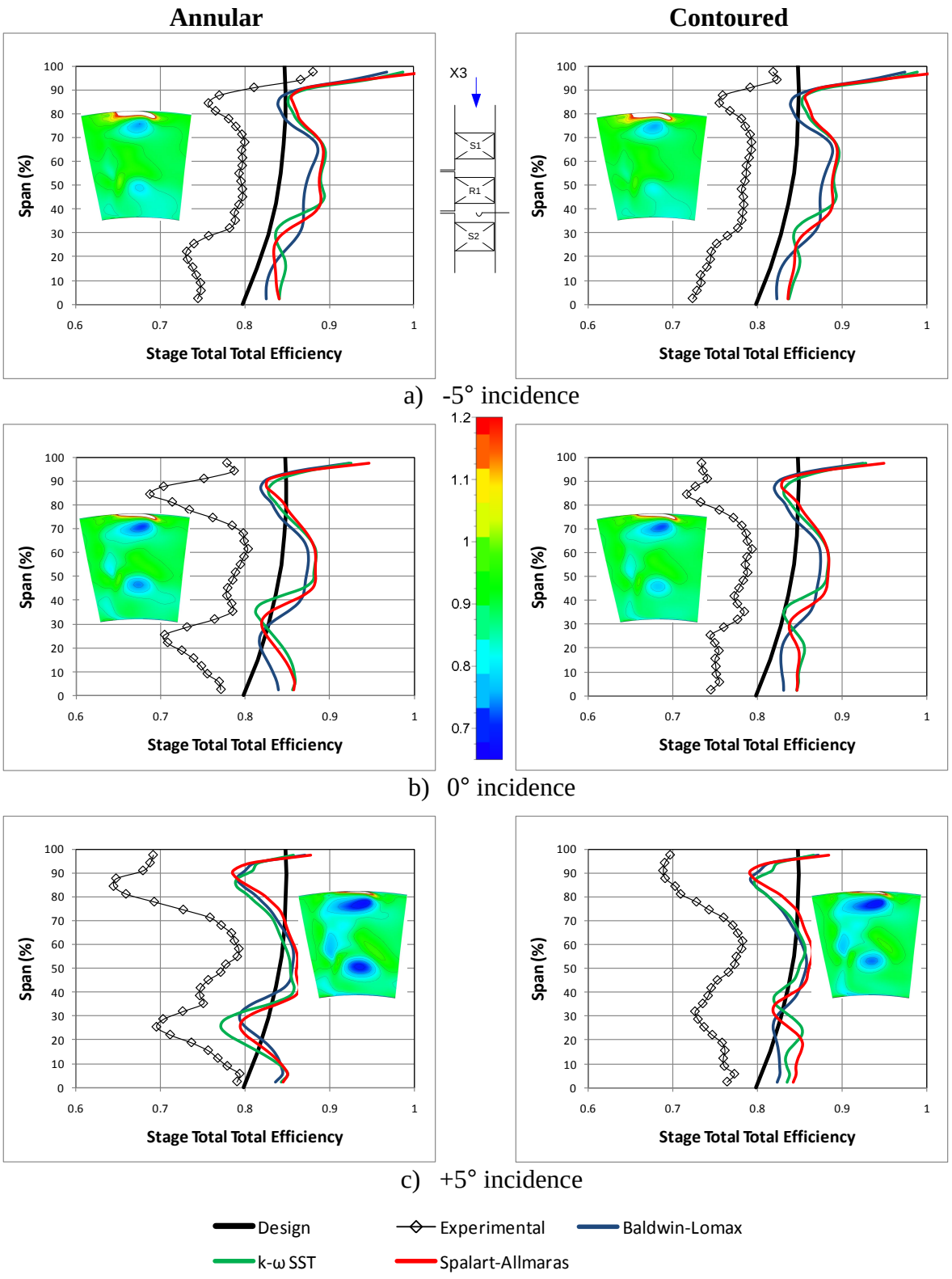

Figure 55: Comparison of stage total total efficiency predictions and experimental data, CFD contours inset

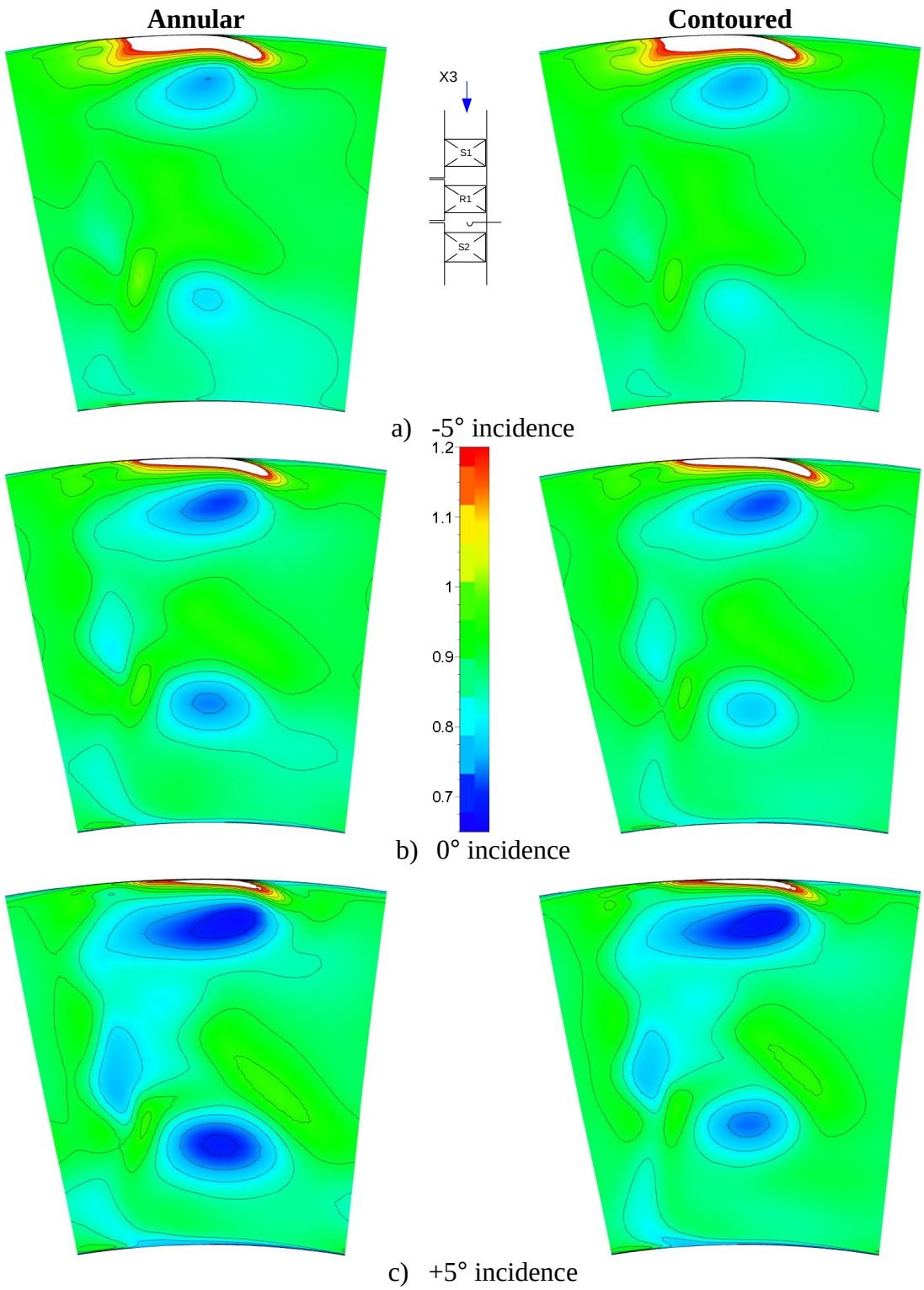

a) -5° incidence

b) 0° incidence

c) +5° incidence

Figure 56: CFD predictions of stage total total efficiency

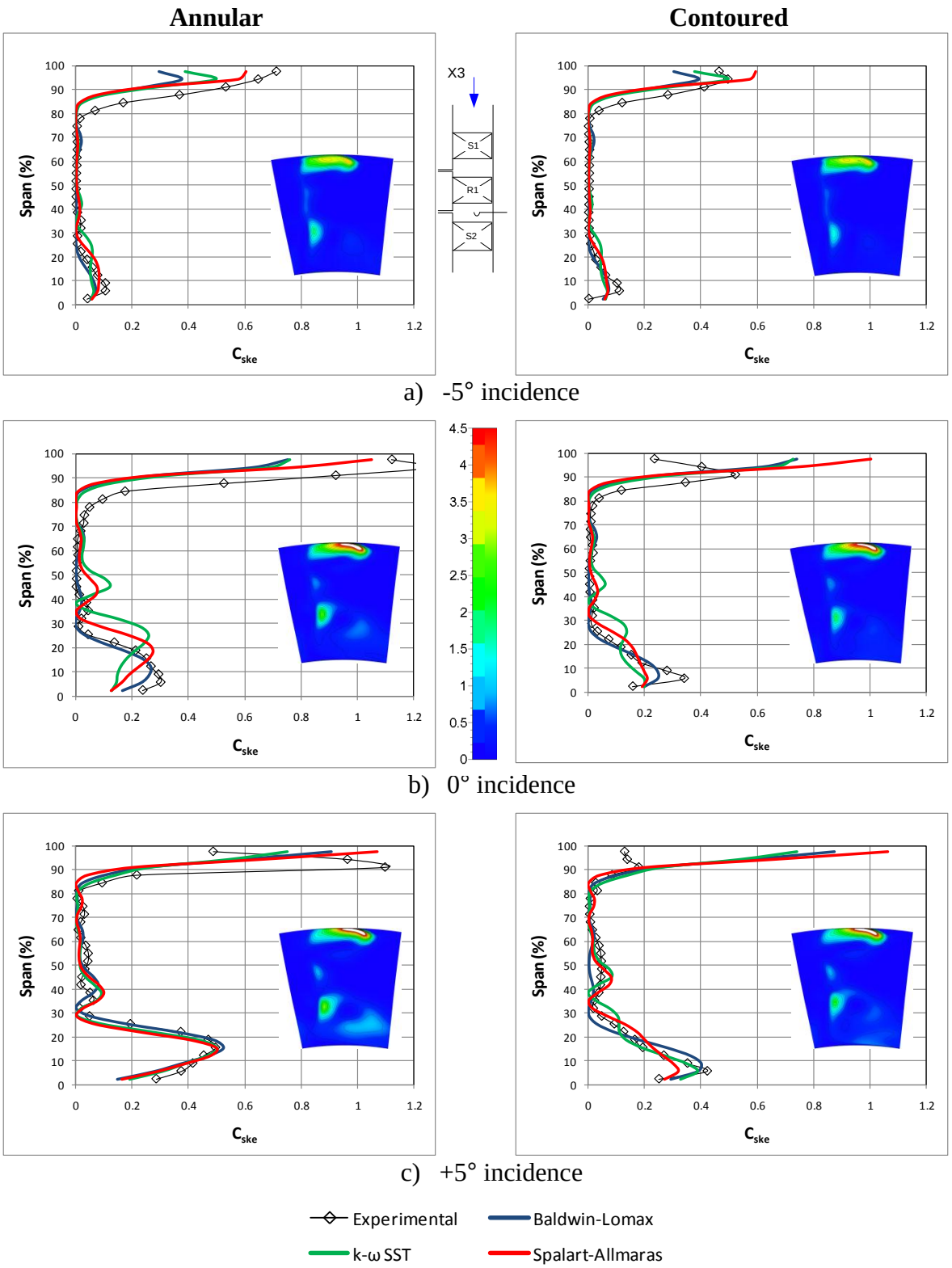

Figure 57: Comparison of rotor exit coefficient of secondary kinetic energy predictions and experimental data, CFD contours inset

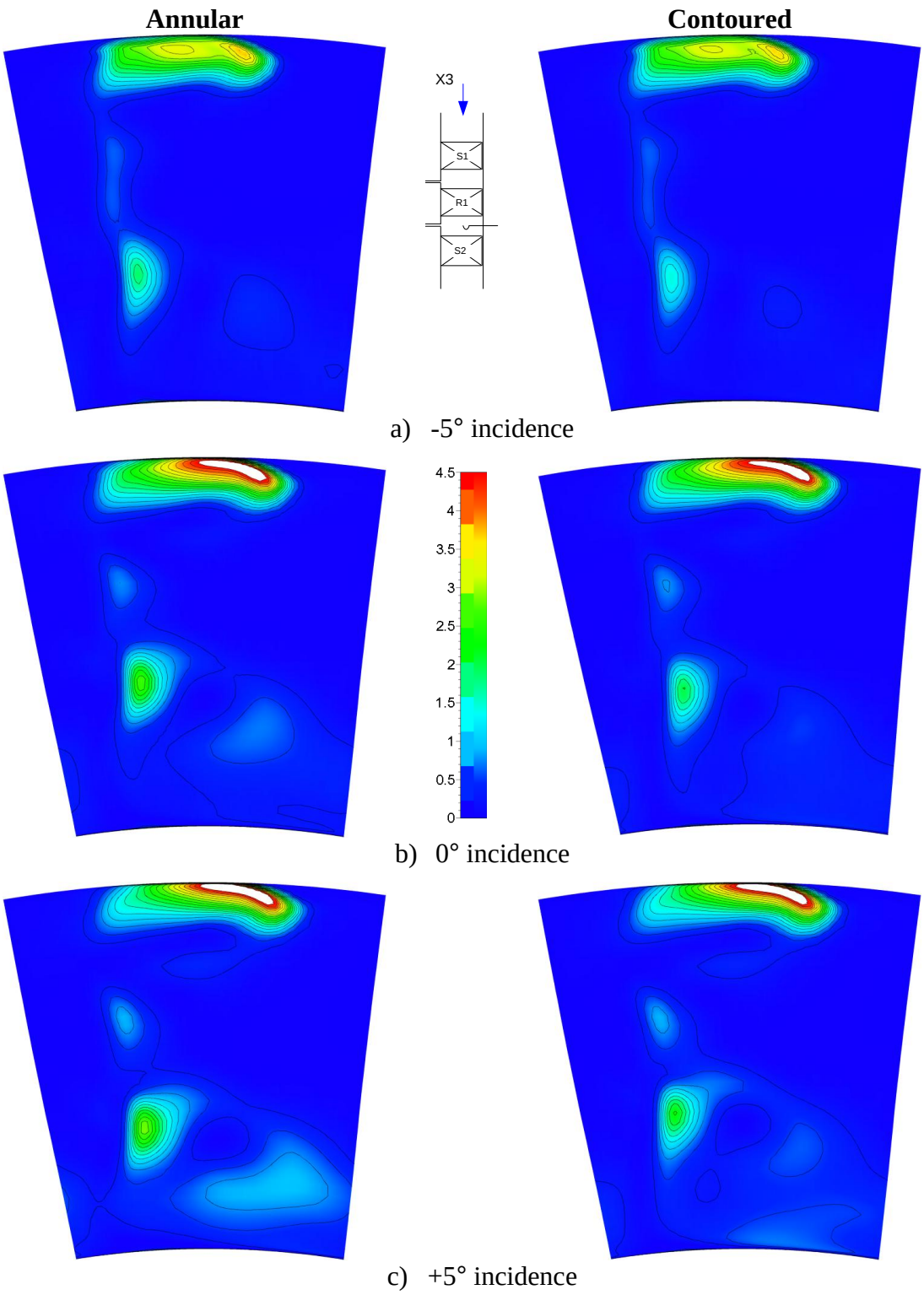

a) -5° incidence

b) 0° incidence

c) +5° incidence

Figure 58: CFD predictions of rotor exit coefficient of secondary kinetic energy

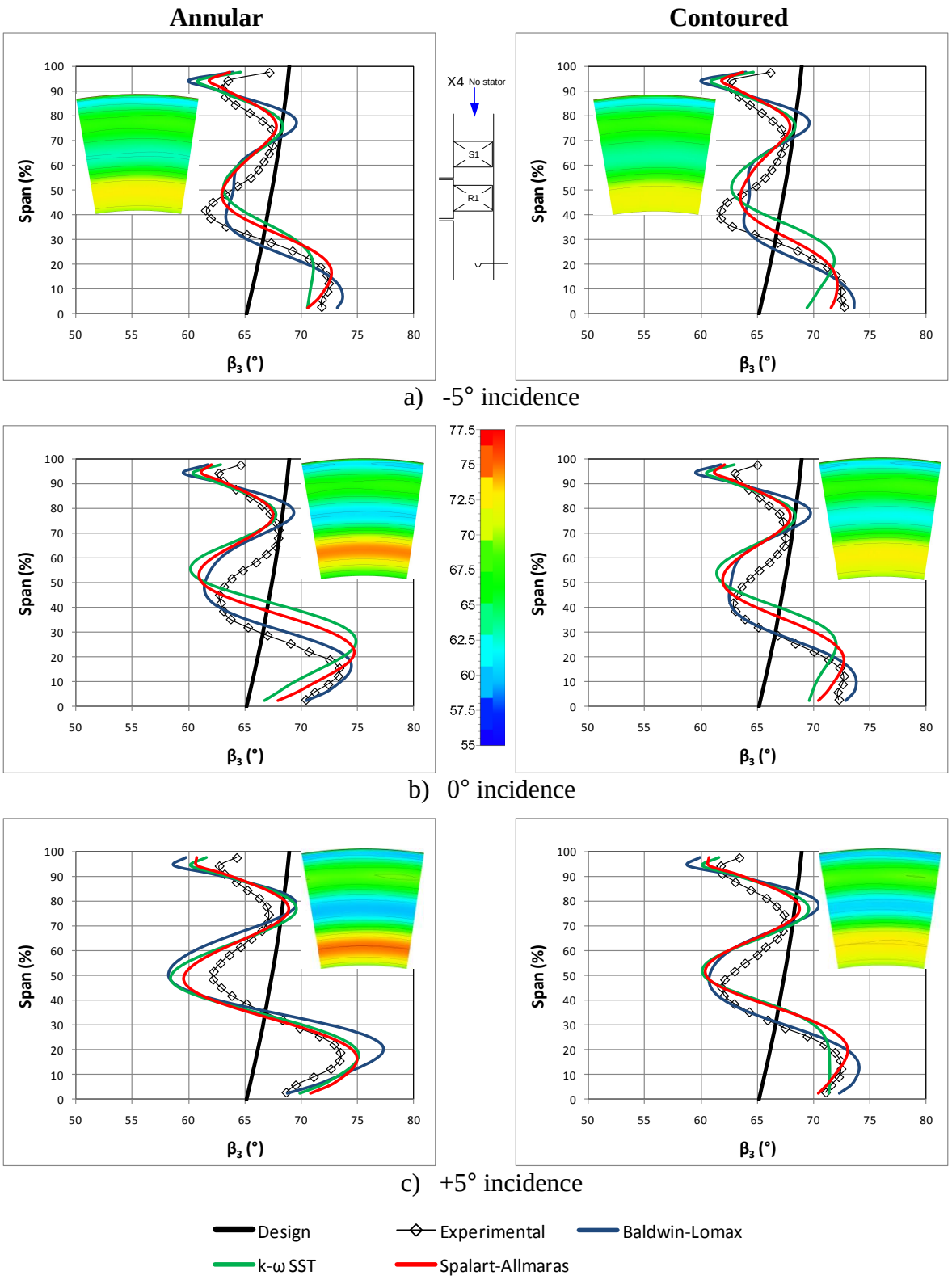

Figure 59: Comparison of rotor exit relative flow angle predictions and experimental data measured at station X4 without the 2nd stator

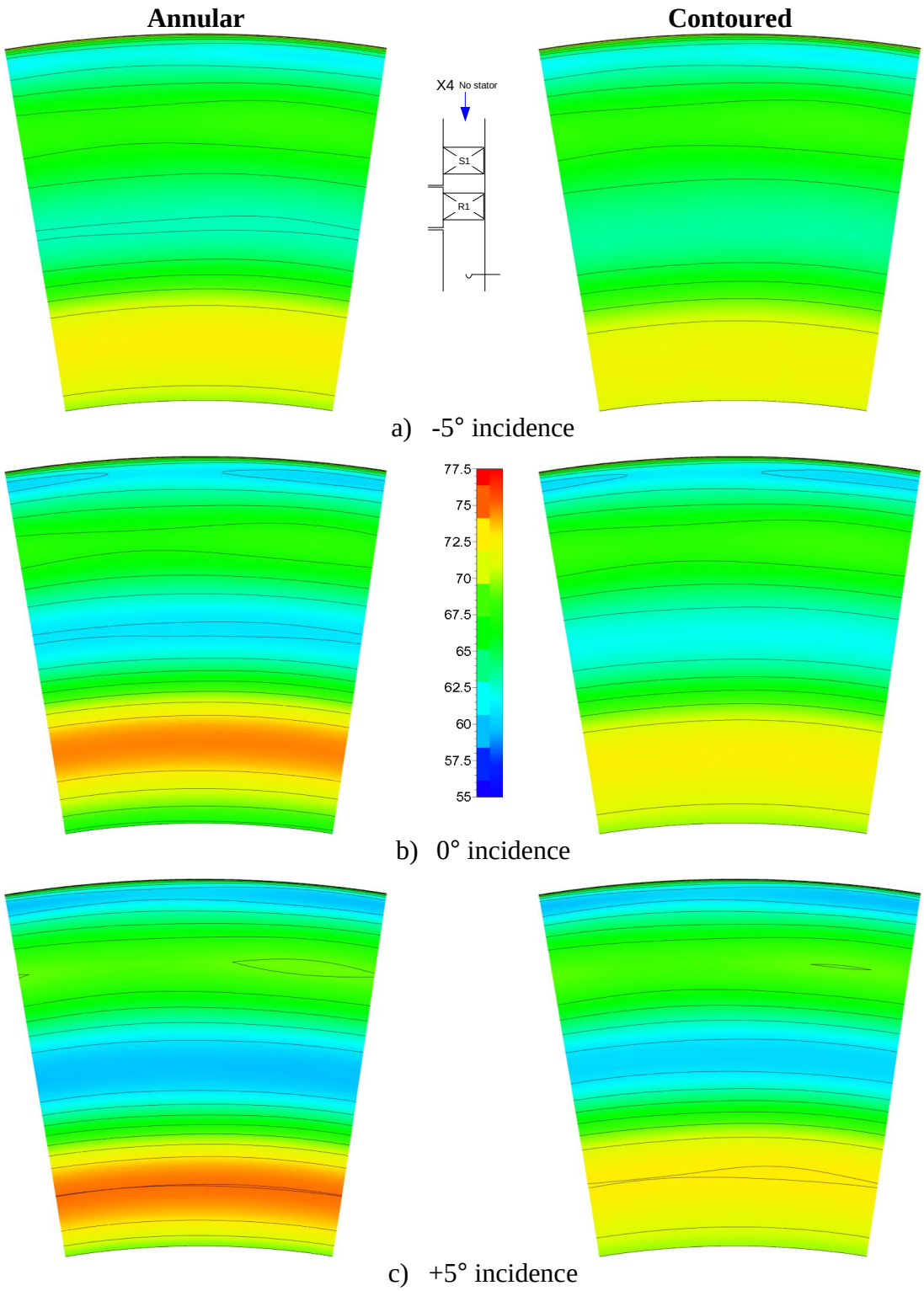

a) -5° incidence

b) 0° incidence

c) +5° incidence

Figure 60: CFD predictions of rotor exit relative flow angle at station X4 without the 2nd stator

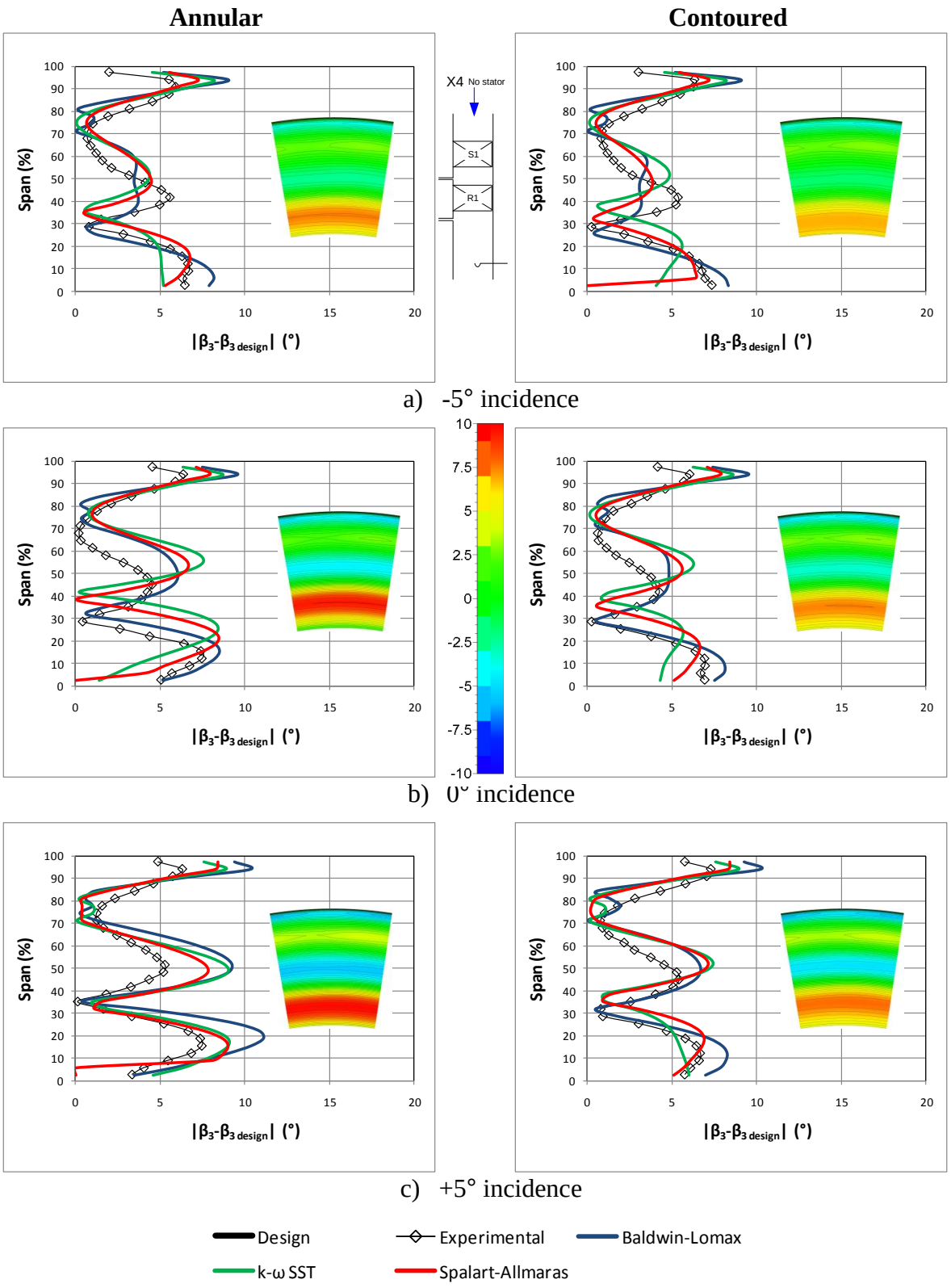

Figure 61: Comparison of the deviation of rotor exit relative flow angle predictions and experimental data from the design angle measured at station X4 without the 2nd stator

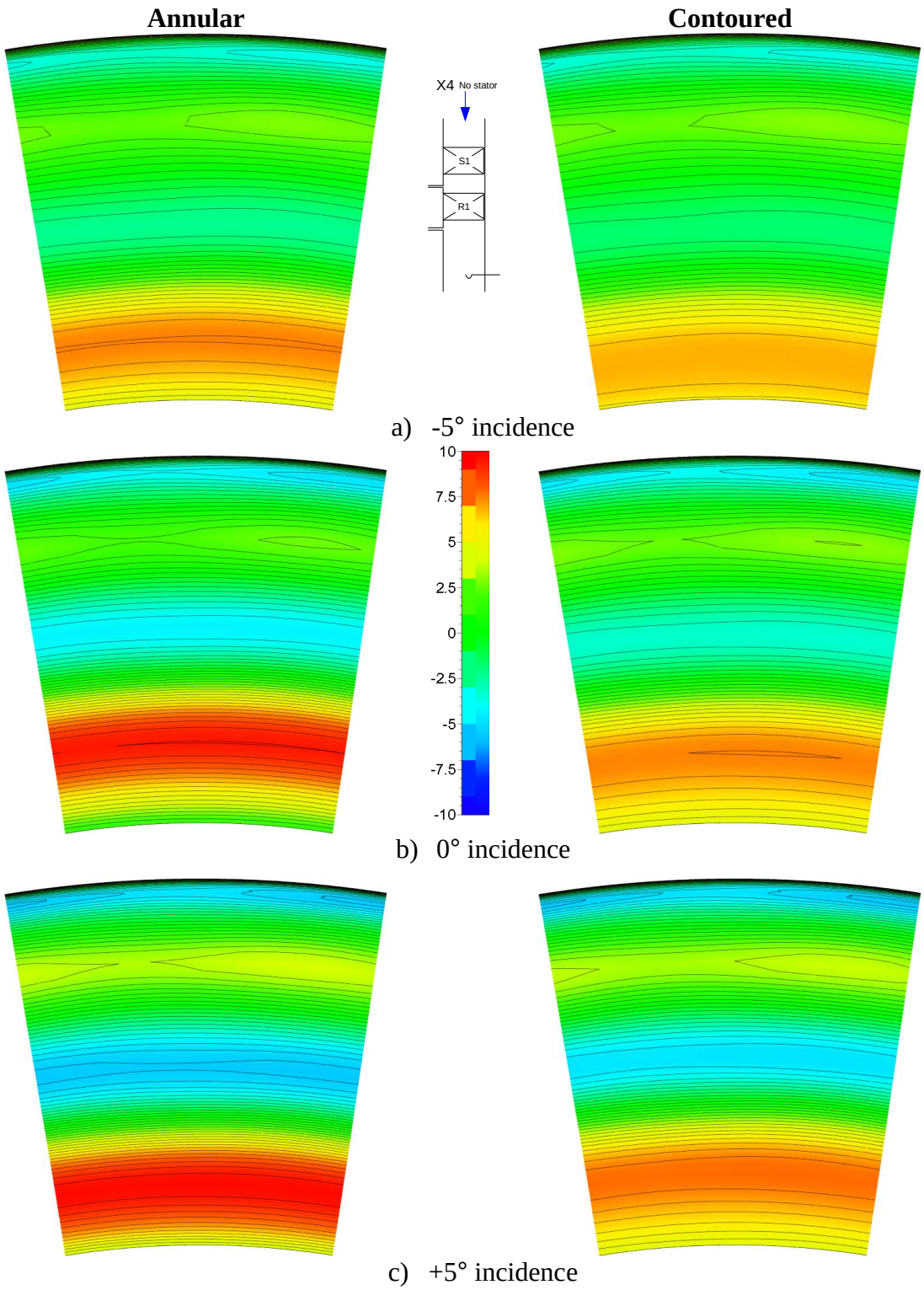

a) -5° incidence

b) 0° incidence

c) +5° incidence

Figure 62: CFD predictions of the deviation of rotor exit relative flow angle from the design angle measured at station X4 without the 2nd stator

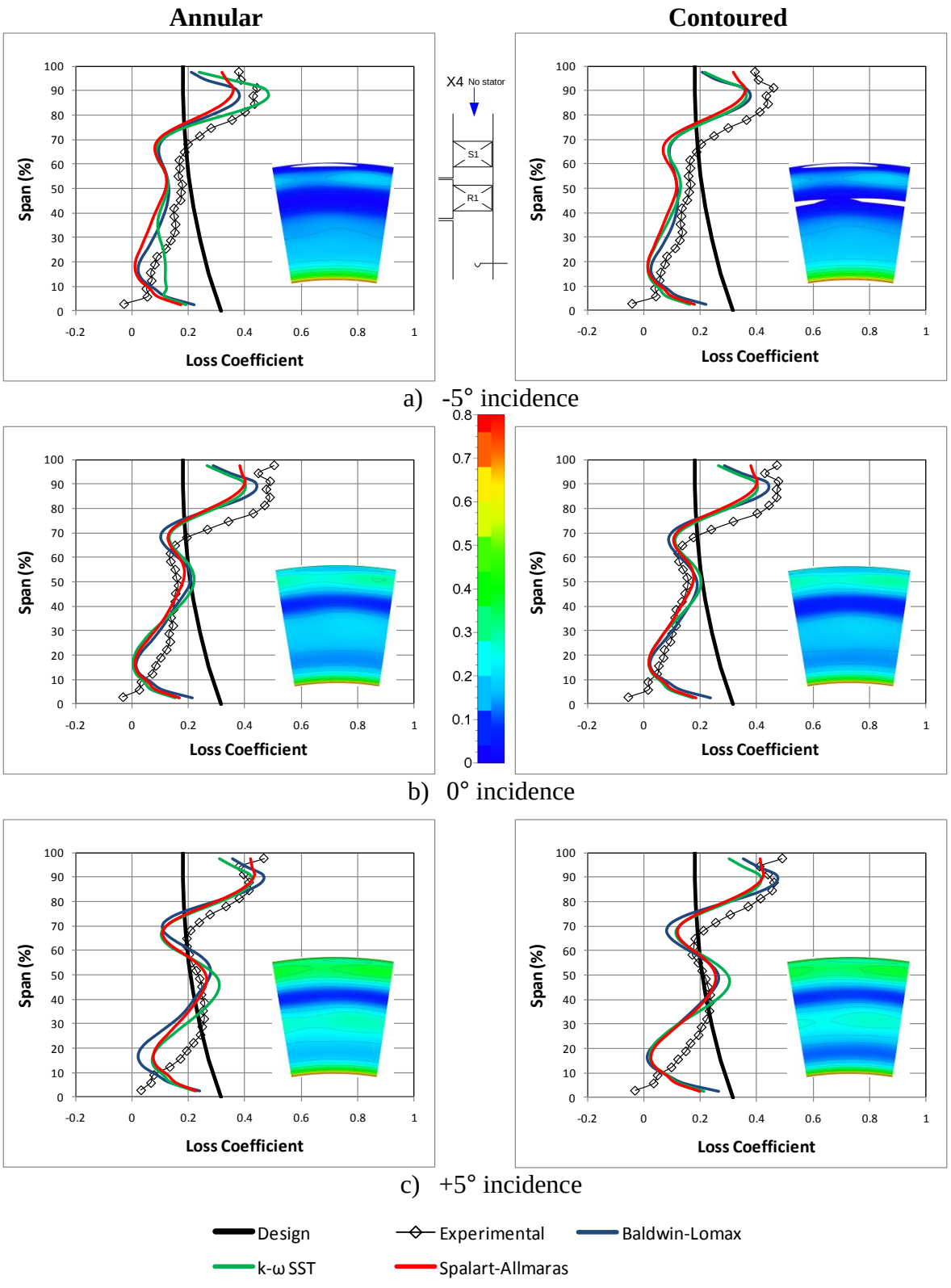

Figure 63: Comparison of rotor loss coefficient predictions and experimental data measured at station X4 without the 2nd stator

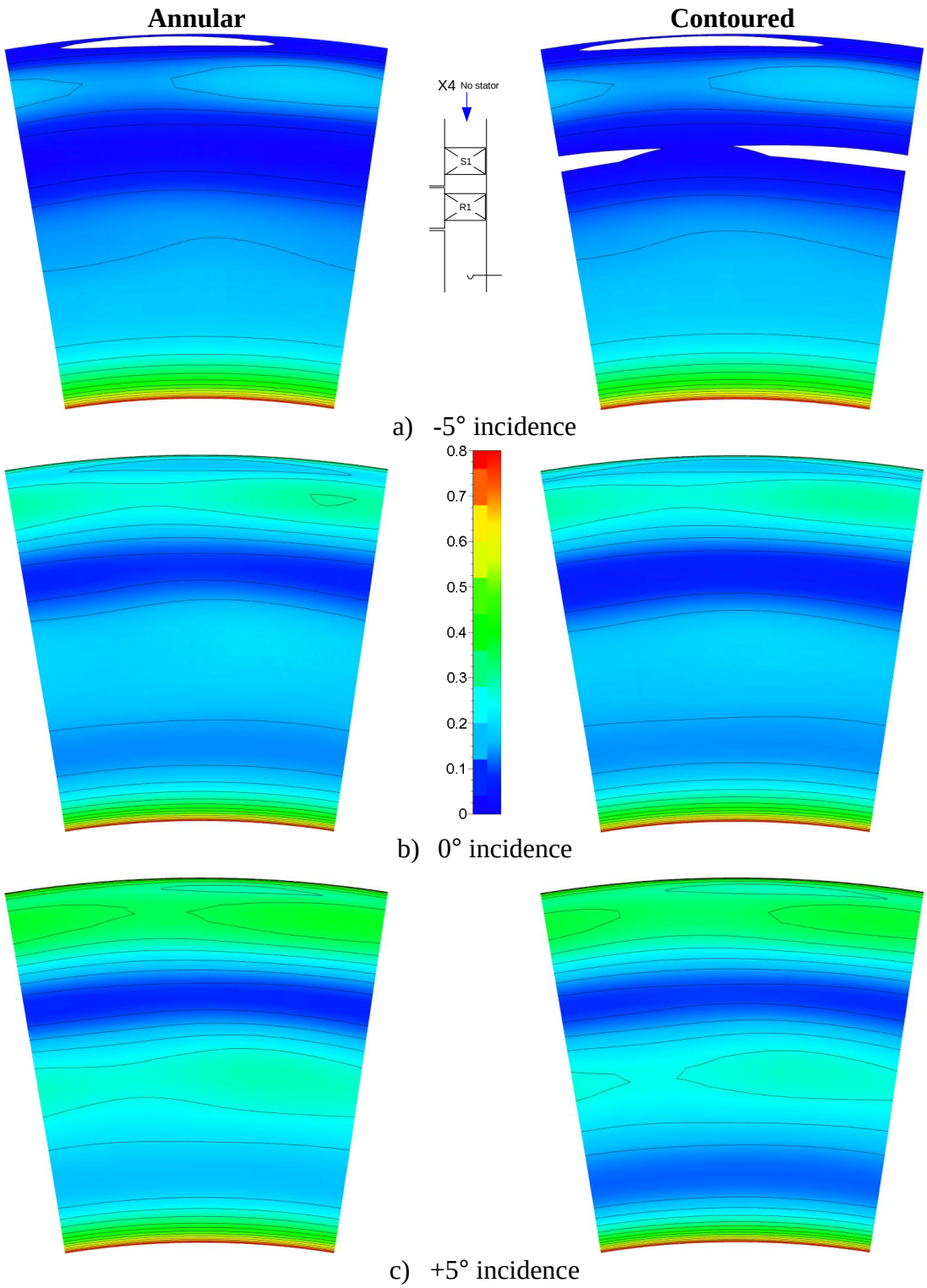

a) -5° incidence

b) 0° incidence

c) +5° incidence

Figure 64: CFD predictions of rotor loss coefficient at station X4 without the 2nd stator

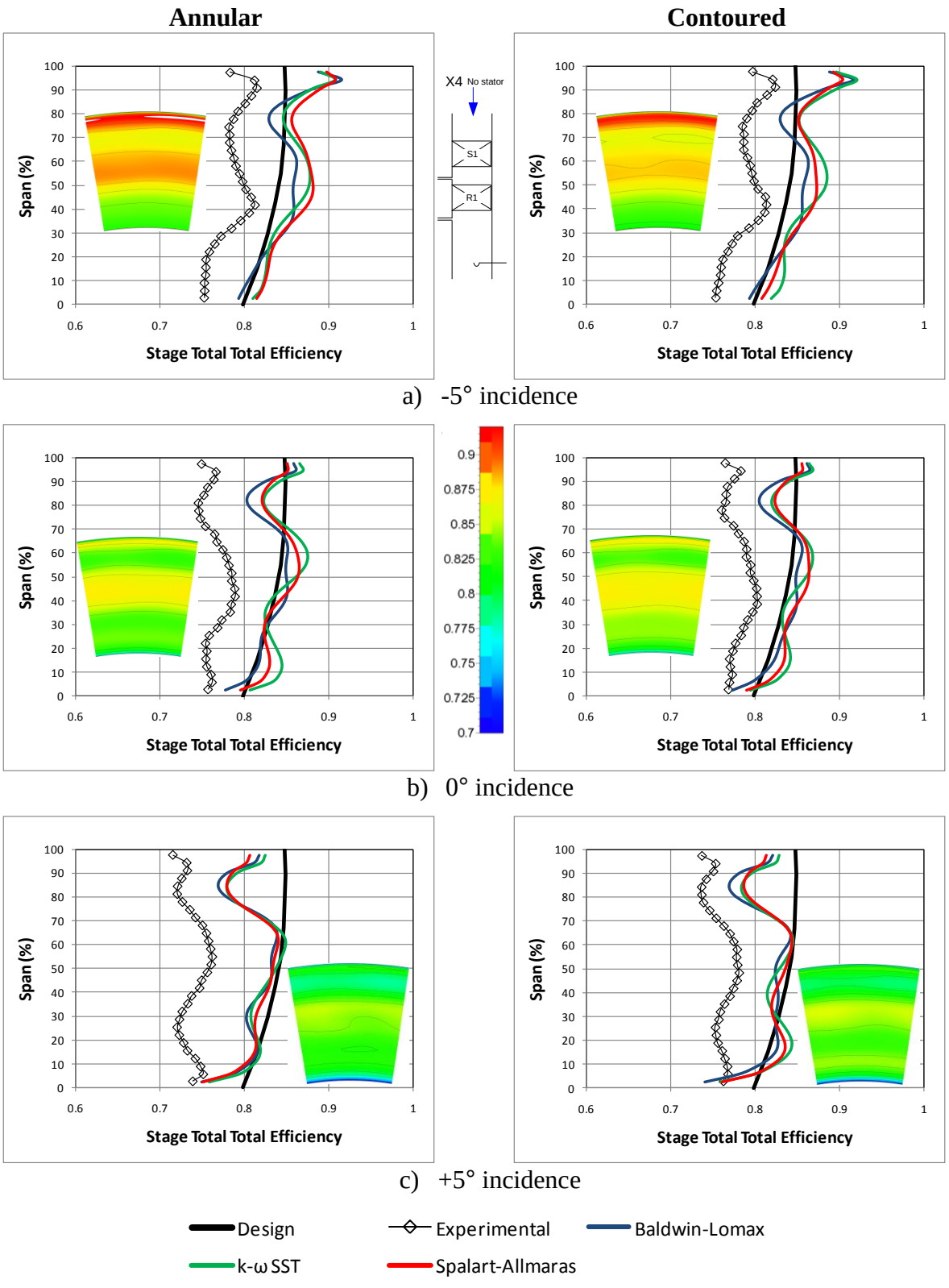

a) -5° incidence

b) 0° incidence

c) +5° incidence

Figure 65: Comparison of stage total total efficiency predictions and experimental data measured at station X4 without the 2nd stator

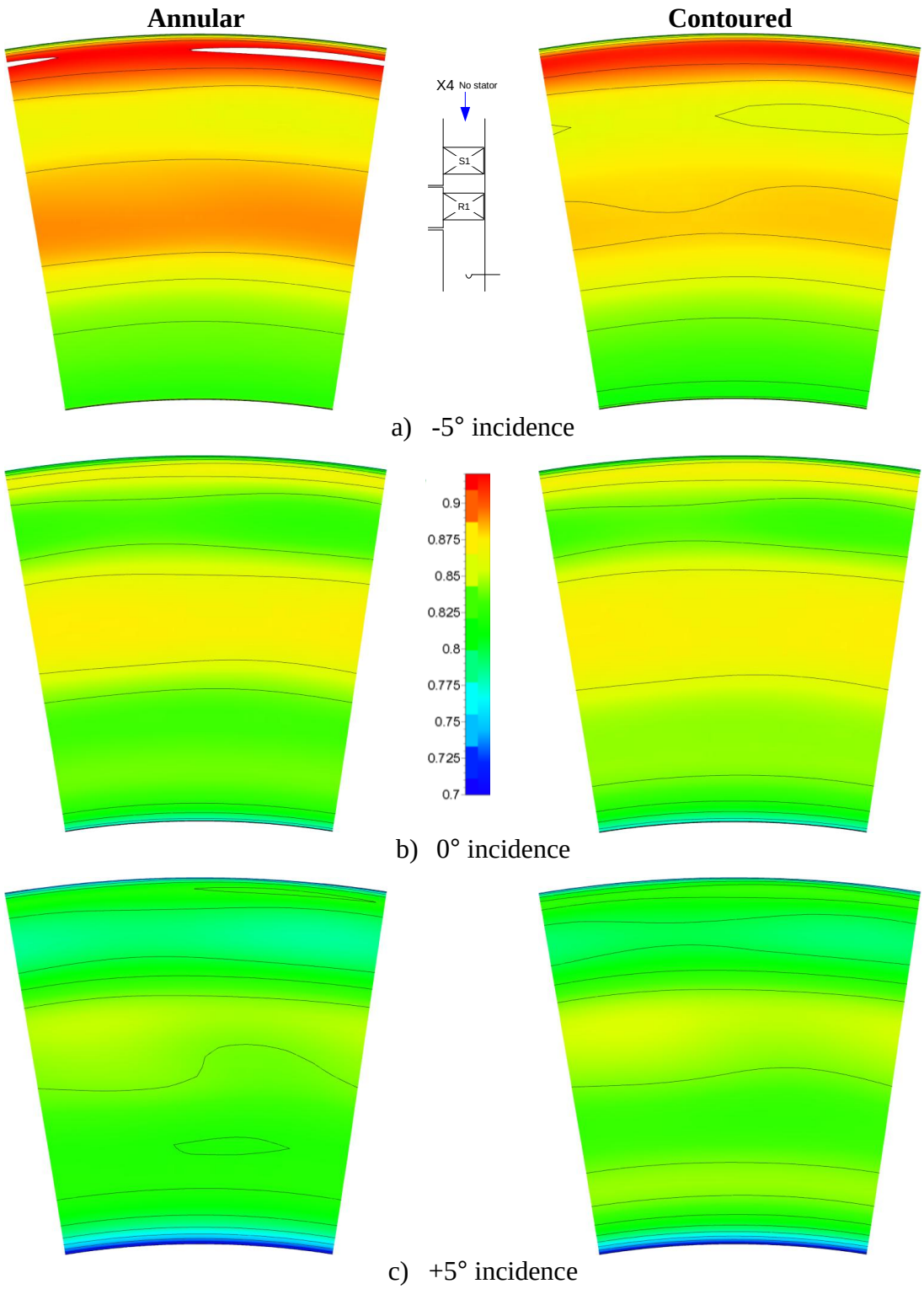

a) -5° incidence

b) 0° incidence

c) +5° incidence

Figure 66: CFD predictions of stage total total efficiency measured at station X4 without the 2nd stator

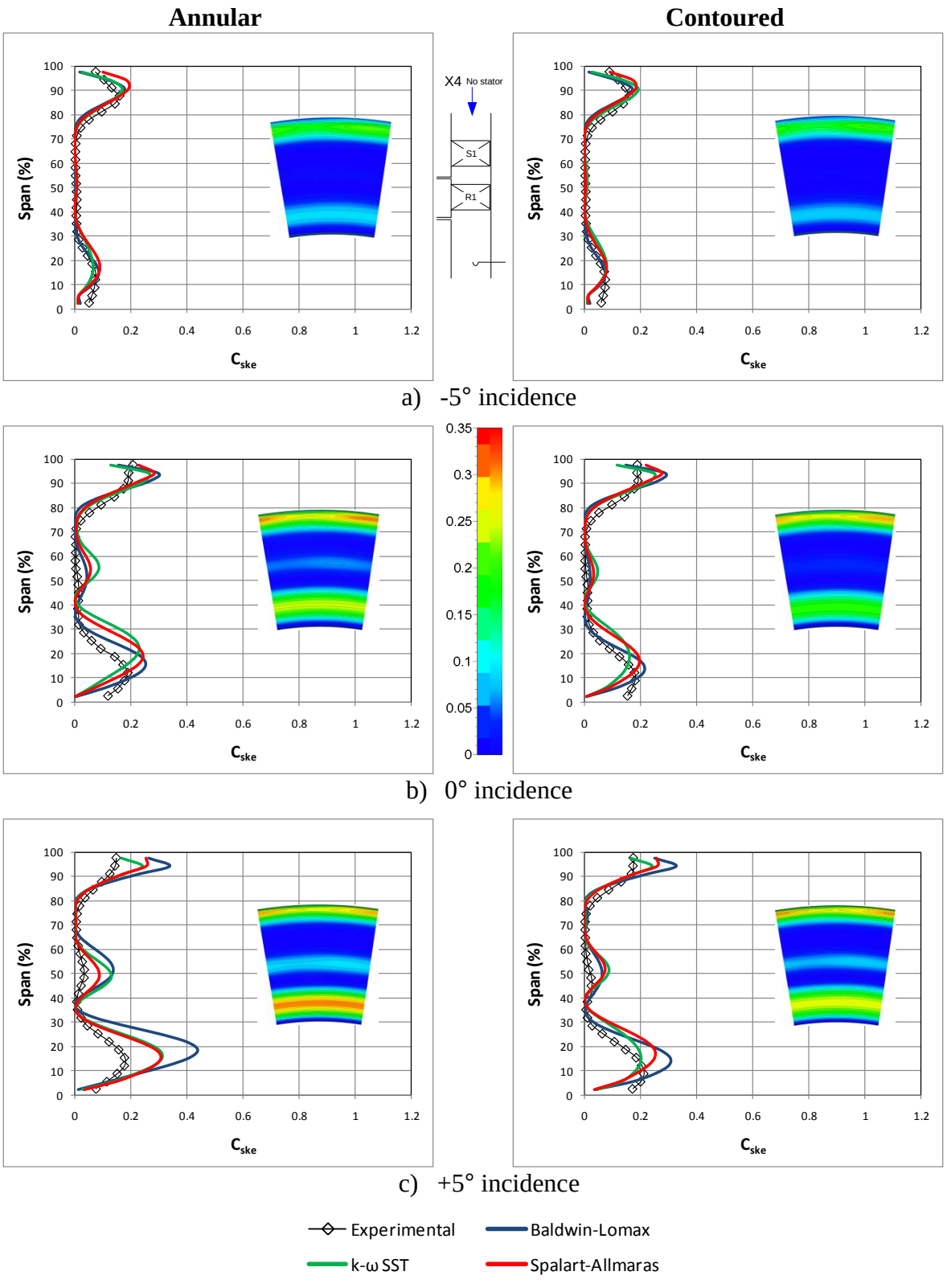

Figure 67: Comparison of rotor exit coefficient of secondary kinetic energy predictions and experimental data measured at station X4 without the 2nd stator, CFD contours inset

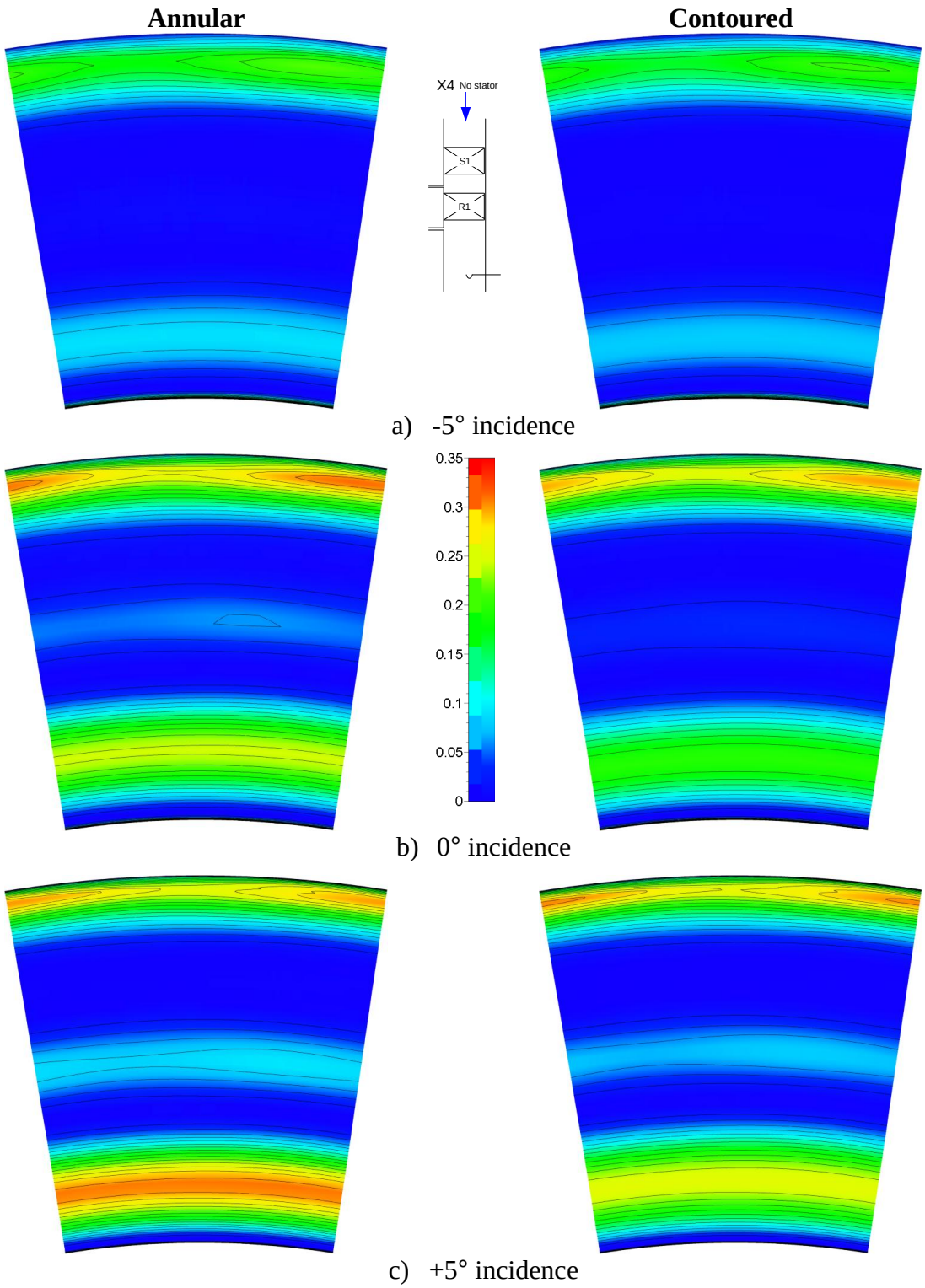

a) -5° incidence

b) 0° incidence

c) +5° incidence

Figure 68: CFD predictions of rotor exit coefficient of secondary kinetic energy measured at station X4 without the 2nd stator

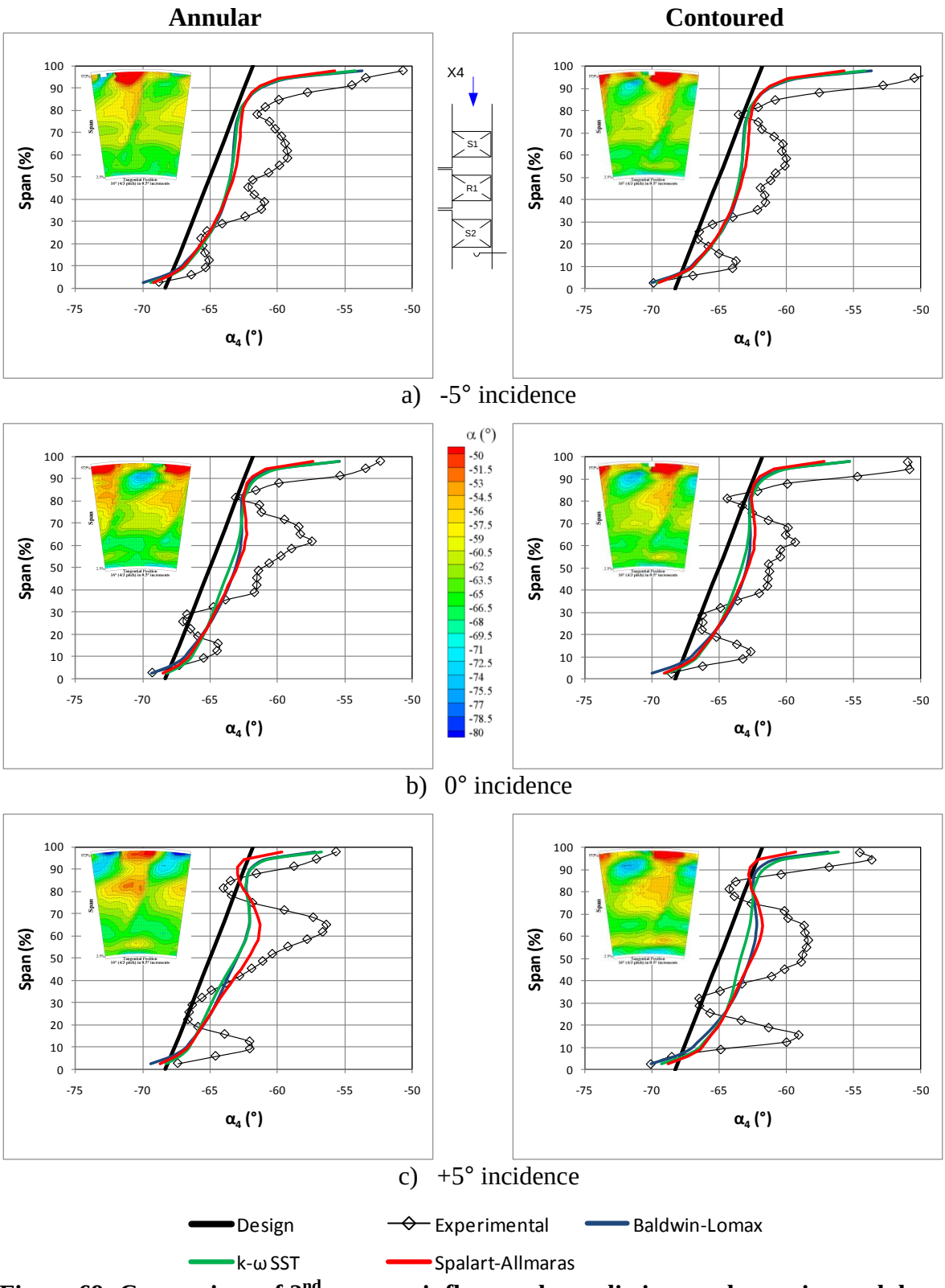

Figure 69: Comparison of 2nd stator exit flow angle predictions and experimental data

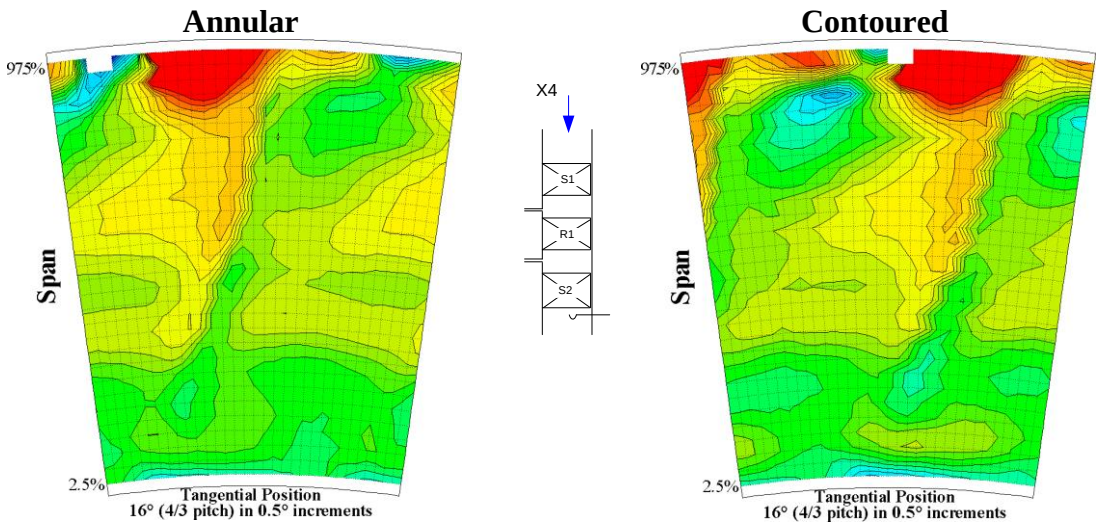

a) -5° incidence

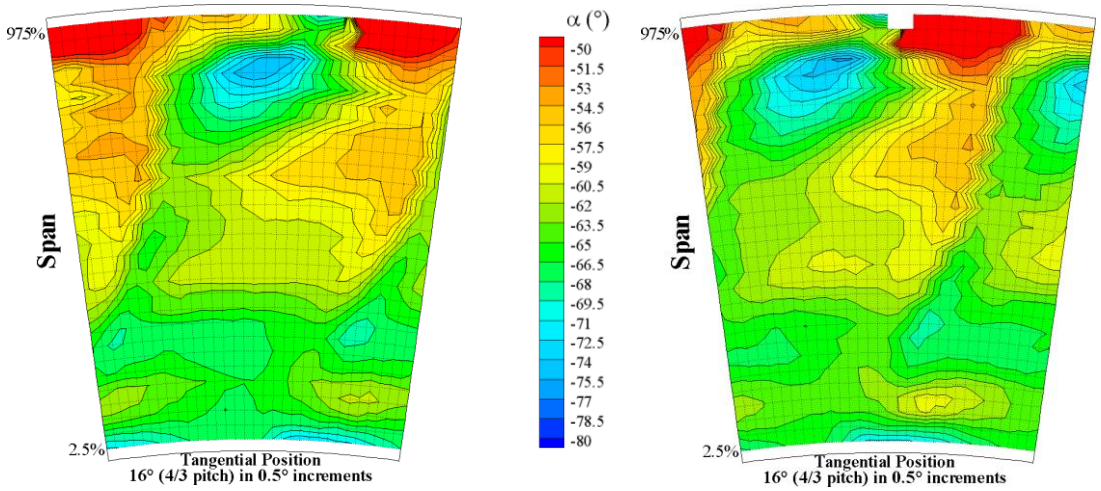

b) 0° incidence

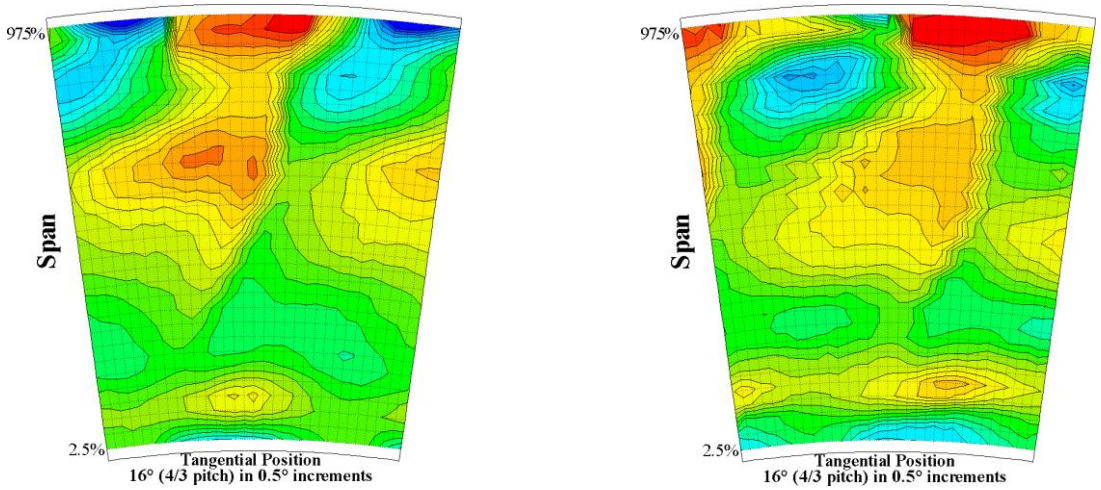

c) +5° incidence

Figure 70: Comparison of 2nd stator exit flow angle contours for experimental results

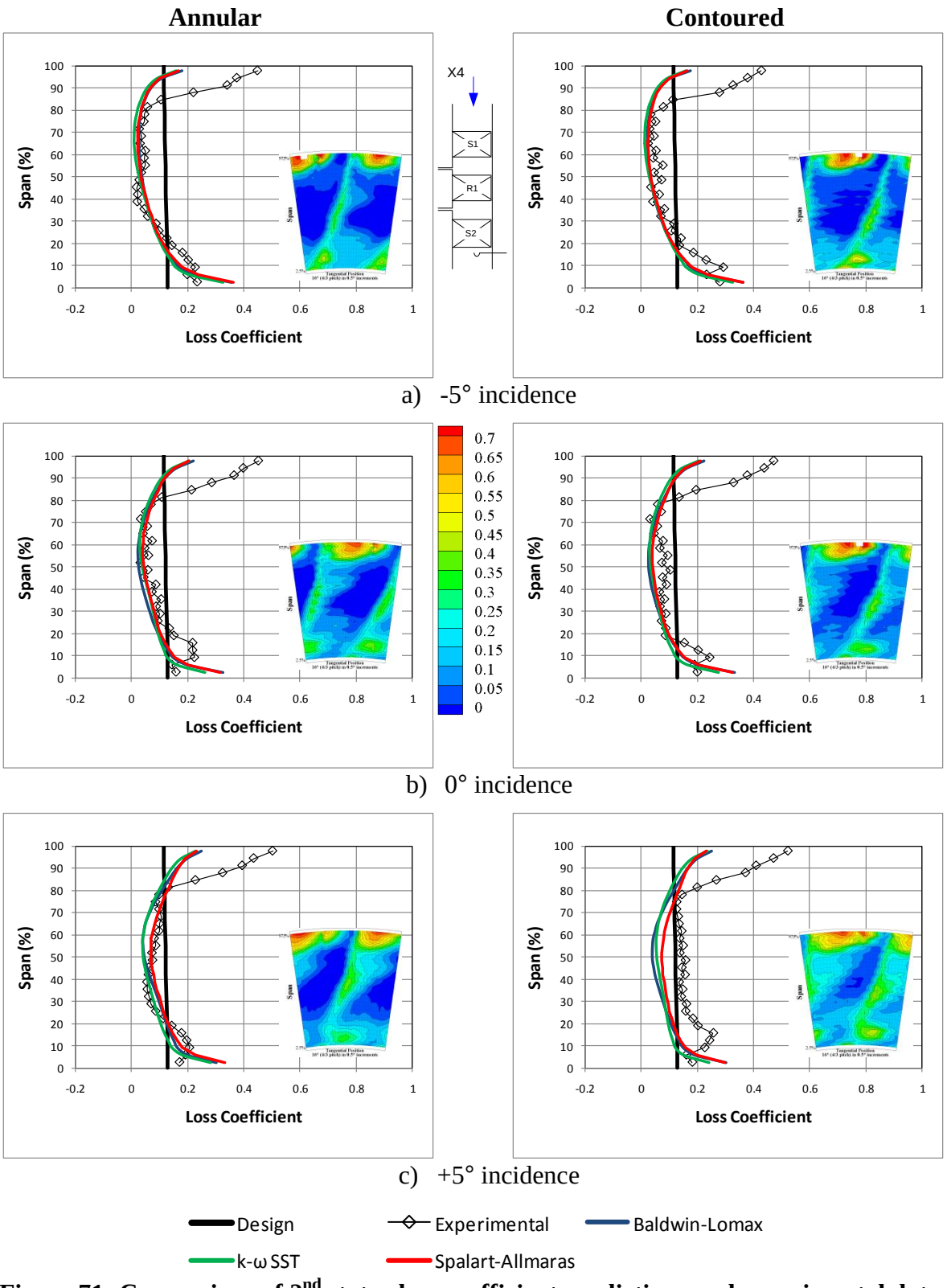

Figure 71: Comparison of 2nd stator loss coefficient predictions and experimental data (experimental contours plots inset for reference)

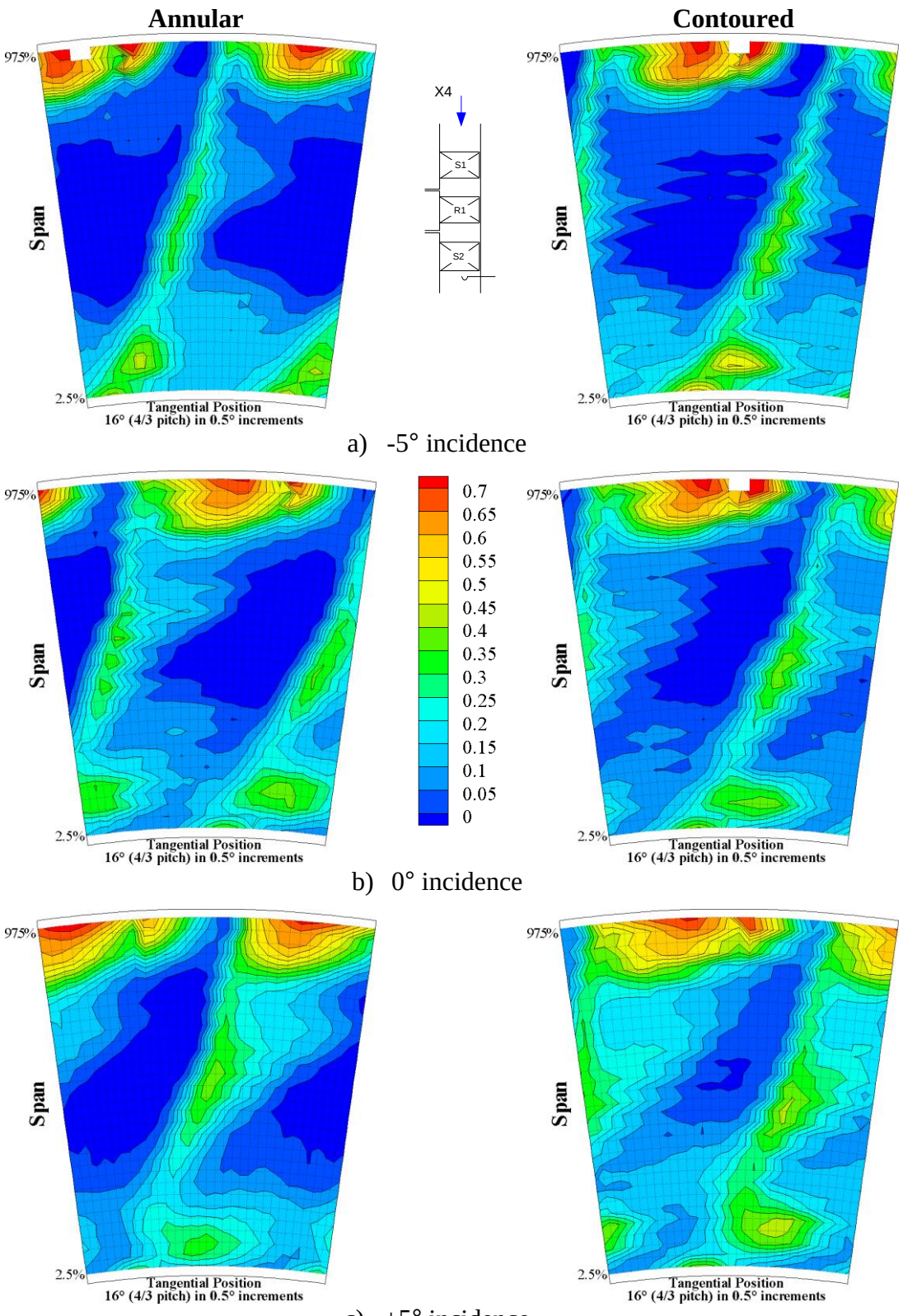

a) -5° incidence

b) 0° incidence

c) +5° incidence

Figure 72: Comparison of 2nd stator pressure loss coefficient contours from the experimental results

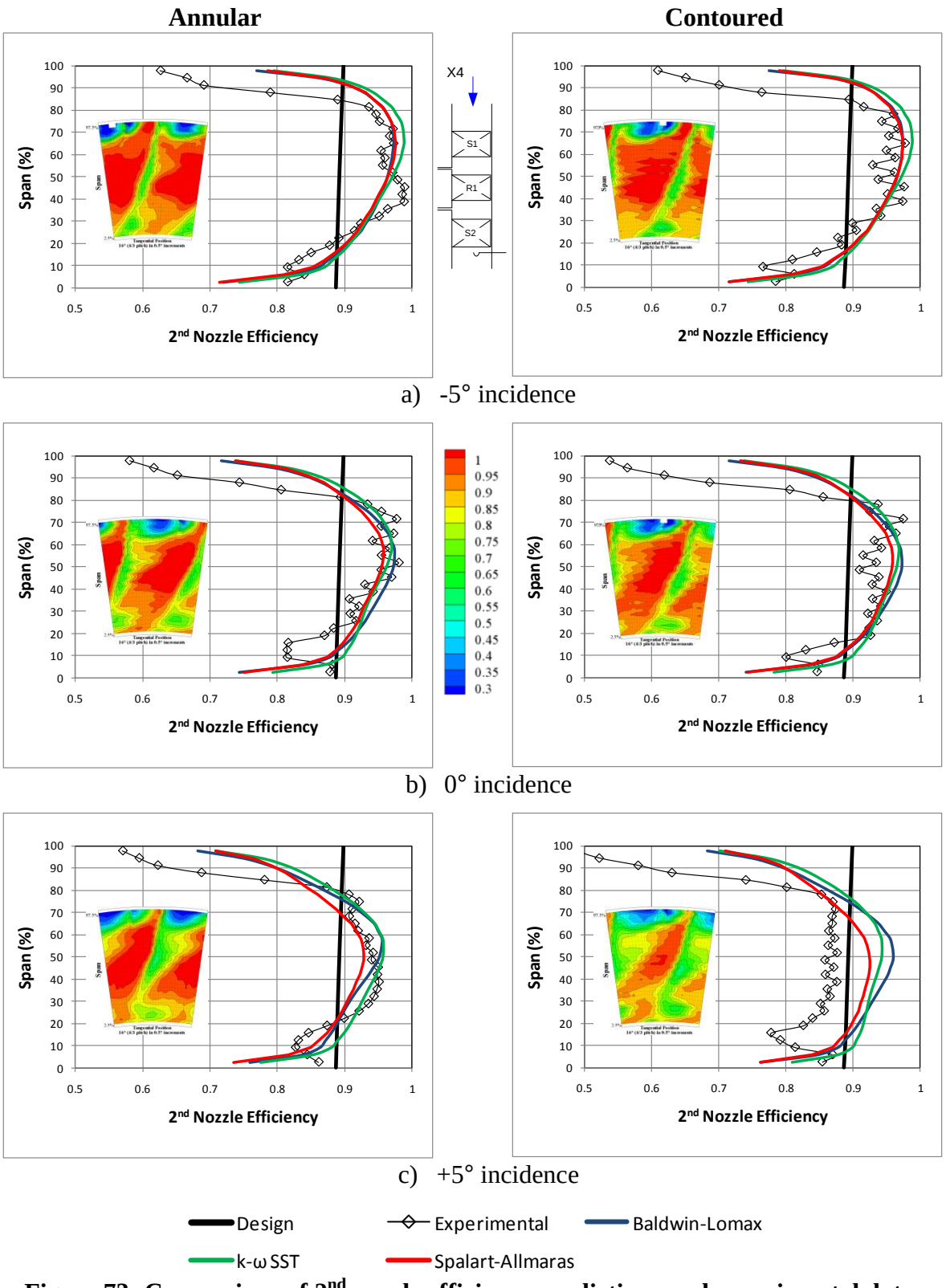

a) -5° incidence

b) 0° incidence

c) +5° incidence

Figure 73: Comparison of 2nd nozzle efficiency predictions and experimental data

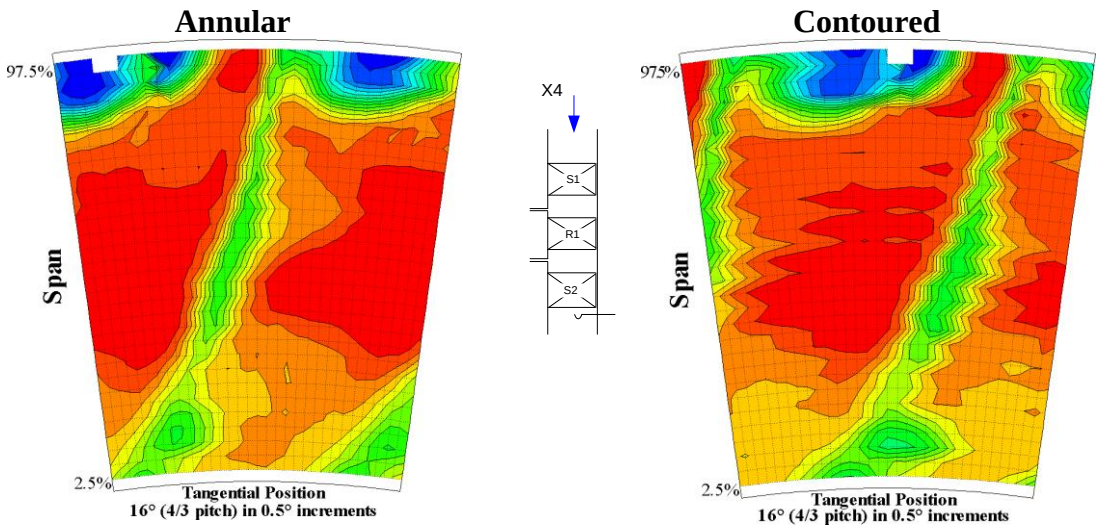

d) -5° incidence

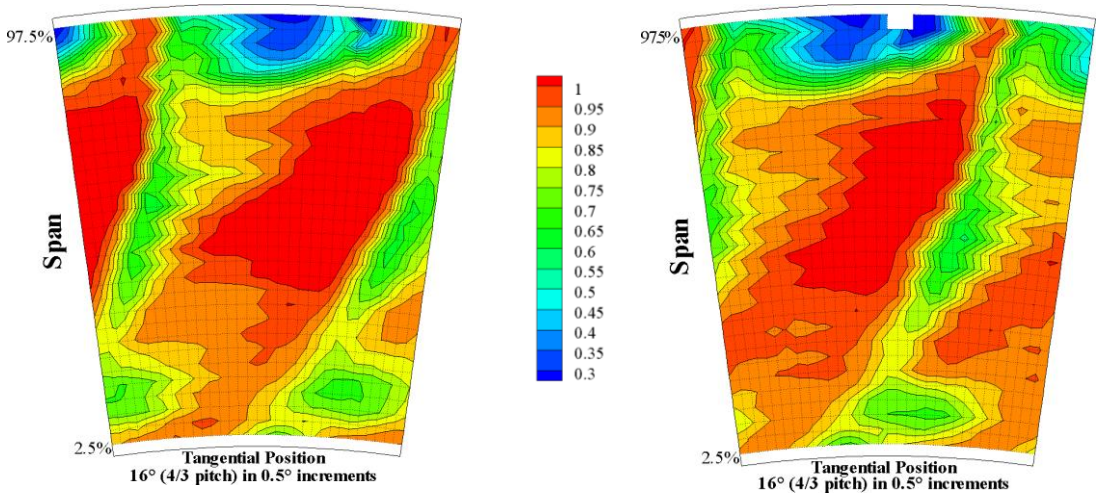

e) 0° incidence

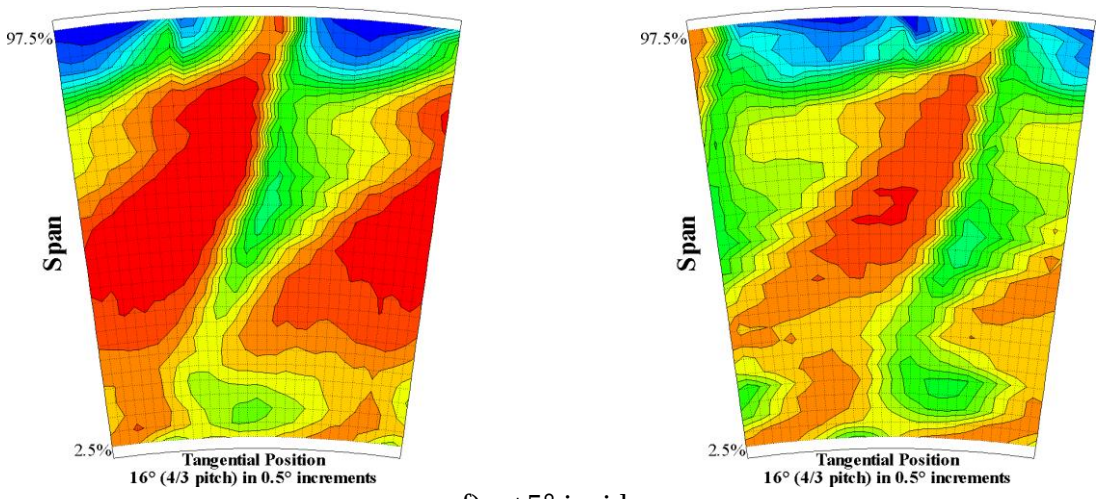

f) +5° incidence

Figure 74: Contours of 2nd nozzle efficiency from experimental data

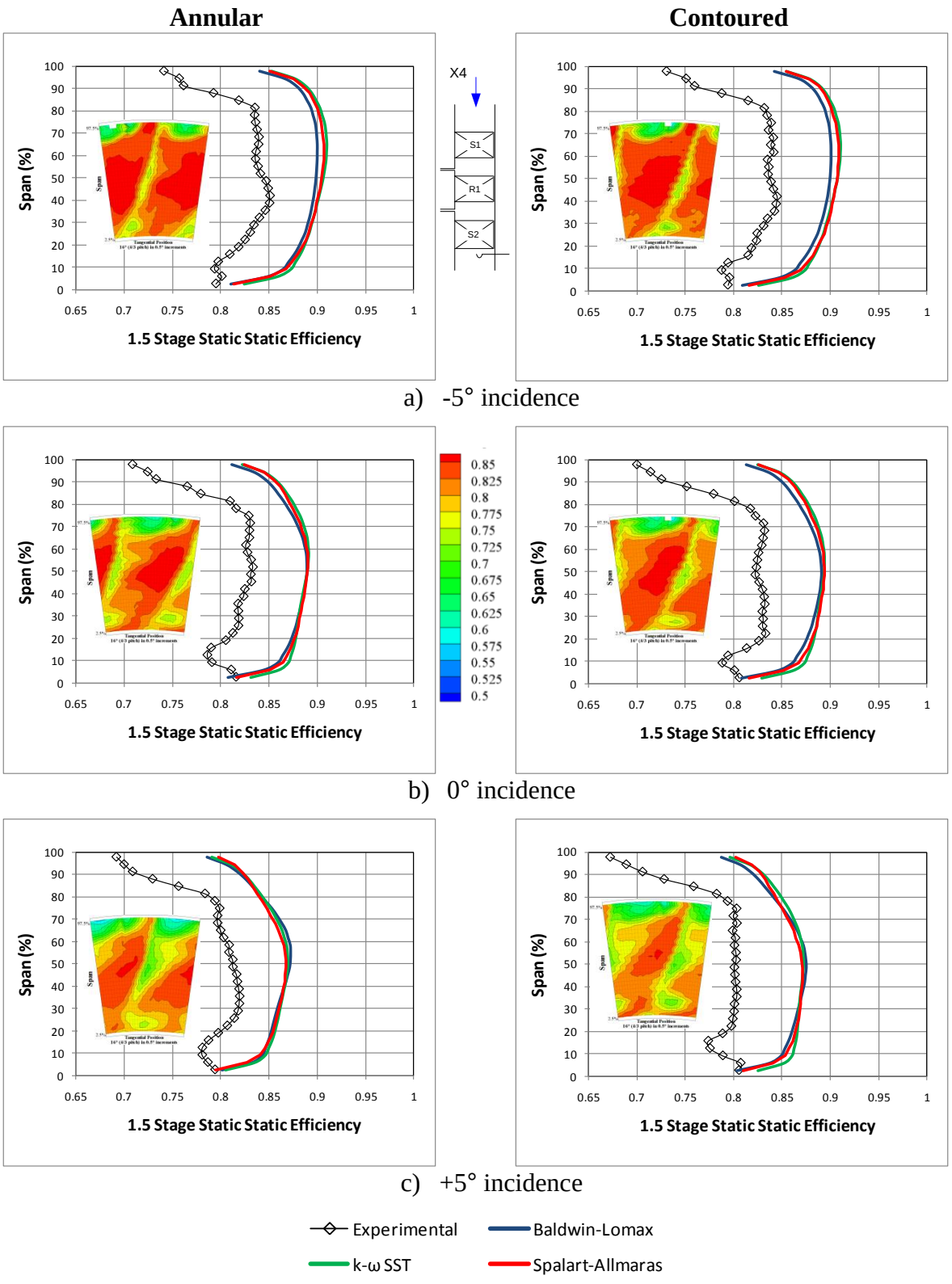

a) -5° incidence

b) 0° incidence

c) +5° incidence

Figure 75: Comparison of 1½ stage static efficiency predictions and experimental data

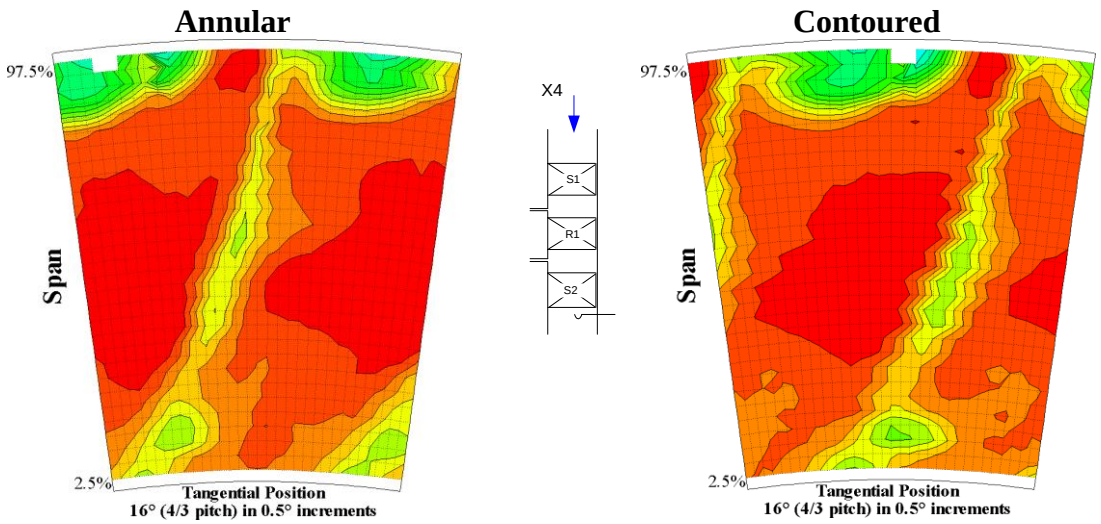

d) -5° incidence

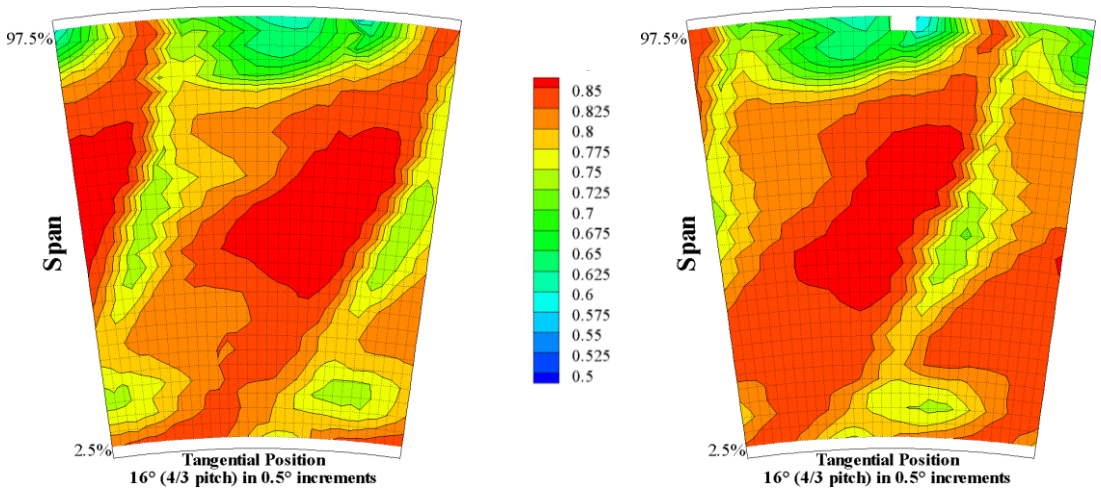

e) 0° incidence

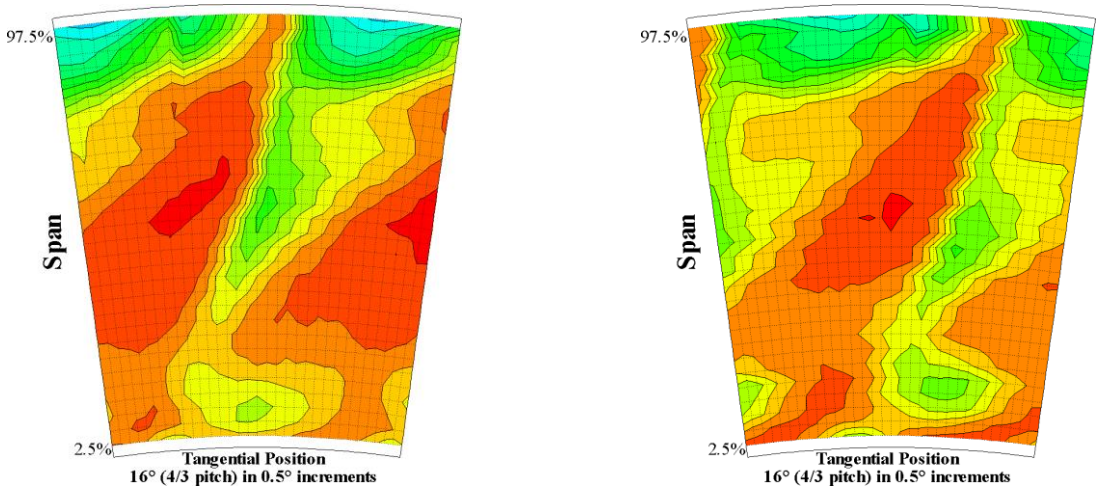

f) +5° incidence

Figure 76: Contours of 1½ stage static efficiency from experimental data

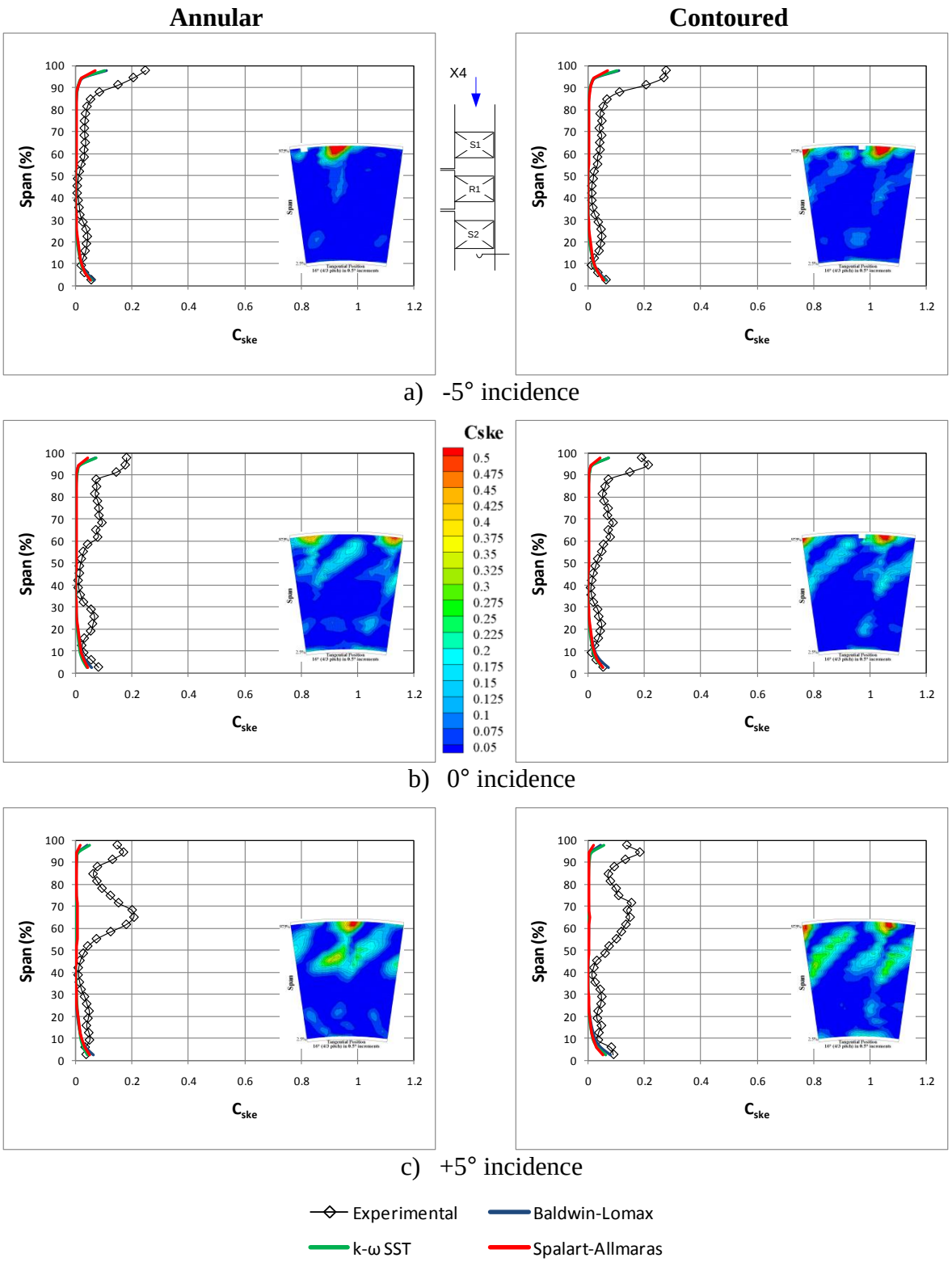

Figure 77: Comparison of 2nd stator exit coefficient of secondary kinetic energy predictions and experimental data (experimental contour plots inset for reference)

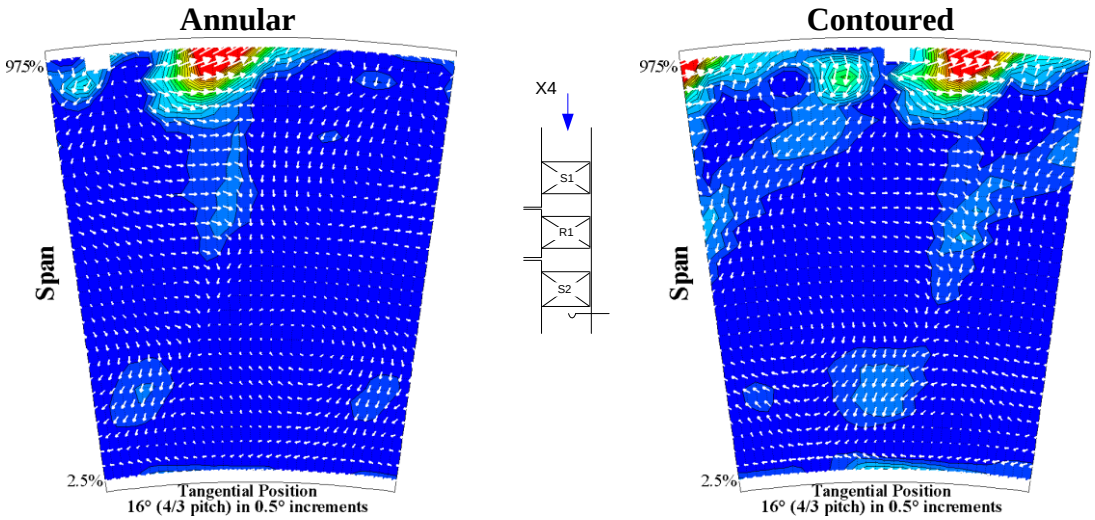

a) -5° incidence

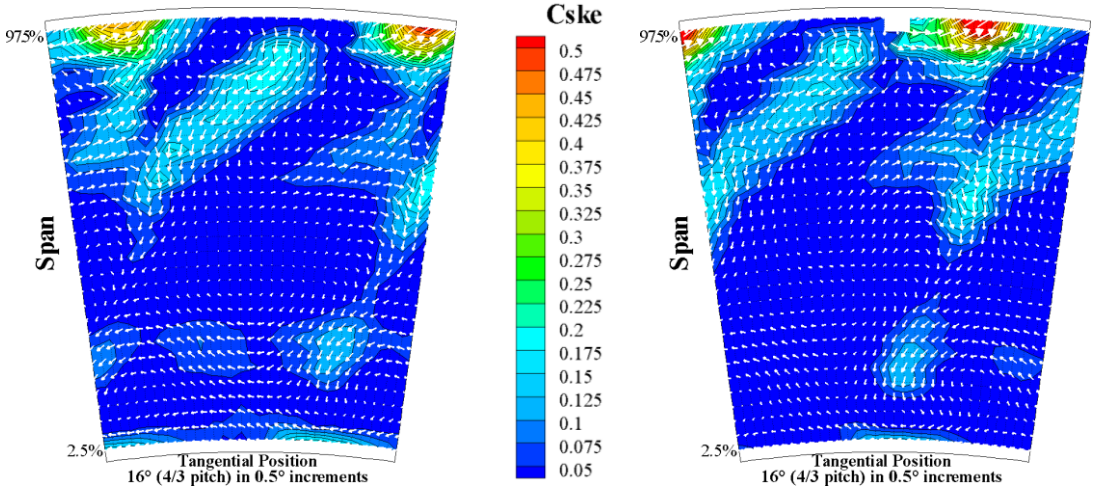

b) 0° incidence

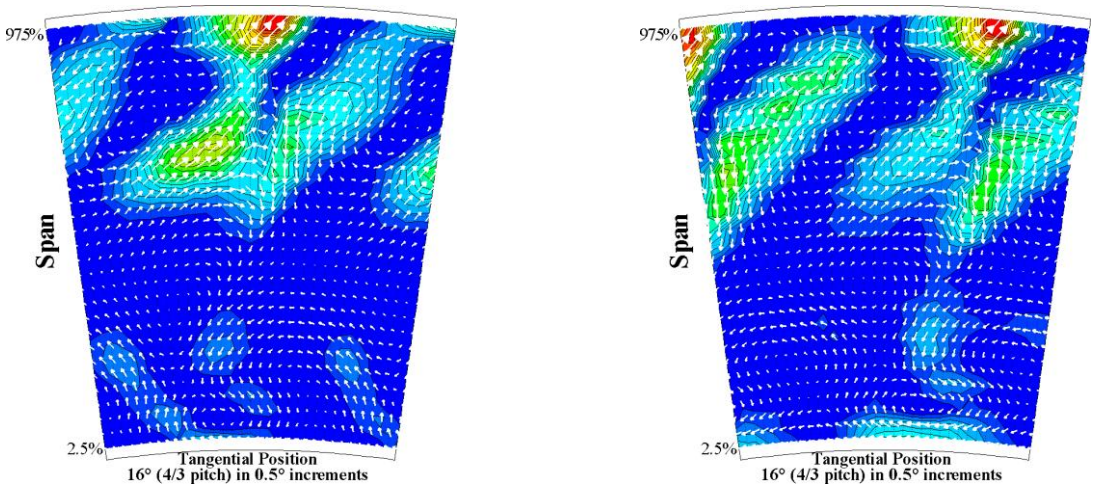

c) +5° incidence

Figure 78: Contours of 2nd stator exit coefficient of secondary kinetic energy from experimental results (vectors of secondary velocity overlaid)

5.5.3 Area averaged results

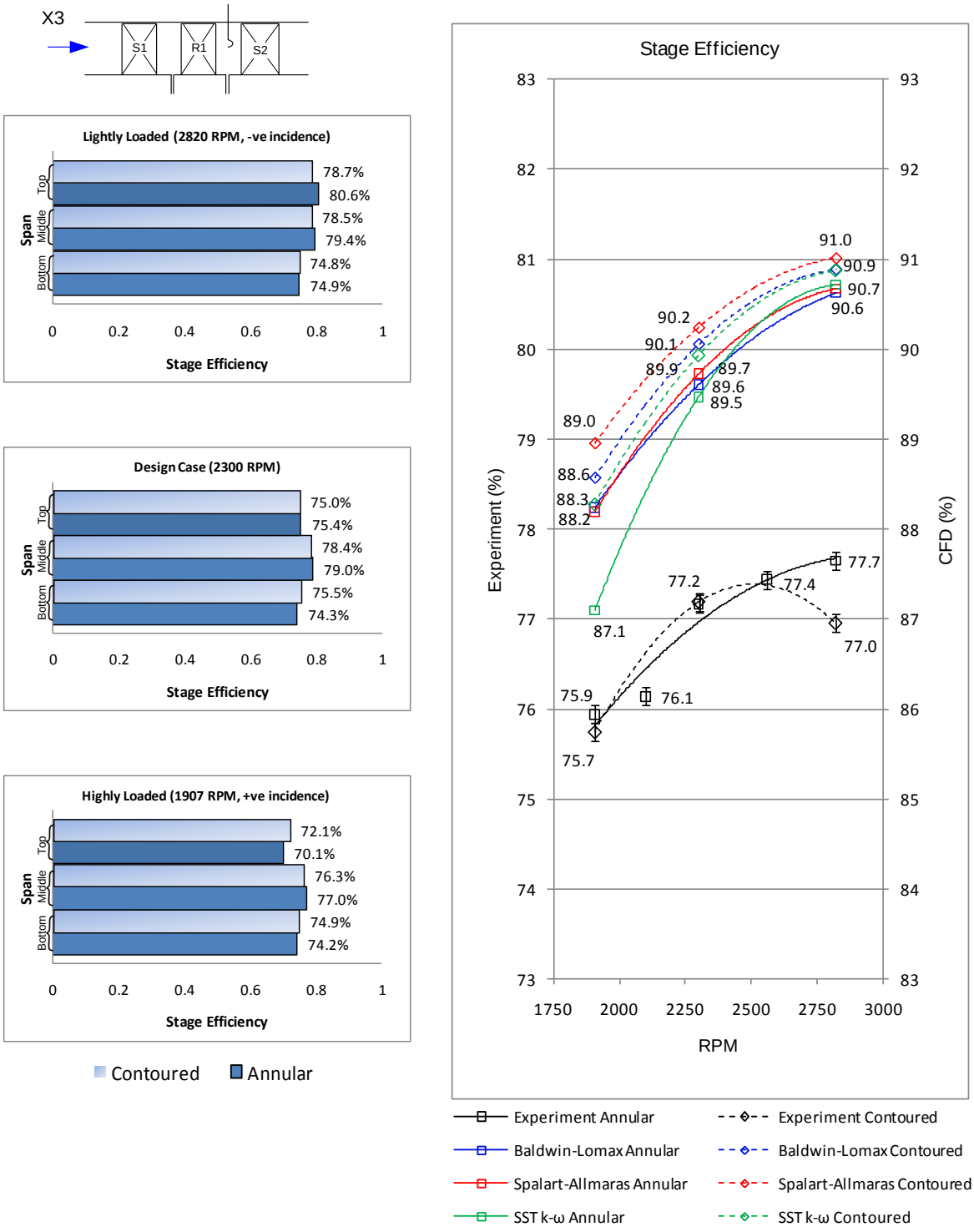

Figure 79: 2/3rd Span mass-averaged stage efficiency measured at X3 comparisons for different load conditions and with experimental third span values (left)

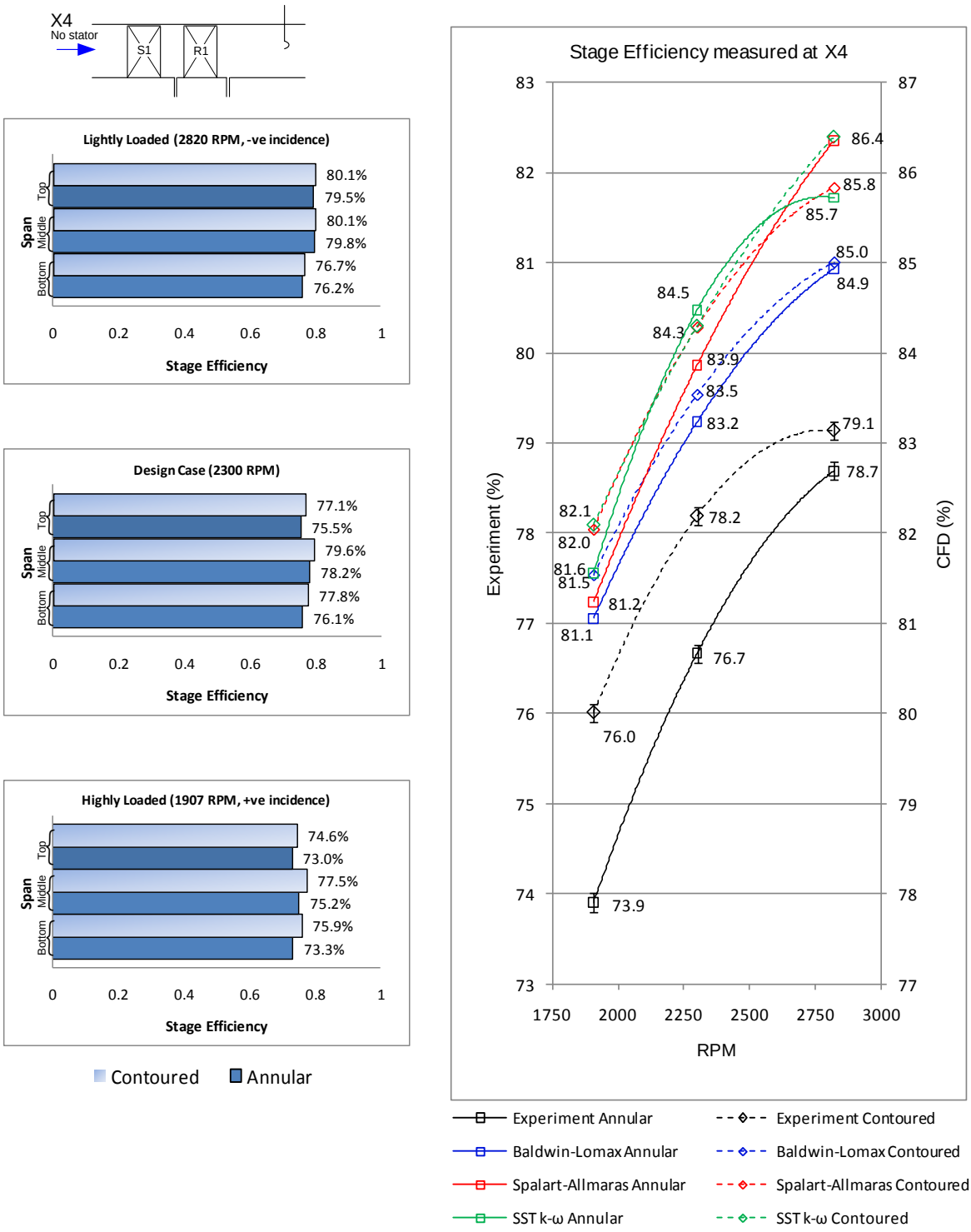

Figure 80: Full span mass averaged stage efficiency measured at X4 comparisons for different load conditions and with experimental third span values (left)

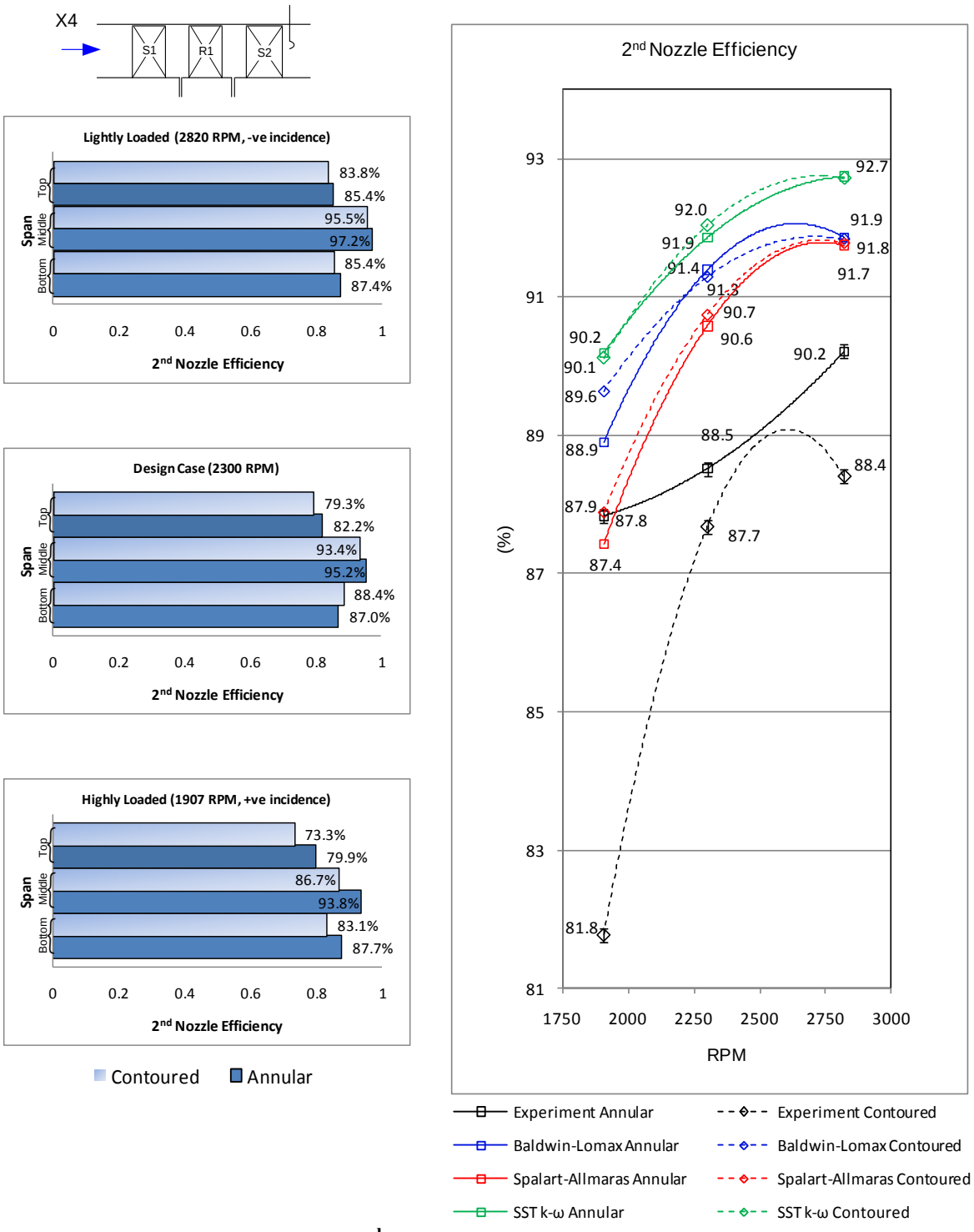

Figure 81: Mass averaged 2nd nozzle efficiency comparisons for different load conditions and with experimental third span values (left)

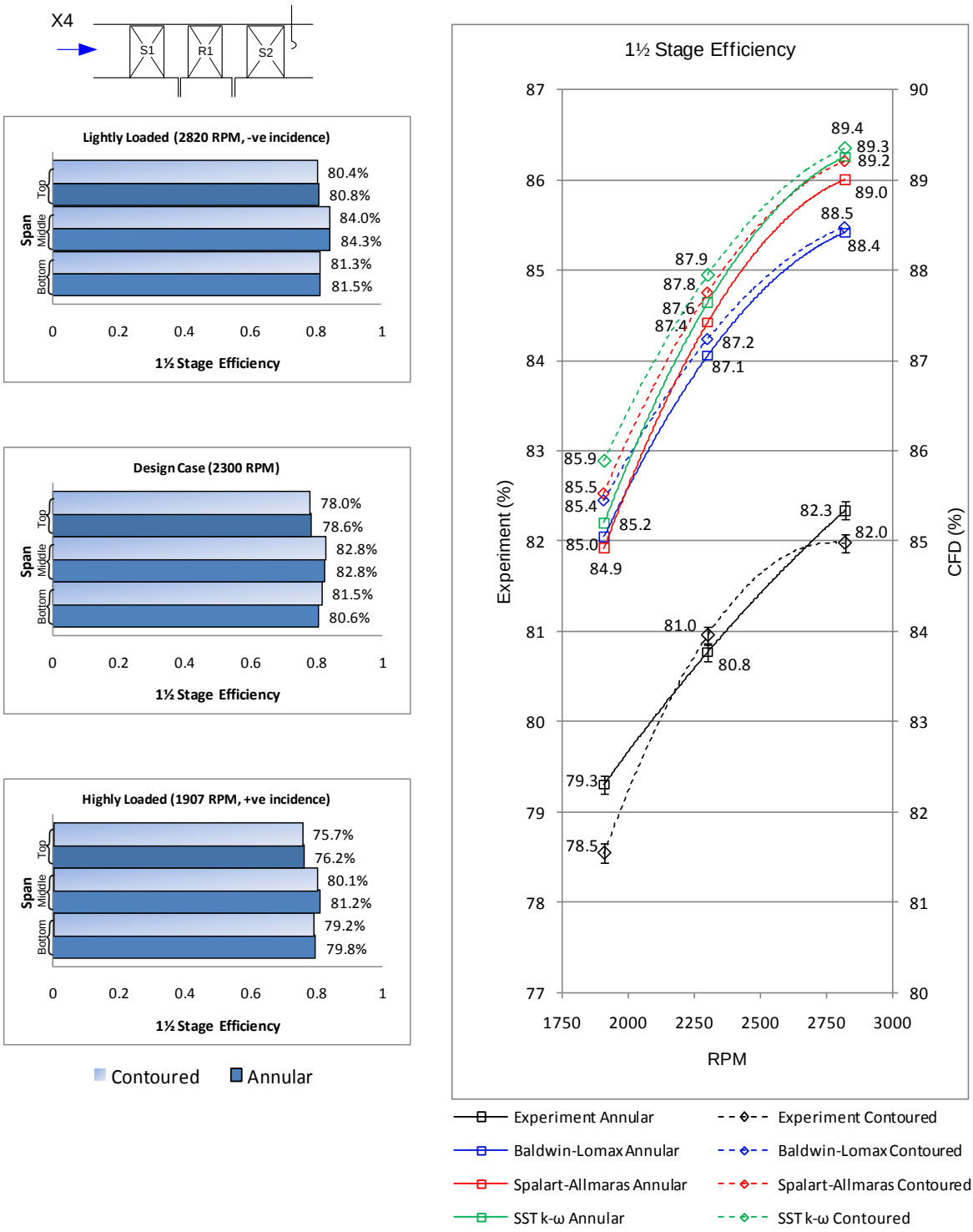

Figure 82: Full span mass averaged 1½ stage efficiency comparisons for different load conditions and with experimental third span values (left)

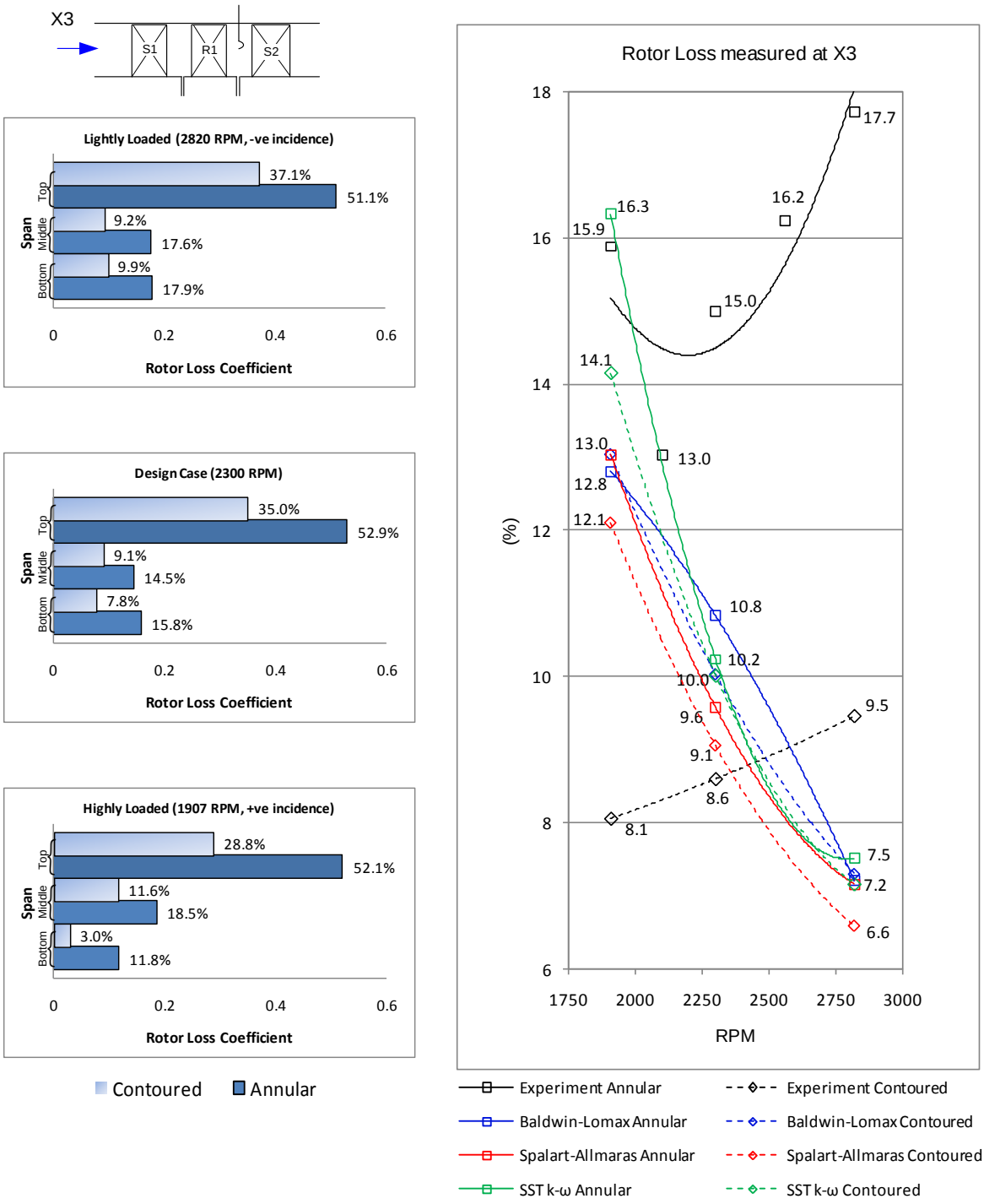

Figure 83: 2/3rd Span mass averaged rotor pressure loss coefficient measured at X3 comparisons for different load conditions and with experimental third span values (left)

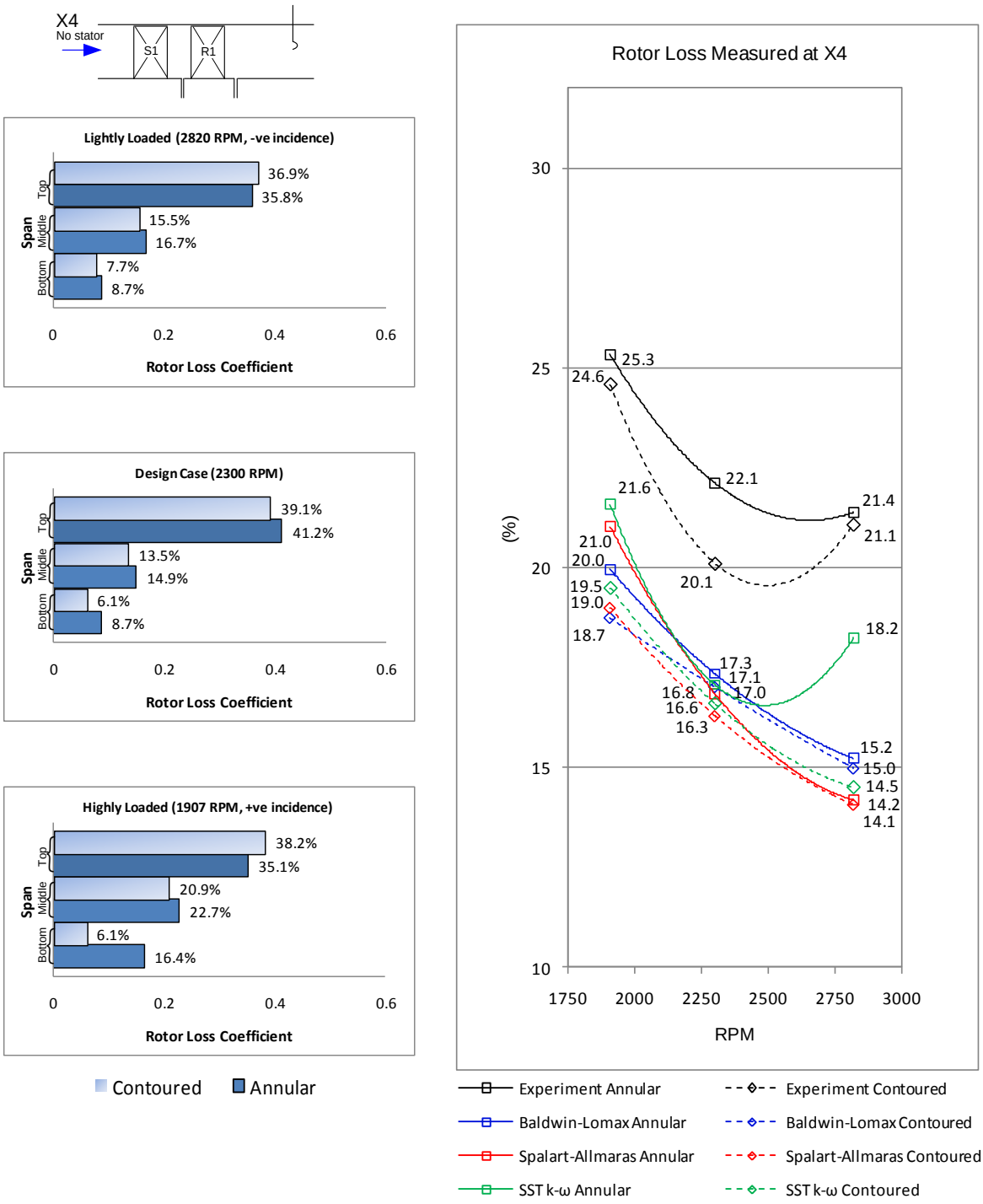

Figure 84: Full span mass averaged rotor pressure loss coefficient measured at X4 comparisons for different load conditions and with experimental third span values (left)

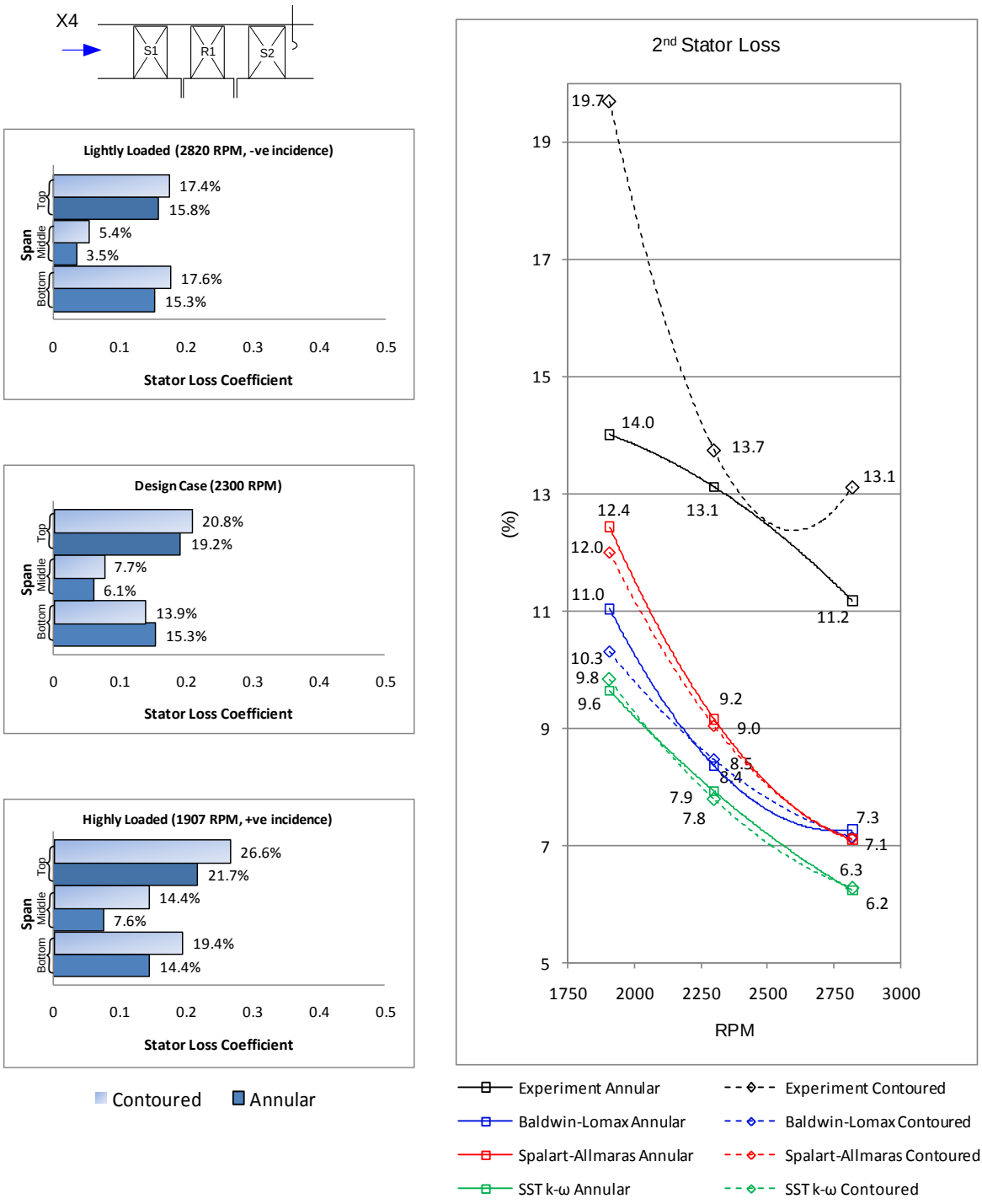

Figure 85: Full span mass averaged 2nd nozzle pressure loss coefficient comparisons for different load conditions and with experimental third span values (left)

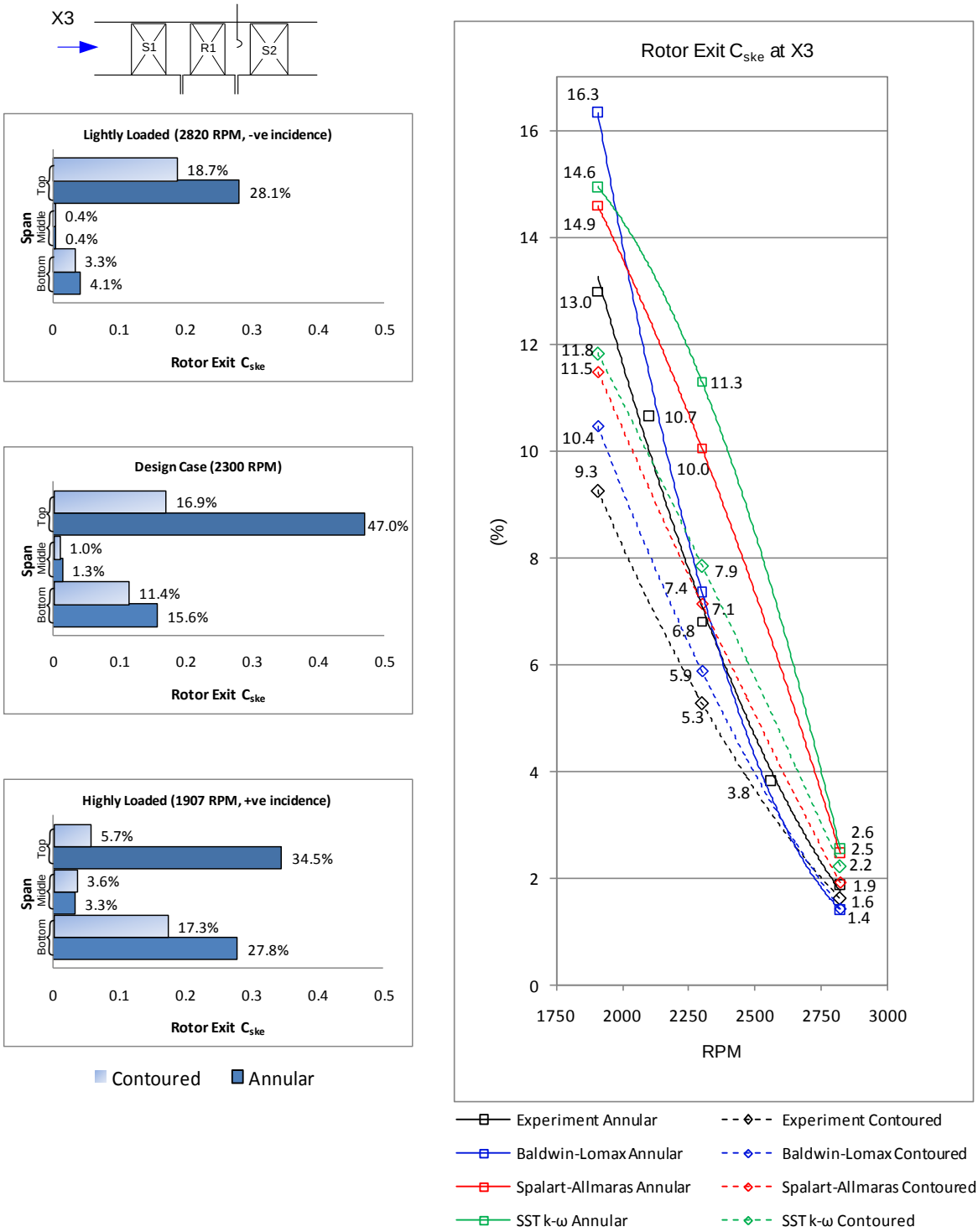

Figure 86: 2/3rd Span mass averaged rotor exit C_{ske} measured at X3 comparisons for different load conditions and with experimental third span values (left)

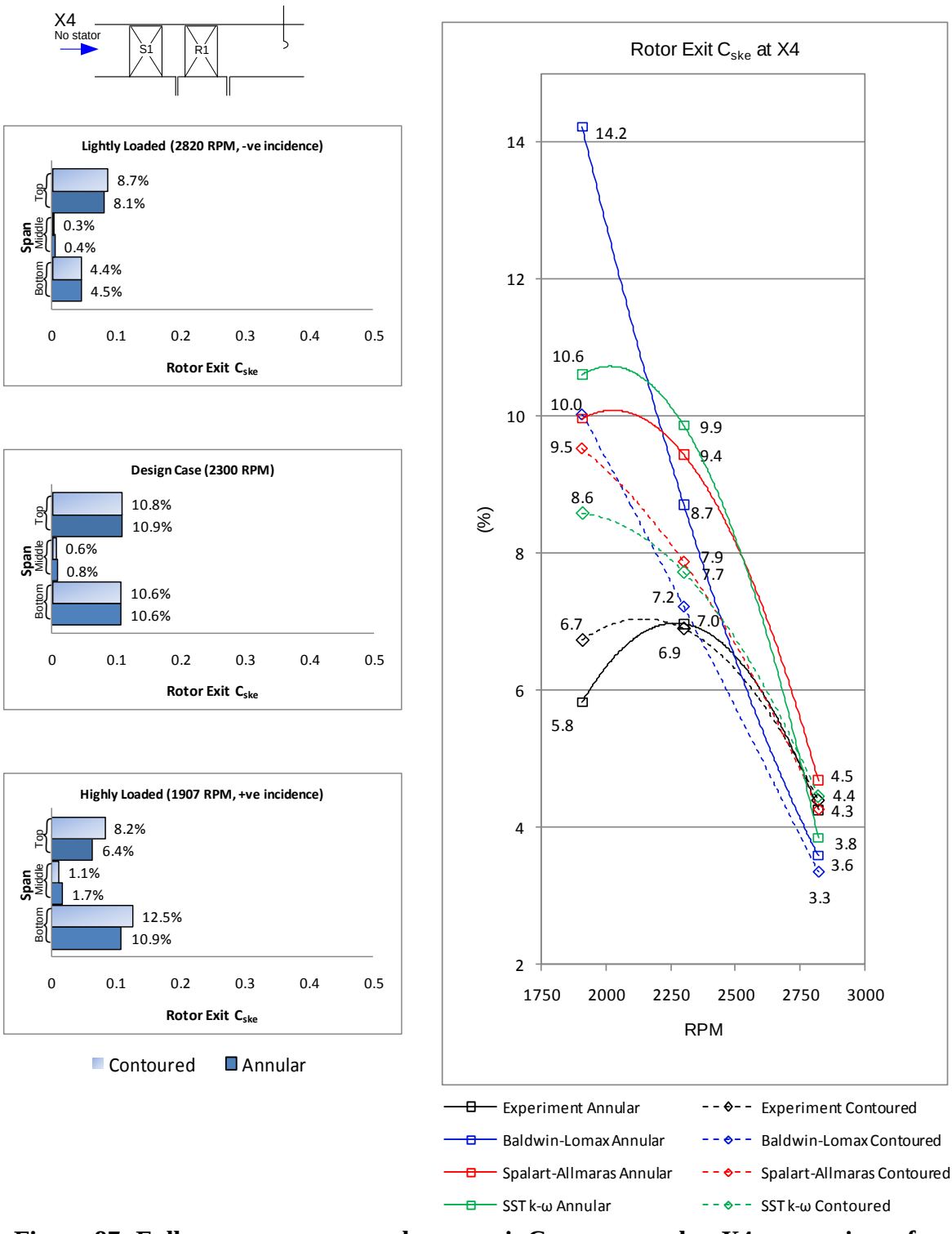

Figure 87: Full span mass averaged rotor exit C_{ske} measured at X4 comparisons for different load conditions and with experimental third span values (left)

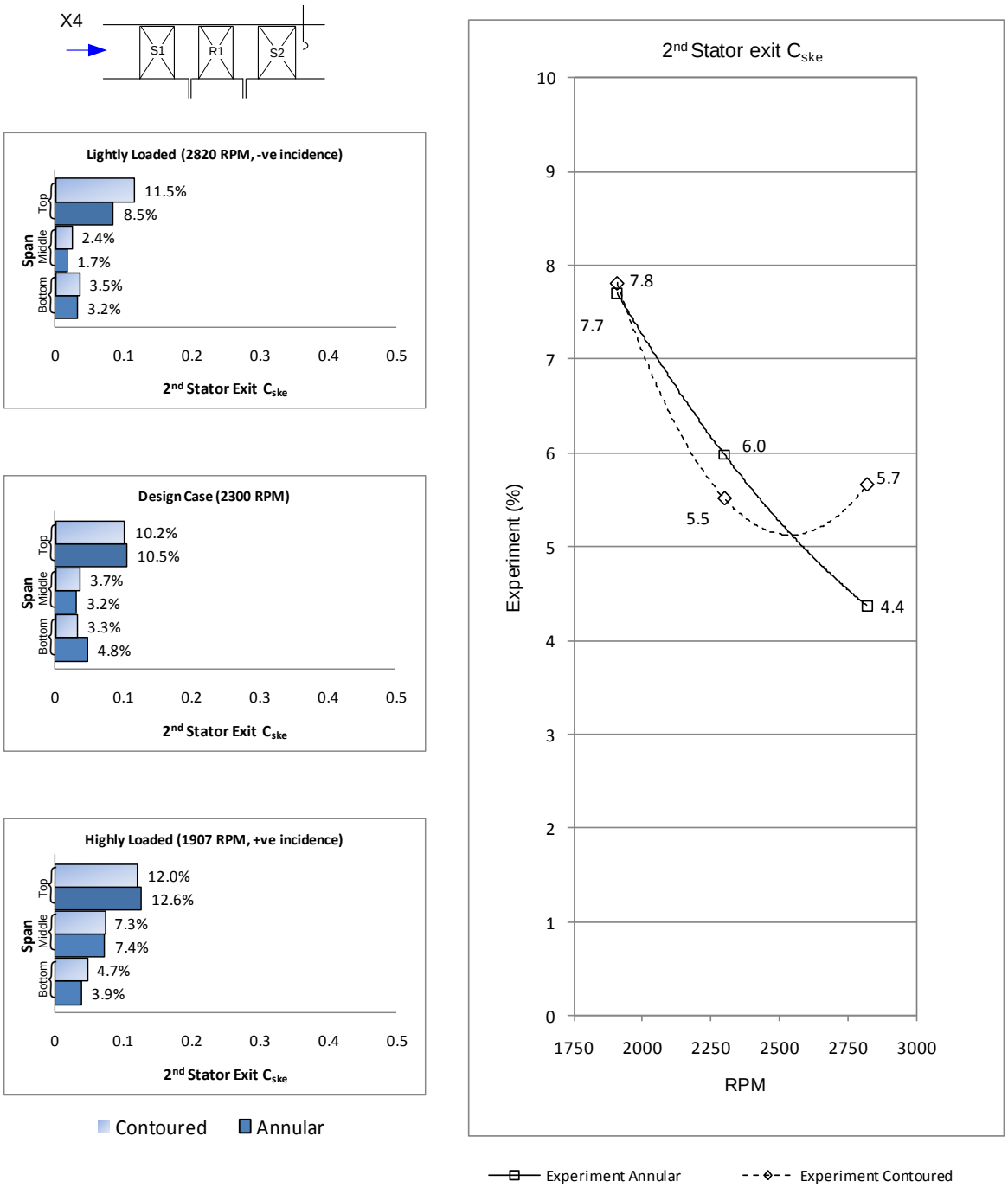

Figure 88: Full span mass averaged 2nd stator exit C_{ske} comparisons for different load conditions and with experimental third span values (left)

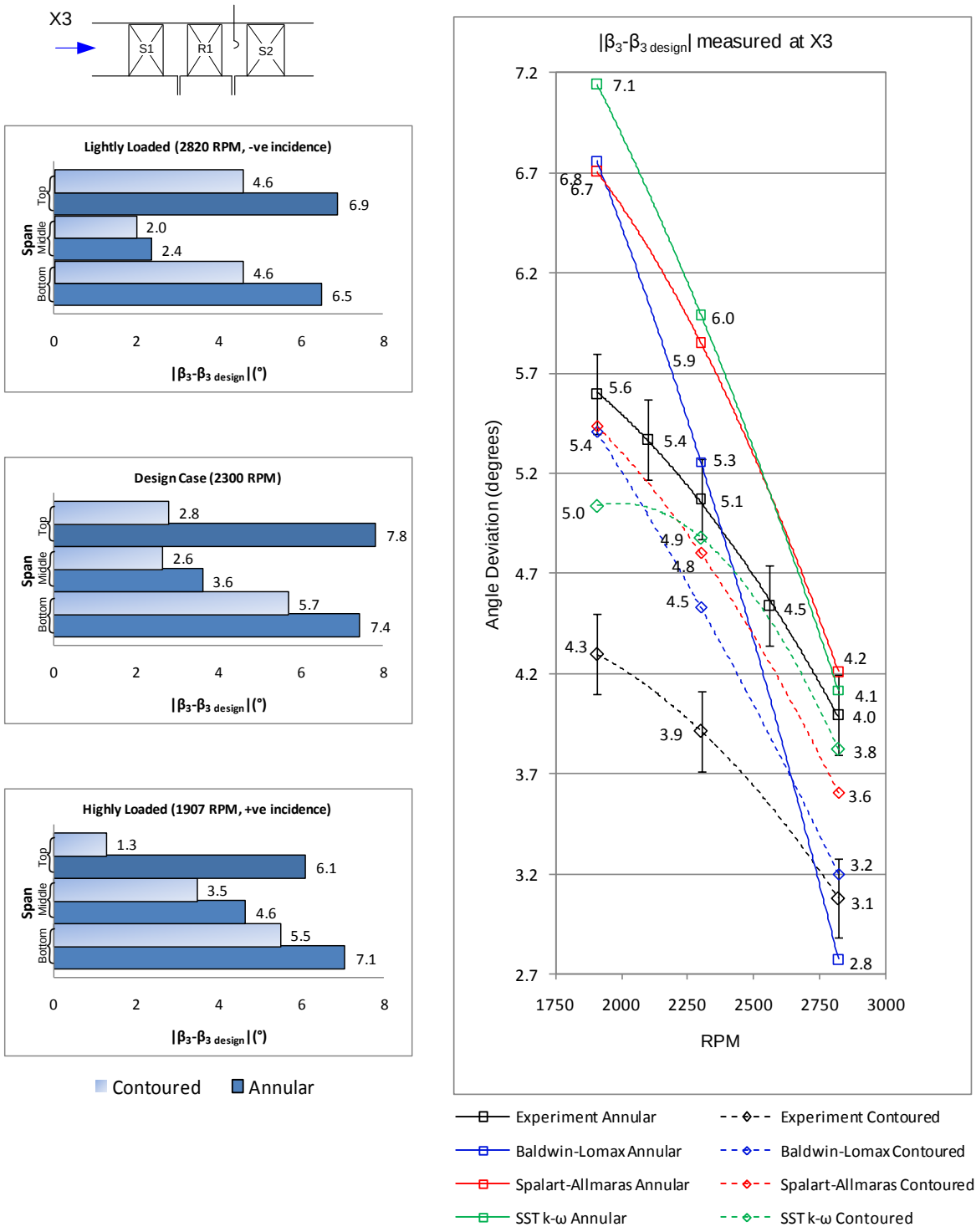

Figure 89: 2/3rd Span mass averaged rotor exit relative flow angle deviation from design measured at X3 comparisons for different load conditions and with experimental third span values (left)

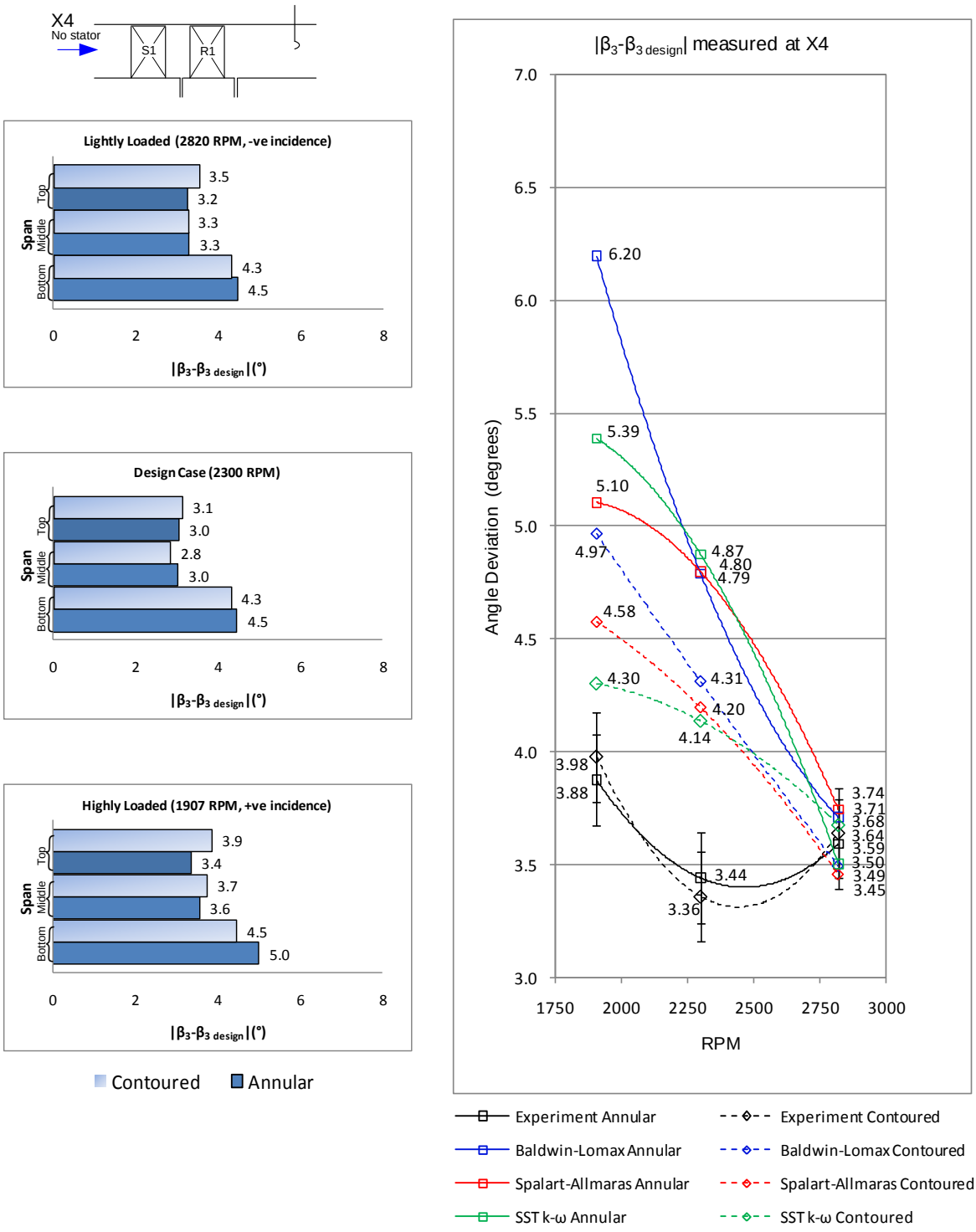

Figure 90: Full span mass averaged rotor exit relative flow angle deviation from design measured at X4 comparisons for different load conditions and with experimental third span values (left)

6 The effect of endwall profiling on the structure of three dimensional flows

The figures presented in this section are derived purely from the CFD solutions which have been validated in the previous chapter. Although the area averaged values do not validate well, the general form and magnitude of the primary values derived from the CFD do validate well with flow angles having been validated to within a few degrees and the span-wise location of features to within 5%. Hence the pressure and streamline plots derived from velocity data in the CFD solutions and displayed in this section can be used with some confidence.

6.1 CFD Pressure Profiles

6.1.1 Hub

Figure 91 shows the endwall pressure distributions and clearly indicate a reduction in the high pressure region against the pressure surface with the introduction of endwall contours, at all incidence angles. The contours in this high pressure region change from an arc to axial lines. There is also a clear reduction in the tongue of low pressure at 20% of the passage width from the suction surface, that marks the position of the horseshoe vortex on the annular endwall, again for all incidence angles. An undesirable development resulting from the contouring is the emergence of a low pressure region on the suction surface at 10-20% axial chord, which strengthens with increased incidence and which may point to the existence of a separation bubble in practise.

6.1.2 Blade

Figures 92 to 94 give composite views of the static pressure profiles on the blading as well as full suction surface contours for both endwall cases at the three incidence angles respectively. As loading increases the area between suction and pressure surface lines increases and the stagnation point moves from suction to pressure surface. By midspan the difference found between annular and contoured endwalls is negligible and although not shown sections taken above midspan also show no differences. The pressure side of all the sections indicate only small differences between annular and contoured cases. At one third of span the suction surface differences only appear at design load and are limited to small differences in the last 20% of chord, at increased load this effect extends forward 20% and changes from the contoured case having a lower cross passage gradient to the reverse. At 20% span the effect at low load remains small but shows a reduced cross passage pressure gradient for the contoured case between 20 and 80% of chord. This is also true at design load, however, there is a small increase in the gradient over the last 20% of chord. Once the highly loaded case is reached the picture at 20% span is more confused with small differences and changes in the net gradient per case nearly every 10% of chord, however the contoured case does show a small peak in pressure at about 27% span.

The hub suction surface pressure profiles, although not strictly comparable as those for the contoured case are not situated at a consistent radius, do show some clear differences between profiled and annular cases although the difference at light load is again small. At

design the contoured endwall appears to offer a decreased (upto 0.18 C_P) net passage gradient only over 25 to 35% of chord and the reverse is true over the remainder of the chord. At high incidence this decreased gradient expands to cover the range 20-60% (upto 0.22 C_P) of chord but there would appear to be a net loss in torque as a result. If the effect of non-axisymmetric endwalls is intended to effectively aft load the blade in the proximity of the endwall then this particular endwall is not functioning ideally. While there is slightly increased loading in the last 40% of chord and a release of load at mid chord, the first 20% of chord is consistently more highly loaded. This increase in load in the forward section of the suction surface results in the potential for a separation bubble, visible in Figure 91.

The pressure contour plots of the blade suction surface indicate further features of the flow, including a number of potential separation bubbles: One at the leading edge between 50 and 90% span at high load, and two in the tip region, one in the tip gap itself indicating a separation on the pressure side of the tip in the last 50% of chord similar to that suggested by Bindon (1989); and one on the suction surface where the tip gap vortex causes a separation as it emerges from the gap, again from 50% chord downstream. Two areas of low pressure appear on the suction surface and by using the lines along which the profiles have been extracted as reference the first (at roughly 18% chord, 33% span) is the point of highest curvature in the profile and hence one is seeing the effect of the accelerating flows. The second, elongated area of low pressure runs up from the endwall at an angle of roughly 30° from a chord of 25% at the hub and extends all the way to the trailing edge. Again by using the profile lines as reference one can note the effect of the contoured endwalls which is to increase the radial component of the angle at which this feature leaves the hub and soften it by expanding its width and slightly decreasing the peak pressures. This low pressure area coincides with the passage of the hub secondary flow vortices up the side of the blade as can be seen in later figures.

Only very small changes in the tip pressure isolines are noticeable.

Previous work by the author, some of which is described in Snedden (2010b), indicates far more extensive changes to the CFD generated suction surface pressure patterns and tip gap flows resulting from the contouring of the endwalls. The changes shown here are not as extensive, however the earlier results represent a solution of the same hub geometry with at constant tip gap and the use of different turbulence model, in that case SST k-ω. This serves to highlight the sensitivity of the solutions to the choice of turbulence models and as a warning regarding the potential effects of hub endwall contouring to the secondary flows at the tip which the experimental results presented in the previous section support.

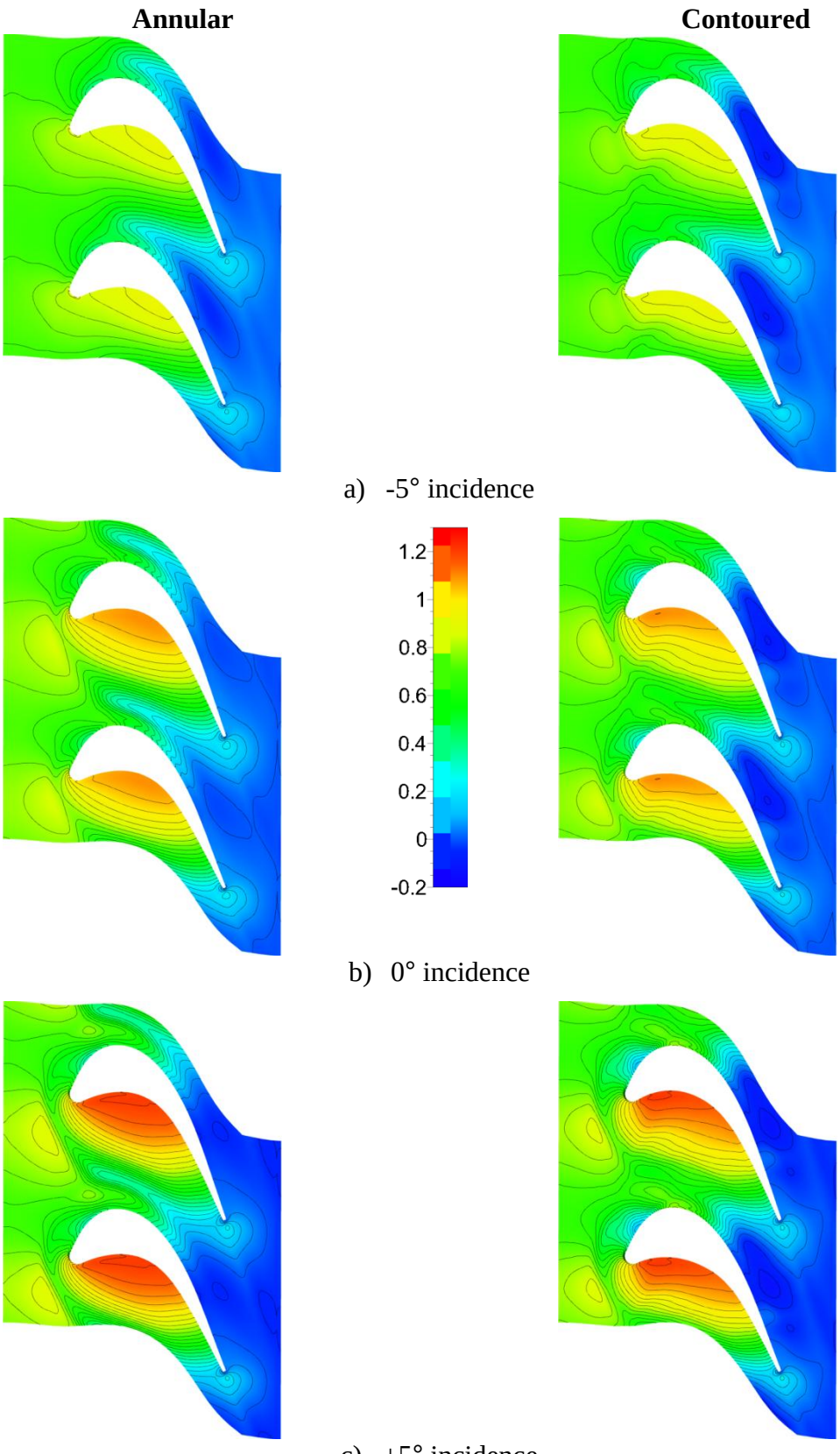

a) -5° incidence

b) 0° incidence

c) +5° incidence

Figure 91: Static pressure coefficient distributions on the rotor hub

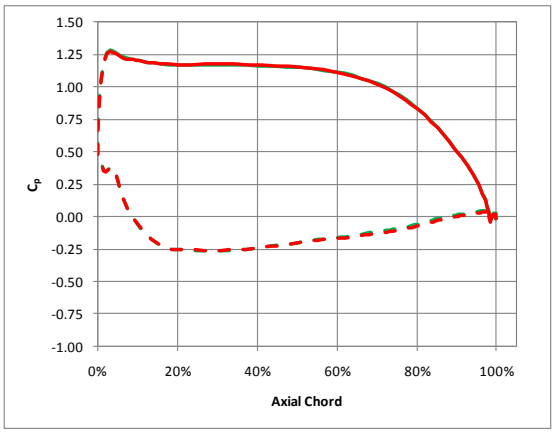

(a) Midspan

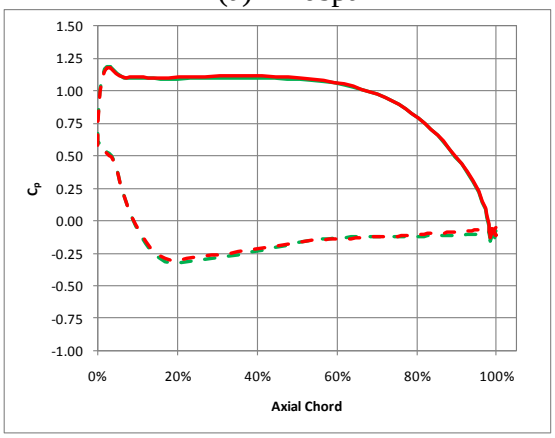

(b) 33% span

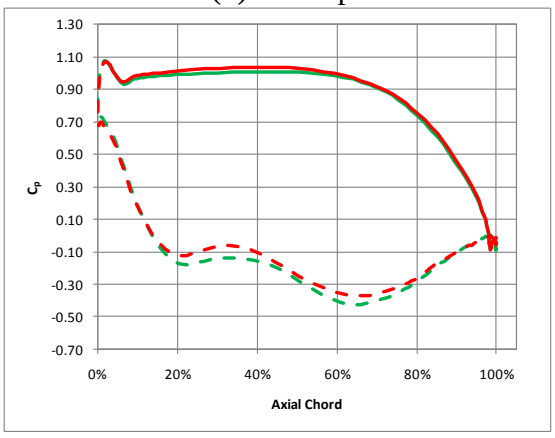

(c) 20% span

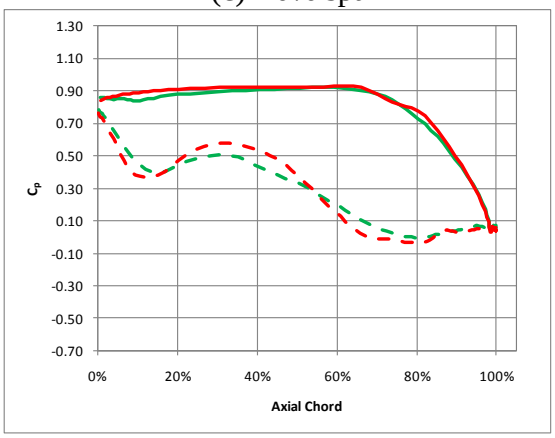

(d) Hub profile

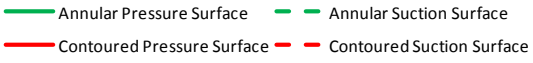

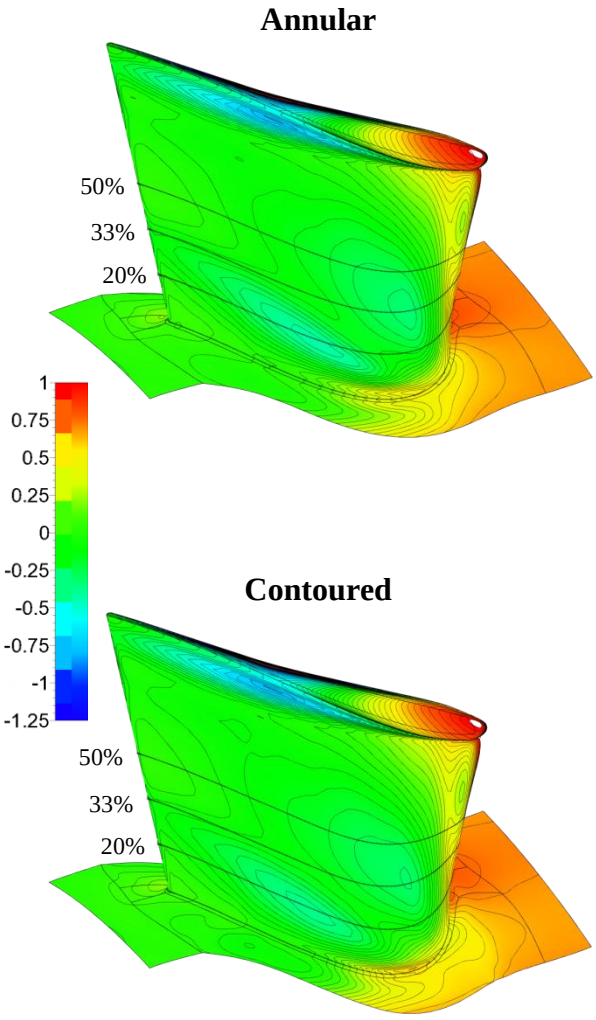

Figure 92: Static pressure coefficient distributions on the blade surface for the lightly loaded case (2820 RPM)

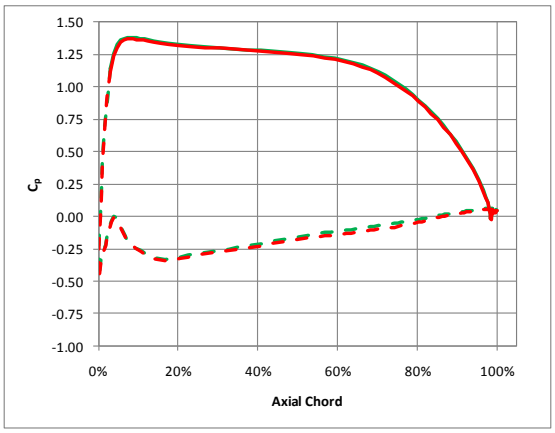

(a) Midspan

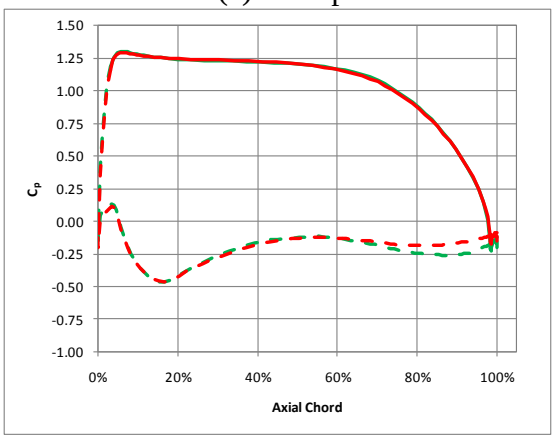

(b) 33% span

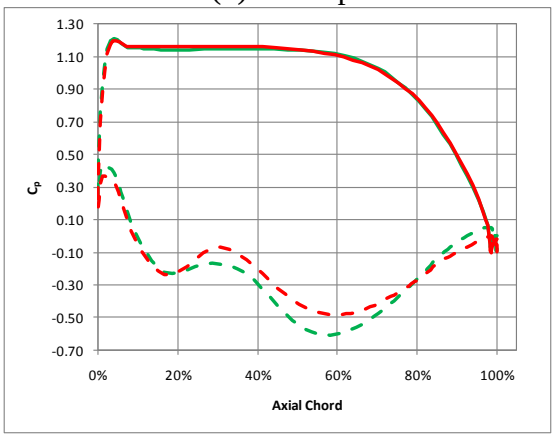

(c) 20% span

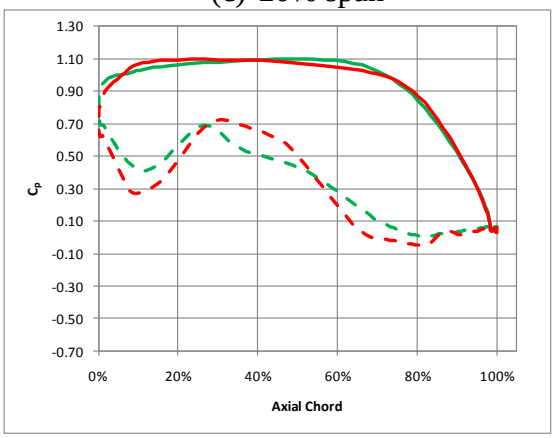

(d) Hub profile

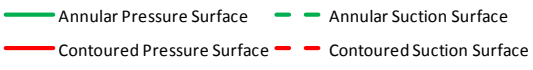

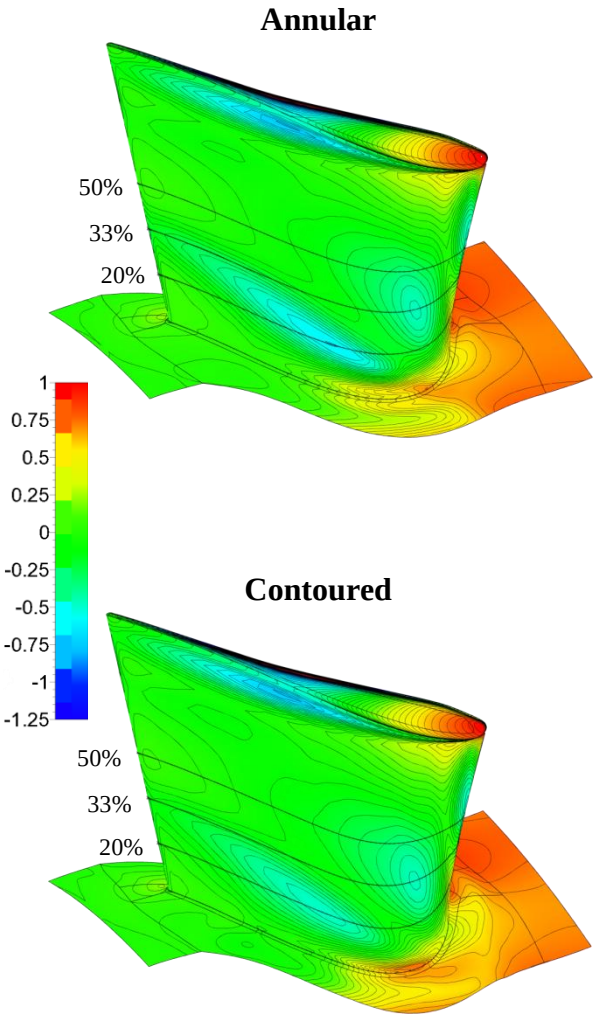

Figure 93: Static pressure coefficient distributions on the blade surface for the design load case (2300 RPM)

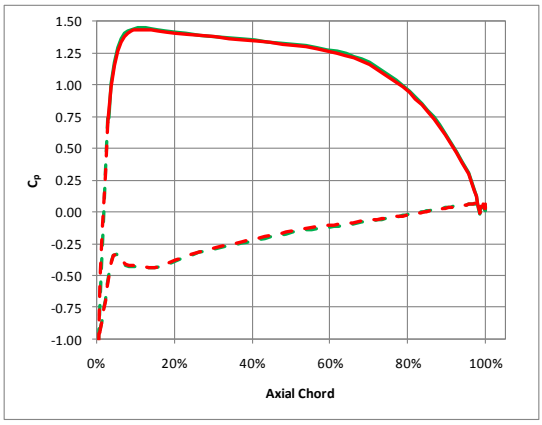

(a) Midspan

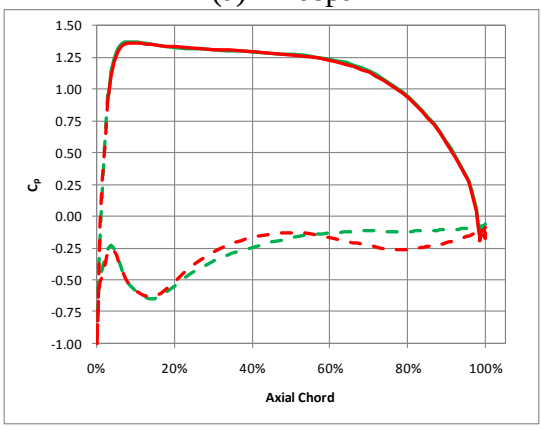

(b) 33% span

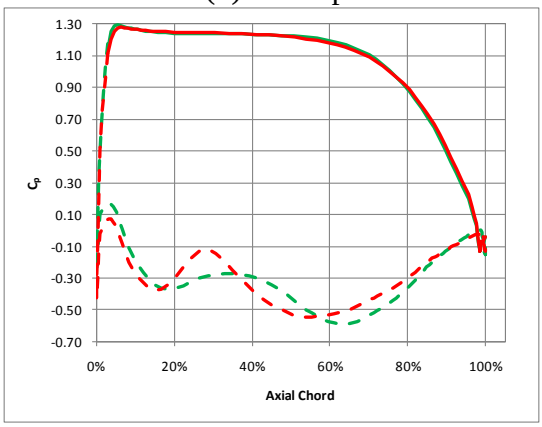

(c) 20% span

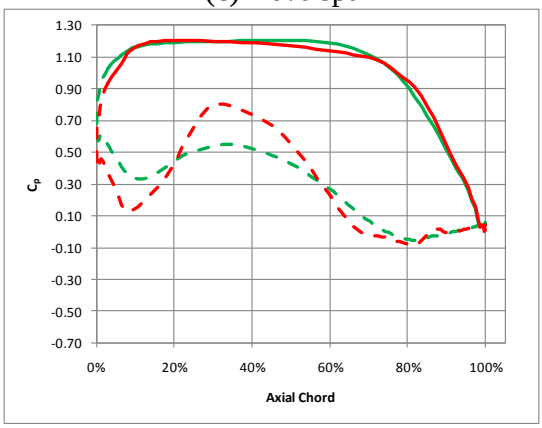

(d) Hub profile

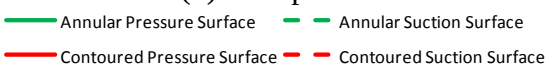

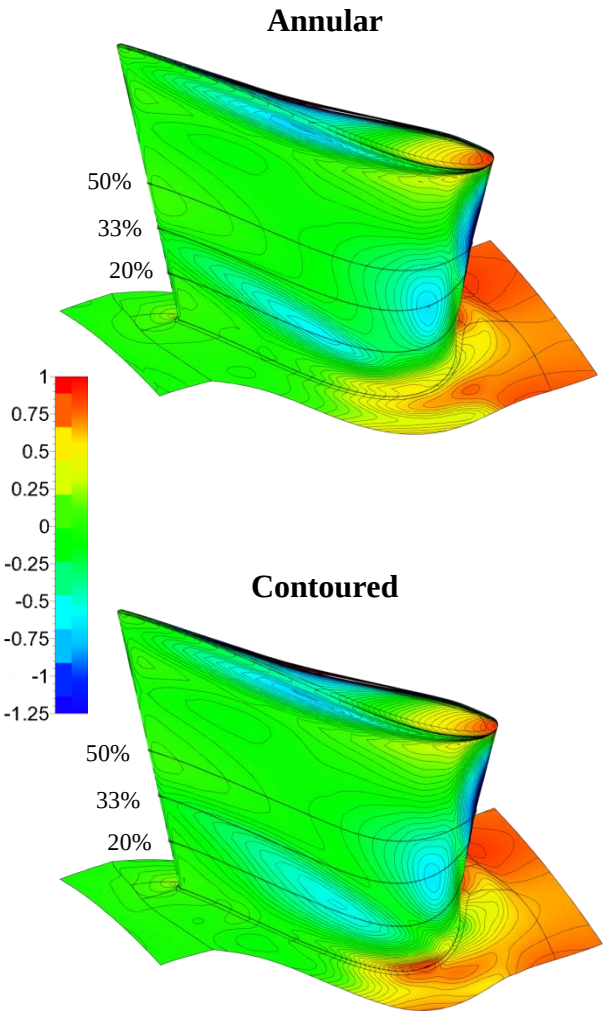

Figure 94: Static pressure coefficient distributions on the blade surface for the highly loaded case (1907 RPM)

6.1.4 Passage

The figures (Figures 95 to 106) which follow should be studied as pairs in order to discover the subtle differences in the driving pressures in the rotor passage between the annular and non-axisymmetrically profiled passages. In addition two pressure coefficients are presented, the first is static and is entirely consistent with the previous four figures while the final ones (Figures 101 to 106) are relative total pressure coefficients similar to the rotor loss coefficient.

Careful study of these figures reveals:

- The development of the hub endwall vortex structure can easily be traced through the entire length of the passage in both relative total pressure and static pressure coefficients
- Distinct differences between annular and non-axisymmetric endwall cases are notable in the hub endwall vortex structure throughout the passage, even at plane (a) just upstream of the blade.
    - The differences are most distinctive on planes (c) and (d) which are located in the midchord region
        - In this region the annular endwall cases exhibit a clear circular, detached passage vortex core close to the suction surface, clearly visible from as early as 24% chord
        - The contoured case yields weaker (0.2 $C_{p\ static}$), distorted loss cores, kidney shaped in nature and clearly attached to the blade surface wake or passage cross-flow. Clearly defined vortex structures are only apparent at 84% chord.
    - At the exit plane the hub endwall loss core are clearly less intense and located at marginally highly (5% span) radial positions in the contoured case. The area covered by the vortices in the contoured cases is however larger.
- Small differences in the top third of span are noticeable in the relative total pressure plots and are particularly noticeable at positive incidence (Figures 105 and 106)
    - In the forward part of the passage this is limited to a strong increase in the radial extent of one isoline of pressure coefficient
    - At the exit smaller shifts are visible in the tip region but involve two or three isoline levels.
    - The tip clearance vortex loss core of the highly loaded annular case is clearly at a lower value that its contoured endwall equivalent (2 isolines).

In summary there is clear evidence that the influence of the endwall contouring extends to the casing. By far the greatest effect is however on the hub endwall flows and the strongest evidence of this is to be found at midchord where the blade loading has been shown to be reduced, but is evident over the entire path of the vortex structure. The structure, position and strength of the outlet loss cores are clearly altered as is shown in Figure 107 where the greatest difference between annular and contoured configurations is seen to be the consistency of the contoured cases versus the larger variation in the annular load cases.

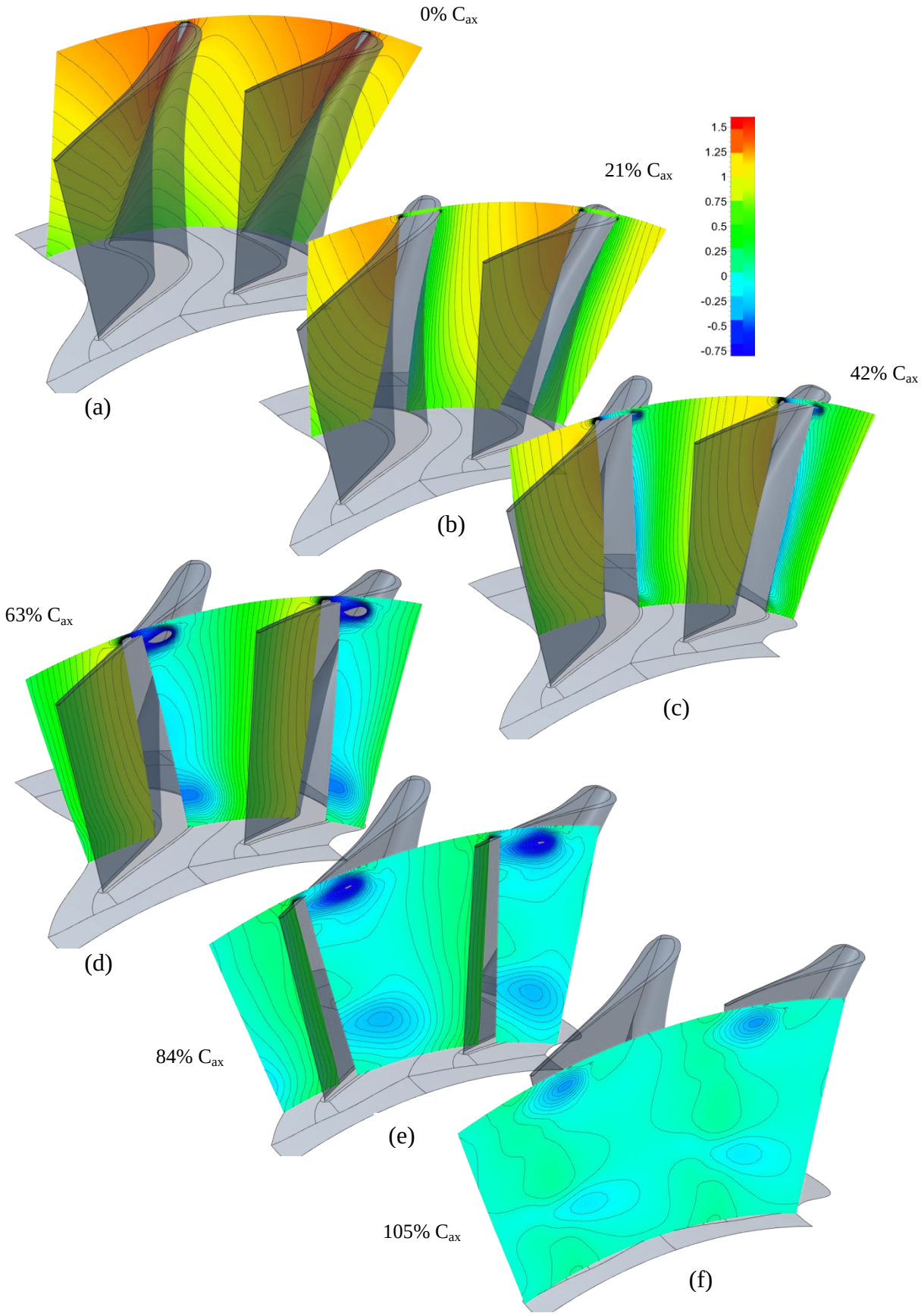

Figure 95: Static pressure coefficient at various planes through the rotor passage for the annular lightly loaded (-5° incidence) case

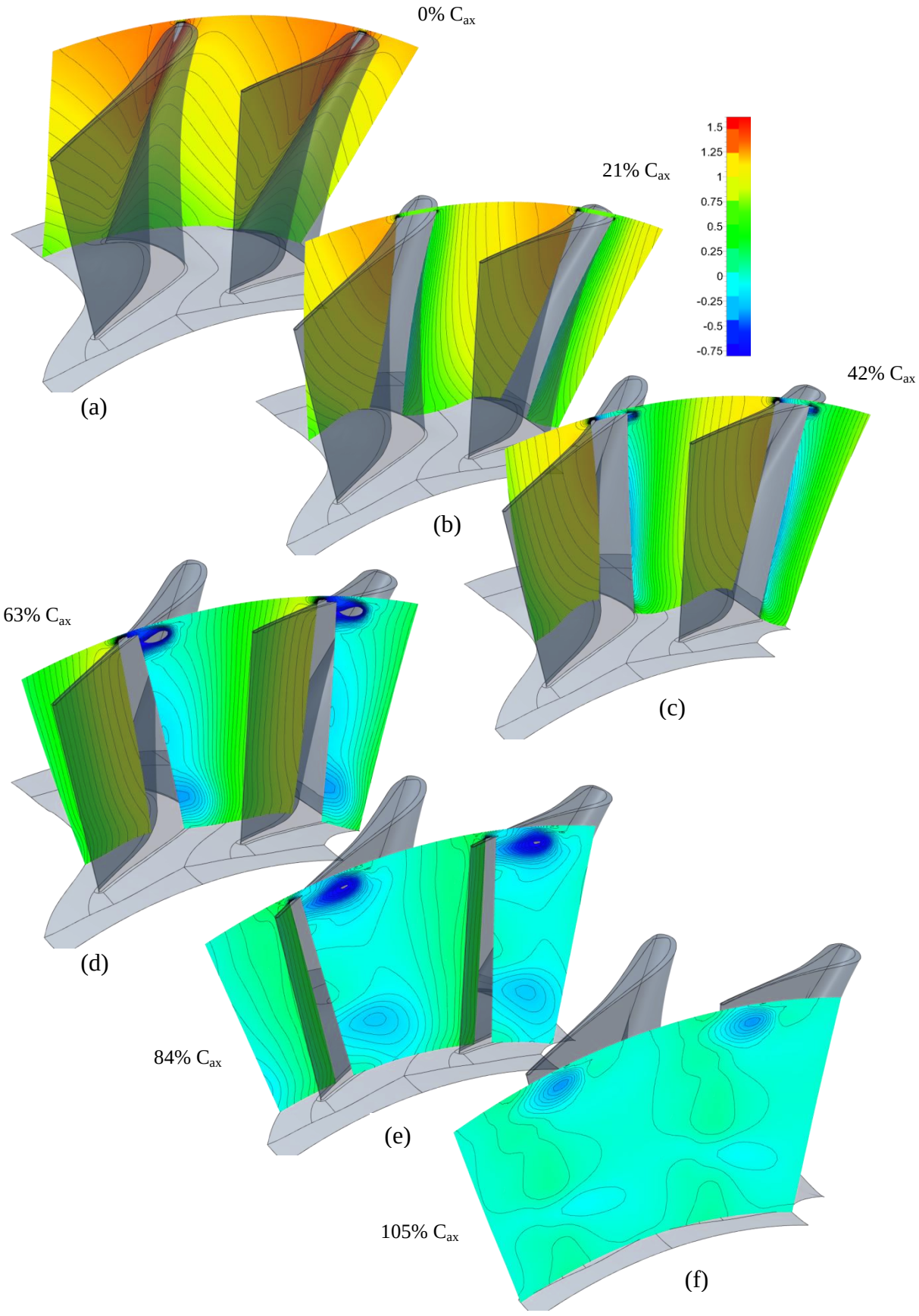

Figure 96: Static pressure coefficient at various planes through the rotor passage for the contoured lightly loaded (-5° incidence) case

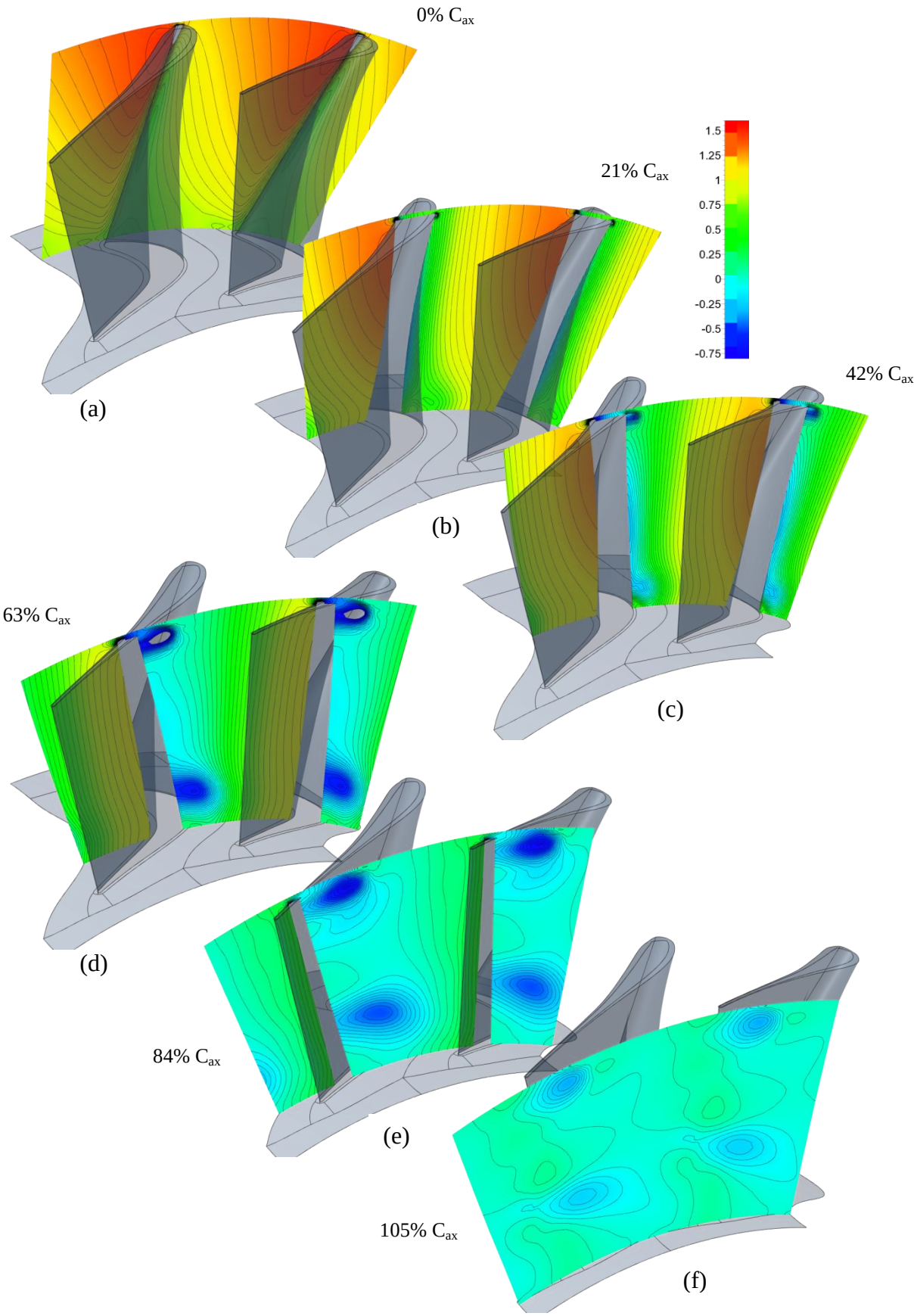

Figure 97: Static pressure coefficient at various planes through the rotor passage for the annular design case

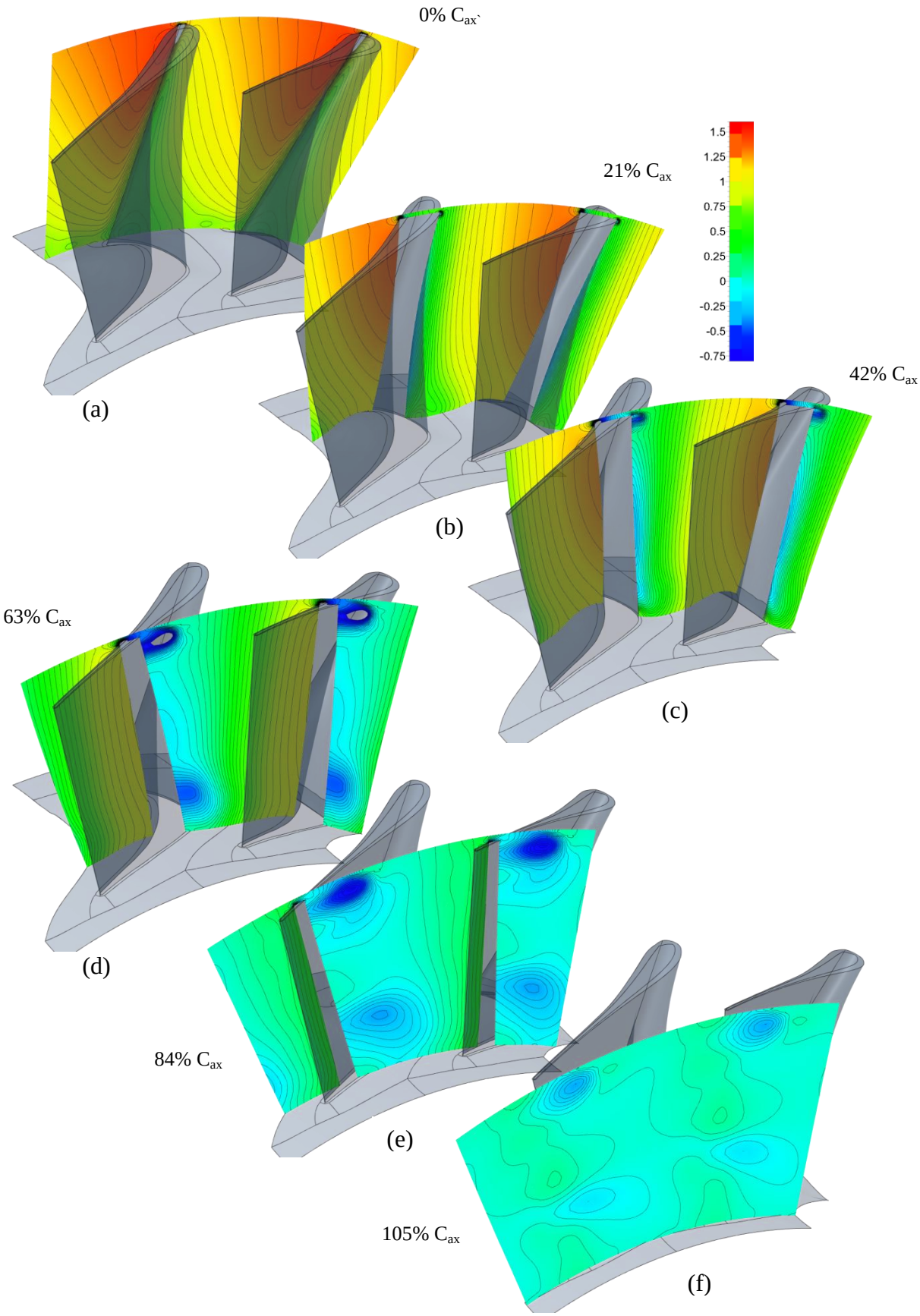

Figure 98: Static pressure coefficient at various planes through the rotor passage for the contoured design case

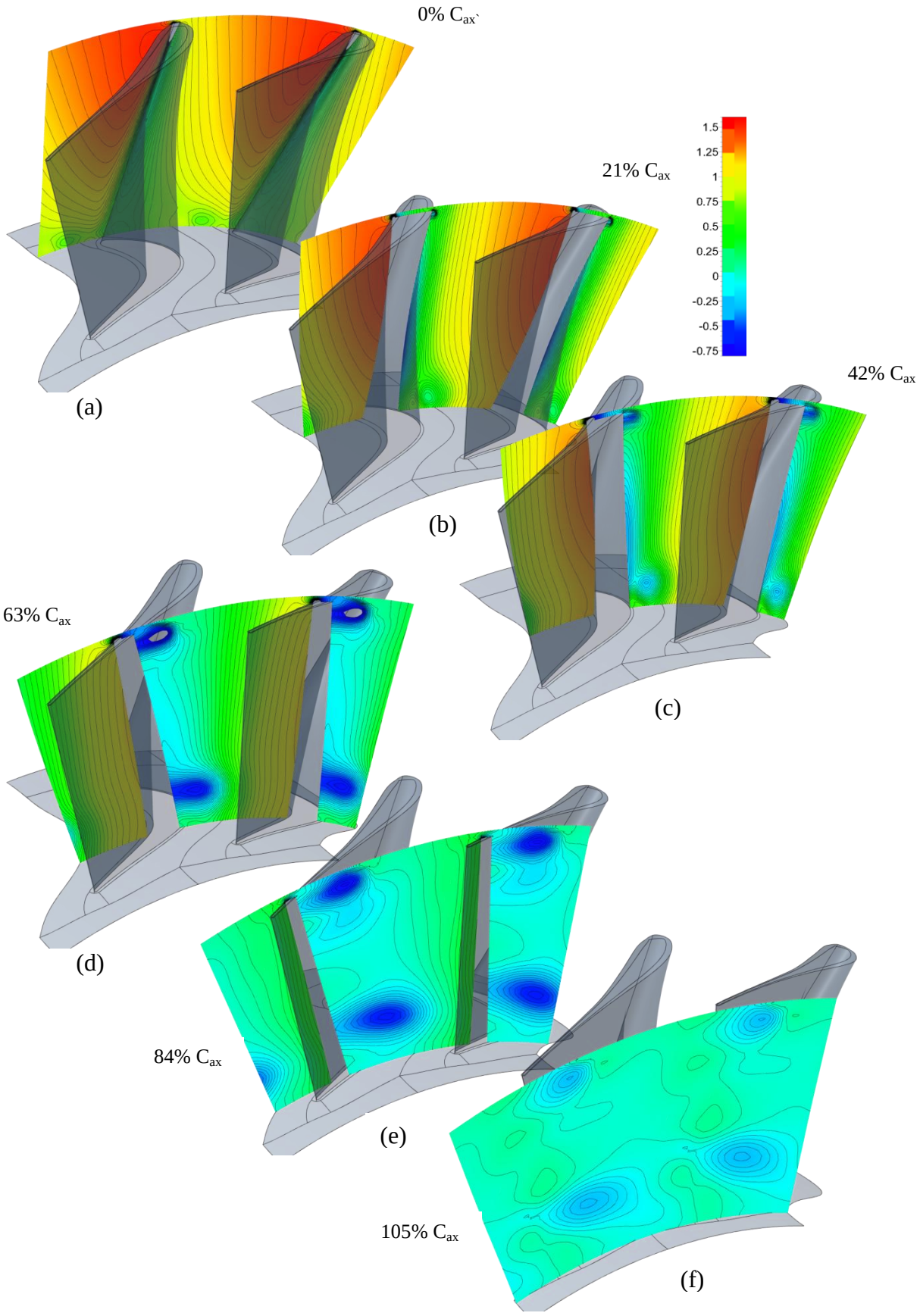

Figure 99: Static pressure coefficient at various planes through the rotor passage for the annular highly loaded (+5° incidence) case

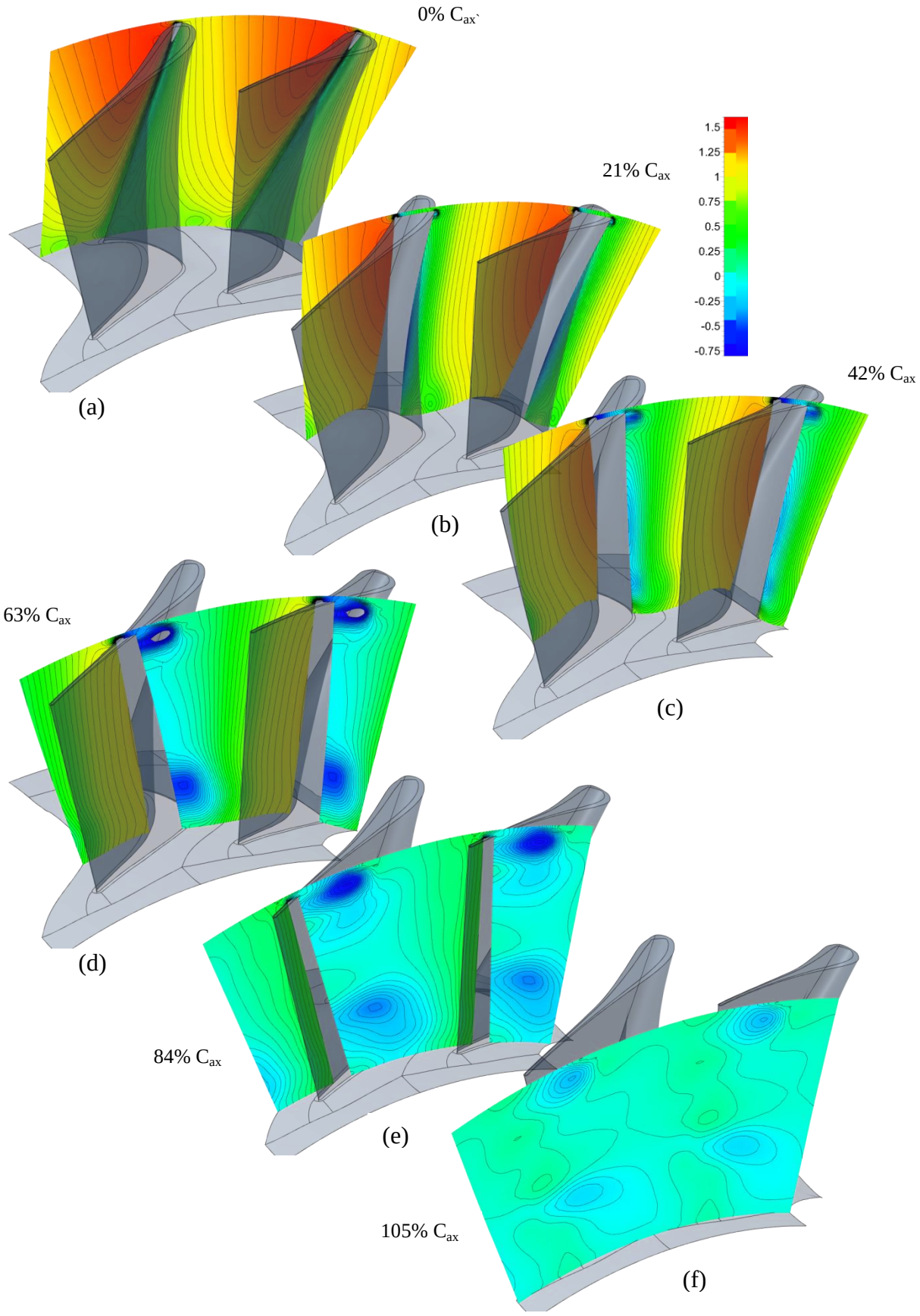

Figure 100: Static pressure coefficient at various planes through the rotor passage for the contoured highly loaded (+5° incidence) case

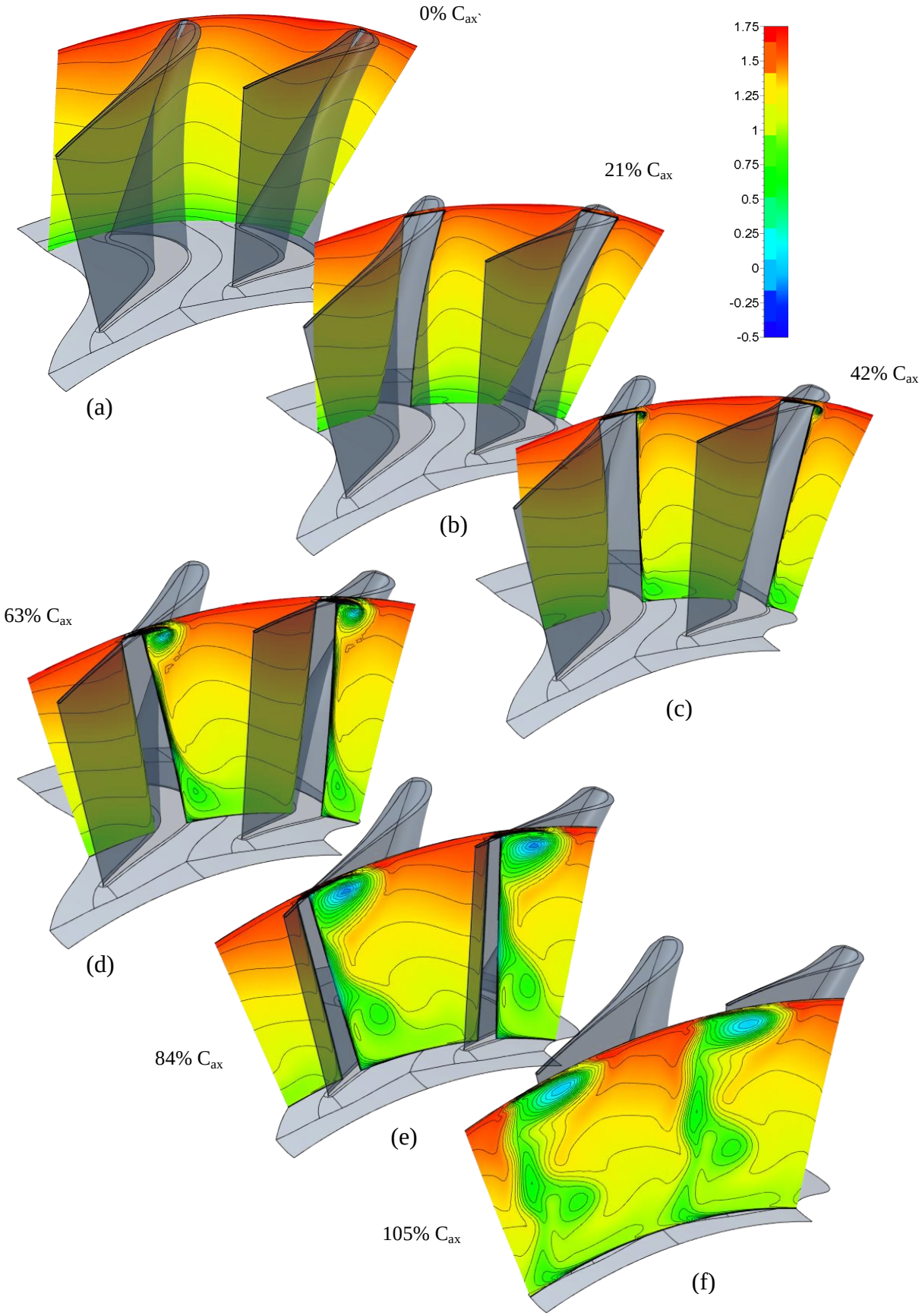

Figure 101: Relative total pressure coefficient at various planes through the rotor passage for the annular lightly loaded (-5° incidence) case

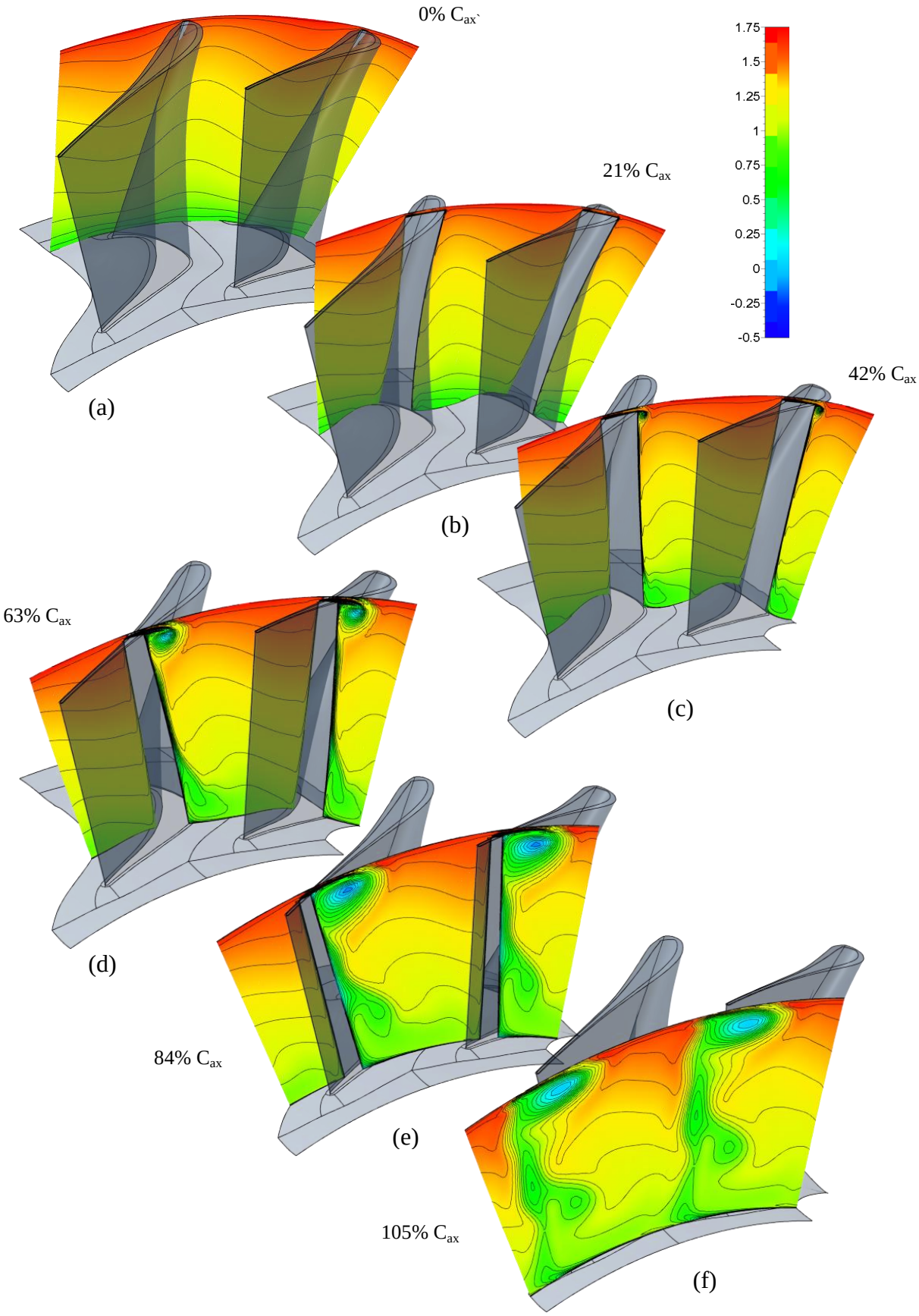

Figure 102: Relative total pressure coefficient at various planes through the rotor passage for the contoured lightly loaded (-5° incidence) case

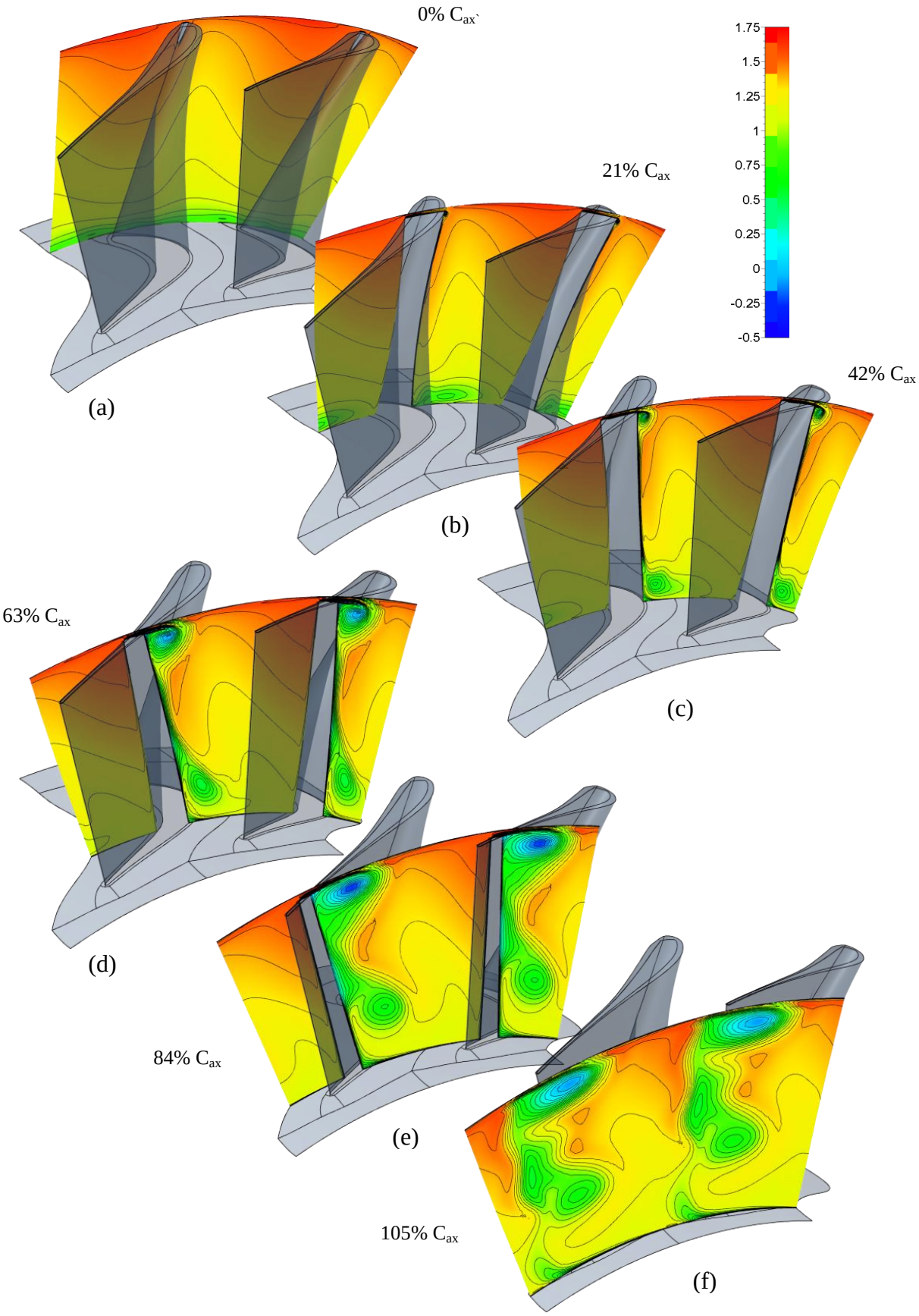

Figure 103: Relative total pressure coefficient at various planes through the rotor passage for the annular design case

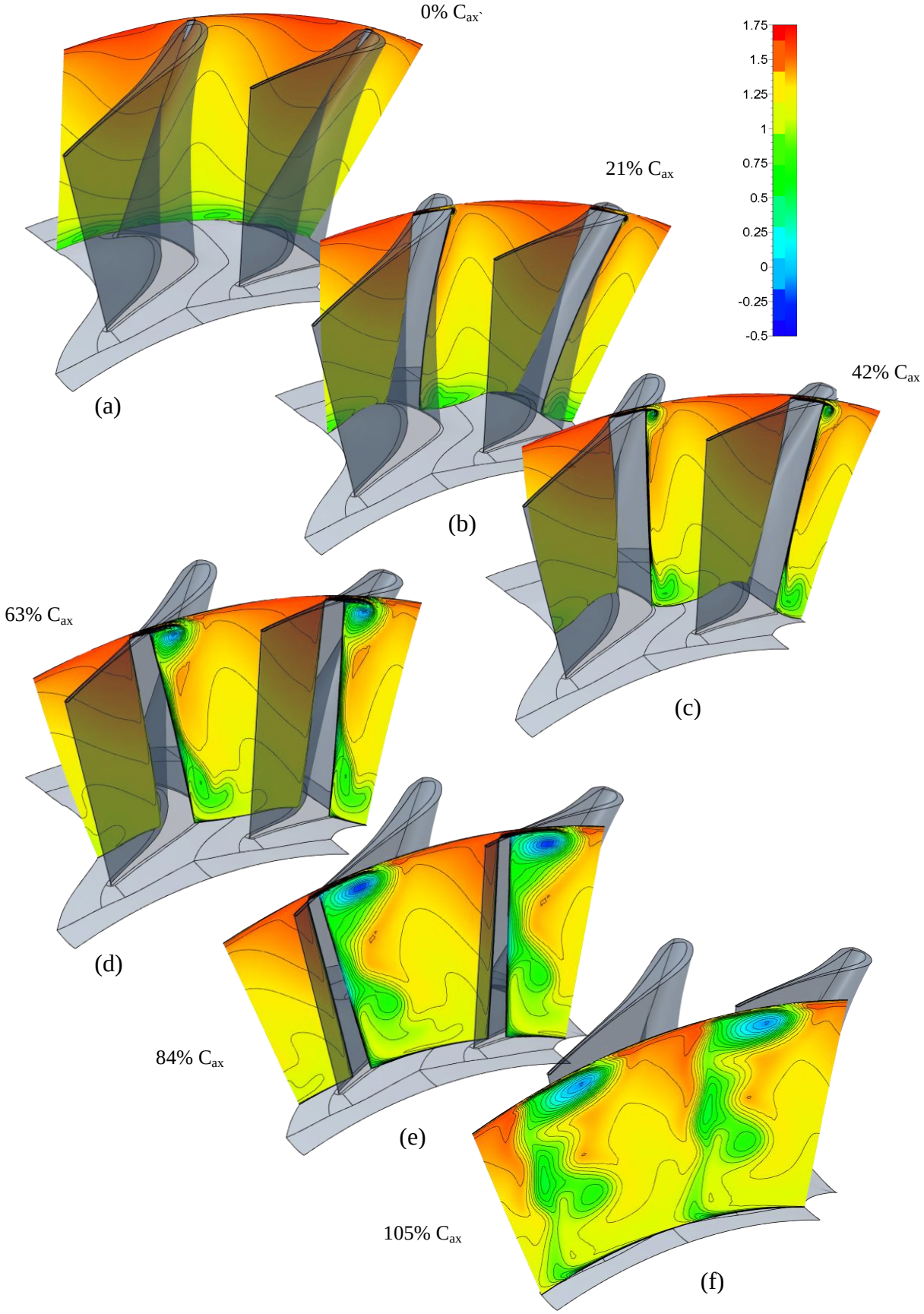

Figure 104: Relative total pressure coefficient at various planes through the rotor passage for the contoured design case

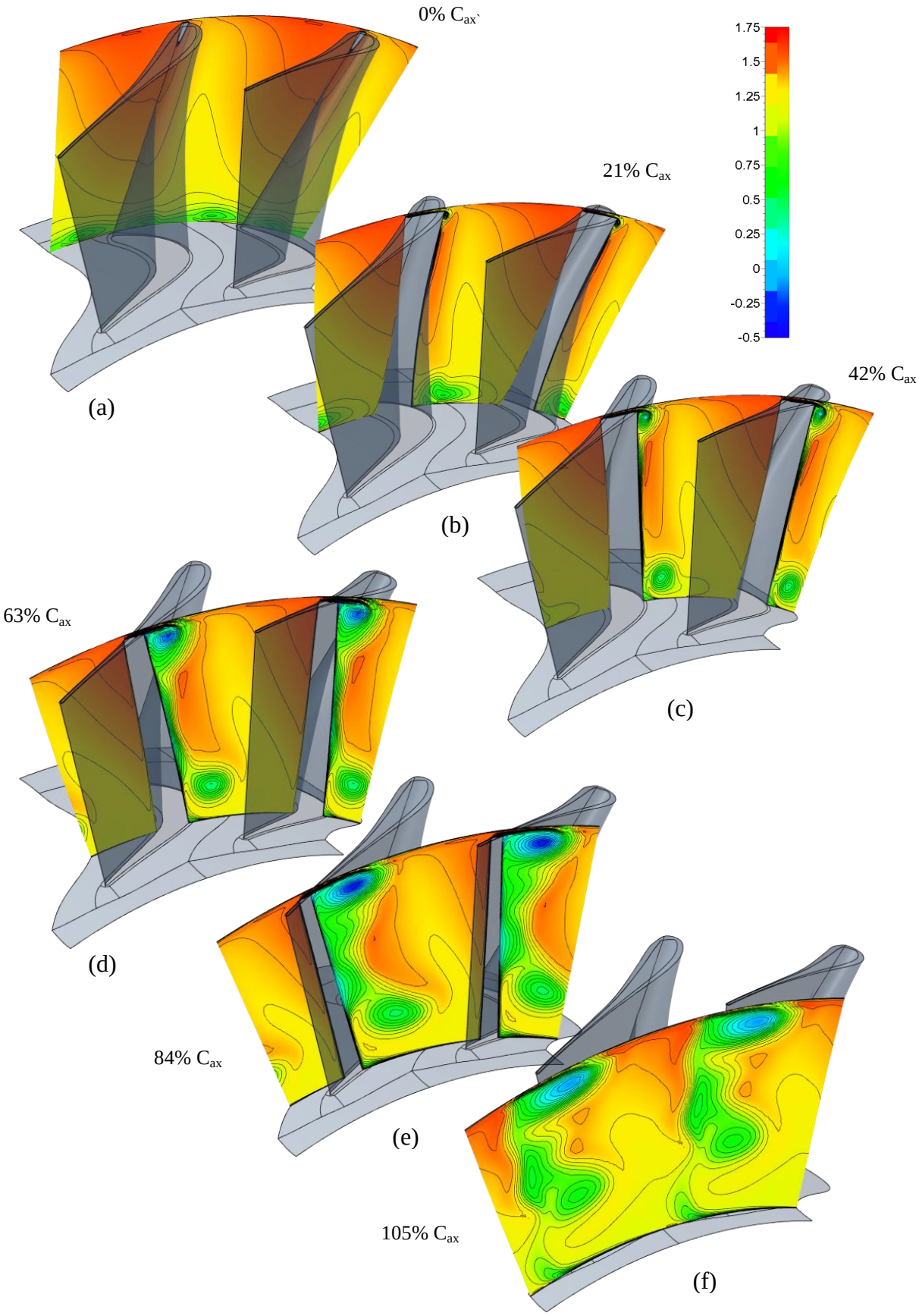

Figure 105: Relative total pressure coefficient at various planes through the rotor passage for the annular highly loaded (+5° incidence) case

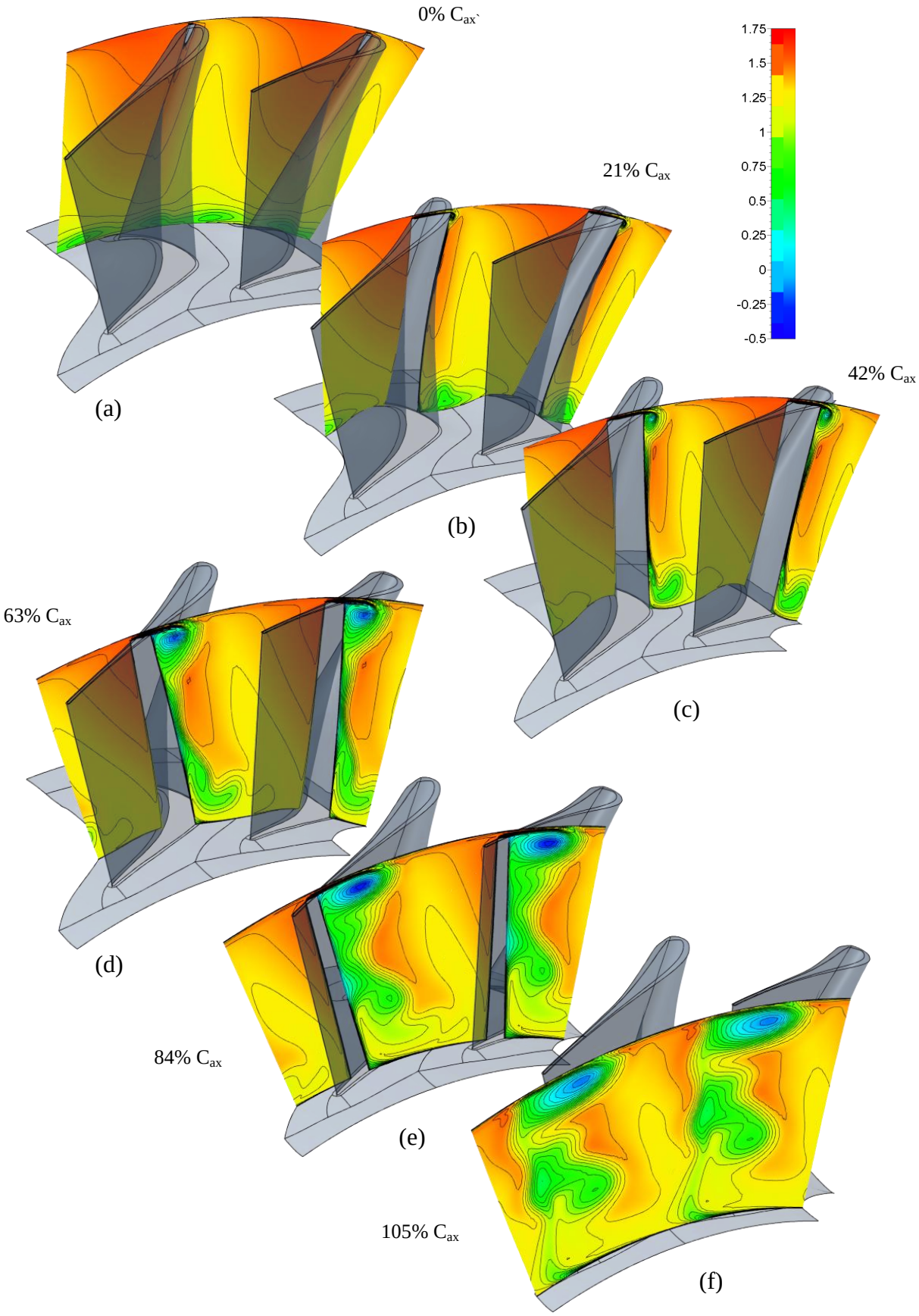

Figure 106: Relative total pressure coefficient at various planes through the rotor passage for the contoured highly loaded (+5° incidence) case

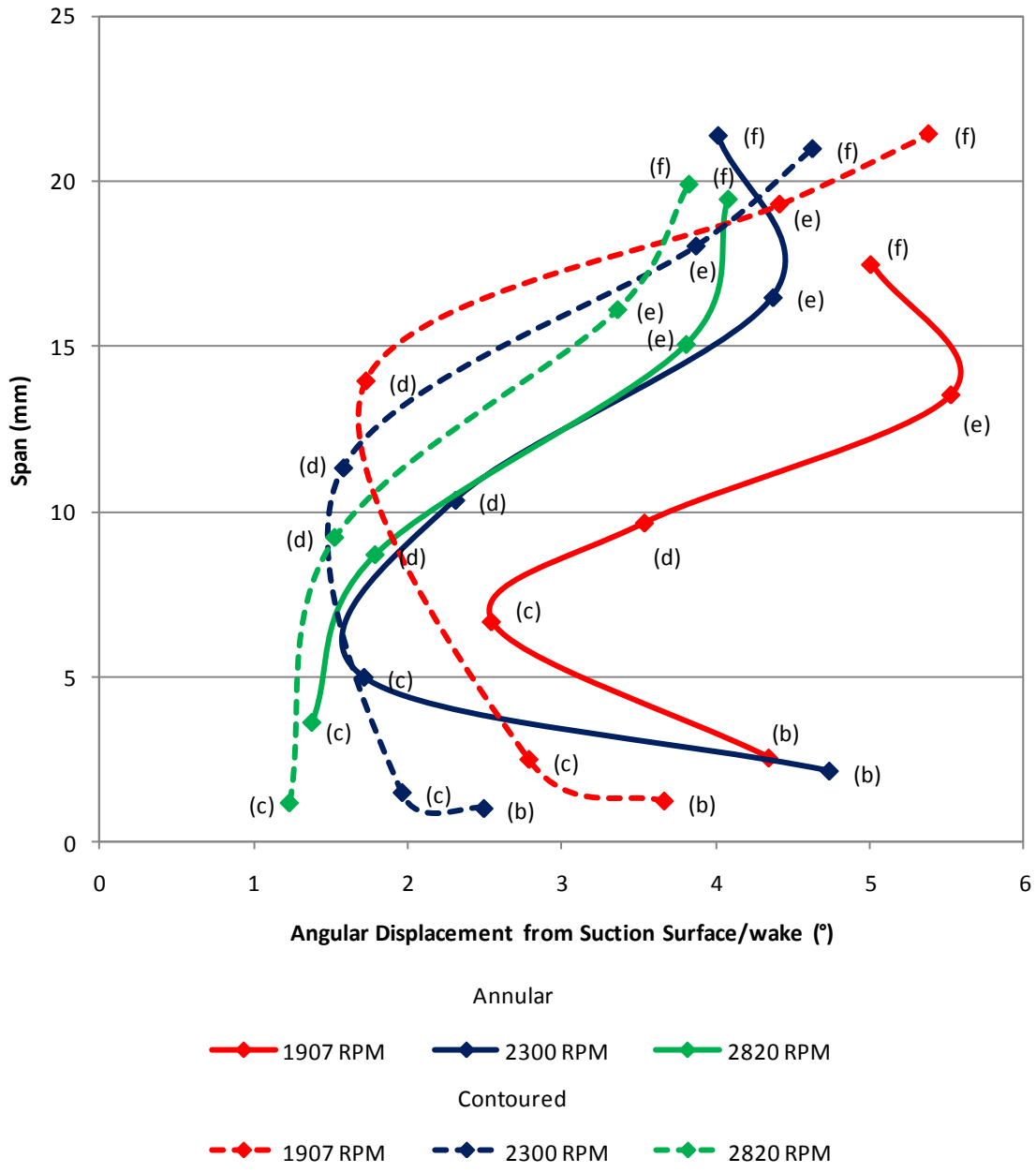

Figure 107: Summary of passage vortex movement (letters correspond to those for the planes used in Figure 106)

6.2 Three dimensional flow structures

Figures 108 to 110 below show the vortex structure in the flow at varying incidence, with and without contouring. The different tubes, ribbons and lines are identified by colour as follows:

- Red stream tubes – pressure side horseshoe vortex
- Blue stream tubes – suction side horseshoe vortex
- Grey ribbons – endwall crossflow and passage vortex
- Yellow ribbons – tip endwall horseshoe vortices
- Orange ribbons – tip clearance vortex
- Purple stream lines – blade suction surface flow.

The starting positions for streamlines were chosen to highlight the vortex structures, but is entirely consistent between cases with the exception of the following:

- The tangential start and end locations for the different legs of the horseshoe vortex which was altered both for the different speed cases and for the change in endwall
- The chordwise location of the initiation points of tip clearance vortices which were varied between the speed cases only to capture the breakpoint between the tip endwall horseshoe vortex the pressure leg of which is pulled through the tip gap, and the pure tip gap leakage flow downstream.

The combination of suction and pressure legs of the horseshoe vortex are quite different between endwalls, with the annular cases generally reflecting close wrapping of the two systems, while the contouring appears to hold the suction leg closer to the endwall and only entraining into the pressure leg as it leaves the passage. Roughly one rotation of the suction leg of the horseshoe vortex occurs through the length of the passage in the profiled case at design while the equivalent annular case exhibits 1½ to 2 turns. This results in a widely spread vortex system at the exit to the row in the profiled case; compared to an intense and localised one for the annular case.

The grey cross passage flow streamlines changes angle with increasing load, becoming more tangential. This occurs in both annular and profiled cases, however the profiled cases exhibit more axial flow in the front of the passage for all cases which is entirely consistent with the endwall pressure contour results. The cross passage flow then interacts quite differently with the combined horseshoe vortices between the different endwall cases in a way which becomes more noticeable with increasing incidence. In the annular case the cross passage flow is immediately wrapped up in the horseshoe vortices. While in the profiled case the flow crosses the passage and is swept up the suction surface before wrapping around the pressure leg of the horseshoe vortex.

In all cases the blade surface flows, are also entrained into the vortex system in the latter half of the passage and as they are loosely wrapped form pools of highly turned flow as filaments are spun out of the vortex core.

The exception to this is the lightly loaded case where the passage cross flow and pressure side leg of the horseshoe vortex appear to interact in such a way as to cause the breakup of the horseshoe vortex in the annular case.

The hub endwall flows consistently climb into the passage earlier and higher and exit the passage at marginally higher spans in the presence of endwall profiling.

The tip clearance flows are almost identical between cases with one almost imperceptible difference in that the yellow ribbons exhibit slightly more turning in the annular case, particularly at the highest incidence.

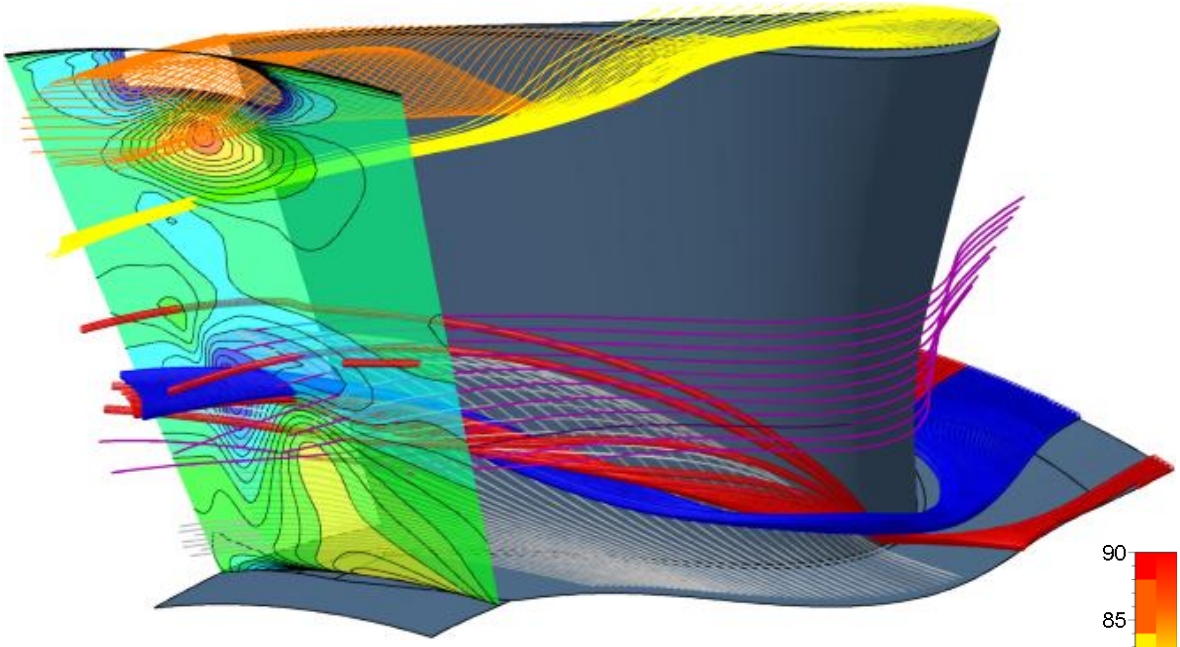

(a) Annular

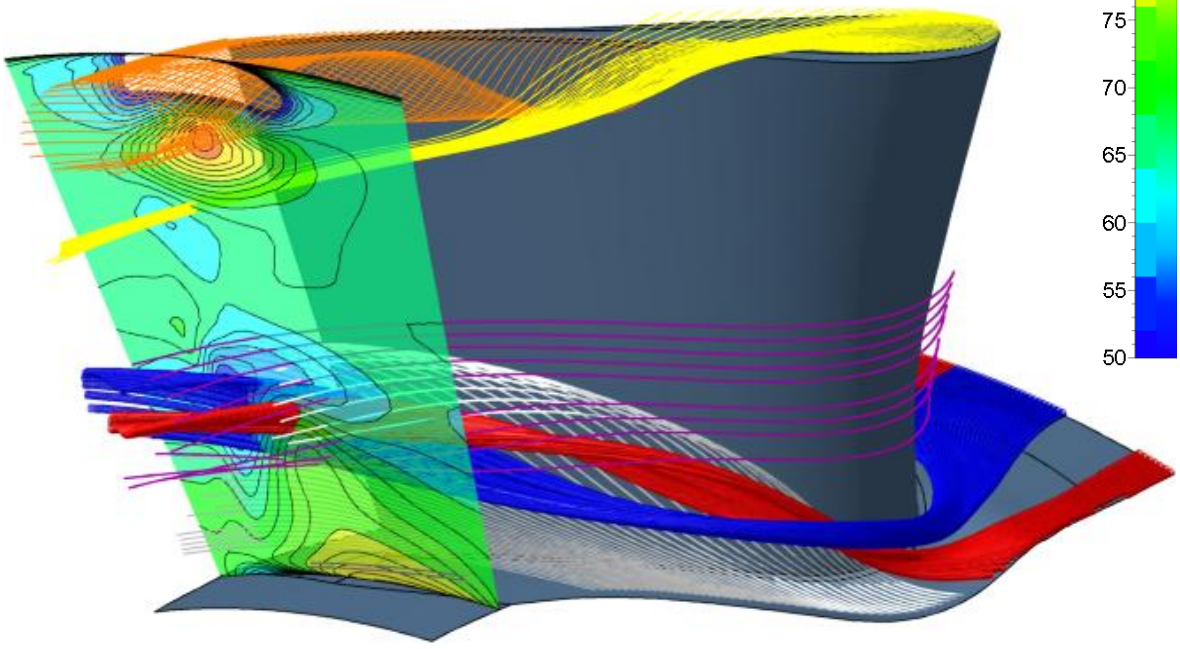

(b) Contoured

Figure 108: Secondary flow streamlines for the lightly loaded -5° incidence case with rotor relative exit flow angle contours shown on the exit plane

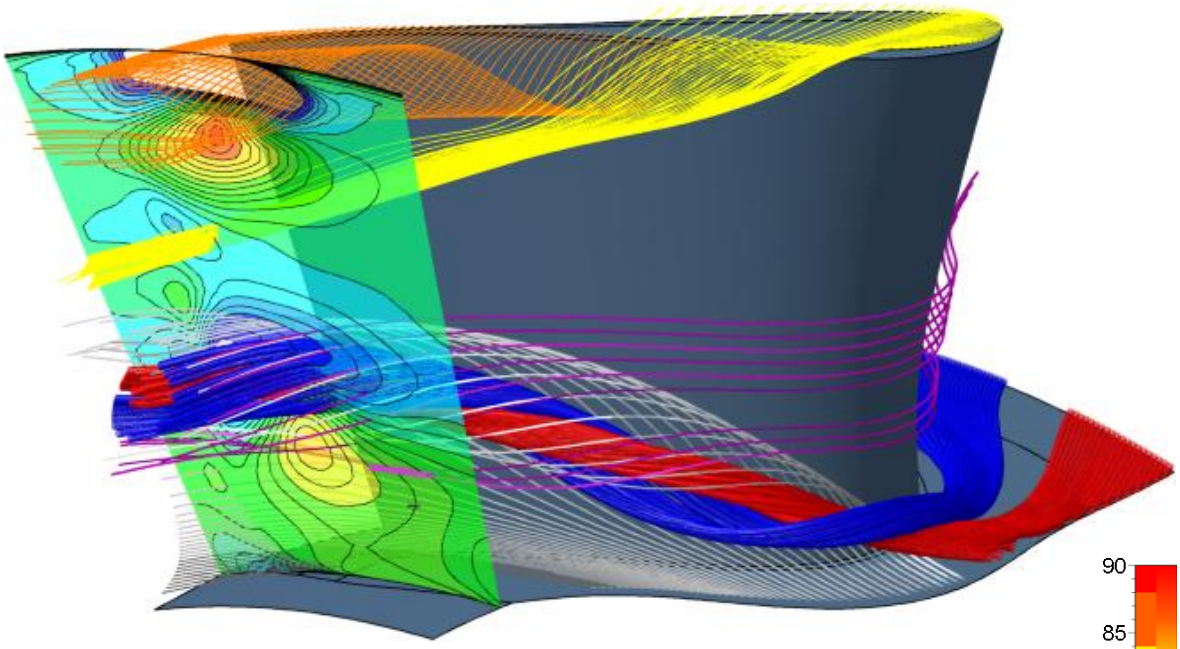

(a) Annular

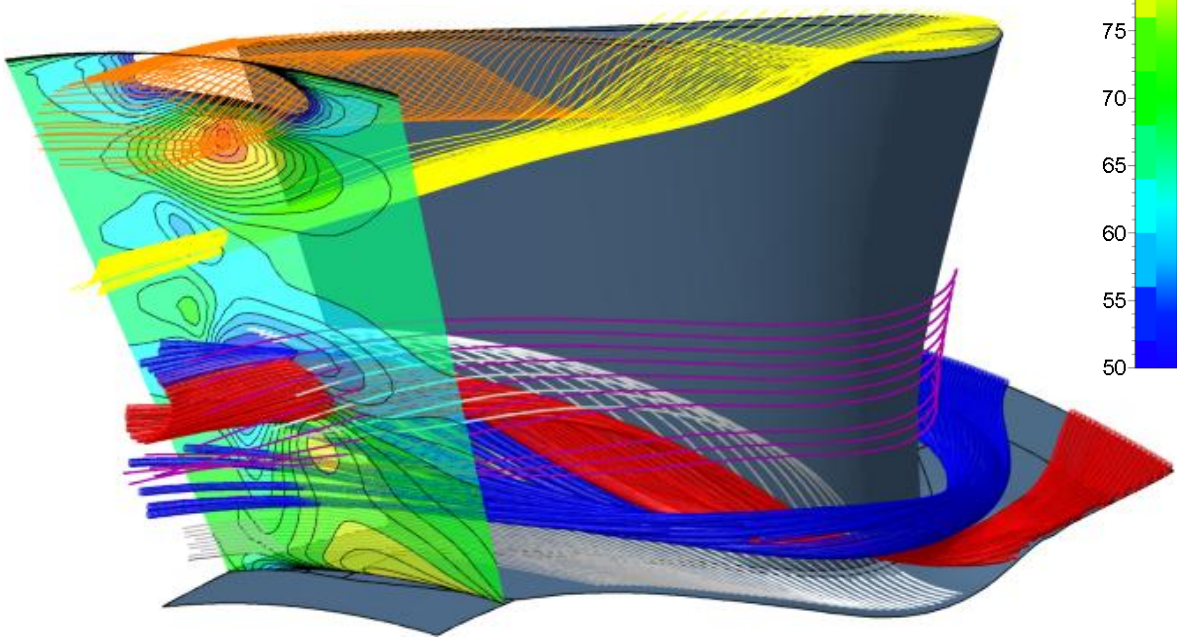

(b) Contoured

Figure 109: Secondary flow streamlines for the design case with rotor relative exit flow angle contours shown on the exit plane

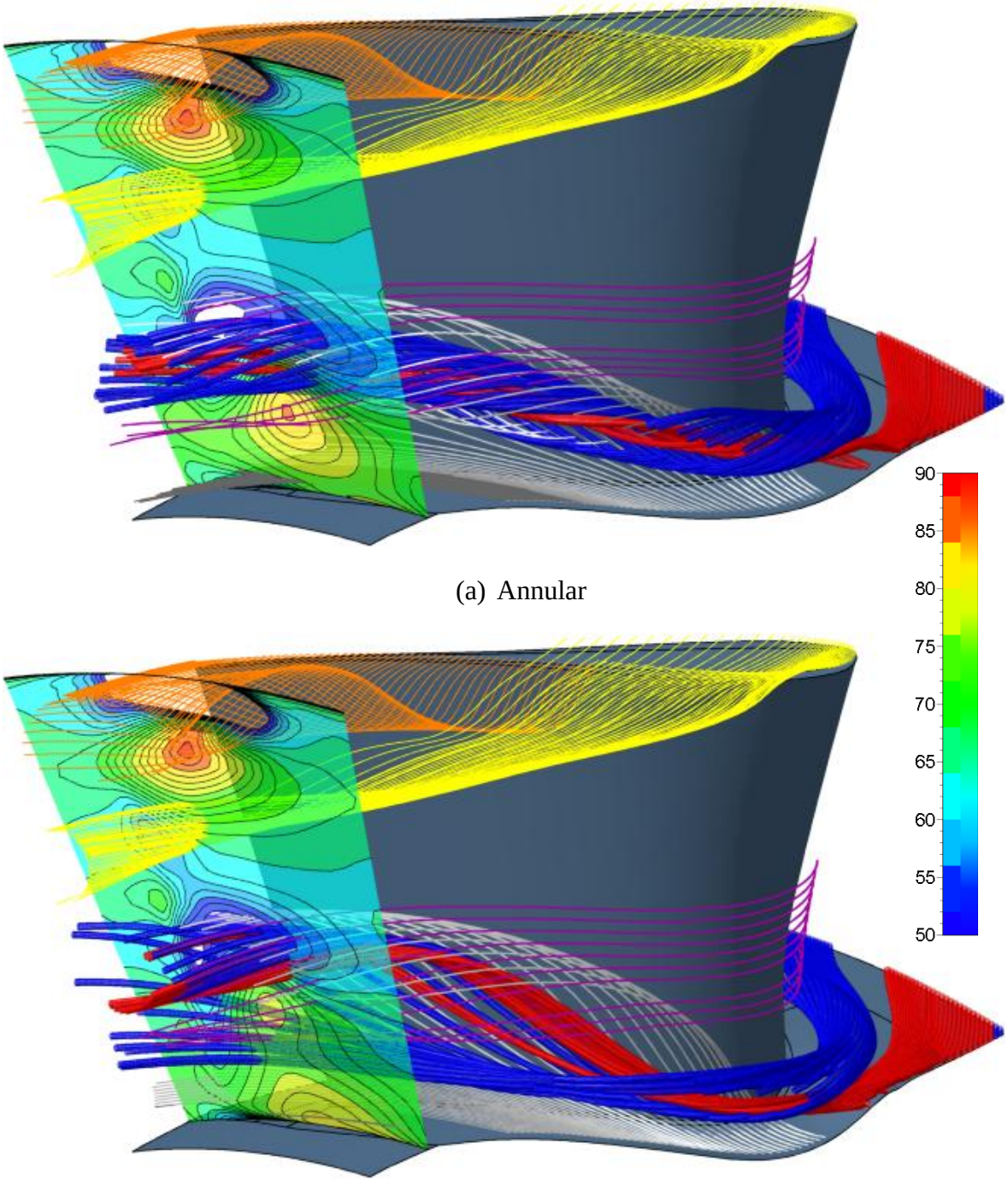

(a) Annular

(b) Contoured

Figure 110: Secondary flow streamlines for the highly loaded +5° incidence case with rotor relative exit flow angle contours shown on the exit plane

Figures 111 to 113 provide greater insight into the initiation of the endwall vortex structures by providing a zoomed in view of the front of the passage for each case and for clarity the horseshoe vortex streamtubes have been limited to just 2 streamtubes per leg. Pressure coefficient contours and isolines (the same as those found in Figure 91) are also plotted for reference.

Probably the most striking feature of these three sets of figures is the lack of clear trends in the development of the vortex structures as the load varies for either endwall. The following statements are however consistently true for the contoured versus annular endwalls:

- The pressure gradient across the passage is slightly reduced (3 isolines) by the introduction of the endwall profiling and the shape and distribution of the isolines clearly altered.
- The introduction of the contoured endwalls sees a clear shift in the cross passage streamlines towards the rear of the passage and as a result the reinforcement of what appears to be the corner vortex. In the front of the passage the contoured endwalls are extremely sparsely populated with streamlines despite the consistent location of their initiation points.

The corner vortex in the junction between the pressure surface and the endwall appears to emanate from the peak pressure point in this junction and is clearly much stronger and separated from the pressure surface in the profiled endwall case. In the lightly loaded case however there are distinct differences in the endwall cross flow. Firstly the annular case exhibits a strong cross passage flow just behind the horseshoe vortices which appears to join the two horseshoe vortices at the same point at which they themselves met. In the profiled endwall case however this is delayed until much later in the passage and it appears as if the corner vortex bifurcates with the first component crossing the passage tangentially. The other significant difference is in the lightly loaded cases is the lack of a rotational component to the streamtubes used to indicate horseshoe vortices in the annular case, while rotation is clearly present in the profiled case.

At design and increased incidence there is a strong component of low momentum fluid from the cross passage streamlines which actually moves around the leading edge from pressure to suction side joining the suction side leg of the horseshoe vortex.

Looking at the rotational component of the horseshoe vortices there is a strongly increasing trend in those for the annular case, while those for the contoured case exhibit a clear increase (0 versus 1 rotation across the width of the passage) between the lightly loaded and design case, but the characteristic of the pressure leg of the vortex changes as load is increased further rather than there being an increase in the vortex diameter.

The angle at which the pressure side leg of the vortex crosses the passage is almost constant with increasing load, and endwall geometry.

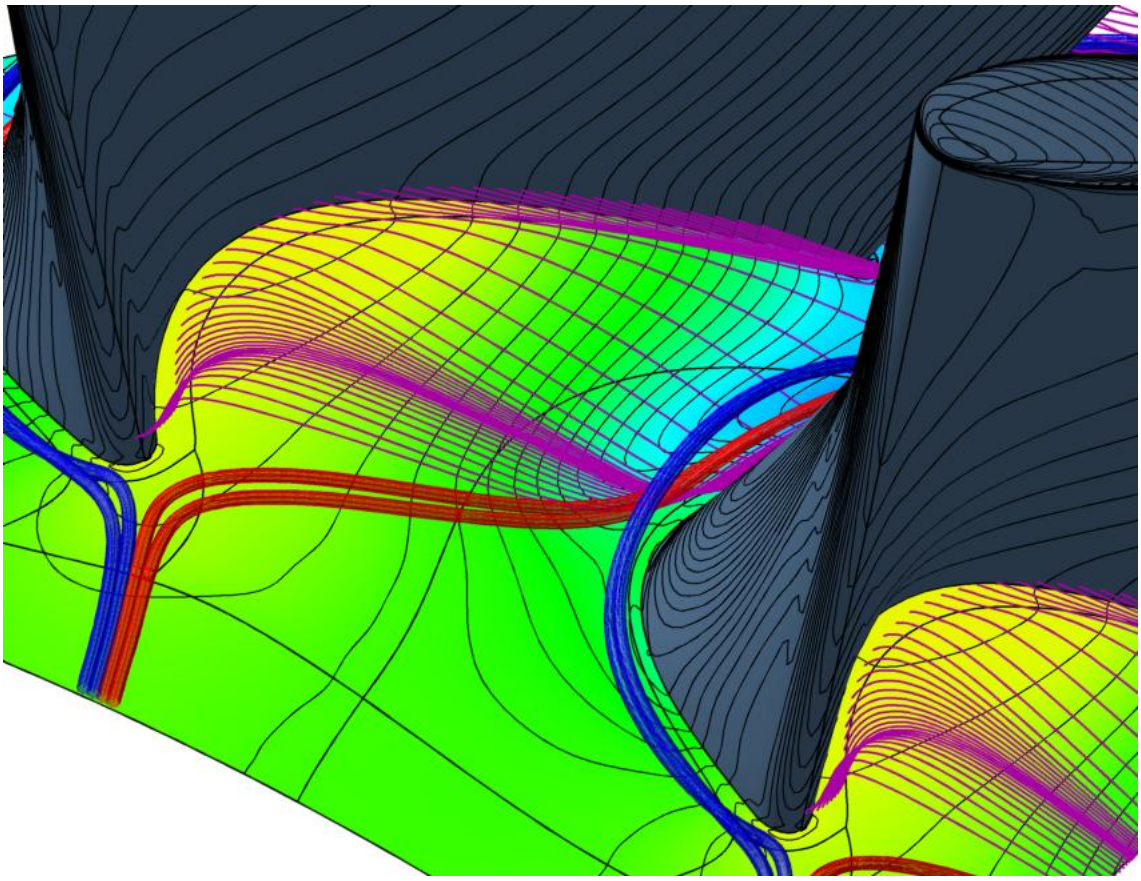

(a) Annular

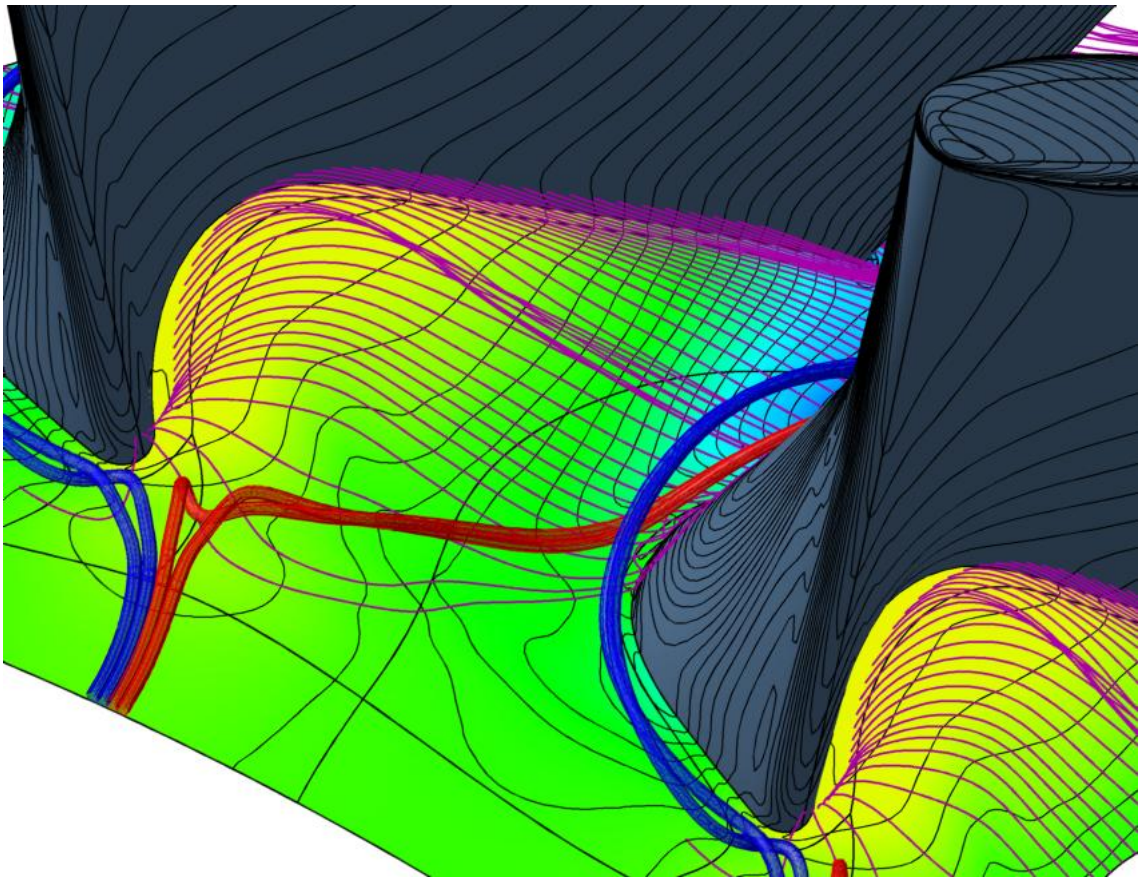

(b) Contoured

Figure 111: Endwall streamlines and oil flow for the lightly loaded -5° incidence case (pressure contours are identical to those of Figure 91)

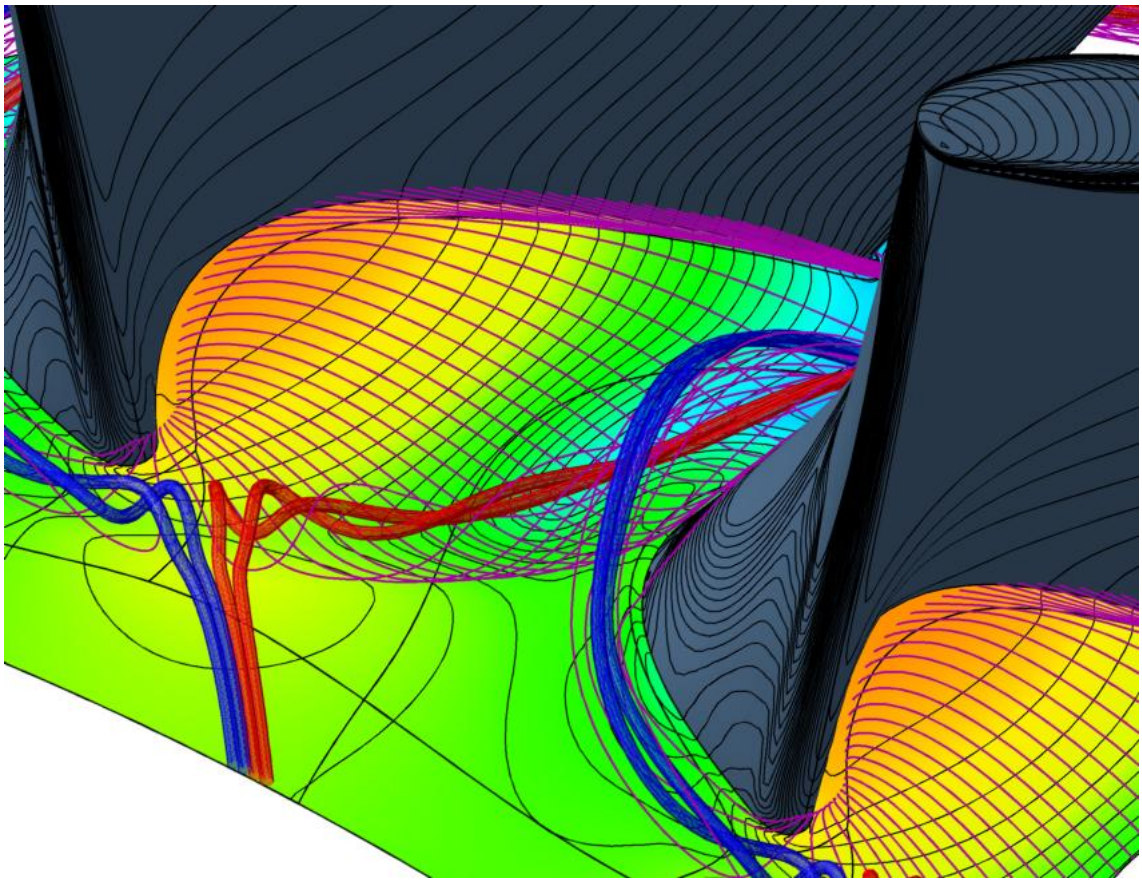

(a) Annular

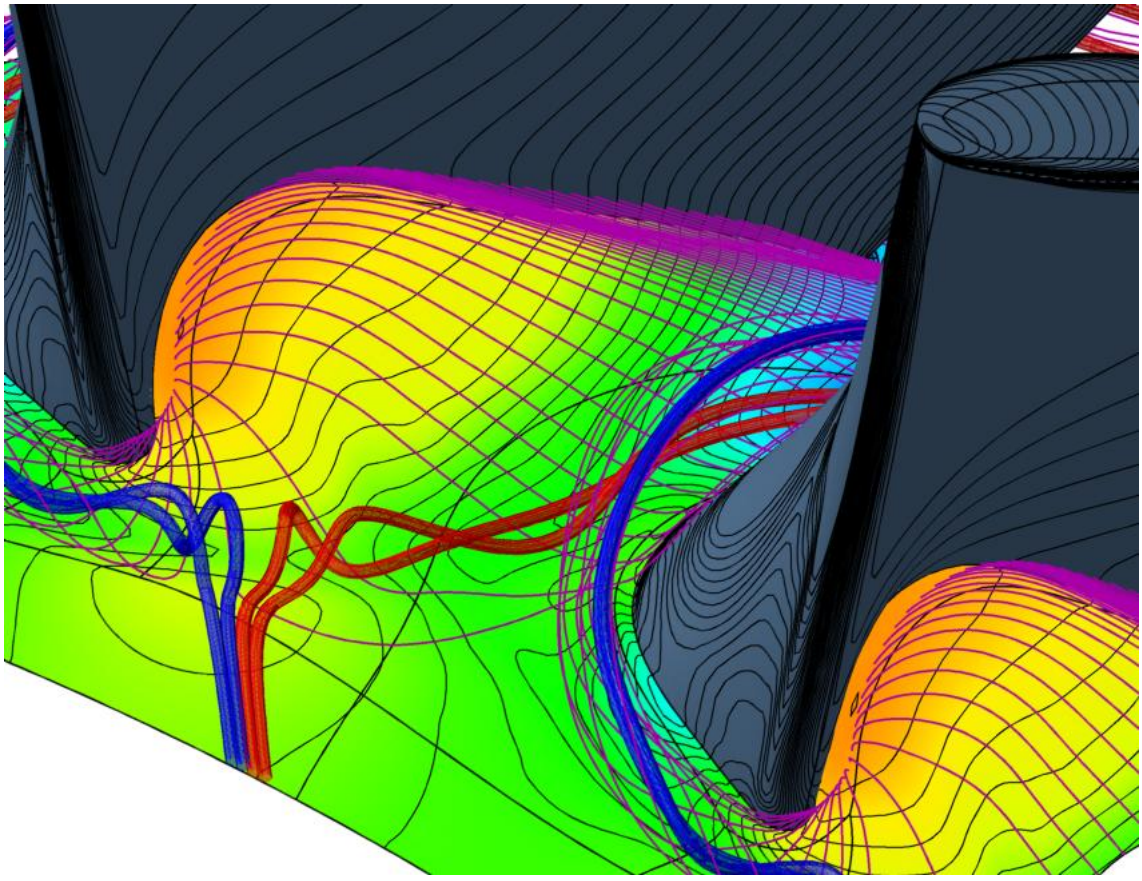

(b) Contoured

Figure 112: Endwall streamlines and oil flow for the design case (pressure contours are identical to those of Figure 91)

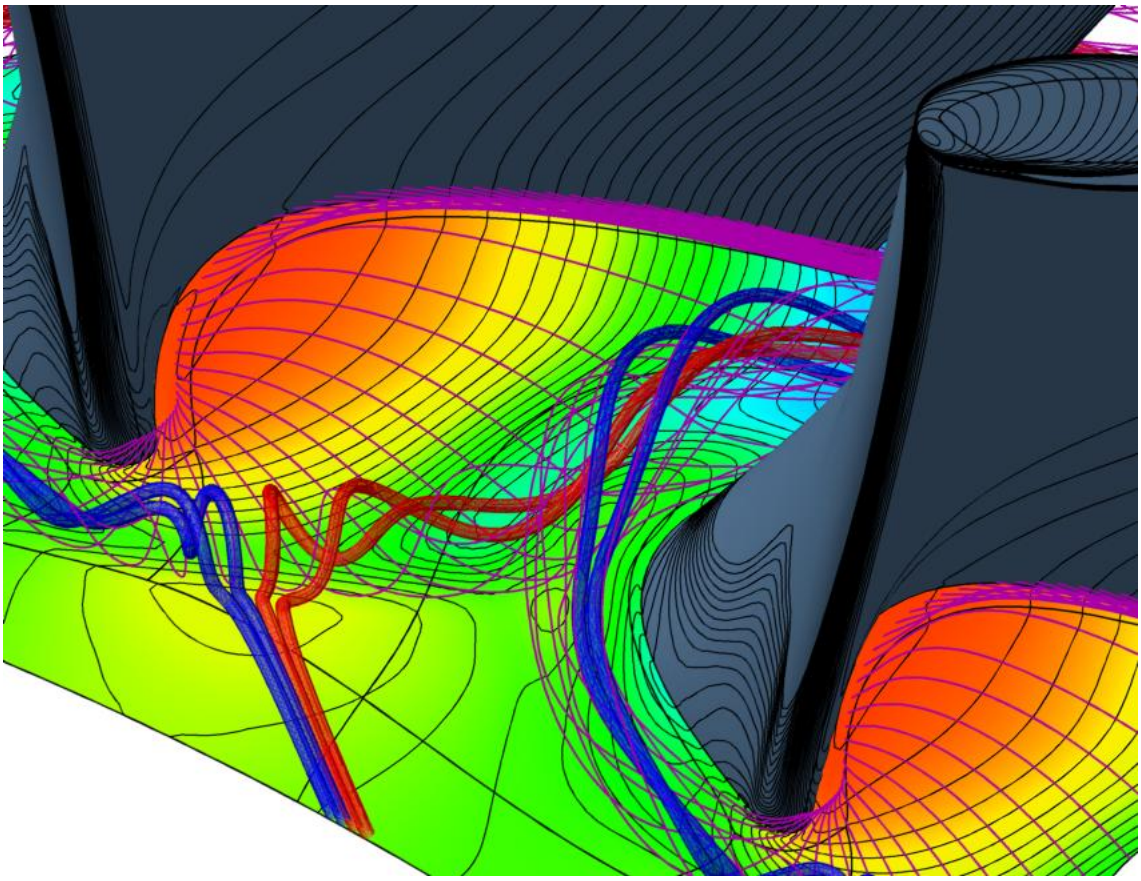

(a) Annular

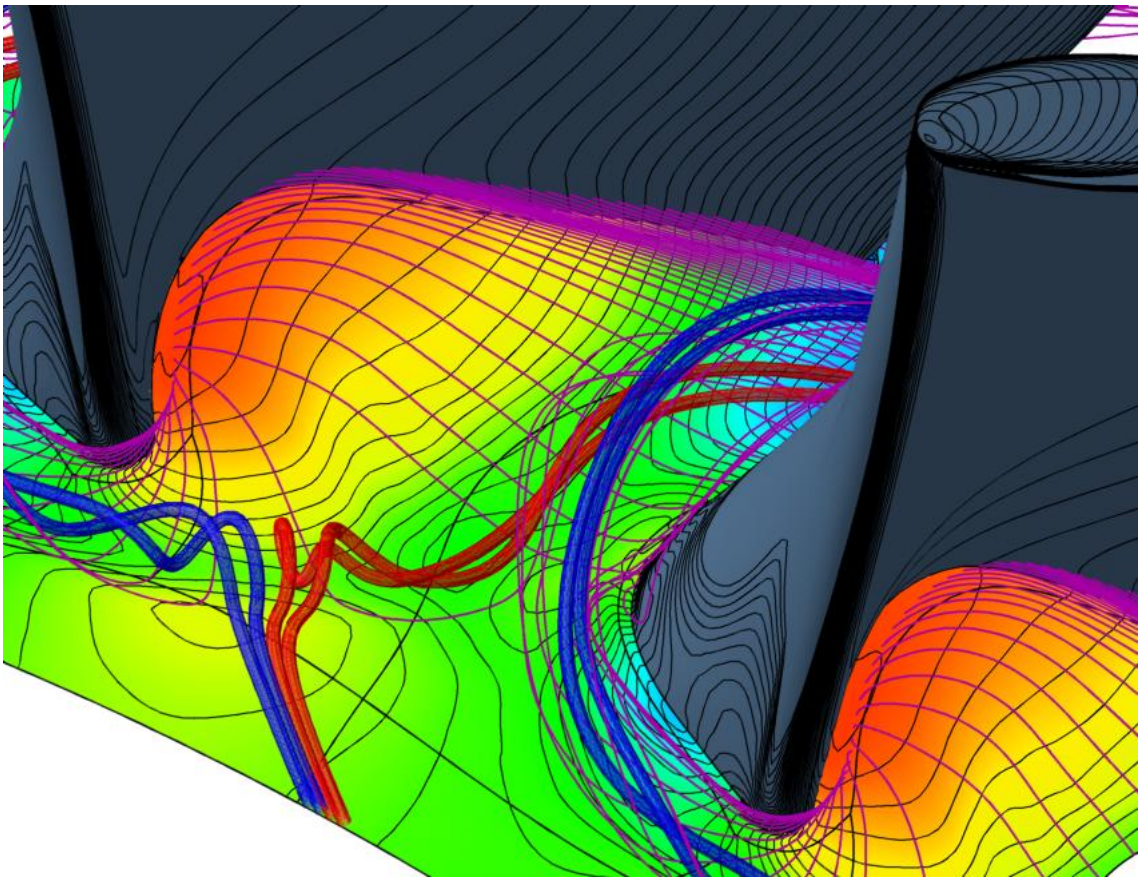

(b) Contoured

Figure 113: Endwall streamlines and oil flow for the highly loaded +5° incidence case (pressure contours are identical to those of Figure 91)

6.3 Overview

Pressure data extracted from the CFD as well as the streamline plots show the generic endwalls to affect the flow in line with the original design intent. That is that the cross passage pressure gradient is reduced and the low momentum flow in the boundary layer crosses the passage in a more axial direction. The crossing angle of the pressure leg of the horseshoe vortex is however unaffected, but its size, strength and even characteristic is affected. The combining of the two legs of the horseshoe vortices are also clearly affected as is the inclusion of the cross passage flow into the vortex system and lead to a wider spread, less intense vortex system at exit to the row in the profiled passages.

The composition of the corner vortices on the pressure side of the blade are also clearly affected and exhibit radically different structures at low incidence. This in combination with the effect of contouring on the strength of the horseshoe vortex probably account for the decreased performance of the profiled blading at reduced load.

Tip secondary flows are only slightly affected in the streamline plots but the pressure plots reveal a clear effect of the hub endwall geometry which extends up to the tip region and is evident throughout the length of the passage.

7 Discussion

7.1 Endwall profiling effectiveness at design and off-design conditions

As has already been found in Chapter 2 typical studies of the performance of geometrical changes intended to influence secondary flows have seldom extended past the design condition for the blading. This can be argued as appropriate given that highly efficient cruise is what is required to save the greatest proportion of fuel in civil operations. On the other hand military engines require a broader range of high performance operation and even the civil aviation application will struggle to accept a solution that is efficient at cruise but results in reduced power and performance at take-off or top of climb conditions. The first section of this Chapter will therefore focus on a brief synopsis and discussion of the results of this study at design and off-design conditions before discussing the merits of a number of potential objective functions for use in the optimisation of endwalls.

7.1.1 On-Design Analysis

The experimental results for this turbine indicate the following at the design condition:

- No advantage from the use of non-axisymmetric endwalls in terms of stage efficiency, importantly there is no reduction in efficiency either. Instead the improvements resulting from the endwall implementation of 1.2% efficiency close to the hub are lost at greater spans (see Figure 79)
- Rotor loss on the other hand is dramatically improved by 11.4% but while the loss is reduced across the full span the largest effect is at the casing (see Figure 83) without which improvements would be 7.4%. If measurements are taken further downstream at X4, where the tangential variations are essentially mixed out the dramatic effects on the tip region flows have disappeared and the result is a 2% improvement overall with the most significant contribution coming from the bottom third of span (see Figure 84).
- The movement to a downstream measurement plane has a similar effect on the stage efficiency result, with the efficiency being improved by a margin of 1.5% (Figure 80). This result is lies outside any uncertainty band and is thus significant.
- Large reductions in secondary kinetic energy are realised close to the rotor exit but are completely washed out once the downstream measurement station is reached (See Figures 86 and 87). Similar evidence can be found for the deviation from design exit angle presented in Figures 89 and 90.

Therefore the results indicate that there are clear improvements in pressure loss coefficient, however this is not translated into an efficiency improvement until the reductions in secondary kinetic energy found at rotor exit are translated into gains in efficiency far downstream. Additionally there are clear indications that these benefits emanate from the hub region.

An investigation of the pressure field indicates that the profiling is indeed acting on the endwalls to reduce the cross passage pressure gradient (Figures 91 and 93). Looking at the vortex structures and secondary flows in Figures 109 and 112 the effect of profiling appears to manifest in the expected change in direction of the cross passage flow, but more importantly in a decoupling of the legs of the horseshoe vortex as a result. The consequent spreading of the different vortex structures at rotor exit, indicates reduced secondary

kinetic energy and therefore a reduction in downstream mixing losses. The flow turning is more uniform as a result of the diffusion of the vortex structures (Figure 52) and this is also evident in other parameters such as loss coefficient (Figure 54) although this evidence is limited to the spread of contours and the elimination of one contour level.

The further design intention of non-axisymmetric endwalls, indeed the original conception, was that the flow into the next blade row would become more uniform and hence the benefits, no matter how tenuous in the row receiving the endwall treatment, would be reaped in the downstream row. Again analysing the design case the following are apparent:

- The flow entering the 2nd stage is marginally more uniform (Figure 51)
- The 1.5 stage efficiency is marginally improved by 0.2% (Figure 82)
- The stator loss is marginally increased by 0.5% (Figure 85)
- The secondary kinetic energy emerging from the last row is marginally improved by 0.5% (Figure 88).

This result for the outlet guide vane validates the approach. However the slight gains are not altogether surprising given the at best marginal improvement in the flow qualities measured at rotor exit (X3). The much greater gains in the mixed out results for the rotor stem from the reduction in secondary kinetic energy and these have not yet been realised due to the close proximity of the rotor and downstream stator.

Furthermore the effect of the contoured endwall on the corner vortex (Figure 112), strengthening and separating it from the suction surface of the blade; resulting in overturning of flow at the rotor exit (Figure 49) and probably also accounting for the failure to see a greater improvement in the 2nd stator as the blading was not designed to take advantage of these effects.

There is a clear discrepancy between CFD and experiment, where, for example, the efficiency level is over-predicted by CFD (Figure 79) but the difference between CFD results for annular and contoured configurations is generally smaller than those of the experiment (Figure 114). However the trends in the data are generally consistent and therefore the CFD results can potentially be used to optimise the geometry of the blade row. In addition there is some evidence that the effect of the endwall profiling does not remain local to the hub (Figures 103 and 104) but this is not as strongly evident in the CFD results as it appears in the experimental results (as discussed in Section 4.4).

7.1.2 Off-Design Analysis

The off-design cases were studied by changing the rotor speed and hence changing the incidence into the rotor stage, affecting the overall turning and load. The changes as a result of the introduction of the non-axisymmetric endwall for a number of performance parameters are shown in Figure 114.

For the rotor exit measurements the following are noted:

- The improvements noted at the downstream, ‘mixed out’ location for stage efficiency, are clear and significant, ranging from 0.4% to 2.1% at the highest load condition. Close to the trailing edge however, the efficiency measurements show a decrease of up to 0.7% at off design conditions with no effect at design, see Figure 114.

- Loss improvements on the other hand are almost constant close behind the rotor at 5.9-8.2% (Figure 83 and Figure 114 (c)) and 0.3 to 2% further downstream (Figure 84).
- As with the design results C_{ske} is consistently improved but the advantage disappears downstream and in the case of the highest load case reversed to reflect a decrease of some 3.7% (Figure 87).

The pressure field reveals no real differences from what has been concluded for the design case, but the streamline plots do reveal a clear difference between the high turning and design case for which the introduction of a profiled endwall brings about consistent changes but at decreased incidence the CFD results indicate a very different behaviour in which the endwalls overcome some features, in the annular case, introduced by the incidence change, namely what appears to be a separation of the flow on the pressure surface just past the leading edge which causes a strong cross passage flow at this point. However increased vorticity is clearly introduced into the horseshoe vortex for the negative incidence case (Figure 111). Another feature of the flowfield that must be highlighted is that at rotor exit the flow is generally more uniform for the contoured configurations which is apparent from the flow turning deviation from design (Figure 52) but also from the vortex tracks found in Figure 107, which clearly establishes that the consistency and uniformity of the flow structure is improved across the load range through the implementation of non-axisymmetric endwall contours.

C_{ske} is only increased by the introduction of endwall contouring at light load, see Figure 88, and is likely to emanate from the increased strength of the rotor horseshoe vortex system (Figure 111). Hence the poor performance of the 2nd stator at off design conditions is likely to be the result of two factors:

- The strengthening of the corner vortex flow and the consequent increase in the degree of overturning (although not the radial extent) in the flow close to the hub entering the stator row (see Figure 49).
- The increased radial movement of hub secondary flows (Figure 107).

The effect of the profiled rotor endwall on the downstream stator performance is to decrease performance when compared to the annular case (Figures 82 and 85) at off design conditions. The secondary flows from the rotor hub pass through the outlet guide vane and emerge at spans between 60 and 80% (see Figure 78). The thickening of the wakes (see Figure 72) dramatically increases the overall loss in the blade row. The effect appears so severe at increased rotor incidence that the stator loss (Figure 71) and nozzle efficiency (Figure 73) see step changes between annular and profiled cases indicating the possible onset of separation over a large proportion of the span, this despite the profiled case showing reduced overall deviation from the design outlet angle (Figure 51).

As turning is known to directly influence the secondary flows, increasing their strength with increased turning, one expects the endwalls to have increasing effect with increased turning, this argument was put forward by Rose *et al.* (2001) and supported his data as shown in Figure 115 as well as that on graphs (d) and (e) of Figure 114. Generally the trends in response to the change in load (such as falling loss with decreasing load,

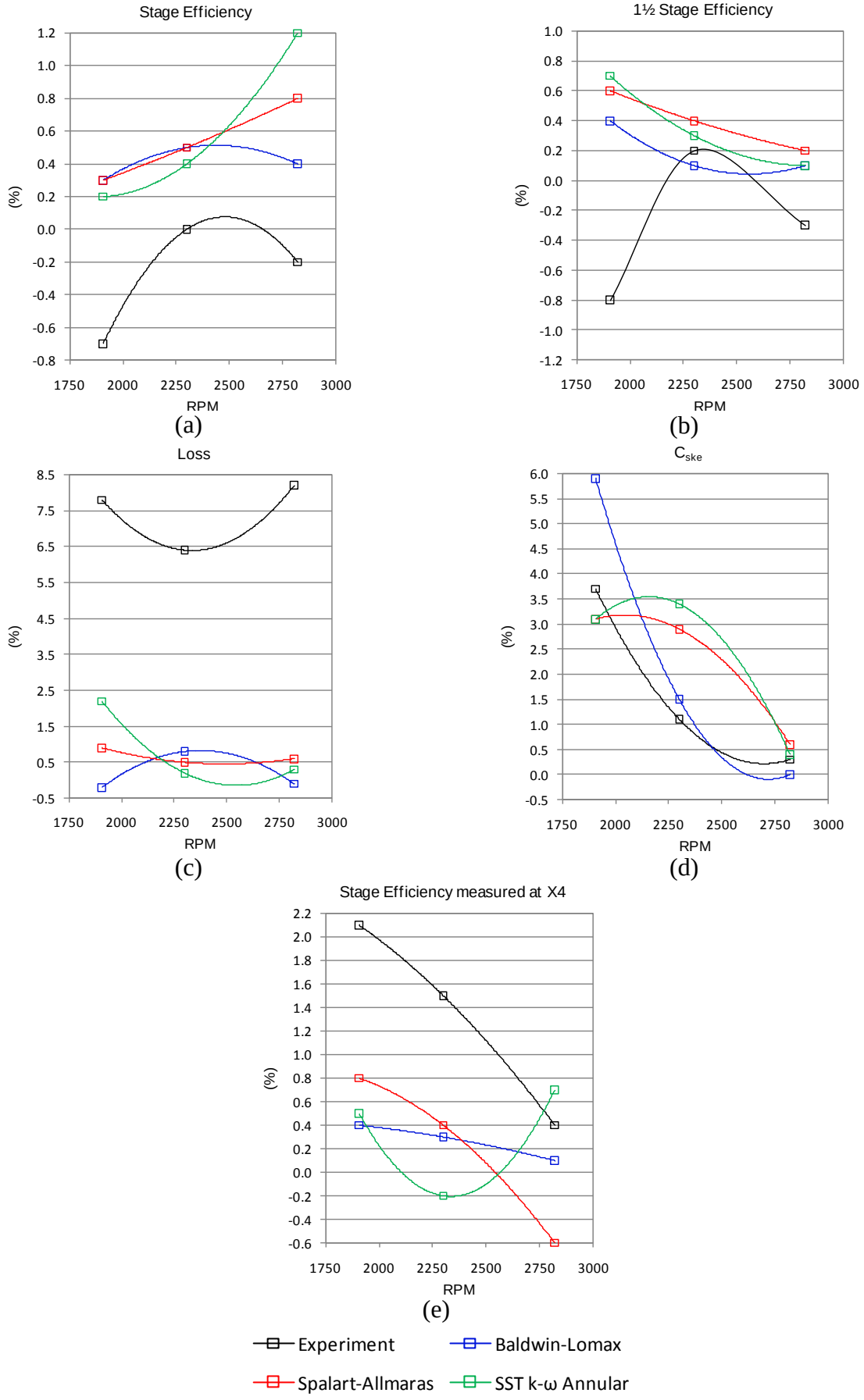

Figure 114: Comparative change in efficiency and loss values between annular and contoured rotor endwall configurations (derived from the full or 2/3^{rds} span area averaged results shown in Chapter 5)

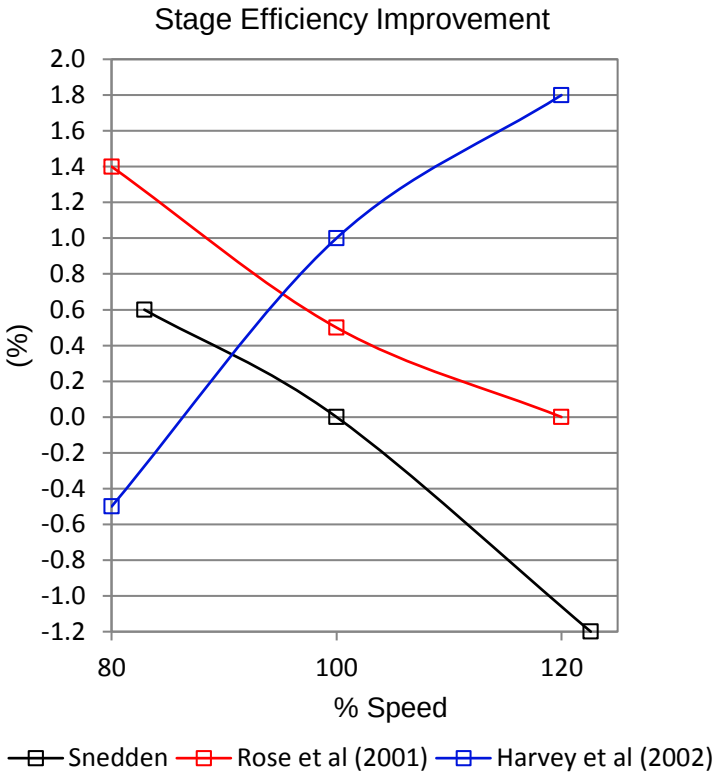

Figure 115: Comparison of stage efficiency gains with those in the literature, the results for Rose and Harvey *et al.* are taken at design work

Figure 83) found throughout this dataset are in line with what is expected and hence the experiment and numerical analysis are well posed and show good agreement in terms of the trends although some exceptions are notable in Figure 114. These exceptions are however not without precedent as shown by the data of Harvey *et al.* (2002) for the intermediate pressure turbine of the same Trent 500 test rig as that of Rose *et al.* (2001) for their high pressure stage. That the gains are generally reduced when compared to those of Rose *et al.* (2001) can be explained by the smaller stage pressure ratio and generic design of the endwall.

7.1.3 The effect of rotation

Only two clear differences exist in this dataset to that of the work of Ingram (2003) as a result of the effects of rotation:

- The first is the presence of tip clearance flows and hence a lack of uniformity in the flow at high radius and to some extent the interaction between hub secondary and tip clearance flows
- Secondly the radial extent of the hub secondary flows is greatly expanded in the rotating case when compared to that of the cascade (see Figures 116 and 117) which is consistent with the findings of Richards and Johnson (1988). These figures should however be viewed with caution as the absolute values of the quantities cannot be directly compared as they depend on very different inlet condition values, the Reynolds numbers are different and so are the measurement locations with respect to the blade. No adjustment of the span for the different blade aspect ratio has been attempted.

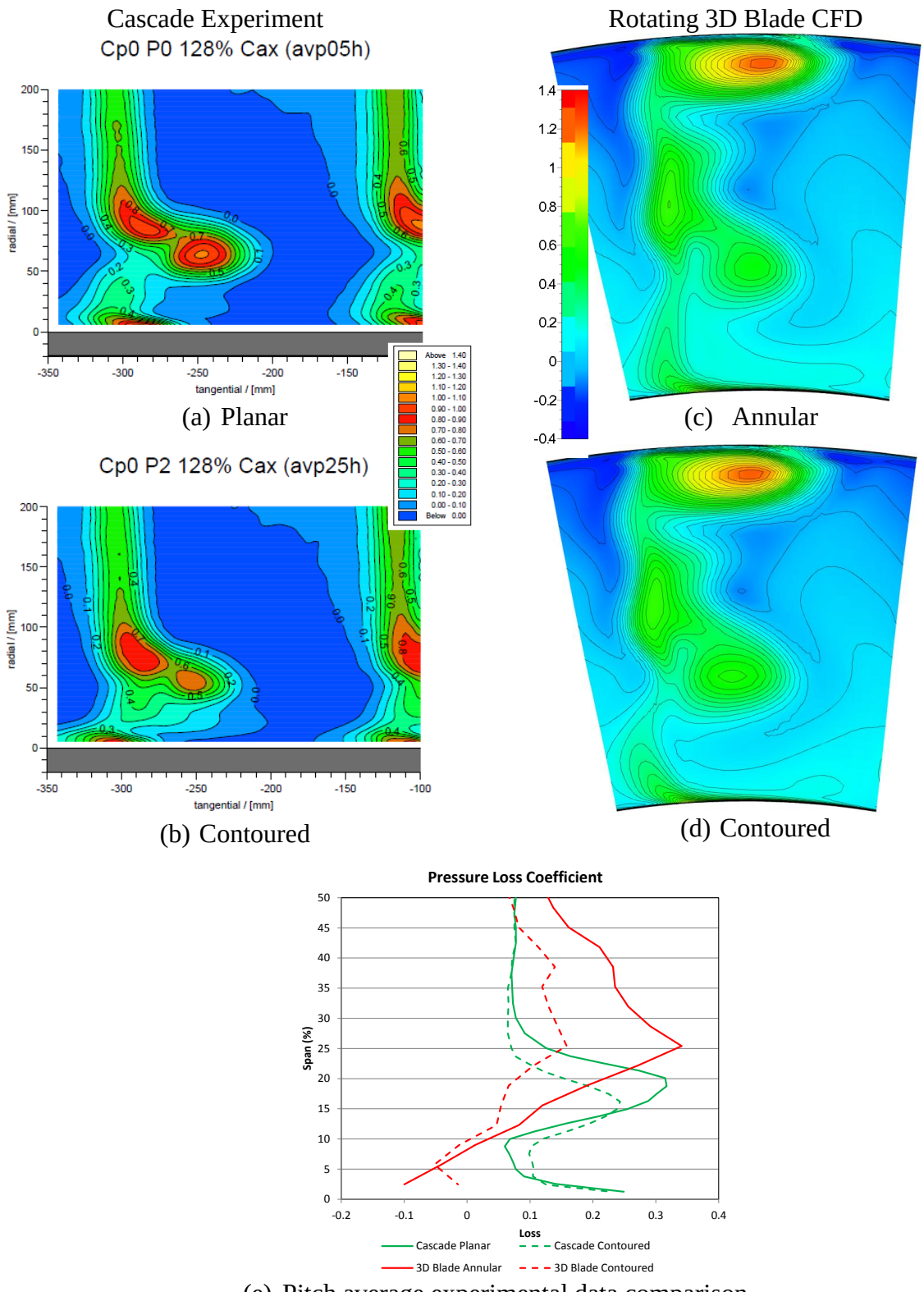

Figure 116: Comparison of pressure loss coefficient for cascade and rotating experiment at rotor exit (Cascade data reproduced from Ingram, 2003)

Cascade Experiment

3D Rotating Blade CFD

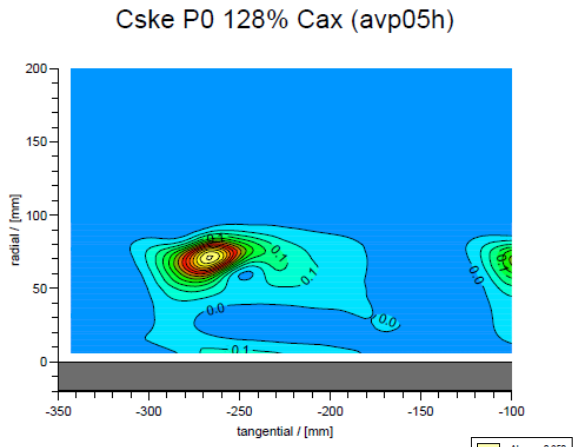

(a) Planar

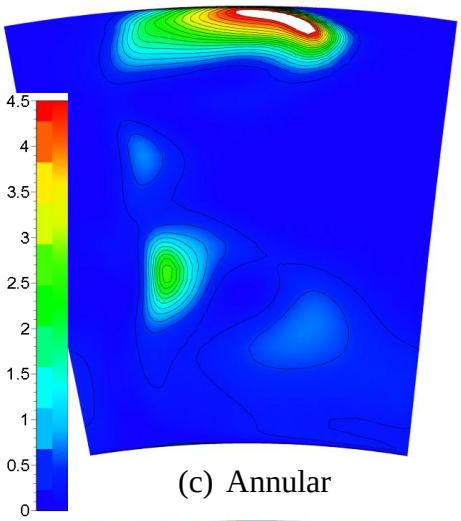

(c) Annular

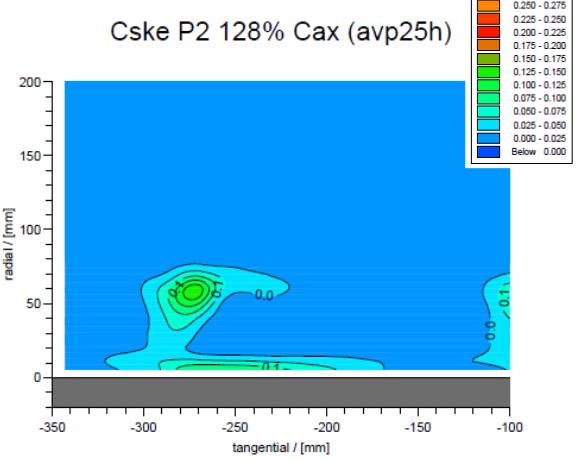

(b) Contoured

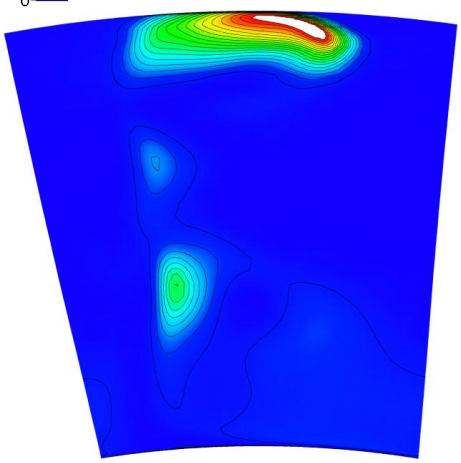

(d) Contoured

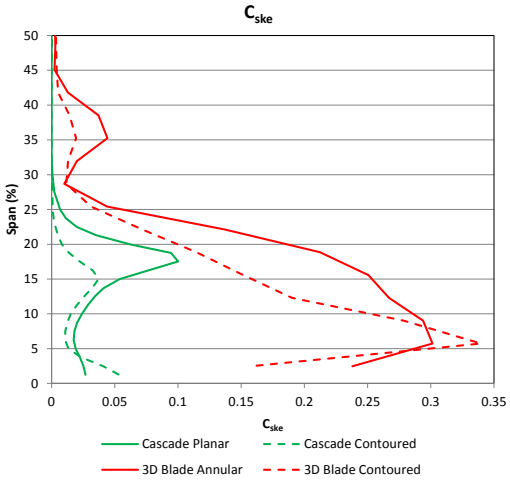

(e) Pitch average experimental data comparison

Figure 117: Comparison of coefficient of secondary kinetic energy for cascade and rotating experiment at rotor exit (Cascade data reproduced from Ingram, 2003)

Table 10: Comparison of cascade and rotating rig results

	Cascade		Rotating Rig	
	Planar	P2 Contoured	Annular	Generic Contoured
Total Loss @ Rotor Exit (ignoring tip gap losses and measurement plane differences)	0.1574	0.1322	0.150	0.086
% Baseline Case	100%	84%	100%	57.3%
Mixed Out Loss	0.2086	0.1724	0.221	0.201
% Baseline Case	100%	82.6%	100%	91%
C_{ske} (ignoring tip gap losses and measurement plane differences)	0.0203	0.0092	0.068	0.053
% Baseline Case	100%	45.3%	100%	77.9%
Maximum Overturning*	0°	2.4°	0°	0°
Overturning Peak Span	0%	0%	20%	7%
Maximum Underturning*	0°	-2.7°	0°	-2°
Underturning Peak Span	19%	16%	35%	35%
(Estimated) Efficiency Improvement	0%	1.55%	0%	1.5% (mixed out)

* Versus a spanwise pitch-averaged design flow angle profile

The averaged data presented in Table 10, shows a summary of the comparisons that can be drawn from the work of Ingram (2003) on the equivalent two dimensional cascade geometry and that of the rotating rig. Loss and secondary kinetic energy is reduced in both cases but to varying extents and once again the spanwise position of the over and underturning peaks shows the greater extend of the secondary flows in the rotating case. Probably the most remarkable piece of data is however the estimation of the efficiency improvement gained from the cascade which correlates very well with that obtained in the mixed out measurements.

7.1.4 Torque output

Table 11 in conjunction with Figure 118 look at the torque available from the rotor, which is reduced by a small margin (3.5% at the highest load measured experimentally). CFD fails to predict the level correctly and the differences between endwall cases is smaller that found experimentally. The CFD can however be used to analyse the sources of the torque surface by surface. Table 11 shows that the resultant torque from the pressure and suction surfaces changes by slightly more that the resultant change in the area resulting from the profiling, this net reduction in the torque generated from the blade surface has to be made up from the endwall, however the profiled endwall produces almost constant torque across the speed range tested (Figure 118) and hence the overall torque is reduced.

Any reduction in torque is not desirable in turbine design, particularly at high load conditions at which some efficiency degradation might be acceptable but a torque reduction not so.

Table 11: Blade area and torque changes

	Annular	Contoured	Difference
Pressure surface area (mm^2)	4309	4198	-2.6%
Pressure surface torque change (all speeds)			-2.7%
Suction surface area (mm^2)	4887	4992	+0.85%
Suction surface torque change (all speeds)			+1%

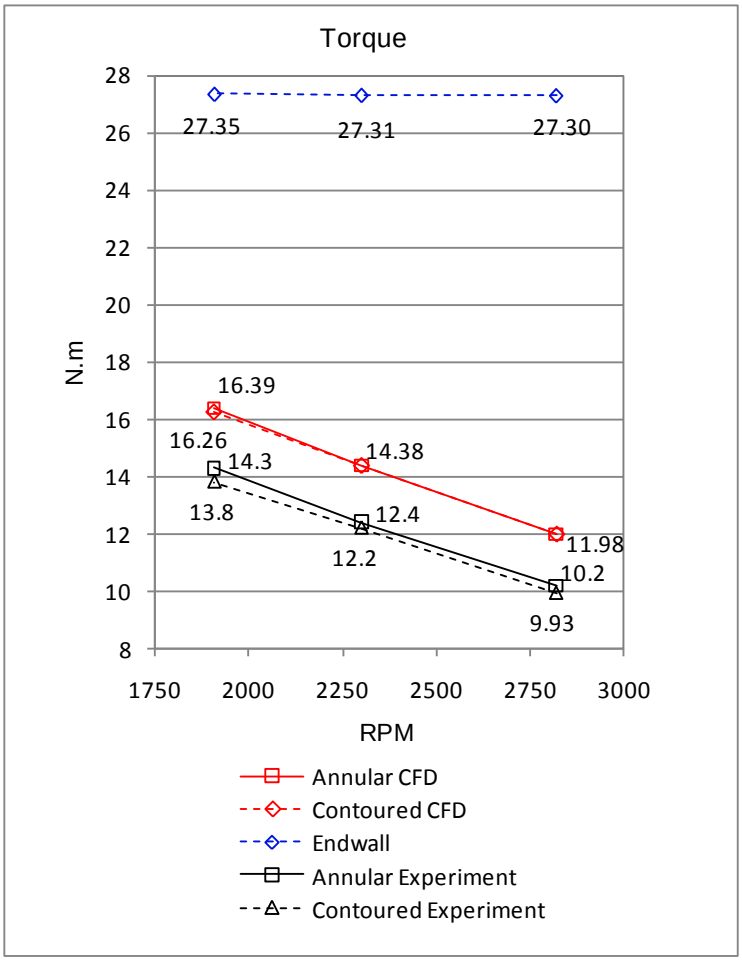

Figure 118: Torque generated

7.1.5 Summary

The generic non-axisymmetric endwall profile introduced into the turbine rotor has successfully reduced outlet secondary kinetic energy and loss over the full range of operation tested. Significant efficiency gains are however only found in downstream measurements which approximate mixed out values. Experimentally these gains come with the penalty of slight reductions (between 0.2 and 0.5Nm or roughly 3.5%) in the torque generated and clearly the second stator requires a significant three dimensional redesign if it is to benefit fully from the more uniform flows exiting the rotor, although small benefits are present at the design condition.

CFD results show that the endwall contouring reduces the cross passage pressure gradient in the vicinity of the hub, this results in the delayed migration of passage cross flow and fundamentally changes the relationship between the pressure and suction side legs of the horseshoe vortex, supporting Ingram's (2003) assertion that the suction surface leg of the vortex is strengthened while the pressure side leg is weakened. This in turn results in a decoupling of the two vortex legs and at the same time the passage cross flow is not pulled into a unified vortex structure and hence the at the rotor exit the vortex structure is dispersed with less potential for mixing losses. In the rotating case the radial pressure gradient then convects this weak association of the two vortices further away from the endwall, increasing the spanwise extent of the secondary flows when compared to the cascade. The net result being that the secondary vortex structures are not held closer to the endwall but rather dispersed over a greater span as a result of the passage contouring.

Generally the rotor outlet flows are more uniform in the secondary flow region at all loads with overturned flow being suppressed towards the hub endwall. This increased overturning close to the hub, together with the greater radial extent of the secondary flows, albeit less intense, results in only marginal improvements in the 2nd stator at design load, and poorer performance at both off-design conditions for all the parameters measured. The overturning at the hub can be traced back, using the CFD results, to the corner vortices emanating from the peak pressure point in the junction between the pressure side of the rotor blade and hub endwall. These corner vortices are strengthened in the profiled endwall configurations when compared to those for the annular case.

Three further items of interest were found in this dataset:

- At reduced incidence a fundamental change in the flow structure is evident with the profiled endwalls producing increased vorticity in the horseshoe vortices and fundamental changes in the corner vortex structure.
- There is a clear influence of the profiling of the endwall on flows extending all the way up to the tip with the potential to affect tip leakage flows.

These have clear implications to applications where part of increased load represents a significant proportion of the machines' duty cycle and where endwalls are used in conjunction with free tips to reduce the mass of the machine.

CFD predictions and the selection of appropriate turbulence models remains a challenge emphasising the need for experimental validation. However CFD can be used to predict the effects of endwall contouring successfully with C_{ske} being the superior quantity indicated in this study. Pressure loss and outlet flow angle deviation are also relatively well modelled and offered as alternative optimisation objectives.

7.2 Objective function selection

One of the key questions to be answered when optimising any component is the selection of an objective function. While the ultimate objective may be to improve the efficiency of the turbine, the stage or component efficiency may not be the best quantity with which to work, for a number of reasons, such as it is not well predicted, cannot easily be validated or does not fully describe the effect of whatever optimisation is performed on the overall efficiency of the system.

7.2.1 Efficiency as an objective function

From Figure 79 it is clear for this case the stage efficiency is either poorly predicted or that validation is not easily attained. The CFD results differ by as much as 13% from the experimental result purely because of a discrepancy in the predicted versus measured torque values (see Figure 118), and trends in terms of both the difference resulting from different endwalls or incidence do not lend confidence to the results. One common way to eliminate the offset between CFD and experimental results would be to examine the relative change predicted and to drive the optimisation on the basis of the improvement from a given baseline (in this case the annular endwall). Figure 114 shows the full set of comparative efficiencies the case presented here. Once again there is little to compare between the experiment and the CFD options, or ever amongst the CFD options themselves, particularly if one expects to see a trend with regard to the effect of changing incidence.

In addition the quantity used is actually isentropic efficiency and not true efficiency and is therefore based on a number of simplifications. Finally the changes resulting from the introduction of non-axisymmetric endwalls simply do not result in a significant variation in the results such that one might expect to clearly distinguish differences between minor subtleties in the endwall design (see Figure 119). As a consequence of this, for the case presented in this thesis, it would be foolhardy to use the efficiency results from CFD predictions to predict whether a given endwall is working better than another.

Figure 119 has been included primarily for reference against Figure 120, Figure 121 and Figure 123 all of which give the results for the parameters discussed in this and later sections for the full span of the CFD results rather than the limited span for comparison to the experimental data given in Chapter 5. This has been done as an endwall optimisation would generally be performed using this method.

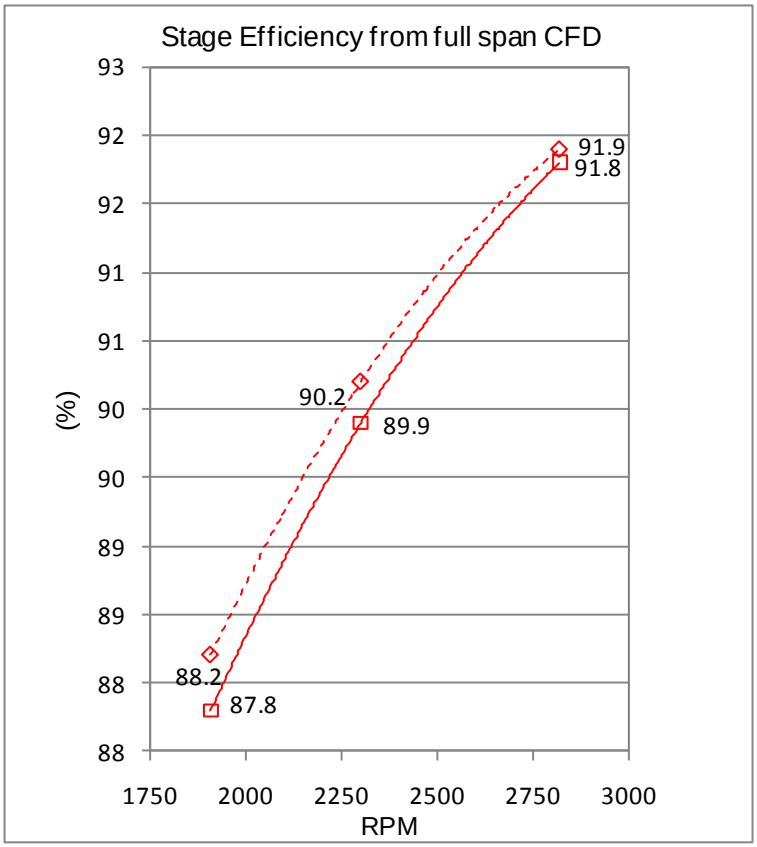

(a)

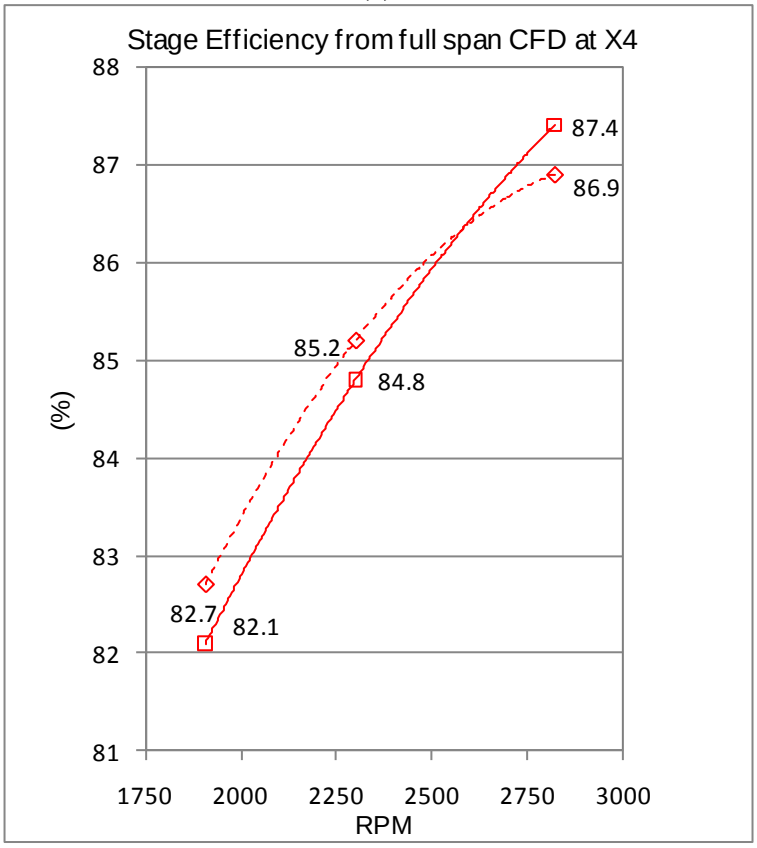

(b)

Spalart-Allmaras Annular Spalart-Allmaras Contoured

Figure 119: Full span stage efficiency results for the Spalart-Allmaras turbulence model

7.2.2 Loss coefficient as an objective function

Loss coefficients are traditionally used for cascades where no work is generated and hence efficiency is not computed. In order to calculate a rotor loss coefficient, assumptions must be made regarding upstream pressure values which are not necessarily very physical and therefore one must limit this effect by at very least maintaining a strictly consistent approach. The loss coefficient formulation (Equation 3-26) consists purely of total pressure terms and as such represents a value which should be well predicted by CFD as it consists of primary solution data, not extrapolations as is the case with the stage efficiency which relies on a torque term. As a result of its formulation, the loss coefficient represents a measure of the total energy loss in the row.

Once again the comparisons between the experimental area averaged results and those for loss coefficient are not encouraging, particularly close to the rotor (Figure 83) although the trending starts to look better further downstream (Figure 84) where the slope of the predictions generally match that of the experiment however the form is more linear than parabolic as in the experiment. In comparison to the stage efficiency numbers the area average loss coefficient predictions are much closer, lying only a 2-3% below the experimental results at some load conditions.

One of the reasons for the apparent poor performance of the CFD close to the rotor exit (X3) is that the apparent influence of the endwalls on the tip region is so overpowering in the experiment (Figure 83) that it overshadows any differences seen in regions more directly affected by the hub endwalls. Again this could be the result of the practicalities of measurement such as the use of an intrusive probe in highly sheared flows as discussed in Chapter 4. In fact the full span loss in the annular case decreases as one moves downstream which is not physical and hence is a clear indication of a poor experimental result emanating from the tip region measurements of pressure for the annular case which would result in a roughly 6% over estimate of total loss of this case. This is not the case for the $2/3^{rds}$ span results which exhibit the correct trend as one travels downstream.

From Figure 120, which represents the data that a turbine designer would typically extract from CFD during the optimisation process, one can see that the differences between annular and profiled endwalls amount to just 0.4% (at X3) or 0.8% (at X4) for the design case. The difference grows consistently with increasing incidence.

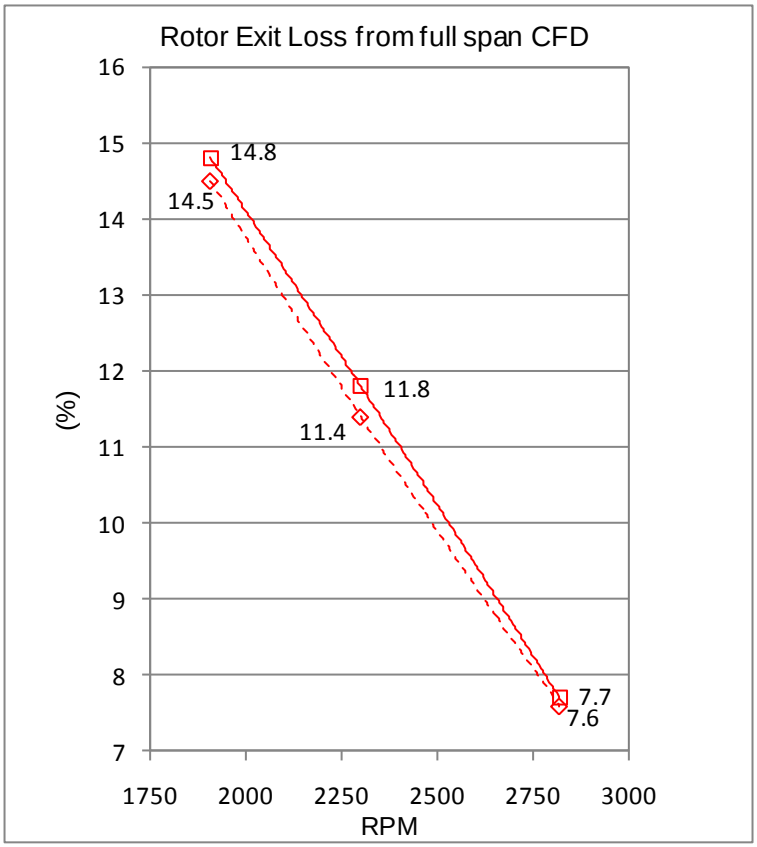

(a)

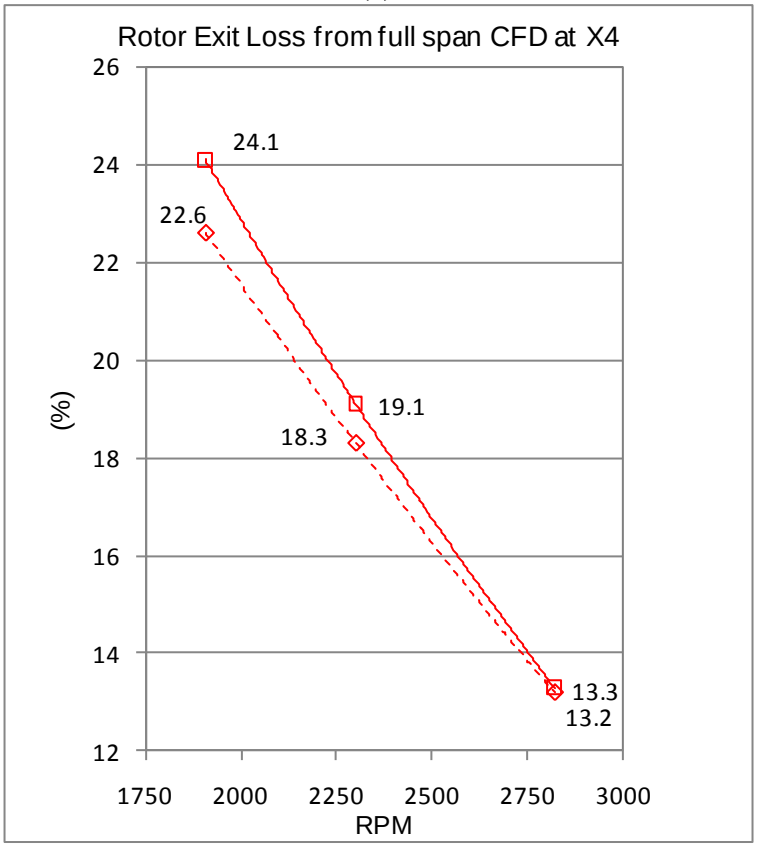

(b)

Spalart-Allmaras Annular Spalart-Allmaras Contoured

Figure 120: Full loss coefficient results for the Spalart-Allmaras turbulence model

7.2.3 C_{ske} and its derivatives as objective functions

If the loss coefficient is a measure of the total energy loss in the exit flowfield at a given point downstream of the turbine, then the coefficient of secondary kinetic energy is an attempt to measure the kinetic energy that is not usable in the exit flowfield. This means that the further downstream one moves from the turbine the less this parameter should become which is apparent in the difference between Figure 86and Figure 87, and which is opposite to the effect on loss. This means that C_{ske} is a measure of a subset of the kinetic energy in the flow; it measures the potential for loss resulting from secondary flows at a given point and cannot therefore be used as a proxy for loss.

C_{ske} is better predicted that the previous two parameters and despite suffering almost identical problems in its definition and in terms of the validation where the annular experimental results have dramatically increased C_{ske} values in the tip region, the correlation between the CFD and experiment are generally good both in terms of level and trend, with the exception of the Baldwin-Lomax results which cannot be expected to capture vorticity in the flow correctly. Furthermore the differences between endwall configurations are relatively large (in the order of 2%, five times that of the loss differences) (see Figure 121).

Therefore C_{ske} is both a physical and well validated quantity by which to measure the potential loss emanating from secondary flows in a flowfield. In addition it has clear potential to identify small differences between endwall designs as evidenced by the separation between endwall cases shown in Figure 121. It does not have the ability to indicate decreased output from the turbine or gross losses (such as separations) that do not result in flow direction changes out of plane with the bulk flow however.

Several authors referenced in Chapter 2 have modified the C_{ske} parameter by the dot product with helicity. Helicity was used to effectively limit the quantity to the identification of vortical flows. Figure 122 is included as a check to ensure that the helicity is not the quantity optimised rather than C_{ske}, a pitfall found by Vasquez and Fidalgo (2010), while Figures 124 to 127 are included to complete the picture and allow the reader to compare these parameters to area plots of previous parameters which can be found in Chapter 5. Figure 125 clearly shows the advantage of this method when compared to Figure 58, however Figure 123 indicates that the result is a narrowing of the difference between the annular and profiled endwall cases which suggests that this method is not indicated for this turbine at least.

7.2.4 Alternative objective functions

As was found in Figure 39 (a) and (b) exit flow angle is the best indicator of the difference between endwall types. This correlates with the results for C_{ske} which is partly derived from the exit flow angle. The change in endwall design leads to small changes in the average flow angle which is, itself, large (60-70°) and hence the quantity "Exit flow angle deviation from design" has been included throughout this work as a simple attempt to increase the sensitivity of an area averaged results, a single number by which optimisation might be performed. In terms of its validation and sensitivity in terms of separation between endwall results the parameter behaves similarly or slightly worse than C_{ske}.

However the logic behind the use of such a parameter lies more in terms of the effect on the downstream rows than on loss reduction in the contoured row itself.

7.2.5 Summary

C_{ske} is clearly a superior parameter for use as an objective function in this case. It performs well close to the rotor exit but not far downstream unlike both loss and efficiency, for which the opposite is true. This alone makes C_{ske} a good parameter for the multistage environment where the proximity of downstream rows makes the analysis of 'mixed out' or far downstream plane losses academic. C_{ske} must be applied with some prudence however as it does not indicate the power performance of the stage, nor act as a proxy for loss and therefore every result should be interrogated for flow separation and other loss generating flows. Modification of this parameter using helicity offers no advantage in this case.

A possible counter to the problems indicated with the use of C_{ske} is the use of a compound objective function combining total pressure loss (as it is not affected by the problems encountered in the prediction or measurement of torque) and C_{ske}, and furthermore if the optimisation is to have a minimum impact on downstream rows then the exit flow angle deviation quantity might be included.

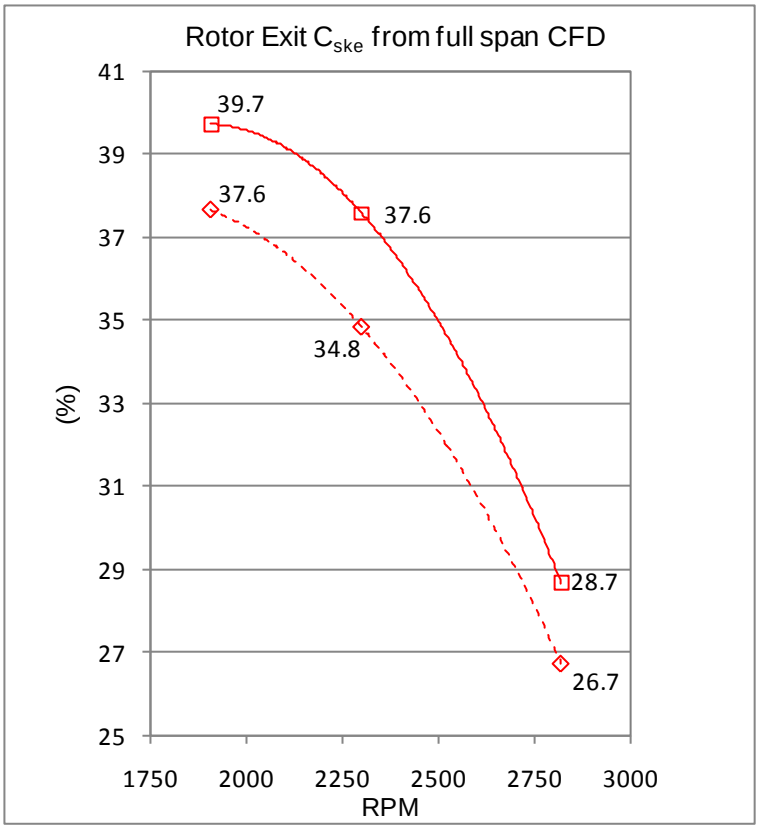

(a)

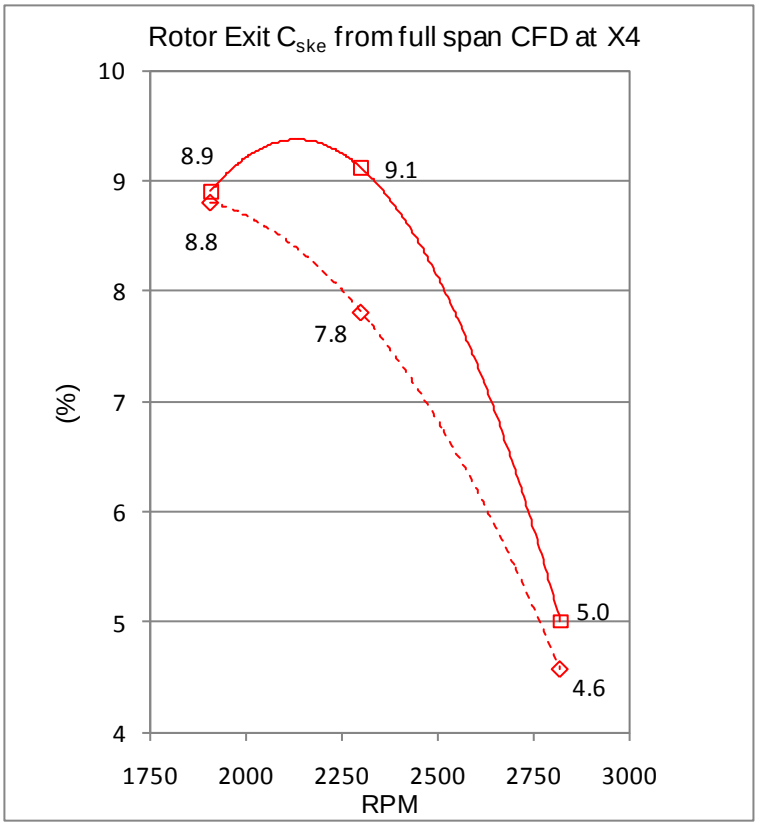

(b)

Spalart-Allmaras Annular Spalart-Allmaras Contoured

Figure 121: Full span rotor exit C_{ske} results for the Spalart-Allmaras turbulence model

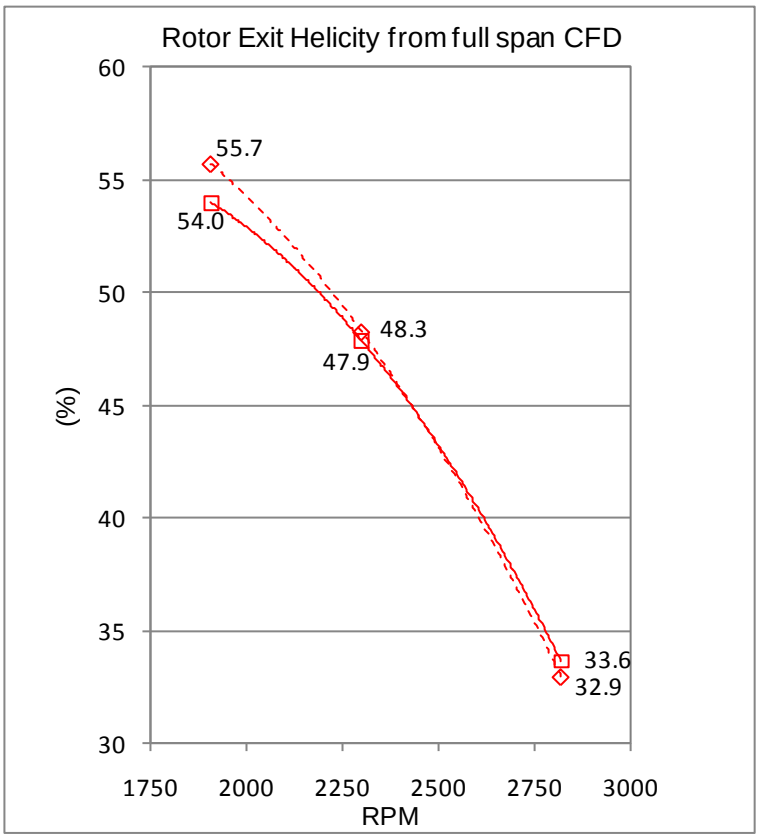

(a)

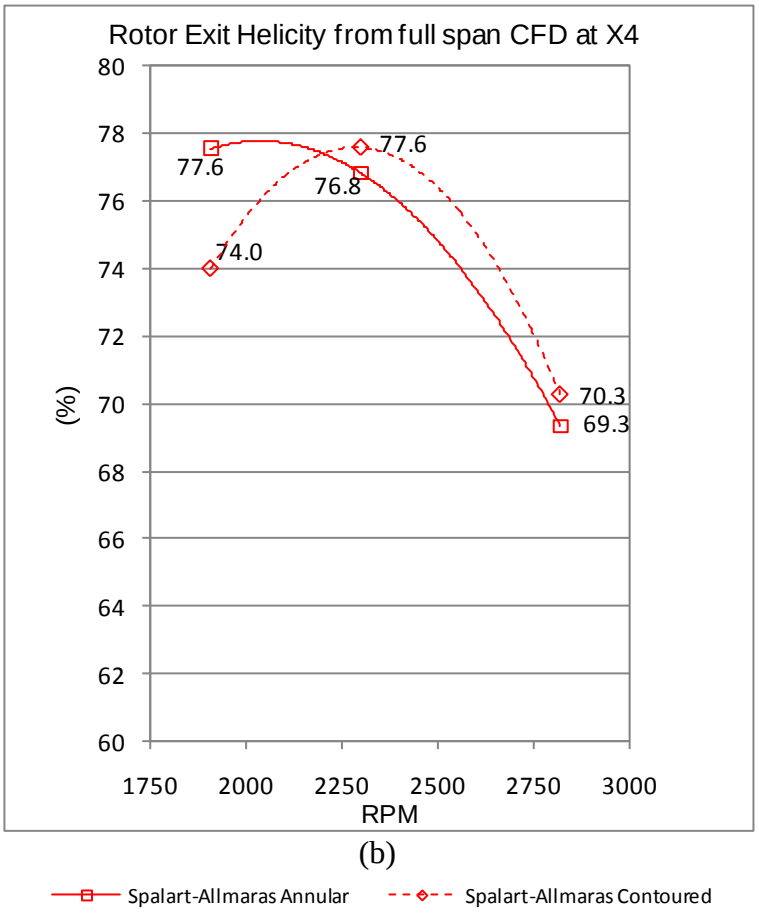

(b)

Figure 122: Full span rotor exit helicity results for the Spalart-Allmaras turbulence model

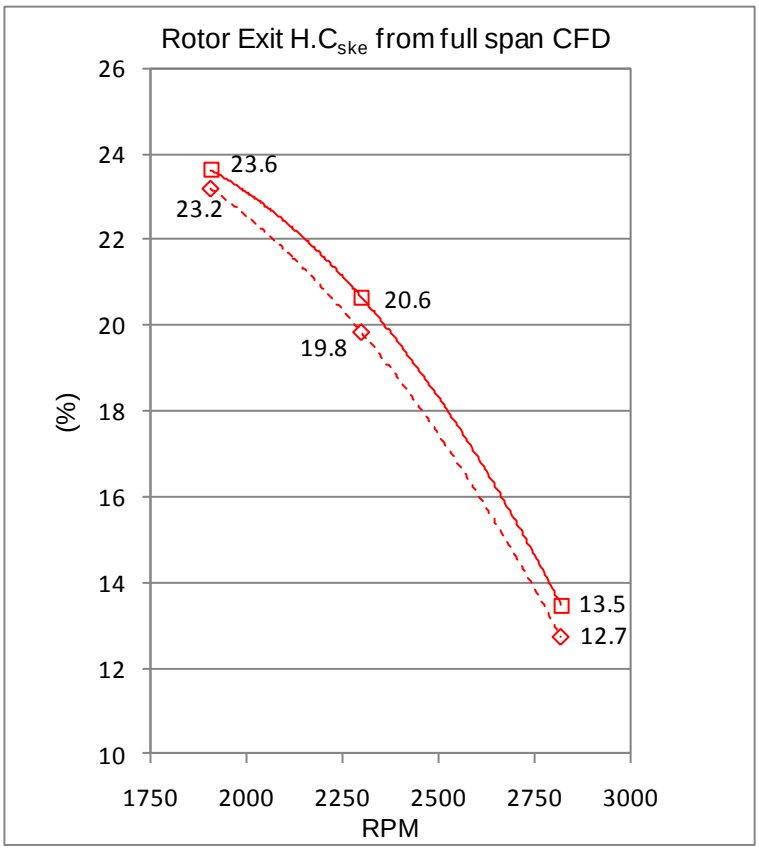

(a)

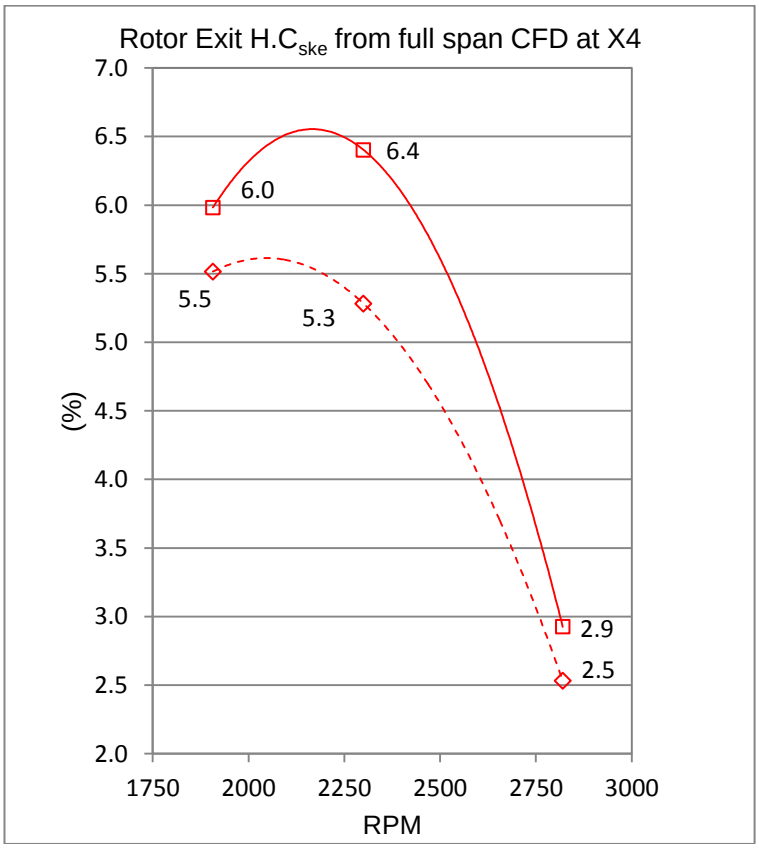

(b)

Spalart-Allmaras Annular Spalart-Allmaras Contoured

Figure 123: Full span H.C$_{ske}$ results for the Spalart-Allmaras turbulence model

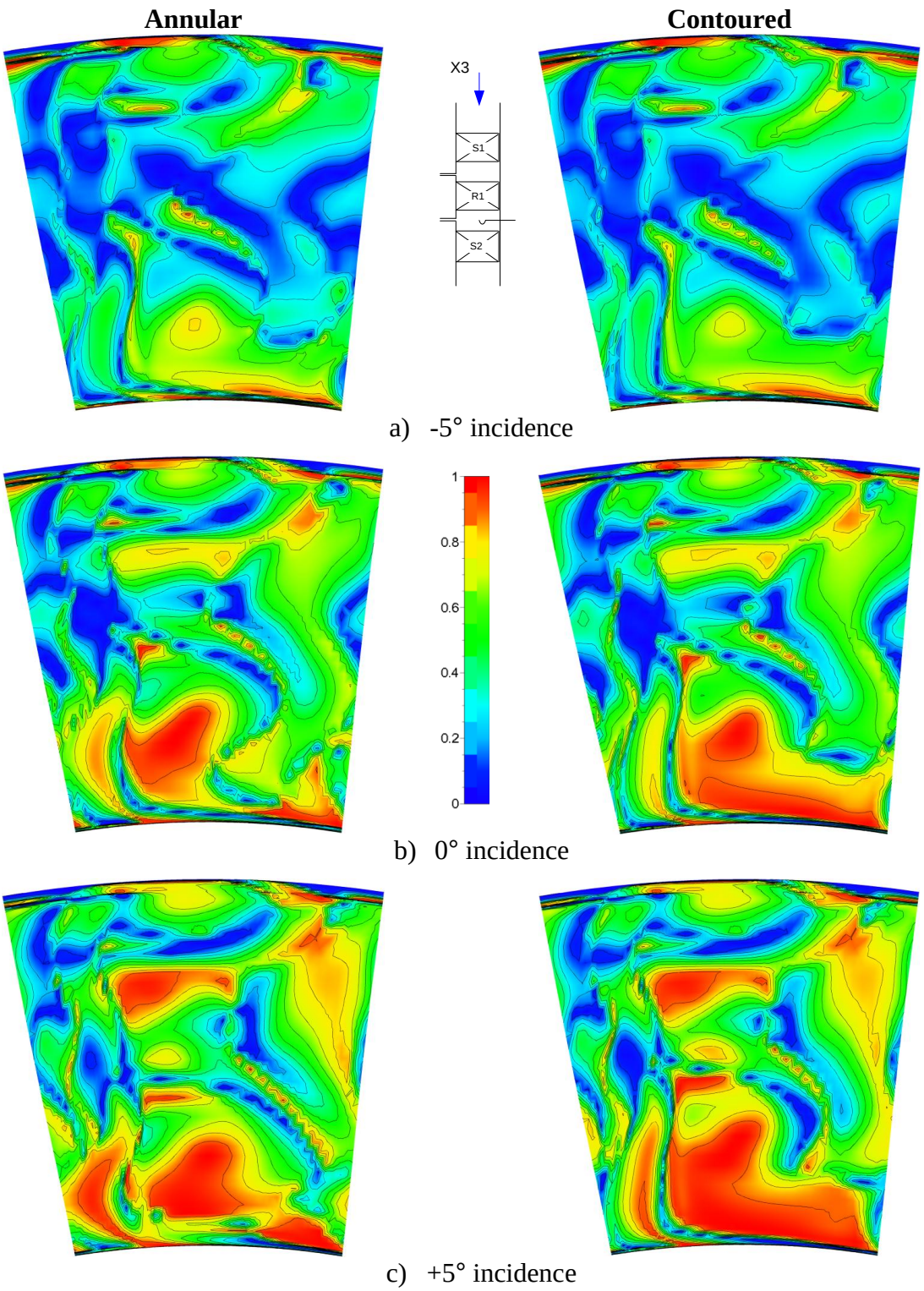

a) -5° incidence

b) 0° incidence

c) +5° incidence

Figure 124: CFD predictions of rotor exit helicity

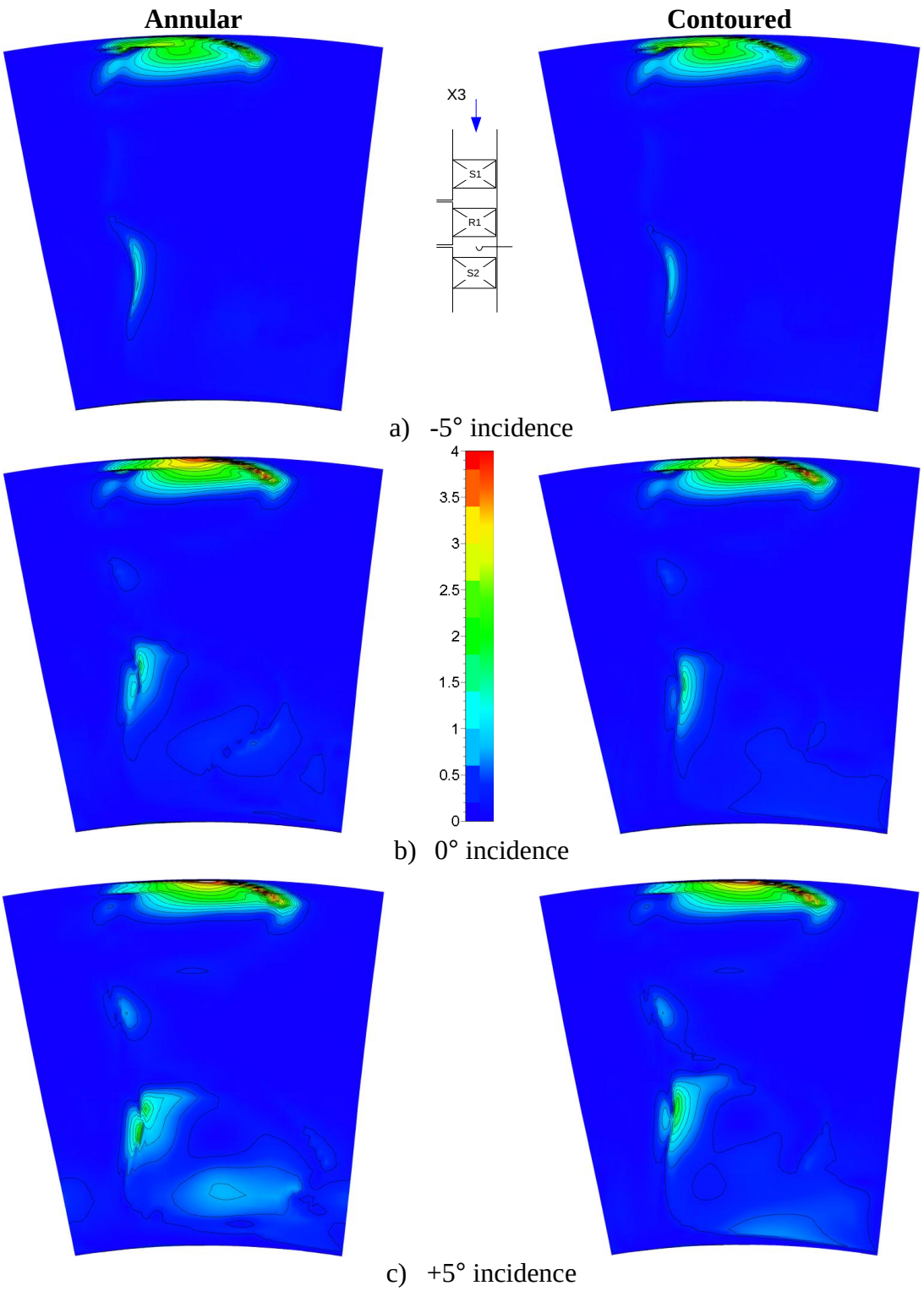

a) -5° incidence

b) 0° incidence

c) +5° incidence

Figure 125: CFD predictions of rotor exit H.C$_{ske}$

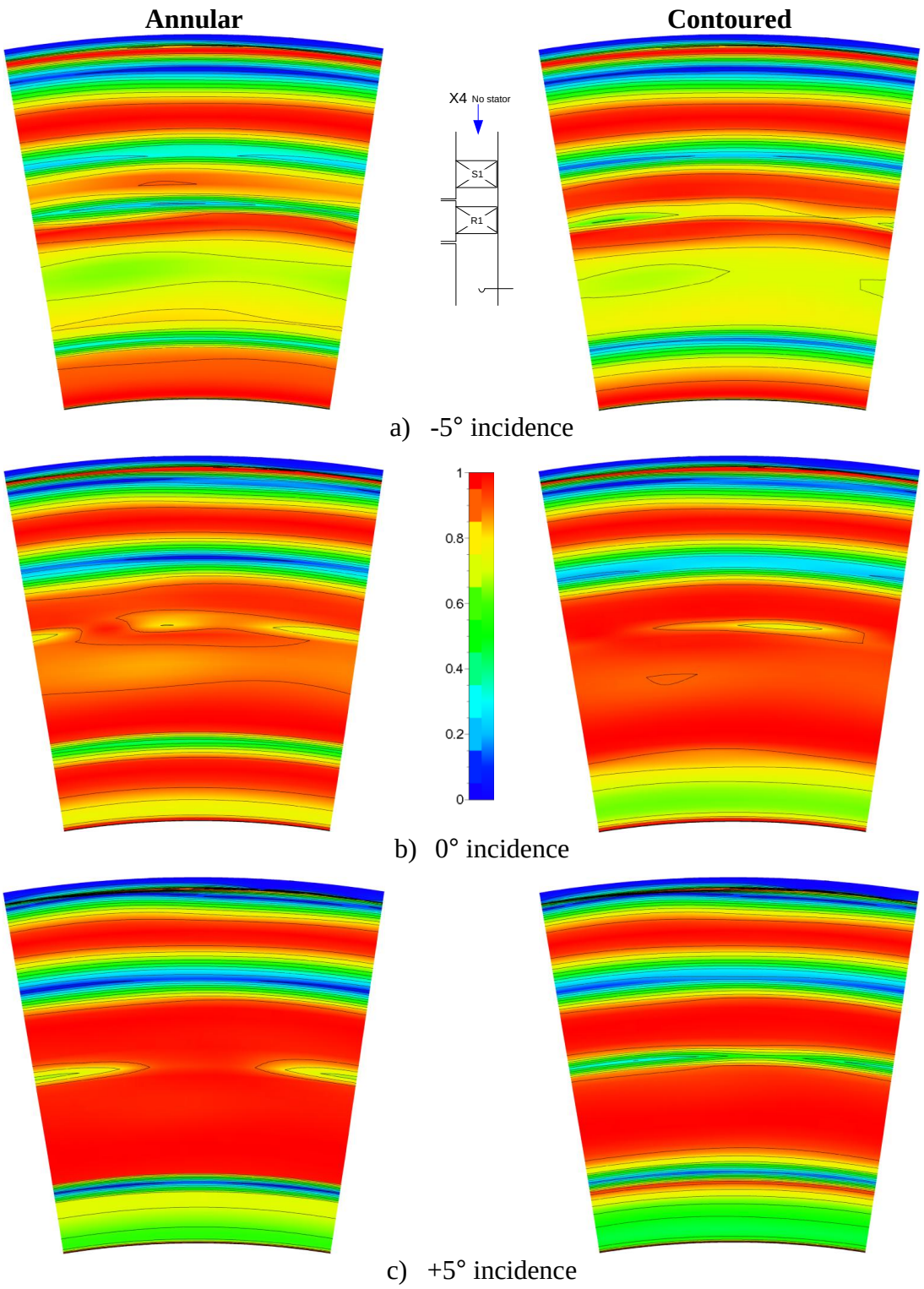

a) -5° incidence

b) 0° incidence

c) +5° incidence

Figure 126: CFD predictions of rotor exit helicity at station X4

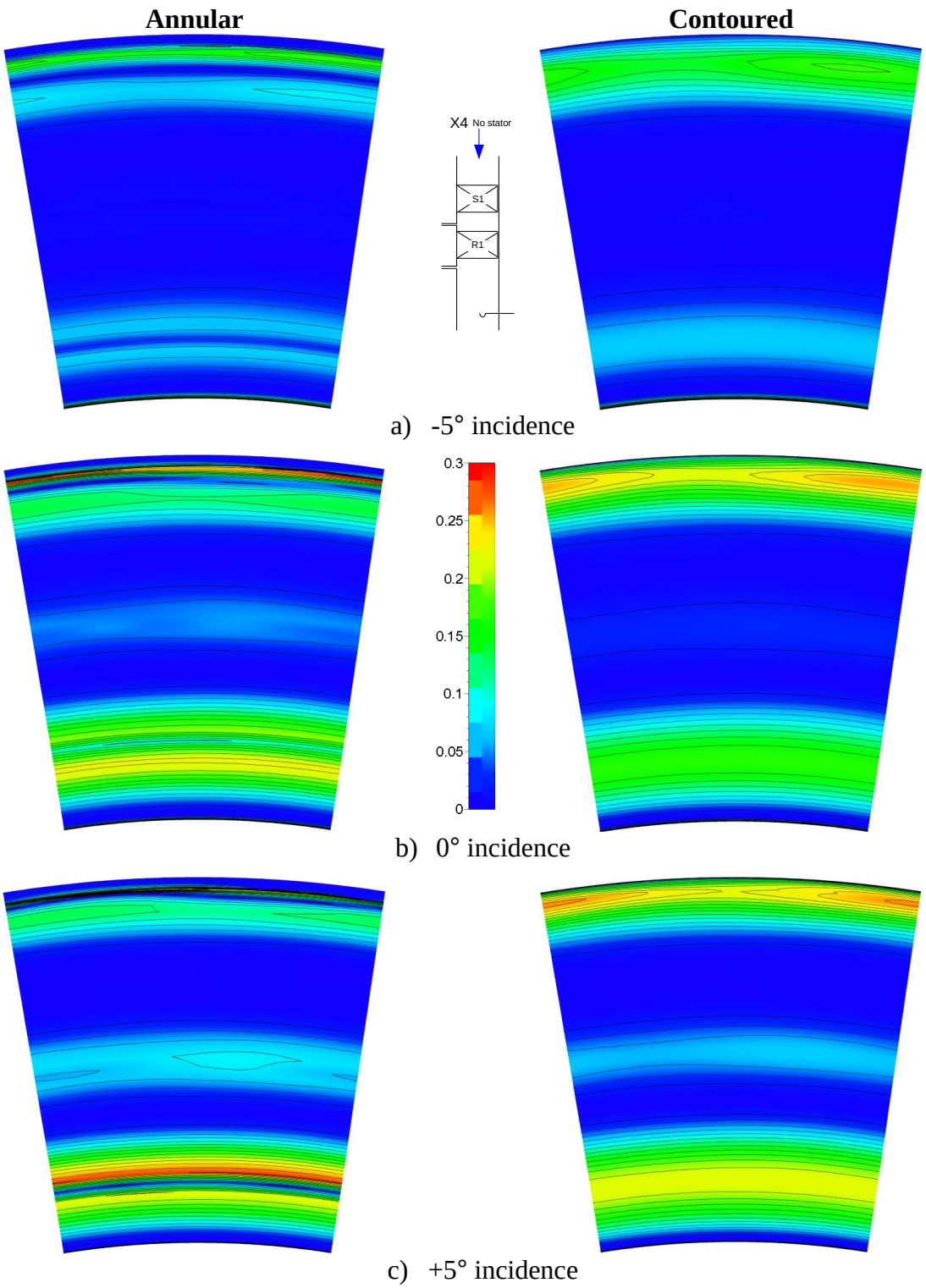

a) -5° incidence

b) 0° incidence

c) +5° incidence

Figure 127: CFD predictions of rotor exit H.C$_{ske}$ at X4

8 Conclusions and recommendations for further work

At the outset a number of goals were outlined for this work: Firstly the introduction of a new three dimensional, rotating, 1½ stage, model turbine rig and open test case for non-axisymmetric endwall contouring based on the Durham cascade blade profile, secondly the investigation of the flow quality within a rotor with an endwall design based one of the more successful Durham designs using steady, 5-hole probe measurements and computational fluid dynamics. Lastly the intention was to investigate this test case at both design and off-design conditions.

In order to achieve the first of these aims, the 1½ stage turbine rig was brought back into operation and significantly refurbished by the author as has been described in Chapter 3. The blade set is representative of an intermediate pressure turbine in terms of its aspect ratio; and features a flow coefficient and loading at design of 0.52 and 0.7 respectively. The hub profile of the rotor matches that of the Durham cascade and as a result is both a relevant high turning angle profile, but can also accommodate the generic endwall contour developed for the cascade. The dataset generated as part of the flow mapping by 5-hole probe now represents one of only a few test cases for profiled endwalls (Durham University best represented by Ingram *et al.* 2002; Carleton University, represented by Praisner *et al.*, 2007) and even fewer rotating model turbines to have been tested with profiled endwalls (Schuepenbach, 2008a and De La Rosa Blanco *et al.*, 2005). No previous study of endwall contouring has provided both the full geometry as a test case for a rotating turbine and investigated the effects of off-design operation.

Experimental evidence has shown a 1.5% improvement in mixed out stage efficiency at the design condition with the application of a generic profiled endwall. This advantage shows a relationship with load, increasing from 0.4% at the negative incidence angle tested to 2.1% at the positive incidence angle. Hence this dataset confirms that non-axisymmetric endwall contouring is not only effective at off-design incidence but can be expected to yield increasing improvements as additional turning is demanded from the rotor with no penalty, in fact a gain at negative incidence. These improvements stem from reduced secondary kinetic energy immediately downstream of the rotor which results in lower mixing loss as one travels downstream. These gains are however not realised immediately downstream of the rotor or in the second stator at all conditions despite a generally more uniform exit flow angle from the rotor.

The effect of rotation has been noted from the translation of the same endwall geometry from the Durham cascade to this rotating case. Most notably the effect of rotation is through the increased migration of the vortex structures of the secondary flows spanwise to the extent that some interaction between hub secondary flows and tip leakage flows are possible. Similar trends are see between performance measures in the cascade and rotating cases when comparing baseline and profiled cases even if quantifiable comparison is not possible between cascade and rotating rig, the agreement in estimate efficiency improvement from the cascade and that realised in the rotating rig is, however, remarkable.

The profiling of the endwall acts by reducing the overall load on the hub section of the turbine and shifting it aft wards. Unlike other techniques aimed at reducing secondary

losses there is no apparent shift in the load towards the midspan and hence no loss penalty is experienced away from the hub, however the potential clearly exists that the overall torque of the stage can be reduced.

It would be best to design an endwall for the given flow; and off-design conditions, where these are important, need consideration. There are clear indications in the detailed flow structures and reduced torque that a custom designed endwall could further improve the efficacy of the endwall in this application, primarily by shifting the load at the hub aft wards but without reducing the total. The success of the generic profile in this study shows the robustness of the concept not only for design condition gains but also at off-design.

8.1 Recommendations for further work

The design of custom non-axisymmetric endwalls for this blading is clearly indicated as best practise. This exercise is underway as a postgraduate study at a local university. The use of hotwire anemometry to resolve the rotor exit flows is also currently receiving attention in a postgraduate study performed by my close collaborator Dwain Dunn and the completion of this study is much anticipated. Unsteady investigations of an Avio Spa designed endwall formed the crux of the EU FP6 VITAL contribution by the CSIR (Snedden *et al.*, 2009a).

Careful attention to observing consistent methodology and experimental setup is required when attempting to distinguish the small effects yielded by the subtle changes to endwall geometry in question. As the effects of endwall profiling extend from hub to tip a solution to the questions raised against the annular rotor exit results in this work and the use of a well in the casing is recommended as is further study of the nature and geometry of the tip gap. Some work on this has already taken place at Durham University where Prestridge and Ingram (2011) have investigated the effect on hub endwall contouring on tip gap flows in the Durham cascade.

If this test rig is to become a more comprehensive test case for CFD then a number of studies should be considered, including the characterisation of the inlet turbulence structure and boundary layer state as well as bearing and windage losses. Numerical study of the effect of the inlet support struts might also considered while experimental studies of the surface roughness of the blading and increased inlet turbulence might be considered.

One final remark highlights a further key aspect of this work. This rig in addition to state-of-the-art turbomachinery CFD has bought a new research direction into the South African research community, spawning further postgraduate studies at three local universities and receiving international recognition for the local community through European Framework funding and publication at the ASME IGTE and ISABE (Snedden *et al.*, 2007, 2009b, 2010b).

References

Abdelfattah SA and Schobeiri MT (2010) “Experimental and numerical investigations of aerodynamic behaviour of a three-stage HP turbine at different operating conditions”, ASME Turbo Expo GT2010-23564.

Atkins MJ (1987) “Secondary losses and end-wall profiling in a turbine cascade”, IMEchE C255/87, 1987.

Aunapu NV, Volino RJ and Flack KA (2000) “Surface flow visualisation in a scaled up turbine blade passage”, Measurement Science Technology, Vol 11, No. 7, pp 987-991.

AVIO SpA (2009) “EU FP6 Project VITAL Meetings and discussions”

Bagshaw DA, Ingram G, Gregory-Smith D and Stokes M (2005) “An experimental study of reverse compound lean in a linear turbine cascade”, Proceedings of IMechE, Part A: Journal of Power and Energy, 2005, 219(A6), pp 443–449.

Bagshaw DA, Ingram G, Gregory-Smith D and Stokes M (2008a) “The design of three-dimensional turbine blades combined with profiled endwalls”, Proceedings of the Institution of Mechanical Engineers, Vol 222, Part A, Journal of Power and Energy, pp 93-102.

Bagshaw DA, Ingram G, Gregory-Smith D and Stokes M (2008b) “An experimental study of three-dimensional turbine blades combined with profiled endwalls”, Proceedings of the Institution of Mechanical Engineers, Vol 222, Part A, Journal of Power and Energy, pp 103-110.

Benner MW, Sjolander SA and Moustapha SH (1997) “Measurements of secondary flows in a turbine cascade at off-design incidence”, ASME International Gas Turbine and Aeroengine Congress & Exhibition 97-GT-382.

Becz S, Majewski MS and Langston LS (2003) “Leading edge modification effects on turbine cascade endwall loss”, ASME Turbo Expo GT2003-38898.

Biesinger TE and Gregory-Smith DG (1993) “Reduction in secondary flow and losses in a turbine cascade by upstream boundary layer blowing”, ASME 93-GT-114.

Bindon JP, Aburwin BA and MacCallum NRL (1979) “Comparison of transverse injection effects in annular and in straight turbine cascades”, ASME 79-GT-17.

Bindon JP (1989) “The measurement and formation of tip clearance loss”, ASME Journal of Turbomachinery, Vol. 111, pp 257-263, July 1989.

Bindon JP (2010) Private communications

Bloxham MJ and Bons JP (2010) “Combined blowing and suction to control both midspan and endwall losses in a turbomachinery passage”, ASME Turbo Expo GT2010-23552.

Boyle RJ, Rholik HE and Goldman LJ (1981) “Analytic investigation of effect of end-wall contouring on stator performance”, NASA-TP-1943, E-719.

Brennan G, Harvey N, Rose MG, Fomison N and Taylor MD (2001) "Improving the efficiency of the Trent 500 HP turbine using non-axisymmetric end walls: Part 1 Turbine design", ASME Turbo Expo 2001-GT-0444.

Chung JT, Simon TW and Buddhavarapu J (1991) "Three-dimensional flow near the blade/endwall junction of a gas turbine: Application of a boundary layer fence", ASME International Gas Turbine & Aeroengine Congress and Exhibition, 91-GT-45.

Coleman, HW, Steele, WG (1989) "Experimentation and uncertainty analysis for engineers", 1st ed., John Wiley & Sons, Inc., United States of America, 1989.

Corral R and Gisbert F (2006) "Profiled end-wall design using an adjoint Navier-Stokes solver", ASME Turbo Expo GT2006-90650.

Cumpsty AN (2009) "Preparing for the future: Reducing gas turbine environmental impact", IGTI Scholar Lecture, Proceedings of the ASME Turbo 2009, Paper GT2009-60367, Orlando Florida, USA, 8-12 June 2009.

De La Rosa Blanco E, Hodson HP and Vasquez R (2005) "Effect of upstream platform geometry on the endwall flows of a turbine cascade", ASME Turbo Expo GT2005-68938.

De La Rosa Blanco E, Hodson HP and Vasquez R (2006) "Effect of the leakage flows and upstream platform geometry on the endwall flows of a turbine cascade", ASME Turbo Expo GT2006-90767.

Denton JD (1993) "Loss mechanisms in turbomachines", ASME Gas Turbine Congress, Scholars Paper.

Denton JD and Xu L (1999) "The exploitation of three-dimensional flow in turbomachinery design", Proceedings of the Institution of Mechanical Engineers, Vol 213, Part C, pp 125-137.

Denton JD (2010) "Some limitations of turbomachinery CFD", ASME Turbo Expo GT2010-22540.

Duden A, Raab I and Fottner L (1999) "Controlling the secondary flow in a turbine cascade by three dimensional airfoil design and endwall contouring", ASME Journal of Turbomachinery, Vol. 121, pp 191-199, April 1999.

Duden A and Fottner L (1999) "The secondary flow field of a turbine cascade with 3D airfoil design and endwall contouring at off design incidence", ASME International Gas Turbine and Aeroengine Congress and Exhibition, 99-GT-211.

Dunham J and Meauze G (1998) "An AGARD working group study of 3D Navier-Stokes codes applied to single turbomachinery blade rows", ASME International Gas Turbine & Aeroengine Congress and Exhibition, 98-GT-50.

Dunn D, Snedden G and Von Backstrom TW (2009) "Turbulence model comparisons for a low pressure 1.5 stage test turbine", ISABE 2009-1258, Montreal, Canada.

Eymann S, Reinmoller U, Neihuis R, Forster W, Beversdorff M and Gier J (2002) “Improving 3D flow characteristics in a multistage LP turbine by means of endwall contouring and airfoil design modification – Part 1: Design and experimental investigation”, ASME Turbo Expo GT-2002-30352.

Funazaki K, Endo T and Tanuma T (1996) "Reduction of secondary flow effects in a linear cascade by use of an air suction from the endwall”, ASME 96-TA-51.

Germain T, Nagel M, Raab I, Schuepbach P, Abhari RS and Rose M (2008) “Improving efficiency of a high work turbine using non-axisymmetric endwalls Part I: Endwall design and performance”, ASME GT2008-50469.

Goldstein RJ and Spores RA (1998) “Turbulent transport on the endwall in the region between adjacent turbine blades”, ASME Journal of Heat Transfer Vol. 110, pp 862-869.

Gonzalez P and Lantero M (2006) “Low pressure turbine design for Rolls-Royce TRENT 900 turbofan”, ASME Turbo Expo, GT2006-90997.

Gregory-Smith D (1984) “Secondary flows and endwall boundary layers in axial turbomachines”, Von Karman Institute for Fluid Dynamics Lecture Series 1984-05, May 7-11, 1984.

Gregory-Smith D, Graves C, and Walsh J (1988) “Growth of secondary losses and vorticity in an axial turbine cascade”, ASME Journal of Turbomachinery, Vol. 110, pp 1-7, January 1988..

Gregory-Smith D (1995) “Calculations of the secondary flow in a turbine cascade”, ASME AD-Vol. 49, Computational Fluid Dynamics in Aeropropulsion, pp 77-87, 1995.

Gregory-Smith, D., Ingram, G., Jayaraman, P., Harvey, N., and Rose, M. (2001) “Non-axisymmetric turbine end wall profiling”, Proceedings of the Institution of Mechanical Engineers.

Gregory-Smith DG and Crossland SC (2001) “Prediction of turbomachinery flow physics from CFD – Review of recent computations of APPACET test cases”, TASK Quarterly 5 No. 4, pp 407-431.

Haas JE (1982) “Analytical and experimental investigation of stator endwall contouring in a small axial-flow turbine. I - Stator performance”, NASA Technical report 2023

Han W, Wang Z, Tan C, Hong S and Zhou M (1994) “Effects of leaning and curving of blades with high turning angles on the aerodynamic characteristics of turbine rectangular cascades”, ASME journal of Turbomachinery, Vol. 116, pp 417-424, July 1994.

Harrison S (1990) “Secondary loss generation in a linear cascade of high-turning turbine blades”, ASME Journal of Turbomachinery, Vol. 112, pp 618-624, October 1990.

Harrison S (1992) “The influence of blade lean on turbine losses”, ASME Journal of Turbomachinery, Vol. 114, pp 184-190, January 1992.

Hartland JC, Gregory-Smith DG and Rose MG (1998) “Non-axisymmetric endwall profiling in a turbine rotor cascade”, ASME International Gas Turbine & Aeroengine Congress and Exhibition, 98-GT-525.

Hartland J, Gregory-Smith D, Harvey N, and Rose MG, (2000) “Non-axisymmetric Turbine End Wall Design: Part II Experimental Validation”, Transactions of the ASME Journal of Turbomachinery, Vol. 122, pp. 286-293.

Hartland J and Gregory-Smith D (2002) “A design method for the profiling of end walls in turbines”, ASME Turbo Expo GT-2002-30433.

Harvey N and Ramsden K (2000) “A computational study of a novel turbine rotor partial shroud”, ASME Turbo Expo 2000, Paper 2000-GT-668.

Harvey N, Rose MG, Shahpar S, Taylor MD, Hartland J, and Gregory-Smith D, (2000) “Non-axisymmetric Turbine End Wall Design: Part I Three dimensional Design System”, Transactions of the ASME Journal of Turbomachinery, Vol. 122, pp. 278-285.

Harvey N and Rose MG (2001) “Blade ducting for turbomachinery”, US Patent 6283713 BA.

Harvey N, Brennan G, Newman DA and Rose MG (2002) "Improving turbine efficiency using non-axisymmetric endwalls: Validation in the multi-row environment and with low aspect ratio blading”, ASME Turbo Expo 2002-GT-30337.

Hildebrandt T (2010) “Personal communications.”

Ho Y-H and Lakshminarayana (1996) “Computational modelling of three-dimensional endwall flow through a turbine rotor cascade with strong secondary flows”, ASME Journal of Turbomachinery, Vol. 118, pp 250-261, April 1996.

Hodson HP and Dominy RG (1987a) “Three-dimensional flow in a low-pressure turbine cascade at its design condition”, ASME Journal of Turbomachinery, Vol. 109, pp 177-185, April 1987.

Hodson HP and Dominy RG (1987b) “The off-design performance of a low-pressure turbine cascade”, ASME Journal of Turbomachinery, Vol. 109, pp 201-209, April 1987.

Holman JP (1985) “Experimental methods for engineers” MCGraw-Hill International Student Edition, 4th Edition, 3rd Printing, 1985.

http://rolls-royce.com

Hunter IH (1982) “Endwall boundary layer flows and losses in an axial Turbine Stage”, ASME Journal of Engineering for Power, Vol. 104, pp 184-193, January 1982.

Ingram G (2003) “Endwall profiling for the reduction of secondary flow in turbines”, Durham University, UK.

Ingram G, Gregory-Smith D, Rose M, Harvey N and Brennan G (2002) “The effect of endwall profiling on secondary loss development in a turbine cascade”, ASME Turbo Expo GT-2002-30339.

Ingram G, Gregory-Smith D and Harvey N (2003) “Experimental quantification of the benefits of end-wall profiling in a turbine cascade”, ISABE 2003-1101.

Ingram G and Gregory-Smith G (2005) “An automated instrumentation system for flow and loss measurements in a cascade”, Journal of Flow Measurement and Instrumentation.

Ingram G, Gregory-Smith D and Harvey N (2005) “Investigation of a novel secondary flow feature in a turbine cascade with end wall profiling”, ASME journal of Turbomachinery, Vol. 127, pp 209-214, January 2005.

Kaiser I (1996) “The effect of tip clearance and tip gap geometry on the performance of a one and a half stage axial gas turbine” University of Natal Durban South Africa.

Kawai T (1994) "Effect of combined boundary layer fences on turbine secondary flow and losses”, JSME International Journal, Series B: Fluids and Thermal Engineering, Vol. 37, No. 2, pp. 377-384.

Knezevici DC, Sjolander SA, Praisner TJ, Allen-Bradley E and Grover EA, (2008) “Measurements of secondary losses in a turbine cascade with the implementation of non-axisymmetric endwall contouring”, ASME Turbo Expo GT2008-51311.

Knezevici DC, Sjolander SA, Praisner TJ, Allen-Bradley E and Grover EA, (2009) “Measurements of secondary losses in a high-lift front-loaded turbine cascade with the implementation of non-axisymmetric endwall contouring”, ASME Turbo Expo GT2009-59677.

Lampart P, Gardzilewicz A, Rusanov A and Yershov S (1999) "Effect of stator blade compound lean and compound twist on flow characteristics of a turbine stage - numerical study based on NS simulations”, Transactions of ASME, Pressure Vessels and Piping, Vol. 397, pp. 195-204.

Langston LS (2001) “Secondary flows in axial turbines – A review”, Annals of the New York Academy of Sciences, Vol. 934, Heat Transfer in Gas Turbine Systems, pp 11–26, May 2001.

Langston LS, Nice ML and Hooper RM (1977) "Three-dimensional flow within a turbine cascade passage”, Transactions of ASME, Journal of Engineering for Power, pp. 21-28.

Lethander AT, Thole KA, Zess GA and Wagner J (2003) “Optimizing the vane-endwall junction to reduce adiabatic wall temperature in a turbine vane passage”, ASME Turbo Expo 2003, GT2003-38939, Atlanta USA.

Lott PT, Hills NJ, Chew JW, Scanion T and Shahpar S (2009) “High pressure turbine stage endwall profile optimisation for performance and rim seal effectiveness”, ASME Turbo Expo GT2009-59923.

Luo J and Lakshminarayana B (1997) “Three-dimensional Navier-Stokes computation of a turbine nozzle flow with advanced turbulence models”, ASME journal of Turbomachinery, Vol. 119, pp 516-530, July 1997.

MacPherson R and Ingram G (2010) “Endwall profile design for the Durham cascade using genetic algorithms”, Seventh South African Conference on Computational and Applied Mechanics, January 2010.

Mahallati A, McAuliffe BR, Sjolander SA and Praisner TJ, (2007) “Aerodynamics of a low-pressure turbine airfoil at low Reynolds numbers Part 1: Steady flow measurements”, ASME Turbo Expo, GT2007-27347.

Mentor FR (1993) “Zonal Two Equation k-ω Turbulence Models for Aerodynamic Flows”, AIAA Paper 93-2906.

Menter FR (1994) “Two-equation eddy-viscosity turbulence models for engineering applications”, AIAA Journal, Vol. 32, pp 269–289, 1994.

Michelassi V, Martelli F and Corradini U (1998) “Secondary flow decay downstream of turbine inlet guide vane with end-wall contouring”, ASME International Gas Turbine & Aeroengine Congress and Exhibition, 98-GT-95.

Moon YJ and Sung-Ryon K (2001) "Counter-rotating streamwise vortex formation in the turbine cascade with endwall fence”, Computers & Fluids, Vol. 30, No. No. 4, pp. 473-490.

Moore H and Gregory-Smith DG (1996) “Transition effects on secondary flows in a turbine cascade”, ASME International Gas Turbine and Aeroengine Congress and Exhibition 96-GT-100.

Morphis G and Bindon JP (1988) “The effect of relative motion, blade edge radius and gap size on blade tip pressure distribution in an annular turbine cascade with clearance”, ASME 88-GT-256.

Morphis G (1993) “The performance of a one and a half stage axial turbine including various tip clearance effects” University of Natal Durban South Africa.

Morphis G and Bindon JP (1994) "The performance of a low speed one and a half stage axial turbine with varying rotor tip clearance and tip gap geometry”, International Gas Turbine and Aeroengine Congress and Exposition, ASME 94-GT-481.

Moustapha SH, Paron GJ and Wade JHT (1985) “Secondary flows in cascades of highly loaded cascades”, ASME Journal of Engineering for Gas Turbines and Power, Vol. 107, pp 1031-1038, October 1985.

Moustapha SH, Okapuu U and Williamson RG (1986) “Influence of rotor blade aerodynamic loading on the performance of a highly loaded turbine stage”, ASME Journal of Engineering for Gas Turbines and Power, ASME 86-GT-56.

Moustapha H, Zelesky MF, Baines NC and Japikse D (2003) “Axial and radial turbines” Concepts NREC, pp49.

Nagel MG, Fottner L and Baier R-D (2001) “Optimization of three dimensionally designed turbine blades and side walls”, ISABE 2001-1058.

NREC (1972) “The design and performance analysis of axial-flow turbines: Volumes I and II”, Northern Research and Engineering Corporation.

Numeca International, (2005) “User Manual FINE/Turbo v8 (including Euranus) Documentation v8a”, v8a edition.

Ollson U (2004) “Aerospace propulsion from insects to spaceplanes” Aerospace Propulsion Short Course, Volvo Aero.

Piggush JD and Simon TW (2005) “ Flow measurements in a first stage nozzle cascade having endwall contouring, leakage and assembly features”, ASME Turbo Expo Gt2005-68340.

Praisner TJ, Allen-Bradley E, Grover EA, Knezevici DC and Sjolander SA, (2007) “Application of non-axisymmetric endwall contouring to conventional and high-lift turbine airfoils”, ASME Turbo Expo GT2007-27579.

Prestridge N and Ingram G (2011) “Investigation into the effects of non-axisymmetric endwall profiling on tip clearance flows”, MEng Research Project, 2011.

Pullan G, Denton J and Curtis E (2005) “Improving the performance of a turbine with low-aspect ratio stators by aft-loading”, ASME Turbo Expo GT2005-68548.

Rao NM and Camci C (2005) “Visualisation of rotor endwall, tip gap, and outer casing surface flows in a rotating axial turbine rig”, ASME Turbo Expo GT2005-68264.

Reising S. and Schiffer H.-P., (2009) “Non-Axisymmetric End Wall Profiling in Transonic Compressors. Part I: Improving the Static Pressure Recovery at Off-Design Conditions by Sequential Hub and Shroud End Wall Profiling”, ASME Turbo Expo GT2009-59133.

Richards PH and Johnson CG (1988) “Development of secondary flows in the stator of a model turbine”, Experiments in Fluids, Vol. 6, pp 2-10, 1998.

Reising S and Schiffer H-P (2009) “Non-axisymmetric end wall profiling in transonic Compressors. Part I: Improving the static pressure recovery at off-design conditions by sequential hub and shroud end wall profiling”, ASME Turbo Expo GT2009-59133, 2009.

Ristic D, Lakshminarayana B and Chu S (1999) “Three-dimensional flowfield downstream of an axial-flow turbine rotor”, Journal of Propulsion and Power, Vol. 15, No. 2, pp 334-344, March-April, 1999.

Roos THR (2006) “Personal communications.”

Rose MG (1994) “Non-axisymmetric endwall profiling in HP NGV’s of an axial flow gas turbine”, ASME Turbo Expo 94-GT-249.

Rose MG (1995) “Gas Turbine Engine Turbine” US Patent 5466123, November 1995.

Rose MG, Harvey NW, Seaman P, Newman DA, and McManus D, (2001) “Improving the Efficiency of the Trent 500 HP Turbine Using Non-Axisymmetric End Walls. Part II: Experimental Validation”, ASME Turbo Expo 2001-GT-0505.

Saravanamuttoo HIH, Rogers CFC and Cohen H (2001) “Gas turbine theory”, 5th Edition, Prentice Hall.

Sauer H, Muller R and Vogeler K (2001) "Reduction of secondary flow losses in turbine cascades by leading edge modifications at the endwall”, Transaction of the ASME, Journal of Turbomachinery, Vol. 123, No. No. 2, pp. 207-213.

Sauer H, Schmidt R and Vogeler K (2001) “Influence of chord length and inlet boundary layer on the secondary losses of turbine blades”, ASME Turbo Expo GT2010-22065.

Schlegel JC, Lu HC and Waterman WF (1976) “Reduction of end-wall effects in a small, low-aspect-ratio turbine by radial work redistribution” ASME Journal of Engineering for Power, pp 130-136, January 1976.

Schuepbach P, Abhari RS, Rose M, Germain T., Raab I., and Gier J (2008a) “Improving efficiency of a high work turbine using non-axisymmetric endwalls Part II: Time resolved flow physics”, ASME Turbo Expo GT2008-50470.

Schuepbach P, Abhari RS, Rose MG, Germain T, Raab I and Gier J (2008b) “Effects of suction and injection purge flow structures of a high work turbine”, ASME Turbo Expo GT2008-50471.

Schuepbach P, Abhari RS, Rose MG and Gier J (2009) “Influence of rim seal purge flow on performance of an endwall-profiled axial turbine”, ASME Turbo Expo GT2009-59653.

Shah N (2006) “The history of UK inflation”, Stone and McCarthy Research Associates, July 2006.

Shahpar S and Lapworth BL (1998) “A forward and inverse three-dimensional linear design system for turbomachinery applications”, ECCOMAS 98, John Wiley & Sons Ltd, 1998.

Sharma OP, Kopper FC, Stetson GM, Magge SS, Price FR and Ni R (2003) “A persective on the use of physical and numerical experiments in the advancement of design technology for axial flow turbines”, ISABE 2003-1035, Cleveland, USA.

Shaw R and Abu-Ghannam BJ (1980) “Natural transition of boundary layer - the effect of turbulence, pressure gradient and flow history’’ Journal of Mechanical Engineering Science, 22 (5), pp 213-228.

Sieverding CH (1985) "Recent progress in the understanding of the basic aspects of secondary flows in turbine blade passages”, Transactions of ASME, Journal of Engineering for Gas Turbines and Power , Vol. 107, pp 248-252, 1985.

Sjolander SA and Amrud KK (1987) “Effects of tip clearance on blade loading in a planar cascade of turbine blades”, ASME Journal of Turbomachinery, Vol. 109, pp 237-245, April 1987.

Snedden G, Roos T, Dunn D and Gregory-Smith D (2007) “Characterisation of a refurbished 1½ stage turbine test rig for flowfield mapping behind blading with non-axisymmetric contoured endwalls”, ISABE 2007-1363, Beijing, China.

Snedden G, Dunn D and Zwane N (2009a) “Deliverable D6.2.10B – Experimental Results Report”, EU FP6 VITAL Report.

Snedden G, Dunn D, Ingram G and Gregory-Smith D, (2009b) “The Application of Non-Axisymmetric Endwall Contouring in a Single Stage, Rotating Turbine”, ASME Turbo Expo GT2009-59169.

Snedden G, Dunn D, Von Backstrom TW and Ingram I (2010a) “Observations on the selection of objective function for the optimisation of turbine endwalls using computational fluid dynamics”, Seventh South African Conference on Computational and Applied Mechanics, January 2010.

Snedden G, Dunn D, Ingram G and Gregory-Smith D (2010b) “The performance of a generic non-axisymmetric end wall in a single stage, rotating turbine at on and off-design conditions”, ASME Turbo Expo GT2010-22006.

Stamatios P (2002) “Control of particles and turbulence using a piezoelectric actuator”, PhD Thesis, University of Minnesota.

Swelbar WS and Belobaba PP (2010) “Airline Data Project”, MIT Global Airline Industry Programme, http://web.mit.edu/airlinedata/www/default.html.

Torre D, Vazquez R, De la Rosa Blanco E and Hodson HP (2006) “A new alternative for reduction of secondary flows in low pressure turbines”, ASME Turbo Expo GT2006-91002.

TSI (2006) “TSI Thermal Anemometry Probe”, Hotwire Catalogue 2980465, TSI Inc. Fluid Mechanics.

Tsujita H, Mizuki S and Yamamoto A (2006) “Numerical investigation of effects of incidence angle on aerodynamic performance of ultra-highly loaded turbine cascade”, ASME Turbo Expo GT2006-90939.

Van Den Berg B and Bertelrud A (1988) “Measurement techniques in low speed turbulent flows: A report on Euromech 202”, Experiments in Fluids 6, pp 61-66, 1988.

Vasquez R and Fidalgo VJ (2010) “The effect of Reynolds and Mach number on endwall profiling performance”, ASME Turbo Expo GT2010-22765.

Versteeg HK and Malalasekera W (1995) “An Introduction to Computational Fluid Dynamics, The Finite Volume Method”, Pearson Prentice Hall, 1995

Vogt H-F and Zippel M (1996) “Sekundarstromungen in Turbinengittern mit geraden und gekrummten Schaufeln; Visualisierung im ebenen Wasserkanal” Forschung im Ingenieurwesen, Engineering Research, Vol. 62, no. 9, pp 247 - 253.

Walsh JA and Gregory-Smith D (1987) “The effect of inlet skew on the secondary flow losses in a turbine cascade”, Proceedings of the Institute of Mechanical Engineering, International Conference - Turbomachinery Efficiency Prediction and Improvement, C275/87, pp 15-28, 1987.

Wang Z, Han W and Xu W (1991) “The effect of blade curving on flow characteristics in rectangular turbine cascades with different incidences”, ASME International Gas Turbine & Aeroengine Congress and Exhibition, 91-GT-60.

Wang HP, Olson SJ, Goldstein RJ and Eckert ERG (1997) “Flow visualization in a linear turbine cascade of high performance turbine blades”, Transactions of the ASME, Journal of Turbomachinery, Vol. 119, pp. 1-8.

Watanabe H and Harada H (1999) "Supression of secondary flows in turbine nozzle with controlled stacking shape and exit circulation by 3D inverse design method”, ASME 99-GT-72.

Weiss AP and Fottner L (1995) “The influence of load distribution on secondary flow in straight turbine cascades”, ASME Journal of Turbomachinery, Vol. 117, pp133-141, January 1995.

White FM (2006) “Viscous Fluid Flow” 3rd Edition, McGraw Hill International Edition

Whittle Commemorative Trust, “A brief history of power jets”, http://www.frankwhittle.co.uk.

Wilcox DC (1998) “Turbulence Modeling for CFD”, DCW Industries, Inc., La Canada, California.

Wild P and Hockman Y (2007) “Stochastic Modelling for Dummies”, Actuarial Society of South Africa Convention, 2007.

Williamson RG (1987) “Discussion of Sjolander and Amrud (1987)” ASME Journal of Turbomachinery, Vol. 109, pp 244-245, April 1987.

Yamamoto A (1988) “Interaction mechanisms between tip leakage flow and the passage vortex in a linear turbine rotor cascade”, ASME Journal of Turbomachinery, Vol. 111, pp 264-275, July 1988.

Yamamoto A and Nouse H (1988) “Three-dimensional flows and loss generation mechanisms in a linear turbine rotor cascade at various incidence conditions”, Technical Report of the National Aerospace Laboratory TR-984T.

Yamamoto A (1989) “Endwall flow/loss mechanisms in a linear turbine cascade with blade tip clearance”, ASME Journal of Turbomachinery, Vol. 110, pp 329-338, July 1989.

Yan J, Gregory-Smith DG and Walker PJ (1999) “Secondary flow reduction in a Nozzle Guide Vane Cascade by non-axisymmetric end-wall rofiling”, ASME International Gas Turbine and Aeroengine Congress and Exhibition 99-GT-339.

Zess GA and Thole KA (2002) "Computational design and experimental evaluation of using a leading edge fillet on a gas turbine vane", Transactions of ASME, Journal of Turbomachinery, Vol. 124, pp. 167-175.

Zhou C and Hodson H (2009) "The tip leakage flow of an unshrouded high pressure turbine blade with tip cooling", ASME Turbo Expo GT2009-59637.

Zoric T, Popovic I, Sjolander SA, Praisner T and Grover E, (2007a) "Comparative investigation of three highly loaded LP turbine airfoils: Part I – Measured profile and secondary losses at design incidence", ASME Turbo Expo GT2007-27537.

Zoric T, Popovic I, Sjolander SA, Praisner T and Grover E, (2007b) "Comparative investigation of three highly loaded LP turbine airfoils: Part II – Measured profile and secondary losses at off-design incidence", ASME Turbo Expo GT2007-27538.

Zweiffel O (1945) "The spacing of turbo-machine blading, especially with large deflection", The Brown Boveri Review, December 1945.

Appendix A: Turbine Geometry

1st Stator Hub

Pressure Surface

X	Y	Z
141.8	7.5	-79.6
141.8	7.2	-79.5
141.8	7.0	-79.4
141.8	6.8	-79.2
141.8	6.7	-79.0
141.8	6.6	-78.8
141.8	6.6	-78.5
141.9	6.5	-78.2
141.9	6.0	-76.2
141.9	5.3	-74.3
141.9	4.3	-72.5
142.0	3.0	-70.9
142.0	1.7	-69.4
142.0	0.2	-67.9
142.0	-1.3	-66.6
142.0	-3.0	-65.4
141.9	-4.7	-64.3
141.9	-6.5	-63.3
141.8	-8.3	-62.3
141.6	-10.1	-61.4
141.5	-12.0	-60.4
141.3	-13.8	-59.5
141.1	-15.6	-58.7
140.9	-17.5	-57.8
140.7	-19.4	-57.0
140.4	-21.2	-56.2
140.2	-22.8	-55.5
140.1	-22.9	-55.4
140.1	-23.0	-55.3
140.1	-23.0	-55.2
140.1	-23.0	-55.1
140.1	-23.0	-54.9
140.1	-23.0	-54.8

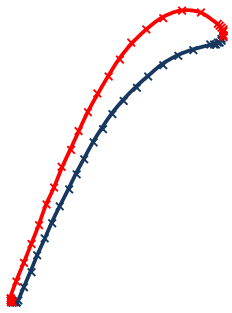

Suction Surface

X	Y	Z
141.8	7.5	-79.6
141.8	7.7	-79.6
141.8	8.0	-79.6
141.8	8.2	-79.6
141.7	8.5	-79.4
141.7	8.7	-79.3
141.7	9.0	-79.0
141.6	10.3	-77.0
141.6	10.5	-74.7
141.7	9.7	-72.5
141.8	8.3	-70.6
141.8	6.7	-68.9
141.9	4.9	-67.4
142.0	2.9	-66.1
142.0	0.9	-64.9
142.0	-1.2	-63.7
142.0	-3.3	-62.7
141.9	-5.4	-61.7
141.8	-7.5	-60.7
141.7	-9.7	-59.8
141.5	-11.8	-58.8
141.3	-14.0	-58.0
141.1	-16.2	-57.1
140.8	-18.4	-56.2
140.5	-20.5	-55.3
140.2	-22.4	-54.6
140.2	-22.5	-54.6
140.2	-22.6	-54.6
140.2	-22.8	-54.6
140.1	-22.9	-54.7
140.1	-23.0	-54.8

1st Stator Tip

Pressure Surface

X	Y	Z
201.8	16.8	-87.7
201.9	16.1	-87.4
201.9	15.7	-86.8
201.9	15.4	-86.2
201.9	15.2	-85.0
202.0	14.1	-82.0
202.1	12.6	-79.2
202.2	10.9	-76.5
202.3	9.0	-73.9
202.4	6.9	-71.5
202.4	4.7	-69.2
202.5	2.5	-66.9
202.5	0.1	-64.8
202.5	-2.3	-62.7
202.4	-4.8	-60.7
202.4	-7.4	-58.8
202.3	-10.0	-56.9
202.1	-12.7	-55.2
201.9	-15.4	-53.5
201.7	-18.2	-51.9
201.4	-20.9	-50.3
201.1	-23.8	-48.9
200.8	-26.6	-47.4
200.4	-29.4	-45.9
200.4	-29.4	-45.9
200.3	-29.6	-45.7
200.3	-29.7	-45.5
200.3	-29.6	-45.2
200.3	-29.6	-45.2

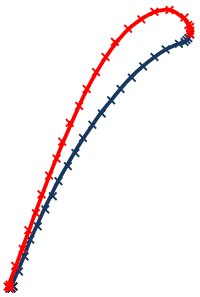

Suction Surface

X	Y	Z
201.8	16.8	-87.7
201.7	17.5	-87.8
201.7	18.1	-87.7
201.6	18.7	-87.3
201.5	19.8	-86.2
201.4	21.4	-83.0
201.4	21.1	-79.4
201.5	19.7	-76.0
201.7	17.8	-72.9
201.9	15.4	-70.2
202.1	12.7	-67.7
202.3	9.8	-65.4
202.4	6.8	-63.3
202.5	3.7	-61.4
202.5	0.5	-59.6
202.5	-2.7	-57.8
202.4	-5.9	-56.1
202.3	-9.2	-54.4
202.1	-12.5	-52.8
201.9	-15.8	-51.2
201.6	-19.1	-49.7
201.3	-22.4	-48.1
200.9	-25.7	-46.6
200.4	-28.9	-45.0
200.4	-29.2	-44.9
200.4	-29.4	-45.0
200.3	-29.6	-45.2

Rotor Hub

Pressure Surface

X	Y	Z
142.0	1.4	-18.8
142.0	2.1	-17.7
142.0	2.1	-16.5
142.0	1.7	-15.4
142.0	1.2	-14.3
142.0	0.7	-13.1
142.0	0.3	-12.0
142.0	0.0	-10.8
142.0	-0.3	-9.6
142.0	-0.5	-8.4
142.0	-0.6	-7.2
142.0	-0.7	-6.0
142.0	-0.7	-4.8
142.0	-0.6	-3.5
142.0	-0.4	-2.3
142.0	-0.1	-1.2
142.0	0.3	0.0
142.0	0.8	1.1
142.0	1.4	2.2
142.0	2.0	3.2
142.0	2.7	4.2
142.0	3.5	5.2
141.9	4.4	6.0
141.9	5.3	6.9
141.9	6.2	7.6
141.8	7.2	8.4
141.8	8.2	9.1
141.7	9.2	9.7
141.6	10.3	10.4
141.5	11.3	11.0
141.5	12.4	11.6
141.4	13.4	12.2
141.3	14.5	12.8
141.1	15.6	13.4
141.0	16.6	13.9
140.9	17.7	14.5
140.7	18.8	15.0
140.6	19.9	15.5
140.4	21.0	16.1
140.3	22.1	16.6
140.1	23.2	17.1
139.9	24.3	17.6
139.7	25.4	18.2
139.5	26.4	18.7
139.3	27.5	19.2
139.1	28.6	19.7
138.9	29.7	20.2
138.6	30.8	20.7
138.4	31.9	21.2
138.1	33.0	21.7
137.9	34.0	22.3
137.9	34.0	22.7

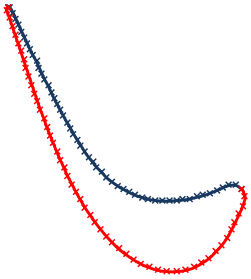

Suction Surface

X	Y	Z
142.0	1.4	-18.8
142.0	0.0	-19.3
142.0	-1.6	-18.9
142.0	-3.0	-18.3
141.9	-4.5	-17.6
141.9	-5.9	-16.9
141.8	-7.3	-16.1
141.7	-8.6	-15.2
141.7	-9.8	-14.1
141.6	-10.9	-13.0
141.5	-11.8	-11.7
141.4	-12.6	-10.3
141.4	-13.1	-8.7
141.4	-13.3	-7.2
141.4	-13.3	-5.6
141.4	-13.1	-4.0
141.4	-12.6	-2.4
141.5	-12.0	-1.0
141.6	-11.2	0.4
141.6	-10.3	1.7
141.7	-9.3	3.0
141.8	-8.2	4.1
141.8	-7.0	5.2
141.9	-5.8	6.2
141.9	-4.5	7.2
142.0	-3.2	8.1
142.0	-1.9	9.0
142.0	-0.5	9.8
142.0	0.9	10.6
142.0	2.3	11.3
142.0	3.8	12.1
141.9	5.2	12.7
141.8	6.7	13.4
141.8	8.1	14.0
141.7	9.6	14.6
141.6	11.1	15.2
141.4	12.6	15.8
141.3	14.1	16.3
141.1	15.6	16.9
141.0	17.1	17.4
140.8	18.6	17.9
140.6	20.1	18.4
140.3	21.6	18.9
140.1	23.1	19.4
139.9	24.6	19.9
139.6	26.1	20.4
139.3	27.6	20.9
139.0	29.1	21.4
138.7	30.6	21.9
138.3	32.1	22.4
138.0	33.5	22.9
137.9	34.0	22.7

Rotor Tip

Pressure Surface

X	Y	Z
200.8	-22.0	-21.4
200.8	-22.0	-21.4
200.8	-21.8	-21.5
200.8	-21.5	-21.5
200.9	-21.3	-21.6
200.9	-21.1	-21.6
200.9	-20.9	-21.6
200.9	-20.7	-21.6
201.0	-20.4	-21.5
201.0	-20.2	-21.5
201.3	-17.0	-19.8
201.6	-13.4	-17.7
201.7	-10.1	-15.1
201.9	-7.0	-12.5
202.0	-3.8	-9.8
202.0	-0.7	-7.2
202.0	2.5	-4.6
201.9	5.8	-2.1
201.8	9.1	0.4
201.6	12.4	2.7
201.4	15.9	4.9
201.1	19.5	6.9
200.7	23.1	8.8
200.2	26.8	10.6
199.7	30.5	12.3
199.1	34.2	14.0
198.4	37.9	15.6
197.7	41.7	17.1
196.8	45.4	18.5
195.9	49.2	19.9
195.1	52.2	21.1
195.1	52.3	21.2
195.1	52.4	21.2
195.1	52.4	21.3
195.1	52.5	21.3
195.1	52.5	21.4
195.0	52.5	21.4
195.0	52.6	21.5
195.0	52.6	21.6
195.0	52.6	21.6
195.0	52.6	21.7
195.0	52.6	21.8
195.0	52.6	21.9
195.0	52.6	21.9

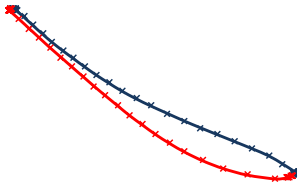

Suction Surface

X	Y	Z
200.8	-22.0	-21.4
200.8	-22.2	-21.3
200.8	-22.3	-21.2
200.7	-22.5	-21.1
200.7	-22.7	-20.9
200.7	-22.8	-20.7
200.7	-23.0	-20.6
200.7	-23.1	-20.4
200.6	-23.5	-18.7
200.8	-21.8	-14.4
201.1	-18.9	-10.7
201.4	-15.5	-7.6
201.7	-11.6	-4.8
201.9	-7.6	-2.4
202.0	-3.5	-0.2
202.0	0.7	1.8
201.9	5.0	3.8
201.8	9.3	5.6
201.5	13.6	7.4
201.2	18.0	9.2
200.8	22.3	10.9
200.2	26.6	12.6
199.6	31.0	14.3
198.9	35.3	16.0
198.1	39.6	17.6
197.2	43.9	19.2
196.2	48.2	20.8
195.2	51.8	22.2
195.2	51.9	22.3
195.2	52.0	22.3
195.2	52.0	22.3
195.2	52.1	22.3
195.1	52.2	22.3
195.1	52.2	22.2
195.1	52.3	22.2
195.1	52.4	22.2
195.1	52.4	22.1
195.1	52.5	22.1
195.1	52.5	22.0
195.0	52.5	21.9
195.0	52.6	21.9

Rotor Non-axisymmetric Endwall Contour

23.3992% scale by C_{ax} of original Durham P2 (Ingram, 2003) wrapped to annular endwall

Leading edge

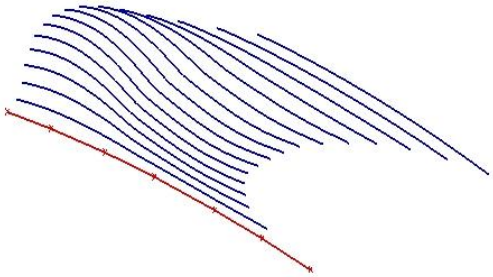

X	Y
137.20	36.59
138.77	29.80
140.40	21.13
141.32	14.08
141.88	6.42
142.00	0.25

5.53% C_{ax}

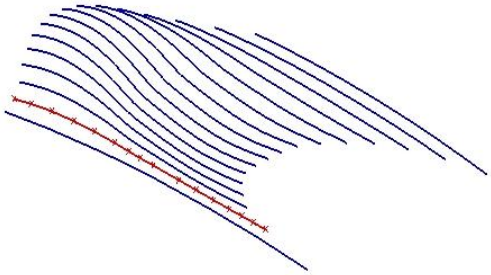

X	Y
137.12	36.13
137.47	34.39
137.80	32.72
138.14	30.98
138.60	28.73
139.13	26.19
139.64	23.73
140.41	20.06
140.76	18.20
141.14	16.55
141.63	14.48
142.19	11.59
142.61	8.68
142.83	5.54
142.80	2.64
142.62	0.28

11.05% C_{ax}

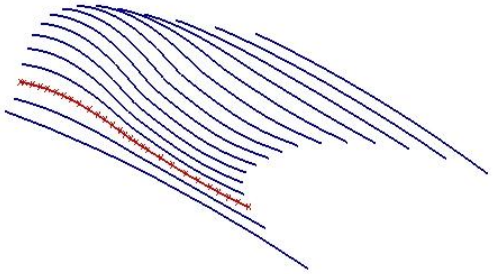

X	Y
137.54	32.36
137.73	30.89
137.92	29.57
138.17	28.14
138.39	26.93
138.73	25.15
139.11	23.45
139.60	21.52
140.04	19.82
140.53	17.99
140.71	17.28
140.98	16.26
141.24	15.49
141.53	14.70
141.80	13.97
142.23	12.85
142.61	11.73
142.90	10.72
143.23	9.47
143.56	8.03
143.75	6.90
143.90	5.85
143.99	4.75
144.00	3.49
143.95	2.52
143.86	1.42
143.71	0.29
143.61	-0.25

16.57% C_{ax}

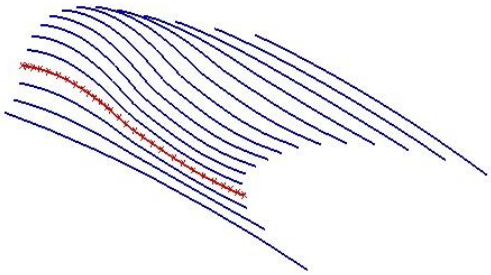

X	Y
137.51	30.59
137.57	29.66
137.66	28.63
137.77	27.65
137.95	26.34
138.19	24.88
138.51	23.38
138.89	21.84
139.25	20.55
139.79	18.75
140.19	17.52
140.65	16.11
141.07	14.87
141.60	13.65
142.15	12.56
142.74	11.39
143.03	10.79
143.44	9.87
143.77	9.02
144.09	8.14
144.37	7.26
144.64	6.22
144.87	5.04
145.03	3.80
145.07	2.40
144.99	1.20
144.86	0.24
144.71	-0.60
144.54	-1.29

22.10% C_{ax}

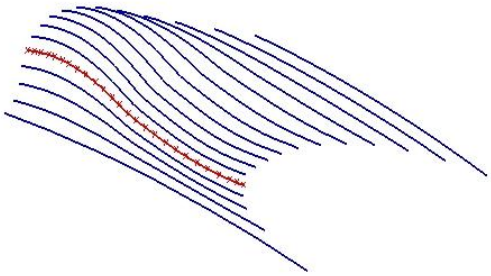

X	Y
137.40	29.24
137.43	28.30
137.48	27.31
137.62	25.88
137.85	24.22
138.14	22.70
138.55	21.08
138.96	19.68
139.44	18.21
140.03	16.59
140.53	15.26
141.09	13.83
141.66	12.68
142.48	11.38
143.13	10.34
143.85	9.02
144.43	7.83
145.02	6.41
145.40	5.24
145.69	3.99
145.83	3.10
145.91	1.97
145.90	1.10
145.80	-0.01
145.63	-0.88
145.39	-1.86

27.62% C_{ax}

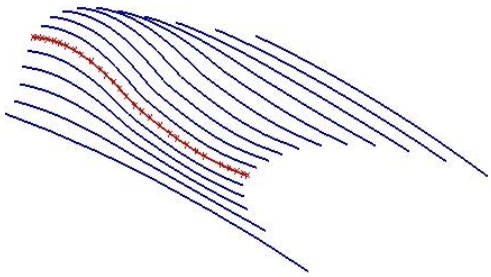

X	Y
137.31	28.49
137.33	27.93
137.34	26.96
137.39	25.93
137.48	24.80
137.84	22.46
138.12	21.28
138.52	19.89
138.97	18.47
139.32	17.48
139.91	15.96
140.50	14.48
141.00	13.34
141.48	12.36
142.39	11.04
143.12	10.01
143.75	9.07
144.37	8.02
144.85	7.15
145.51	5.77
146.00	4.38
146.25	3.35
146.42	2.24
146.49	1.27
146.48	0.46
146.39	-0.49
146.26	-1.23
146.08	-1.91
145.92	-2.46

33.15% C_{ax}

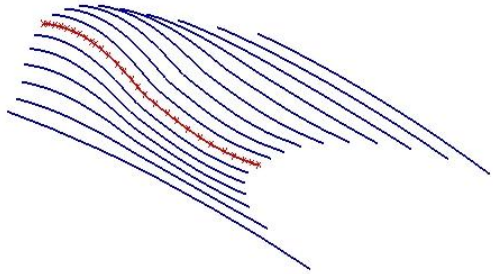

X	Y
137.25	28.54
137.22	27.55
137.23	26.55
137.29	25.11
137.44	23.76
137.78	21.80
138.17	20.27
138.76	18.50
139.38	16.83
139.94	15.46
140.70	13.71
141.42	12.17
142.20	11.10
142.93	10.16
143.76	9.01
144.40	8.04
145.20	6.68
145.72	5.65
146.09	4.75
146.26	4.28
146.52	3.39
146.72	2.48
146.81	1.57
146.84	0.69
146.80	-0.15
146.69	-0.99
146.47	-1.97
146.26	-2.58

38.67% C_{ax}

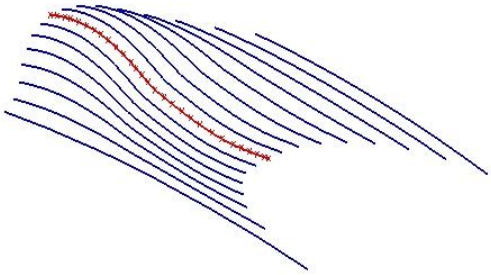

X	Y
137.17	29.01
137.18	28.46
137.17	27.42
137.19	26.34
137.26	25.19
137.37	24.05
137.61	22.46
137.94	21.04
138.47	19.25
138.9	17.96
139.44	16.64
140.03	15.28
140.55	14.07
141.14	12.77
141.87	11.67
142.59	10.76
143.25	9.90
143.81	9.12
144.60	7.96
145.23	6.89
145.82	5.72
146.26	4.64
146.55	3.723
146.79	2.62
146.88	1.45
146.87	0.29
146.82	-0.47
146.62	-1.58
146.35	-2.48

44.20% C_{ax}

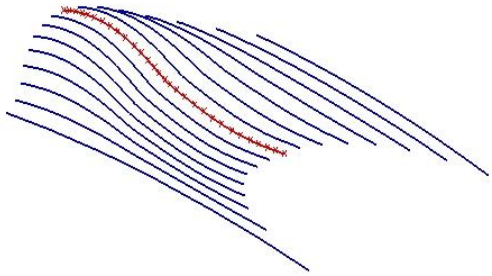

X	Y
137.10	29.80
137.11	28.54
137.11	27.45
137.16	26.19
137.27	25.04
137.47	23.63
137.71	22.42
138.11	20.91
138.49	19.65
138.99	18.30
139.51	17.01
140.12	15.54
140.65	14.32
141.08	13.37
141.52	12.62
142.19	11.74
142.74	11.03
143.44	10.08
144.17	9.02
144.77	8.04
145.49	6.68
145.97	5.56
146.32	4.50
146.59	3.33
146.72	2.18
146.74	1.28
146.69	0.51
146.58	-0.44
146.38	-1.308
146.15	-2.06

49.72% C_{ax}

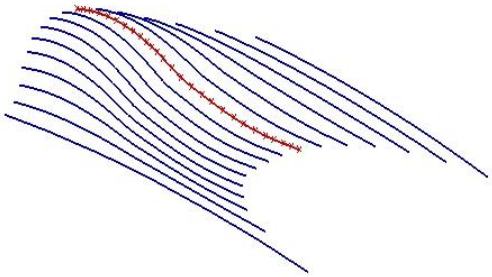

X	Y
137.09	30.81
137.15	29.70
137.17	28.60
137.22	27.22
137.32	26.08
137.55	24.60
137.90	22.93
138.28	21.51
138.81	19.96
139.41	18.27
139.94	16.94
140.58	15.38
141.29	13.84
142.23	12.48
143.13	11.16
143.70	10.27
144.17	9.48
144.59	8.70
145.04	7.77
145.47	6.75
145.85	5.57
146.13	4.30
146.27	3.10
146.27	1.87
146.14	0.67
145.92	-0.37
145.68	-1.20

55.25% C_{ax}

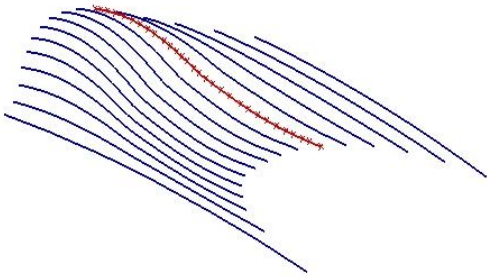

X	Y
136.78	35.13
136.94	34.16
137.08	32.99
137.21	31.88
137.39	30.71
137.67	29.16
137.88	28.17
138.16	26.85
138.46	25.58
138.80	24.31
139.13	23.17
139.57	21.66
139.92	20.48
140.24	19.42
140.54	18.48
140.87	17.47
141.31	16.46
141.77	15.45
142.29	14.25
142.64	13.37
143.02	12.29
143.34	11.31
143.71	9.97
144.00	8.52
144.18	7.26
144.27	5.87
144.26	4.61
144.11	3.12
143.91	2.10

60.78% C_{ax}

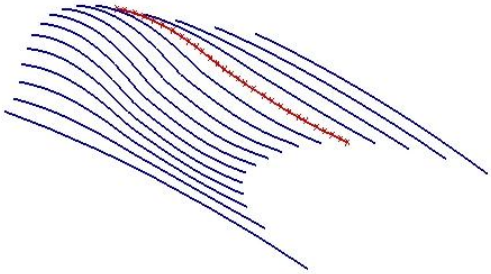

X	Y
136.44	37.91
136.76	36.28
136.95	35.29
137.23	33.86
137.61	32.09
138.02	30.28
138.52	28.13
138.97	26.33
139.42	24.51
139.82	22.85
140.30	20.96
140.79	19.25
141.24	17.79
141.59	16.57
141.89	15.43
142.30	13.68
142.52	12.55
142.74	11.13
142.89	9.82
142.99	8.42
143.02	6.92
142.98	5.81
142.85	4.85

66.30% C_{ax}

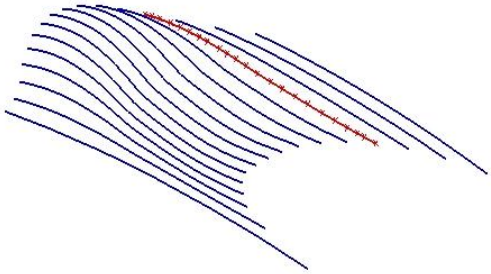

X	Y
135.68	41.44
136.00	40.27
136.43	38.67
136.91	36.69
137.36	34.88
137.78	33.16
138.28	31.09
138.57	29.91
139.03	27.94
139.33	26.58
139.68	24.98
139.95	23.69
140.16	22.72
140.42	21.51
140.64	20.52
140.92	19.00
141.33	16.62
141.55	14.92
141.74	13.41
141.85	12.15
141.95	10.91
142.01	9.86
142.02	8.85
141.94	7.99

71.82% C_{ax}

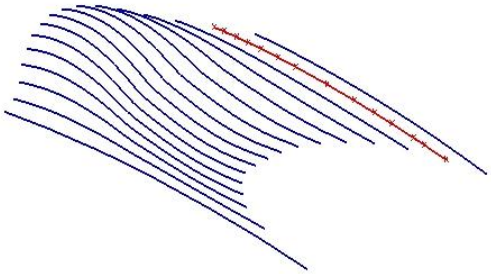

X	Y
134.50	45.54
135.48	42.42
135.95	40.84
136.85	37.68
137.49	35.21
138.20	32.29
139.09	28.37
139.96	23.90
140.37	21.39
140.72	18.96
140.96	17.14
141.14	15.45
141.31	13.69
141.34	12.28

82.87% C_{ax}

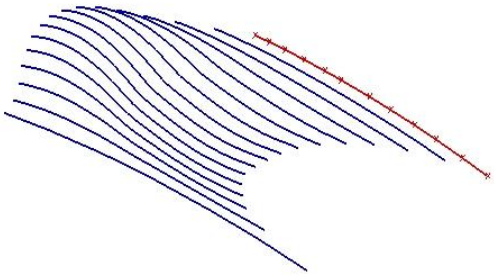

X	Y
132.81	50.35
134.11	46.71
135.38	42.85
136.31	39.76
137.25	36.30
138.03	33.25
138.92	29.18
139.39	26.84
139.92	23.89
140.35	21.16
140.64	18.91
140.83	16.88

Thereafter annular

2nd Stator Hub

Identical to rotor hub, mirrored and scaled to an axial chord of 28.16 mm

2nd Stator Tip

Pressure Surface

X	Y	Z
202.2	11.2	47.3
202.2	11.1	47.4
202.2	10.9	47.5
202.2	10.7	47.6
202.2	10.6	47.8
202.2	10.5	48.0
202.2	10.5	48.2
202.2	10.4	48.4
202.2	10.4	48.6
202.2	10.5	49.6
202.3	10.0	52.6
202.3	9.1	55.5
202.3	7.8	58.2
202.4	6.2	60.8
202.5	4.4	63.1
202.5	2.3	65.4
202.5	0.1	67.4
202.5	-2.3	69.3
202.4	-4.7	71.1
202.4	-7.2	72.8
202.3	-9.7	74.5
202.1	-12.3	76.1
202.0	-14.8	77.7
201.7	-17.4	79.2
201.5	-20.0	80.7
201.2	-22.7	82.2
200.9	-25.3	83.6
200.6	-27.9	85.1
200.2	-30.4	86.5
200.2	-30.5	86.6
200.2	-30.6	86.6
200.2	-30.6	86.7
200.2	-30.7	86.8
200.2	-30.7	87.0
200.2	-30.7	87.1
200.2	-30.6	87.2
200.2	-30.6	87.3

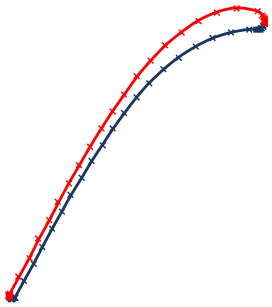

Suction Surface

X	Y	Z
202.2	11.2	47.3
202.2	11.4	47.2
202.2	11.6	47.2
202.2	11.8	47.2
202.1	12.0	47.3
202.1	12.2	47.3
202.1	12.4	47.4
202.1	12.5	47.6
202.1	13.2	48.4
202.0	13.7	51.6
202.1	13.1	54.7
202.2	11.8	57.7
202.3	10.0	60.4
202.3	8.0	62.9
202.4	5.7	65.2
202.5	3.2	67.4
202.5	0.6	69.3
202.5	-2.0	71.2
202.4	-4.7	73.0
202.4	-7.5	74.8
202.2	-10.2	76.4
202.1	-13.0	78.1
201.9	-15.9	79.7
201.6	-18.7	81.2
201.4	-21.5	82.8
201.0	-24.4	84.3
200.7	-27.2	85.9
200.3	-29.9	87.4
200.3	-30.0	87.4
200.2	-30.1	87.5
200.2	-30.2	87.5
200.2	-30.3	87.4
200.2	-30.4	87.4
200.2	-30.5	87.3
200.2	-30.6	87.3

Appendix B: Turbine Test Section Overview